VORTEX-INDUCED VIBRATIONS OF STRUCTURES

Thesis by

Shawn Anthony Hall

In Partial Fulfillment of the Requirements

for the Degree of

Doctor of Philosophy

California Institute of Technology

Pasadena, California

1981

(Submitted on December 22, 1980)

ACKNOWLEDGEMENTS

For his guidance throughout this investigation, I owe many thanks to Professor W.D. Iwan, whose insight has often kept me from exploring the wrong avenues, and whose unflagging optimism has helped me persevere in darker moments.

The financial support of the National Science Foundation and the California Institute of Technology is gratefully acknowledged.

I wish also to express my gratitude to a number of people in the Caltech community whose helpfulness has been invaluable. In particular, many thanks to my friends in the Aeronautics Shop, who have generously lent technical advice and assistance whenever I have needed them; to Edith Huang of Caltech's Computer Center, whose cheerfulness and expertise have saved the day on may occasions; to my colleague, Dr. Charles Krousgrill, for the use of his convenient and versatile plotting routine GRPLOT; to Professor T.K. Caughey for help with analog computer simulations; to Mrs. Beth Cooper for tips on *troff;* to Mr. Raul Relles for assistance with the spectrum analyzer; to Mrs. Cecilia Lin and Mrs. Gloria Jackson for help with several Tables and Figures; and to Professor Andreas Aebi for an oral translation of Strouhal's paper.

Special thanks are due to numerous personal friends who, throughout the course of this research, have listened to gripes, offered suggestions, lended moral support, and shared a thousand experiences. In particular to my colleague, Dr. Edward Ruth, goes heartfelt gratitude for his good friendship. And for Miss Charlotte Clark, whose companionship has brightened many tedious months of writing, I reserve my fondest thanks, with a wish for good luck in her continuing study at Caltech.

Finally, to the members of my family, who have undergirded my education with years of encouragement and guidance, I wish to express my gratitude and my love. Deepest appreciation goes to my mother, Mrs. Violetta M. Hall, whose efforts and sacrifice have made my education possible. For a quarter-century of support in spirit as well as in substance, this thesis is lovingly dedicated to her.

ABSTRACT

Vortex-induced oscillations, often of concern when a bluff structure is exposed to fluid cross-flow, are considered herein using a semi-empirical modeling approach. Based on the fluid momentum theorem, the model involves a highly simplified abstraction of the complex flow field, and major assumptions concerning the nature of the coupling between the fluid and the oscillating structure.

Three prototype problems are studied, including harmonically forced cylinders, spring-mounted cylinders, and taut elastic cables; in each case the structure is assumed to be of circular cross-section and situated in a uniform cross-flow. Only oscillations transverse to the flow are considered. The problem of modal interaction for elastic cables, typically of interest when the fluid flow excites high-mode-number resonances, is given particular attention.

The model produces a set of nonlinear, ordinary differential equations describing the coupled fluid/structure oscillations. Steady-state oscillatory solutions to these equations are found analytically and are examined for stability. Using various regression techniques, the steady-state solutions are then fit to experimental data for forced and spring-mounted cylinders. Finally, the model's predictions for elastic cables are used to postulate a qualitative picture of modal interaction, certain features of which have been observed experimentally.

TABLE OF CONTENTS

CHAPTER I

INTRODUCTION

Vortex induced oscillations are possible whenever a bluff object is exposed to a flowing fluid. In most structural engineering applications, the induced vibrations of interest are those of the bluff object itself, typically a cable or beam exposed to a cross-flow of air or water, examples of which are mooring lines, guy wires, electric transmission lines, towers, masts, and antennas. Such structures, as well as more complex ones such as bridges, may be damaged or even destroyed by severe oscillations of this type.

In other, somewhat different examples of the same phenomenon, the induced vibrations are not those of the bluff object (which may in fact be rigid), but those of some auxilliary mechanical system, often a resonating column of air. Several familiar musical instruments operate in this fashion, and serve as useful illustrations in the following discussion.

1.1 Basic Mechanisms: Vortex Shedding and Lock-in

Periodic vortex shedding takes place when a flowing fluid is unable to negociate its way smoothly around a bluff object. For example, in the case of a circular cylinder, one cycle of the shedding process is sketched in Fig. 1.1. First, flow separation occurs at points S_1 and S_2, and the resulting pair of vortex sheets, being unstable, roll up into vortices V_1 and V_2 (Fig. 1.1a) [1, 54]. Next, the developing vortices interfere: V_1 draws fluid from the other side across the wake (Fig. 1.1b), causing the detachment or "shedding" of V_1 (Fig. 1.1c) [21]. To complete the cycle, the shedding process is repeated for V_2 (Figs. 1.1d,e). Subsequently, as new vortices are formed to replace V_1 and V_2, the cycle repeats itself with a frequency f_v. Flowing downstream, the detached vortices typically

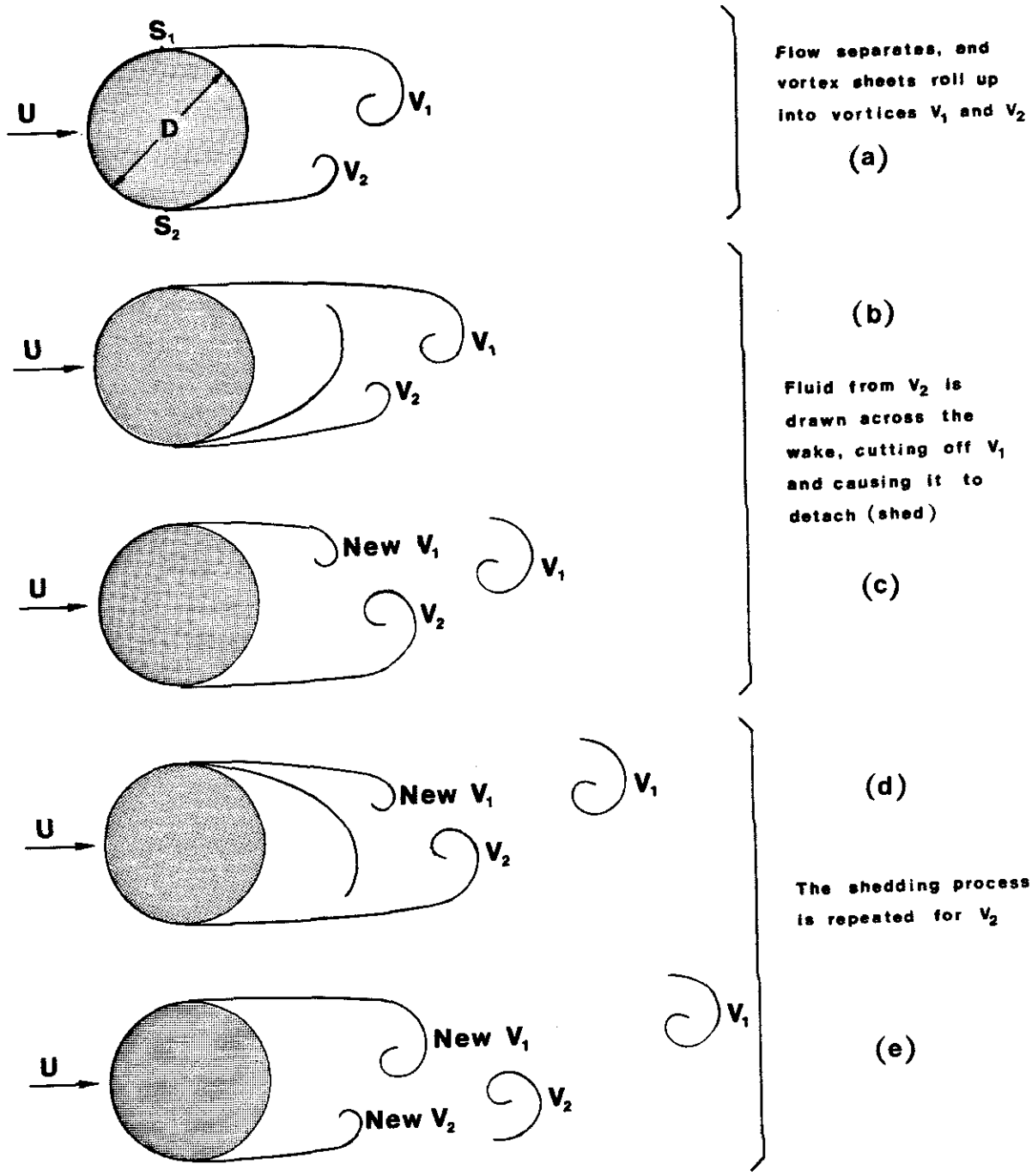

Fig. 1.1: The Mechanism of Vortex Shedding.

arrange themselves in two staggered parallel rows, called a "vortex street," as shown in the flow visualization photograph, Fig. 1.2.

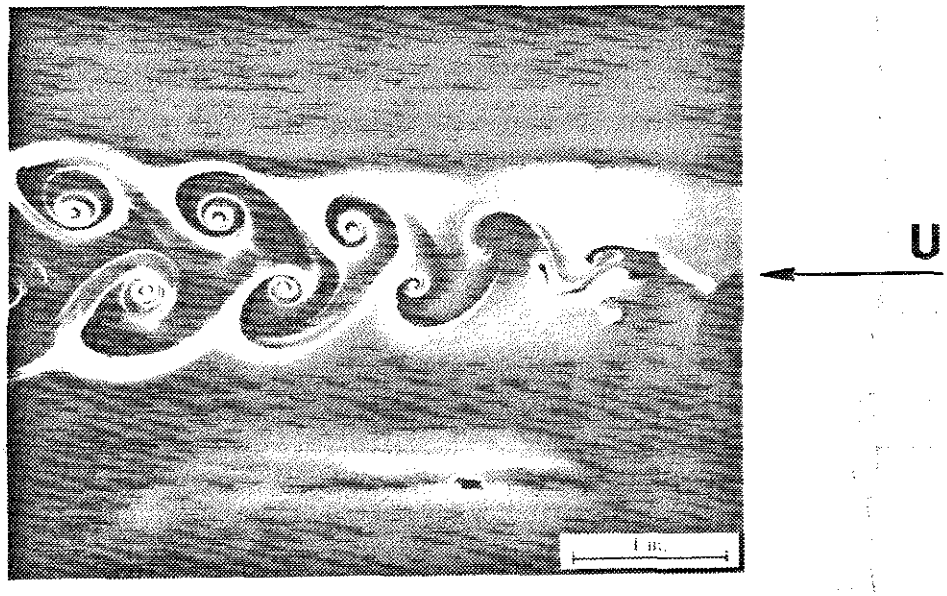

Figure 1.2. The Wake of a Stationary Cylinder (Re = 200, f_v = 28) [37].

In the absence of induced structural oscillations, the vortex-shedding frequency satisfies, according to experiment,

$$f_v = f_s, \tag{1.1}$$

where the **natural vortex-shedding frequency** f_s, also called the **Strouhal frequency**, is defined by

$$f_s = \frac{SU}{D}. \tag{1.2}$$

In this experimentally determined relationship, U is the free-stream velocity, D is a characteristic cross-sectional dimension of the bluff body, and S, the so-called **Strouhal number**, is an experimentally specified parameter which depends significantly on geometry and weakly on Reynolds number [7].

When a mechanical system with **natural frequency** f_n is exposed to the periodic pressure forces of such a flow, the resulting mechanical vibrations, at

response frequency f, are said to be vortex induced. If the induced oscillations are sufficiently small, the vortex shedding proceeds undisturbed at its own natural frequency f_s, and induces the mechanical system to oscillate likewise, thus

$$f = f_v = f_s. \tag{1.3}$$

However, for a range of f_s (i.e. a range of flow speed U) bracketing the resonance condition $f_s = f_n$, induced vibrations may become large enough to cause the mechanical system to take control of the response, initiating a condition called "lock-in," where the natural shedding frequency f_s is suppressed in favor of the natural mechanical frequency f_n, such that

$$f = f_v \approx f_n. \tag{1.4}$$

Once lock-in is initiated, mechanical oscillations grow to much larger amplitudes, not only on account of the near-resonance condition $f \approx f_n$, but also because the mechanical motion provides a synchronous tripping mechanism for the vortices which strengthens and organizes the shedding process, producing greater fluctuating pressures. Such large amplitude mechanical oscillations are usually of the greatest interest in practical situations.

As previously mentioned, the most familiar examples of this phenomenon are musical. When air is directed into the foot of a reedless organ pipe, it impinges on a bluff, vortex-shedding lip. The flow speed and lip geometry are arranged to produce a natural vortex-shedding frequency (f_s) lying close to the natural acoustic frequency of the pipe (f_n), whereby lock-in is initiated, and an audible musical tone is produced. Flutes and other reedless woodwinds operate similarly.

Such instruments owe their practical usefulness to the persistence of lock-in

over a fairly wide range of flow speed (i.e. a range of f_s), called the **lock-in band.** If the lock-in band were very narrow, audible musical sounds would disappear whenever an organ's wind-pressure regulation or a flutist's breath control were not perfect. However, *in reality the width of the lock-in band is sufficient to permit* a certain amount of variability in the air stream, the only effect being a slight rise or fall in the pitch of the instrument [53, §322a], in accordance with the approximate condition $f \approx f_n$ in Eq. (1.4).

1.2 The Focus of This Investigation

In the current investigation, attention is restricted to the type of problem most significant to structural engineering, as discussed at the opening of this chapter, for which the vibrating mass is the bluff, vortex-shedding body itself. A *simplified, semi-empirical, mathematical* model for such oscillations is proposed, based on previous work by Iwan and Blevins [35]. Assuming uniform flow, the model is analyzed and compared to experimental results for three types of spanwise-uniform structures of circular cross-section, including

- *harmonically forced* rigid cylinders
- spring-mounted rigid cylinders
- taut elastic cables

In the latter analysis, considerable attention is given to the problem of interacting cable modes. Each natural frequency f_n $(n = 1, \ldots, \infty)$ of a cable possesses an associated lock-in band, which may interfere with that of either neighbor (f_{n-1} or f_{n+1}) as the two modes compete for control of the shedding process. When adjacent frequencies f_n are very close together, the interference may extend to three or more modes. The importance of such modal interaction has long been recognized, even in the pioneering experimental work of Strouhal [65].

and has been further emphasized in recent years by practical problems with long, undersea cables [12]. Yet, because of the mathematical difficulties involved, the problem has hitherto been neglected in semi-empirical investigations of the current type [36, 64].

1.3 The Organization of This Document

In Chapter 2, a brief historical account of the subject is given, after which experimental data for rigid cylinders and cables are discussed. Results from a modern reproduction of Strouhal's experiment are included, as obtained during the course of this investigation in an effort to study the problem of modal interaction.

In Chapter 3, the aforementioned mathematical model for vortex-shedding structures is developed, using intuition provided by the rigid cylinder experiments. Extension of the model to cables is made tractable by finite-mode approximations, in which modes not likely to be locked-in are neglected. In particular, a two-mode approximation is used to study the effects of modal interaction.

In Chapters 4 and 5, the nonlinear differential equations generated by the model are solved analytically in an approximate sense, using a well-known asymptotic method. Emphasis is placed on unifying the mathematical treatment for all of the cases considered (Chapter 4 and Section 5.2), although the final stage of solution for each type of structure must be carried out independently (Sections 5.3 through 5.6).

In Chapter 6, optimization methods are developed for selecting numerical values of certain constants embedded in the model. The objective of these methods is to obtain the best possible model fit to the experimental data for

rigid cylinders, as presented in Chapter 2.

In Chapter 7, results derived in Chapters 3 through 6 are presented graphically and compared to experimental data. Conclusions and a summary are given in Chapter 8.

1.4 Notation

Following Chapter 8, a complete list of symbols used in this document is given. Verbal definitions are stated whenever possible, together with reference information, including

- the location in the text where each symbol is first defined or used
- the extent (Chapter-wise or Section-wise) over which the given definition is valid
- cross-references to relevant Equations, Figures, Tables, or Sections
- the physical dimensions of the symbol.

In general, vectors are indicated by **bold** type, while matrices are enclosed in square brackets.

Special remarks are warranted regarding the notation for frequencies:

- Although the symbol f is occasionally used otherwise, whenever it refers to freqency, the dimensions are Hertz.
- The symbol ω is always reserved for angular frequency, such that $\omega_k \equiv 2\pi f_k$, where k is any subscript, provided f_k refers to a frequency.
- The symbol Ω is always reserved for dimensionless frequencies wich have been normalized by the angular Strouhal frequency ω_s, such that $\Omega_k \equiv C\frac{\omega_k}{\omega_s}$, where k is any subscript, while C is a constant, usually equal to 1 (but not always).

CHAPTER II

EXPERIMENTAL OBSERVATIONS

2.1 Historical Backgound

Vortex-induced oscillations have been utilized for musical purposes since ancient times, although vortex shedding was not recognized as the source of vibration until quite recently. For example, the principle of the organ pipe, mentioned in Chapter 1, was discovered accidently in the third century B.C. by Ktesibios of Alexandria [13], and thereafter the art of organ building developed empirically without any fundamental knowledge of the sound-generating mechanism involved [72, p. 401].

During the Renaissance, Leonardo da Vinci made several crude sketches of vortices in the wakes of bluff bodies (Fig. 2.1.1), but, as suggested by some Leonardo scholars [48, pp. 190-191], these sketches appear to depict recirculating vortices[1] rather than the periodically shedding vortices which cause vibration, so it is doubtful that Leonardo could have perceived the connection between vortices and structural vibration.

Figure 2.1.1. Bluff body wakes, as sketched by Leonardo da Vinci [48].

1. See Fig. 2.2.1, the second sketch from the top.

The first systematic investigation of vortex-induced oscillations was completed in 1878 by Strouhal [65], whose experiment consisted of spinning a stretched wire or rod about an axis parallel to its length, thus creating a lengthwise-uniform crossflow. Although he obtained important results, discussed below in connection with more recent experiments, Strouhal himself had no knowledge of the vortex-shedding mechanism per se. In fact, in accordance with a notion prevalent at the time, he believed that the stretched wire oscillated parallel to the wind, and that oscillations were induced by a friction-like force akin to the action of a bow on a violin string. These misconceptions were dispelled by Rayleigh, who observed experimentally in 1879 that the wire actually vibrates perpendicular to the wind [52],[2] and later correctly identified the source of vibration as the instability of vortex sheets [53, p. 412].

Subsequently, vortex wakes themselves were studied. In 1908 Bénard [3] experimentally observed the periodic vortex-shedding phenomenon and measured the spacing of vortices, while von Karman [71] in 1912 theoretically established why the two rows of vortices should be staggered rather than symmetrical, and predicted a numerical value for the ratio of longitudinal to lateral vortex spacing.

Since von Karman's analysis, numerous studies of vortex wakes and induced vibration phenomena have been published, both theoretical [1, 6, 21, 33, 35, 36, 39, 54, 55, 62, 63, 64] and experimental [2, 5, 10, 12, 14, 15, 16, 17, 18, 19, 20, 22–30, 31, 37, 38, 41, 42, 45, 49, 50, 51, 56, 57, 58–60, 67, 69, 70], reviews of which have been compiled by Marris in 1964 [40] and Blevins in 1977 [7]. Results most pertinent to the current investigation, dealing with circular rigid cylinders and elastic cables, are presented below.

---

2. Rayleigh noted that the wire sometimes whirls in an elliptical shape, with the major axis perpendicular to the flow. This phenomenon is associated with non-ideal wires, for which the tension varies with the level of vibration [43]. Such behavior is neglected in the analyses herein, which assume ideal wires having constant tension.

2.2 Stationary Cylinders

The flow behind a rigid circular cylinder at rest changes dramatically with the free-stream Reynolds number, as indicated in Fig. 2.2.1, but vortex shedding at a well-defined natural frequency f_s persists, first in a laminar state and then in a turbulent state, over the entire Reynolds number range from 40 to 3×10^5, as well as for Reynolds numbers above 3.5×10^6.

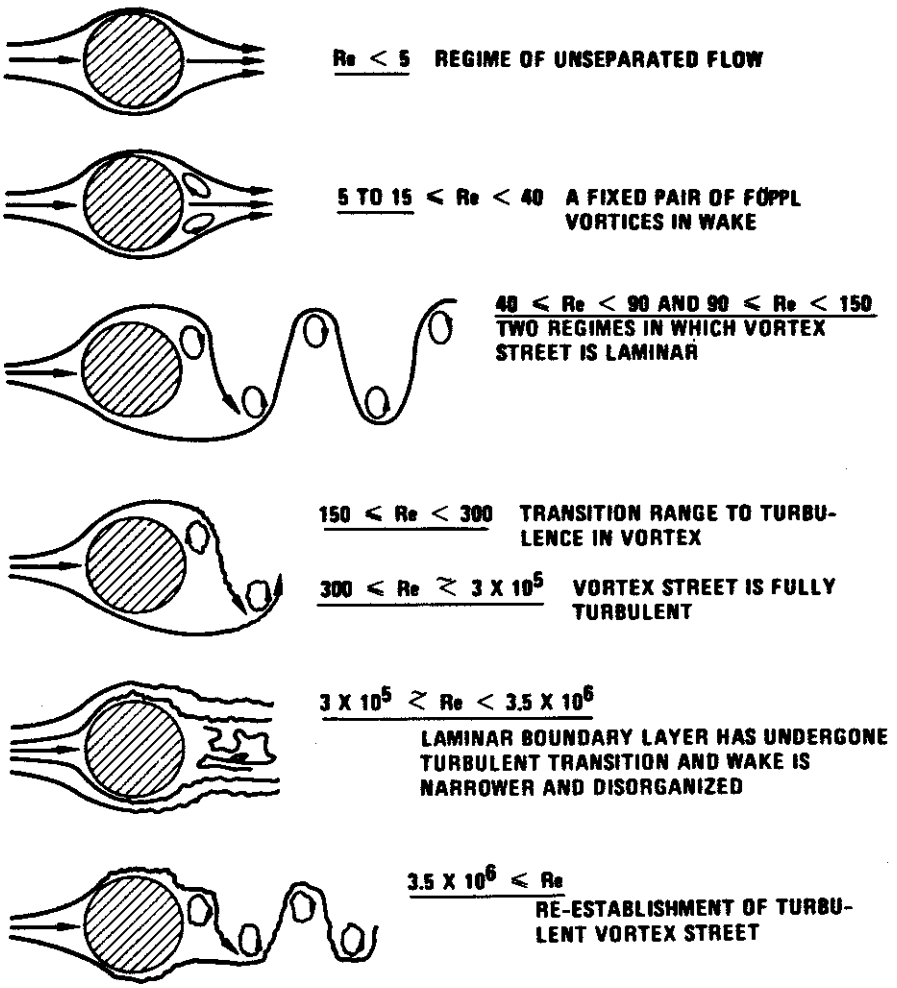

Figure 2.2.1. The Wake of a Stationary, Circular Cylinder [7].

The natural shedding frequency f_s is given by Eq. (1.2), a relationship first deduced by Strouhal in an experiment previously described.[3] For a circular

cylinder, D is the diameter, while the Strouhal number S depends on the Reynolds number $\frac{UD}{\nu}$ as shown in Fig. 2.2.2, which is a compilation of results from numerous experiments.[4] The region bounded by solid lines indicates scatter in the data, while that bounded by dotted lines signifies, in accordance with Fig. 2.2.1, that there is a broad band of shedding frequencies in the Reynolds number range from 3×10^5 to 3.5×10^6 [57].

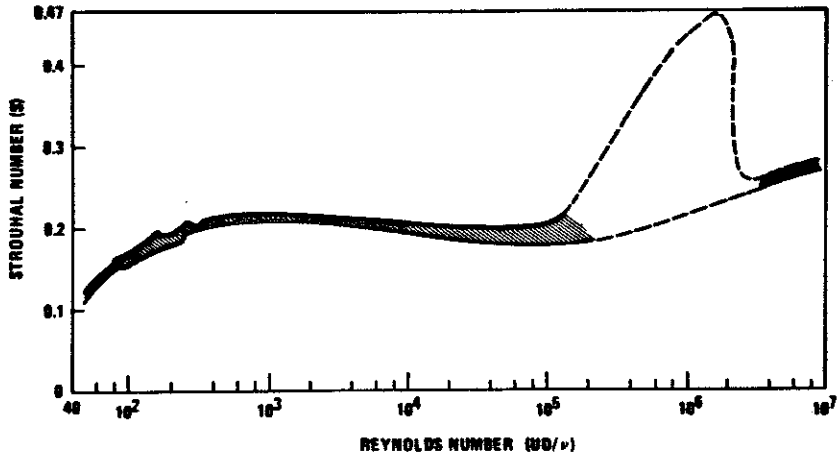

Figure 2.2.2. The Strouhal Number for Circular Cylinders [7].

---

3. Although Strouhal used flexible wires as well as rigid rods in his experiments, a stretched wire, free to vibrate, adequately approximates a stationary rigid cylinder if the vibration amplitude is very small, which is generally true outside the lock-in band.

4. Strouhal's original results are not included. The concept of Reynolds number, introduced by Reynolds in 1883 [61] , was unknown to Strouhal in 1878. In fact, the Re range of Strouhal's experiments was $200 < Re < 6000$, but Strouhal presumed S to be constant, and simply averaged all of his results, obtaining $S = 0.185$. This value is sightly lower than the average value according to the more recent experiments (Fig. 2.2.2). The reason for the discrepancy is probably the crudeness of Strouhal's apparatus, discussed further in Section 2.5.

2.3 Forced Cylinders

When the vibrations of a vortex-shedding structure are forced by an external driving mechanism (e.g. Fig. 2.3.1) rather than induced by the flow itself (e.g. Fig. 2.4.1), the concept of lock-in is somewhat different than that discussed in Chapter 1. For both cases, lock-in involves the violation of Strouhal's relationship $f_v = f_s$, and the synchronism of vortex shedding with structural vibration at a frequency characteristic of the structure. However, as discussed in Chapter 1, the locked-in response frequency f for the induced case is very close to the natural structural frequency f_n, depends somewhat on f_s, and is unknown *a priori*, whereas for the forced case, the locked-in response frequency is necessarily the forcing frequency f, which is known *a priori*. Thus, the locked-in condition for the forced case, replacing Eq. (1.4), is simply

$$f_v = f, \tag{2.3.1}$$

while the non-locked-in condition is

$$f_v \neq f. \tag{2.3.2}$$

Koopman [37] has measured the extent of lock-in for rigid circular cylinders which are harmonically forced (as in Fig. 2.3.1) and exposed to cross-flow at low Reynolds numbers. For each value of Re, the natural shedding freqency f_s was determined directly for the stationary cylinder by means of a hot-wire in the wake. Then, for a fixed, dimensionless forcing amplitude

$$B = \frac{\frac{1}{2}[\text{ Peak-to-peak displacement of cylinder axis}]}{D}, \tag{2.3.3}$$

the forcing frequency f was varied slowly about f_s until synchronism of the vortex wake with the cylinder vibration was lost, first at the lower lock-in limit f^-, and again at the upper limit f^+. These measurements, repeated for several values of B at each of three Reynolds numbers, are recorded on Fig 2.3.2, where the independent variable σ is a measure of detuning between the forcing fre-

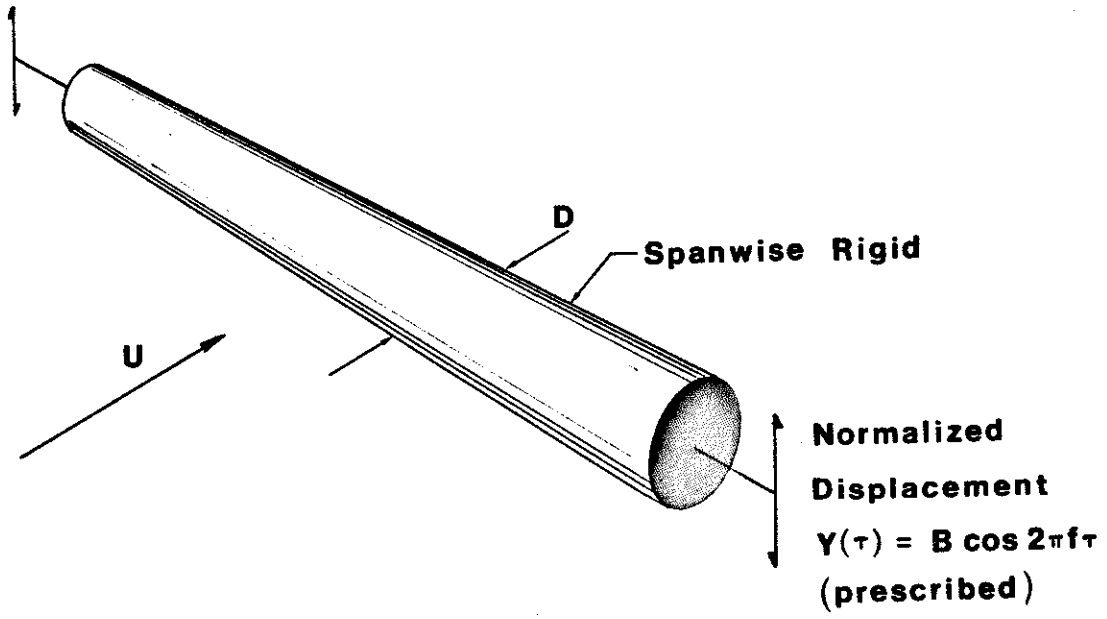

Figure 2.3.1. Forced Cylinder.

quency f and the natural vortex-shedding frequency f_s,

$$\sigma \equiv \frac{f - f_s}{f_s}. \tag{2.3.4}$$

Experimentally, there was additionally a well-determined amplitude threshold B_0 below which lock-in failed to exist even for values of σ approaching zero. The locked-in region thus lies above the threshold amplitude B_0 and between the boundaries (σ^-, σ^+), where (σ^-, σ^+) are the normalized counterparts of (f^-, f^+).

In the same investigation Koopman obtained a pair of flow-visualization photographs, reproduced here as Figs. 2.3.3, which clarify the nature of lock-in, particularly the amplitude threshold. Both photographs are top views. Fig. 2.3.3a shows the locked-in wake of a vibrating cylinder ($B > B_0$, $\sigma^- < \sigma < \sigma^+$), with the vortex filaments aligned parallel to the axis. In contrast, Fig. 2.3.3b shows the non-locked-in wake of a stationary cylinder ($B = 0$), with the vortex filaments inclined to the axis. Apparently, within the lock-in frequency band, a sufficiently large amplitude of cylinder vibration provides a tripping mechanism

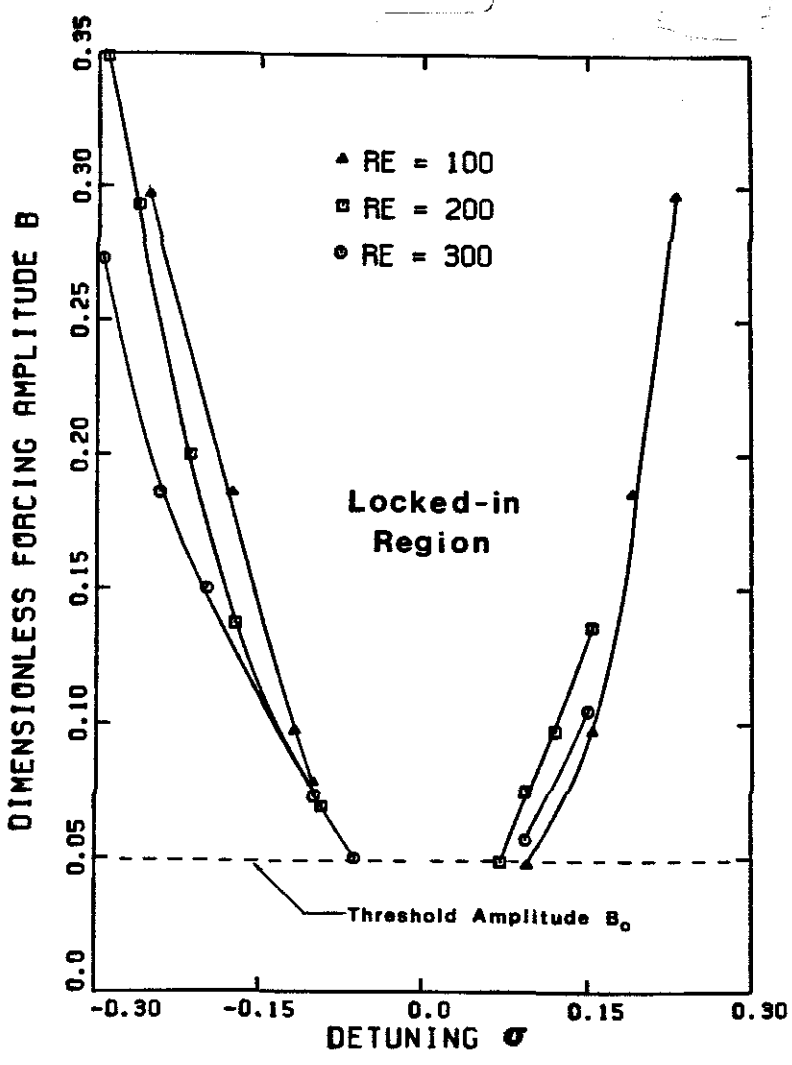

Figure 2.3.2. Experimental Lock-in Boundaries for Forced Cylinders [37].

for the vortices, favoring a certain fixed phase relationship between the periodic shedding and the periodic cylinder displacement. Therefore, at least for the low Reynolds numbers studied by Koopman, locked-in vortex shedding is nearly two-dimensional and well correlated along the span,[1] while non-locked-in shedding is highly three-dimensional and uncorrelated.

A study by Toebes [67] at Reynolds numbers of 46,000 and 68,000 indicates that these distinctions may be less clear for more turbulent flows; the degree of correlation between two points (P_1, P_2) along the span then appears to increase

1. There are tunnel wall effects in Koopman's photograph.

continuously with the cylinder vibration amplitude rather than increasing suddenly at a certain amplitude threshold, and also appears to decrease sharply with increasing spanwise distance between P_1 and P_2.

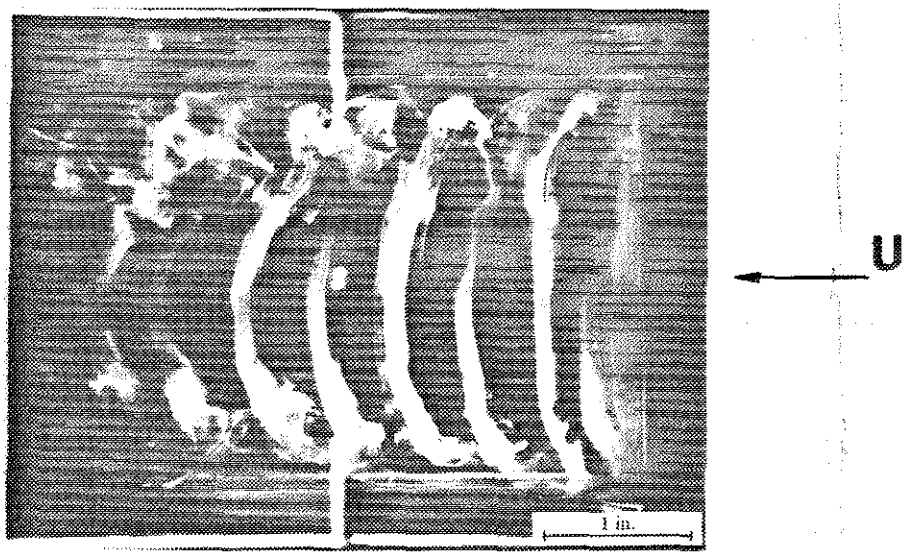

Figure 2.3.3a. Locked-in Vortex Shedding; Re = 200, f_v = 28 [37].

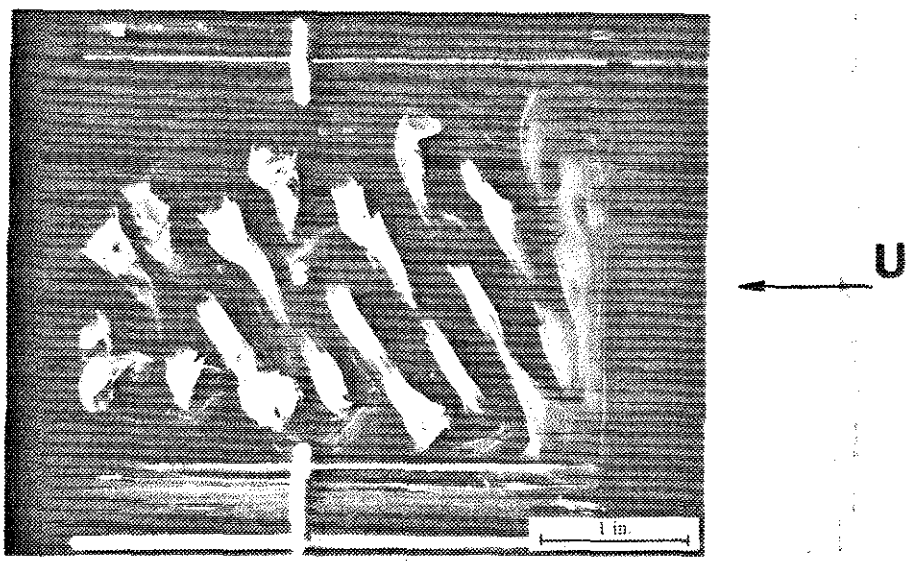

Figure 2.3.3b. Non-locked-in Vortex Shedding; Re = 200, f_v = 28 [37].

2.4 Spring-Mounted Cylinders

Feng [16] has measured response amplitudes and frequencies versus flow velocity for 3" diameter circular cylinders mounted elastically in a wind tunnel. Fig. 2.4.1 is a schematic of such a cylinder and its elastic mounting, for which the first (and only)[1] natural freqency is

$$f_n \equiv f_1 = \frac{1}{2\pi}\sqrt{\frac{k}{M}}\,, \tag{2.4.1}$$

while the fraction of critical damping ζ and mass ratio η are defined by

$$\zeta \equiv \frac{b}{2\sqrt{kM}}, \qquad \eta \equiv \frac{\rho D^2}{M}. \tag{2.4.2}$$

In these equations, ρ is the fluid density, while M, k, and b are, respectively, the per-unit-length structural mass, damping coefficient, and spring constant.

Experimental results for five values of ζ are shown in Fig. 2.4.2. The independent variable has been converted, according to Eq. (1.2), from flow speed U to the **fluid-structure detuning** d_f, defined as

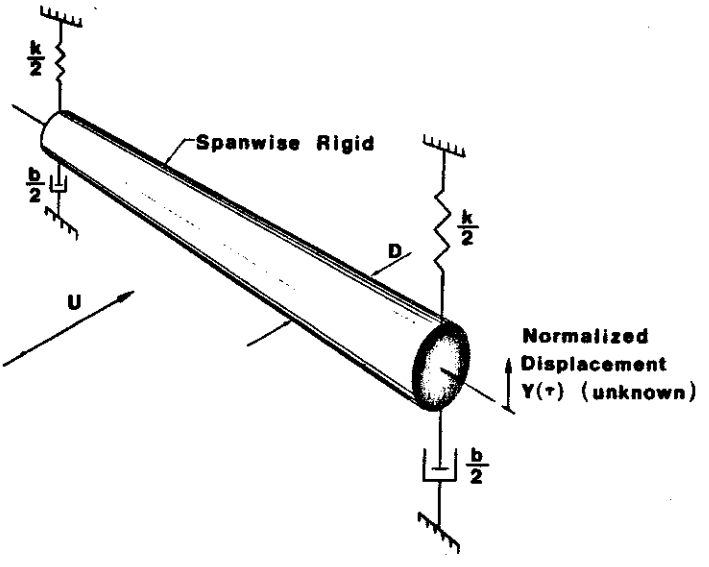

Figure 2.4.1. Spring-Mounted Cylinder.

---

1. The cylinder is not permitted to rock side-to-side.

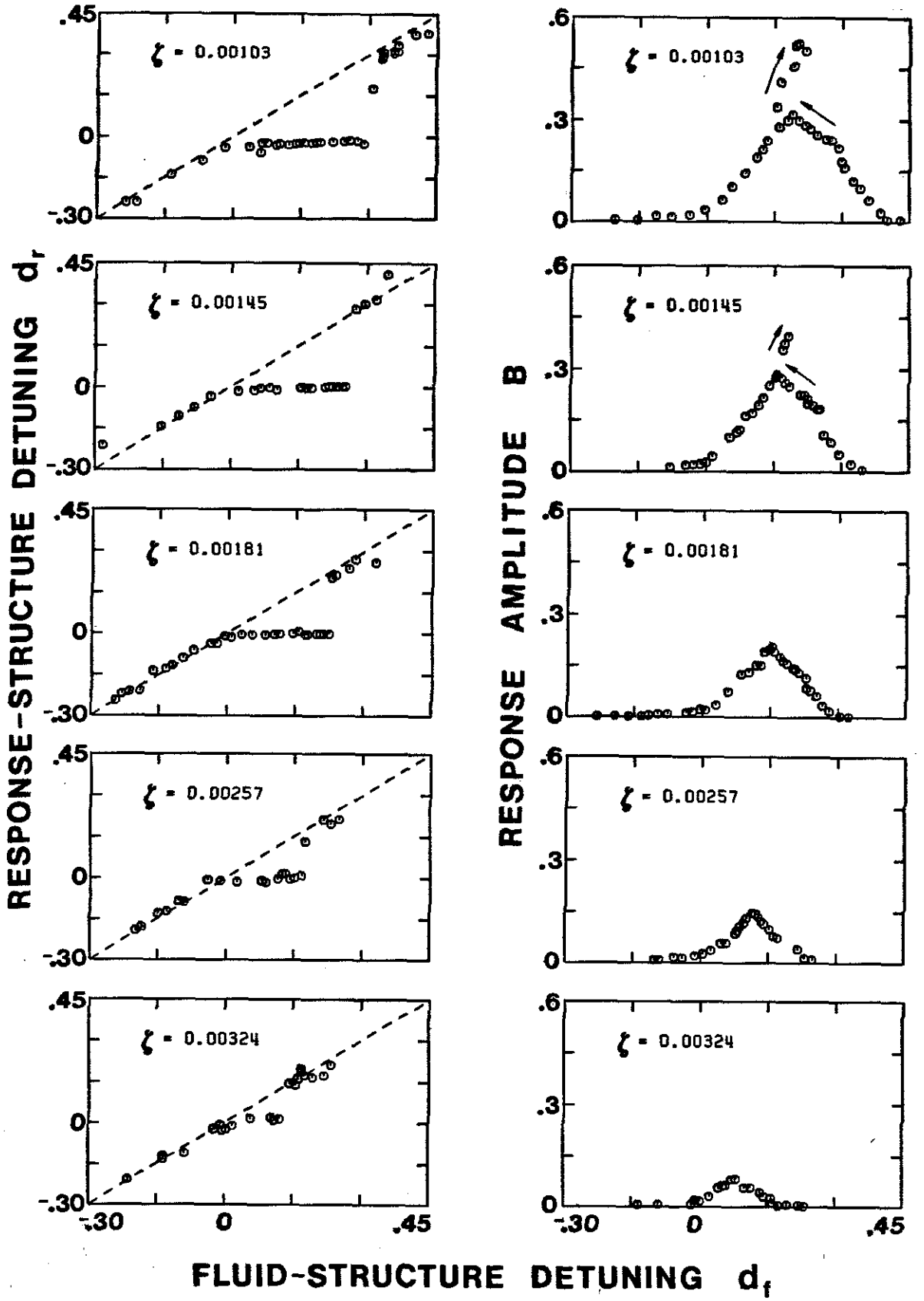

Fig. 2.4.2: Response of Spring-Mounted Cylinders; $\eta = 0.00514$.

$$d_f \equiv \frac{f_s - f_1}{f_s} = 1 - \frac{Df_1}{SU}. \qquad (2.4.4)$$

Likewise, the dependent frequency variable has been converted from the system response frequency[2] f to the **response-structure detuning** d_r, defined as

$$d_r \equiv \frac{f - f_1}{f_s} = \frac{Df_1}{SU}\left[\frac{f}{f_1} - 1\right]. \qquad (2.4.5)$$

The normalized response amplitude B is defined as in Eq. (2.3.3). To implement the conversions (2.4.4) and (2.4.5) it is necessary to assume a value for the Strouhal number S. Referring to Fig. 2.2.2, the value $S = 0.20$ is adopted, since Feng's experiments involve Reynolds numbers from 10,000 to 50,000.

On each frequency plot, data points lying along a nearly horizontal line at $d_r \approx 0$ comprise the lock-in band [see Eq. (1.4)], during which the vortex shedding is observed to be spanwise correlated [16, pp. 26-29], and the cylinder amplitude B rises to its peak.[3] Conversely, the points lying along the line $d_r = d_f$ represent unlocked response [see Eq. (1.3)], for which the vortex shedding is spanwise uncorrelated and the amplitude response is small.

It is interesting to contrast these results to those for the forced cylinder. In both cases, spanwise correlation of vortex shedding occurs during lock-in. However, for the spring-mounted cylinder, the lock-in band is highly skewed to the right of the exact resonance point $d_r = d_f = 0$ ($\Omega = \Omega_1 = 1$), whereas for the forced cylinder, the lock-in band is symmetrically located on either side of the exact resonance point $\sigma = 0$ ($\Omega = 1$). As suggested by the discussion at the opening of Section 2.3, this discrepancy may be attributable to the qualitative difference between forced vibrations and vortex-induced vibrations.

---

2. Feng actually measured the vortex-shedding frequency f_v with hot-wires. For steady-state induced vibrations however, according to Eqs. 1.3 and 1.4, $f_v = f$ always.
3. Hysteretic behavior in the amplitude response, experimentally observed at low values of ζ, is indicated by the arrows on Figs. 2.4.2a,b.

2.5 Elastic Cables: A Modern Reproduction of Strouhal's Experiment

2.5.1 Motivation for the Experiment

Using the experimental apparatus described in Section 2.1, Strouhal [65] measured the frequency response of taut, freely vibrating wires (i.e. cables) having fixed ends. He observed lock-in for mode numbers as high as $n = 27$, and witnessed the phenomenon of modal interference extending to two and even three modes, as discussed briefly in Section 1.2.

Unfortunately, Strouhal's description of lock-in and modal interference are very crude. In particular, the concept of lock-in bands is absent from his data; for each mode he cites a single flow speed corresponding to lock-in, rather than a range of flow speed. This shortcoming is undoubtedly attributable to the crudeness of his apparatus, notably the unsteadiness of the rotational speed used to create the cross-flowing air-stream.[1] Although Strouhal recognized the importance of steadiness in the airstream and paid considerable attention to it, he was limited by nineteenth-century technology, and found that the best available system to produce steady rotation was simply a hand-operated crank.

Since Strouhal's work, although numerous laboratory and field experiments have been conducted to study the vortex-induced vibration of cables [12, 27, 38, 41, 49, 69], only a few studies present data on the modal lock-in bands [12], and virtually none has dealt specifically with the interaction of lock-in bands for high mode numbers. Therefore, to obtain valuable physical insight into the problem of modal interference, a simple, modernized version of Strouhal's experiment was constructed during the course of this investigation.

---

1. Recall from Section 2.1 that the stretched wire is revolved about an axis parallel to its length.

2.5.2 Experimental Equipment

Two photographs of the apparatus used are shown in Fig. 2.5.1, while a drawing is given as Fig. 2.5.2. Labeled features of the drawing are described below:

- *Vibrating Wire:* Steel music wire, diameter D = 0.013", length L = 16.75". The ends were wrapped around taper pins, which allowed tuning to a fundamental frequency f_1 = 440 Hz (± 1 Hz). The spin radius (i.e. the distance from the axis of rotation to the wire) was R = 7.75".
- *Center Shaft:* $\frac{3}{8}$ inch diameter threaded rod.
- *Vertical Struts:* Streamlined tube, whose closest surface was located approximately 57 diameters D from the vibrating wire.
- *Cross-braces:* Three pairs of cross-braces (shown in the photographs but not in sketch) were used, consisting of stranded steel wire tightened by turnbuckles. These served two purposes: first, to stiffen the structure; second, to permit alignment of the motor shaft with the lower bearing, by adjustment of tension in the wires.
- *Optical Pick-up:* General Electrics model H13A2 interrupter module, consisting of an infra-red emitting diode optically coupled to a photo transistor, all in a plastic housing. Through the gap in the housing, the light beam was chopped once per revolution by the *interrupter strip*, thereby briefly switching the output transistor from an "on" to an "off" state. These pulses were used to measure the period of revolution T, and hence the flow speed U.
- *Flywheel:* Steel, mass 10 lbm, diameter 6". Addition of the flywheel improved the speed regulation by a factor of 4.

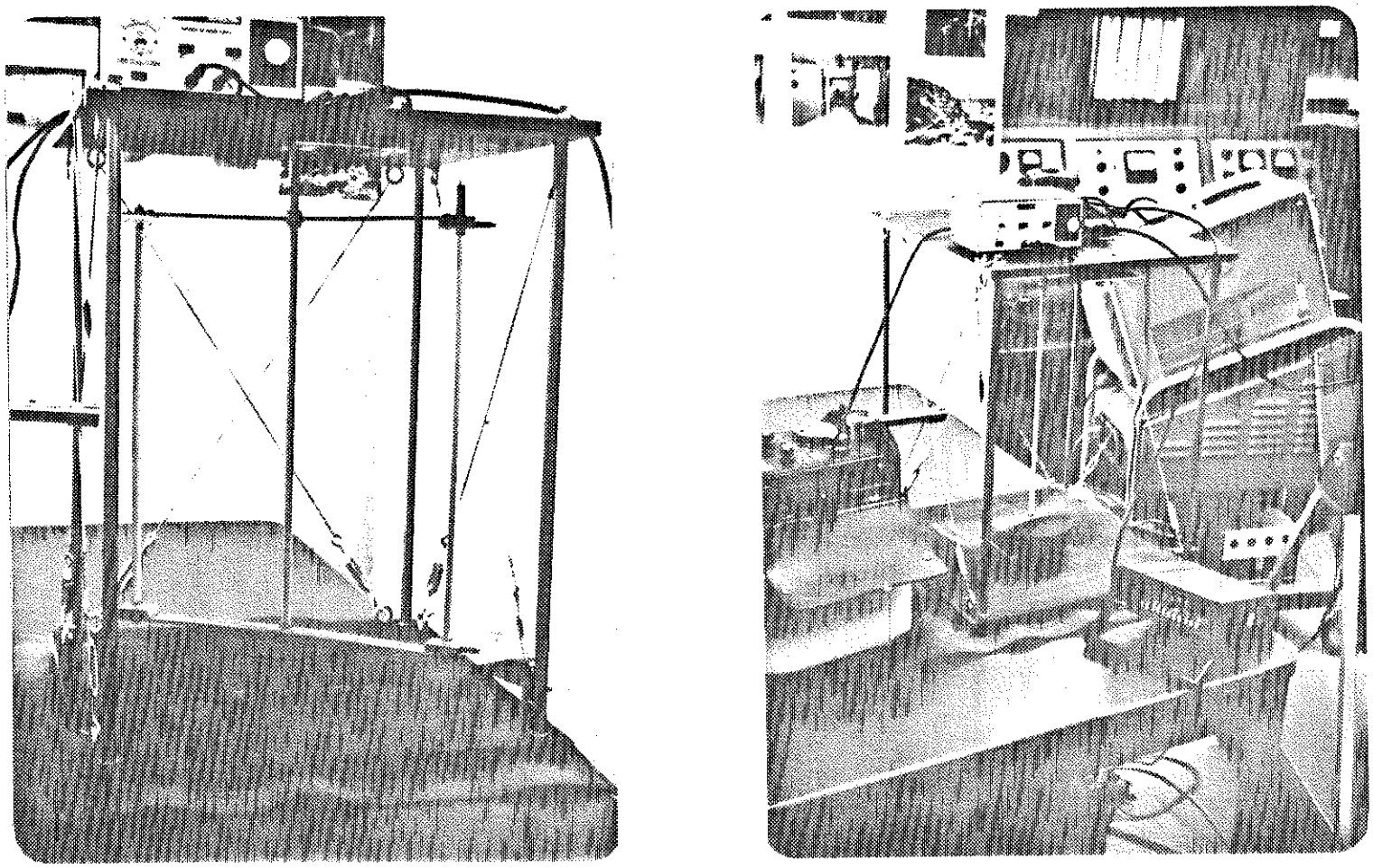

(a) (b)

Fig 2.5.1: Experimental Apparatus; (a) At Rest, (b) During Operation.

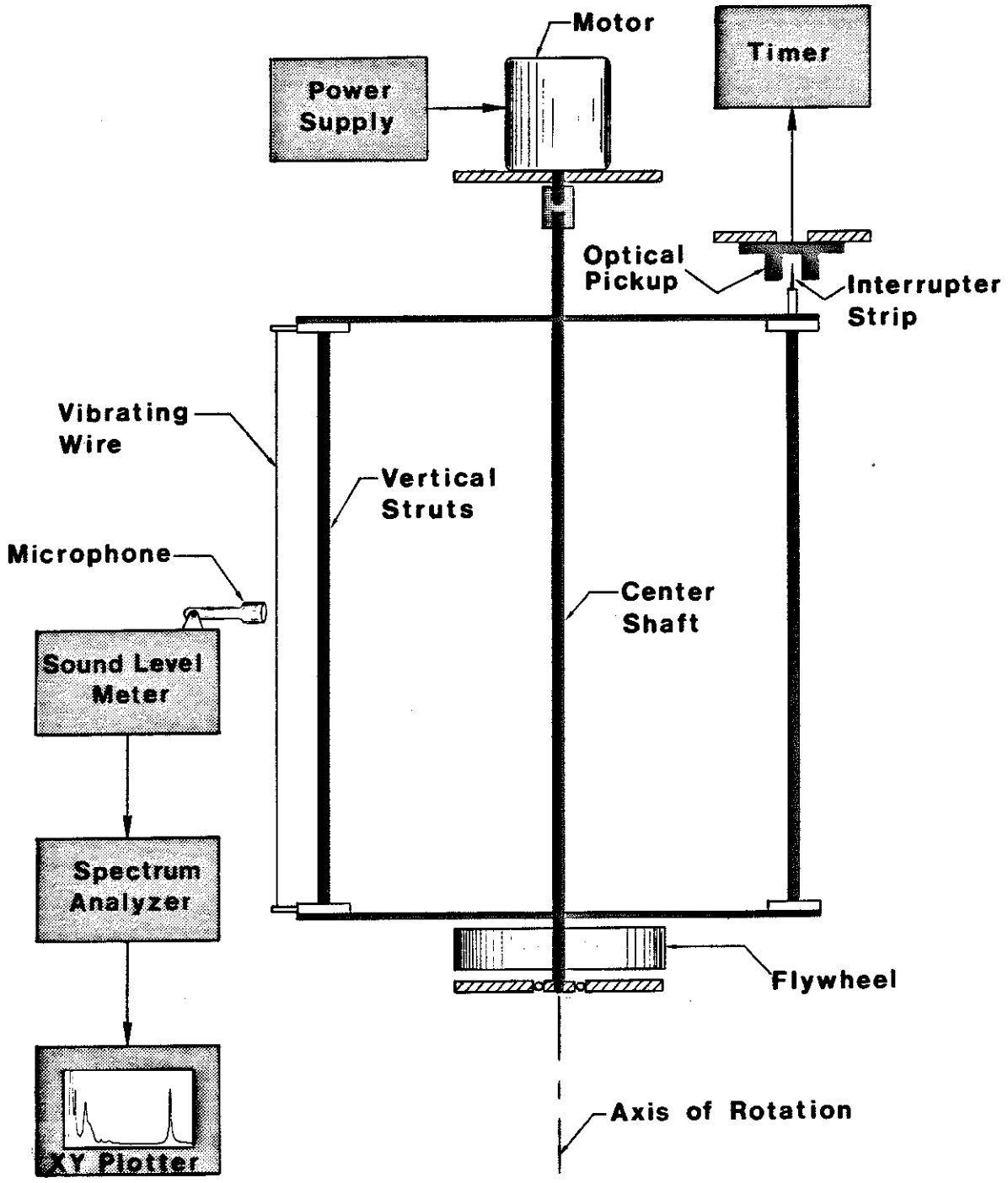

Fig. 2.5.2: Experimental Apparatus.

- *Motor:* Robbins and Myers, DC series motor, rated 24 VDC, 1.7 A, 3150 RPM.
- *Power Supply:* Hewlett-Packard Harrison 6824A; 0-50 VDC, 0-1 A.
- *Sound-Level Meter:* General Radio Corp. model 1551-C. Measurements were taken using the "A" setting.
- *Spectrum Analyzer:* Spectral Dymancis model SD 360. Over the frequency range $0 < f < 5000$ Hz, 1024 sampling points were used, so the frequency resolution was 4.88 Hz.
- *Timer:* Hewlett-Packard model 5245M, triggered by pulses from the optical pick-up. Readout precision of the timer was set to 0.1 milliseconds, while the measured value of rotational period T varied from 260 to 160 milliseconds, thus the precision of period measurement varied from 0.06% to 0.04%.
- *XY Plotter:* Hewlett-Packard model 7015B, electronically linked to the spectrum analyzer.

2.5.3 Experimental Procedure

During the experiments, all windows and doors of the room were closed to minimize spurious air currents. The power supply, timer, and spectrum analyzer, each possessing a cooling fan, were located about 15 feet from the vibrating wire in order to minimize not only the associated air currents, but also the fan noise reaching the microphone.

For each run, the motor supply voltage, approached from below, was fixed. The period of rotation was monitored continuously until 5 successive readings remained constant (to within 0.2% in the worst case), indicating that a steady-state rotational speed had been achieved. The signal from the sound-level meter

was then played into the spectrum analyzer for 7.75 seconds, producing a time-averaged, discrete Fourier transform of the wire's vibration, which was subsequently output to the plotter. Finally, five additional measurements of the rotational period were taken. Comparing these readings to those taken at the beginning of the run, the greatest difference was found to be (in the worst case) 0.4%.

The Reynolds number range of the experiments was

$$95 < \mathrm{Re} < 155. \tag{2.5.1}$$

In this regime, the Strouhal number S, used subsequently to infer f_s from the flow speed, varies significantly with Reynolds number (see Fig. 2.2.2). Since the Reynolds number depends on ambient temperature through the kinematic viscosity ν, the temperature was noted periodically throughout the experiment.

2.5.4 Normalizing the Independent Variable

Experimentally, the independent variable was the period of revolution T, as measured by the optical pick-up. However, as described below, T is directly related to the frequency ratio $\frac{f_s}{f_1}$ appearing on subsequent plots, where f_s is the Strouhal frequency and f_1 is the fundamental frequency of the wire (440 Hz).

The Reynolds number for each run is derived from the period T according to

$$U = \frac{2\pi R}{T}; \qquad \mathrm{Re}(T) = \frac{UD}{\nu}, \tag{2.5.2}$$

where R is the spin radius of the wire, D is the wire diameter, and ν is the kinematic viscosity of air, equal to $17.3 \times 10^{-5} \frac{\mathrm{ft}^2}{\mathrm{sec}}$ for the temperature range of the experiment (84° F to 85.5° F) [34]. For the range of Reynolds number given by (2.5.1), the empirical formula

$$S(T) = 0.21[1 - \frac{20}{\mathrm{Re}(T)}] \qquad (2.5.3)$$

holds approximately for the Strouhal number S.[2] Thus the frequency ratio

$$\frac{f_s}{f_1}(T) = \frac{SU}{Df_1} = \frac{\nu}{D^2 f_1} S(T)\mathrm{Re}(T) \qquad (2.5.4)$$

may replace T as independent variable.

For comparison to Section 2.3 as well as later chapters, it should be noted parenthetically that the ratio $\frac{f_s}{f_1}$, as used here to represent normalized flow speed U, is exceptional in this thesis. It is useful in this Section because many structural modes are being considered simultaneously, hence the nominal resonance conditions $f_s = f_n = nf_1$ $(n = 1, \ldots, \infty)$ occur conveniently at integral values of $\frac{f_s}{f_1}$. However, elsewhere in the thesis, when only one specific structural mode (e.g. $n = k$) is considered, it is analyitically more convenient to measure normalized flow speed by the detuning d_f between f_s and f_k, and to normalize by f_s rather than by f_1 [see for example Eq.(2.4.4)]. Likewise, if only two structural modes are considered (e.g. $n = k$, $k+1$), it is convenient to measure the flow speed by the detuning between f_s and $\frac{1}{2}(f_k + f_{k+1})$. In every case, the normalization is arranged such that the independent frequency variable (i.e. the normalized flow speed) increases as the flow speed increases.

2.5.5 Results

Figure 2.5.3 (consisting of 5 pages) shows the Fourier-transformed audio signals for selected experimental runs, which are arranged in order of increasing $\frac{f_s}{f_1}$. The response frequency f, like f_s, has been normalized by f_1, while the amplitude scale, although fixed over the course of the experiment, is arbitrary.

---

2. See Fig. 2.2.2, and also Schlichting, p. 32.

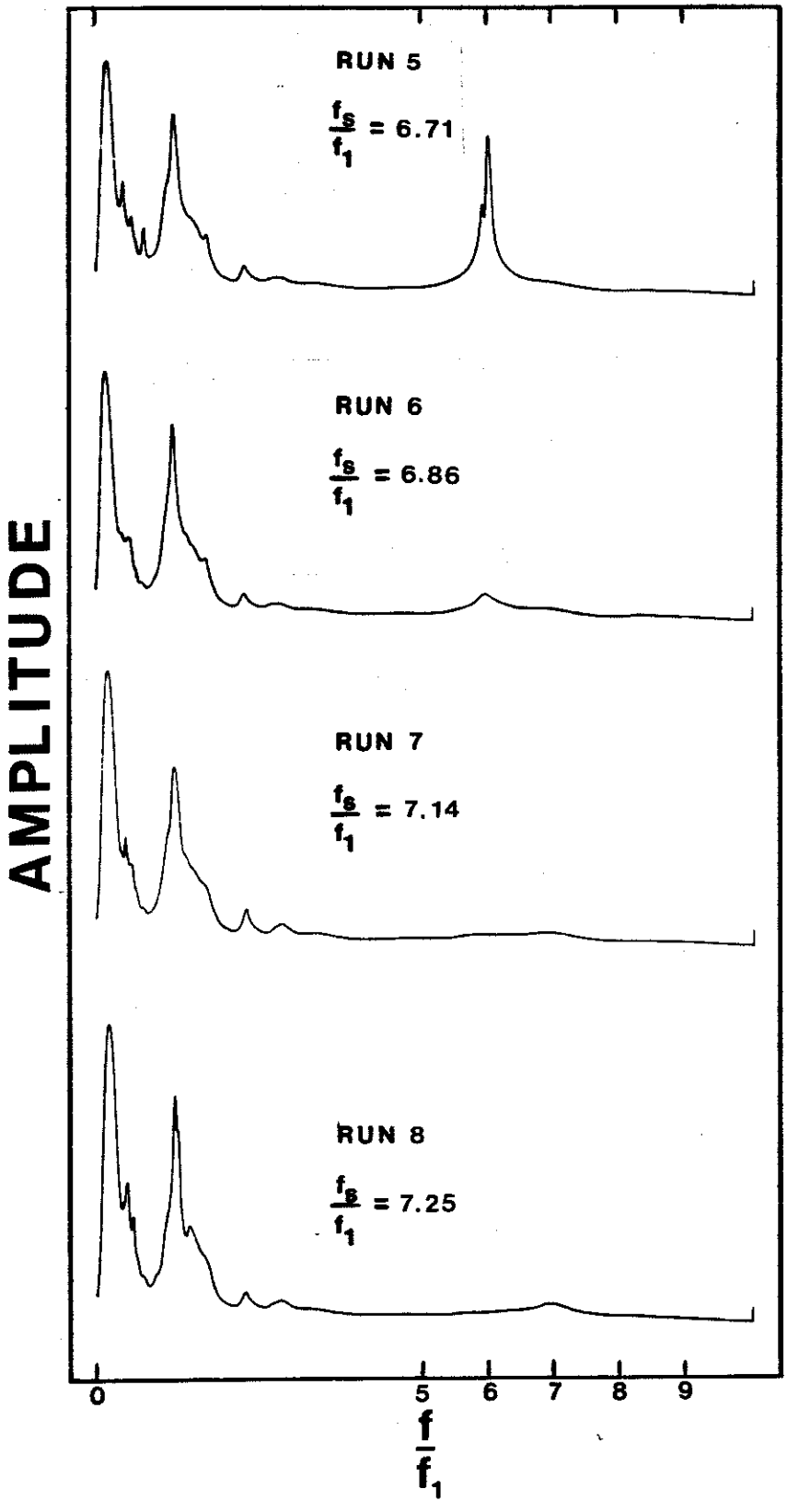

Fig. 2.5.3a: Experimental Response Spectra.

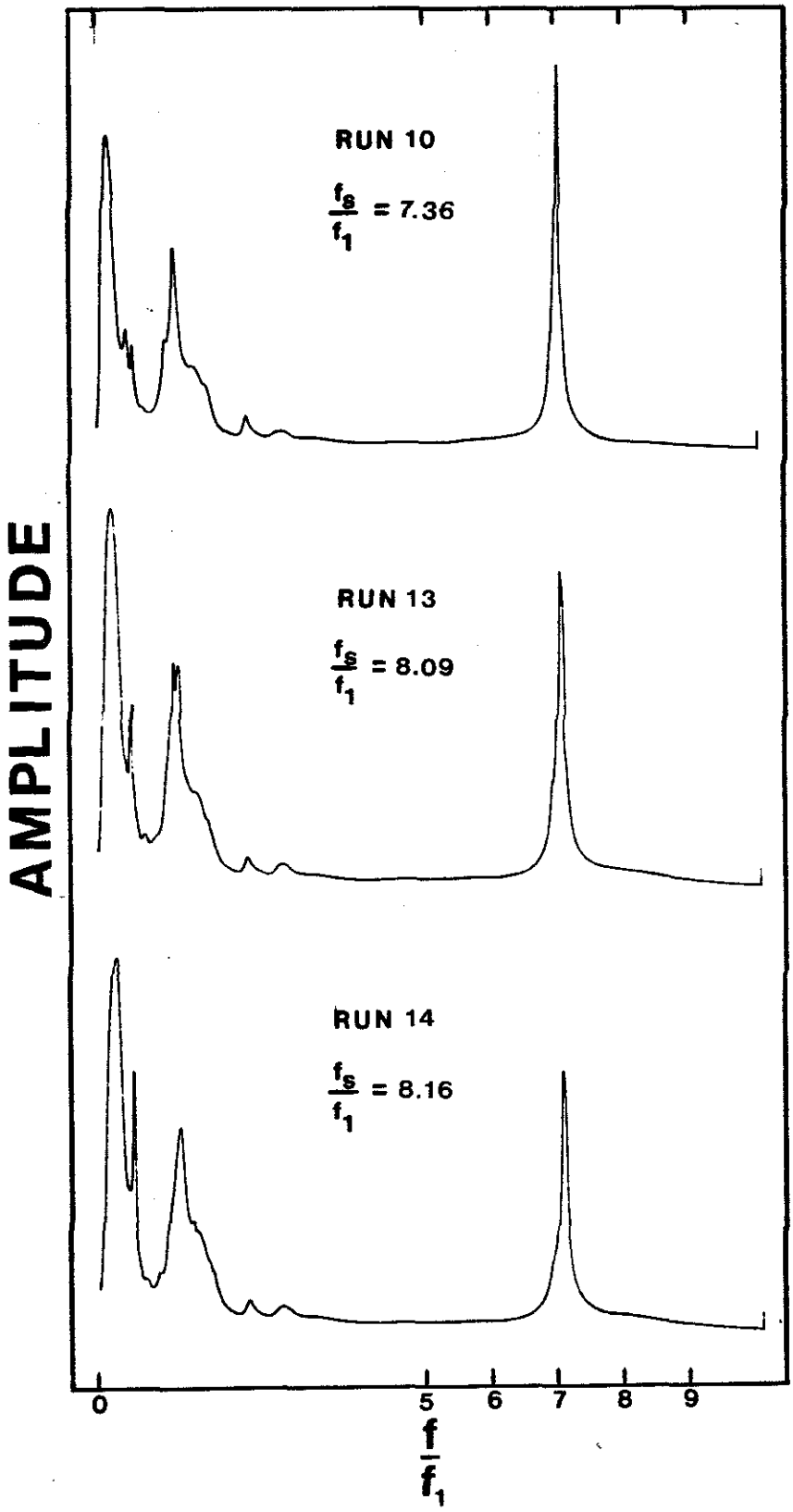

Fig. 2.5.3b: Experimental Response Spectra.

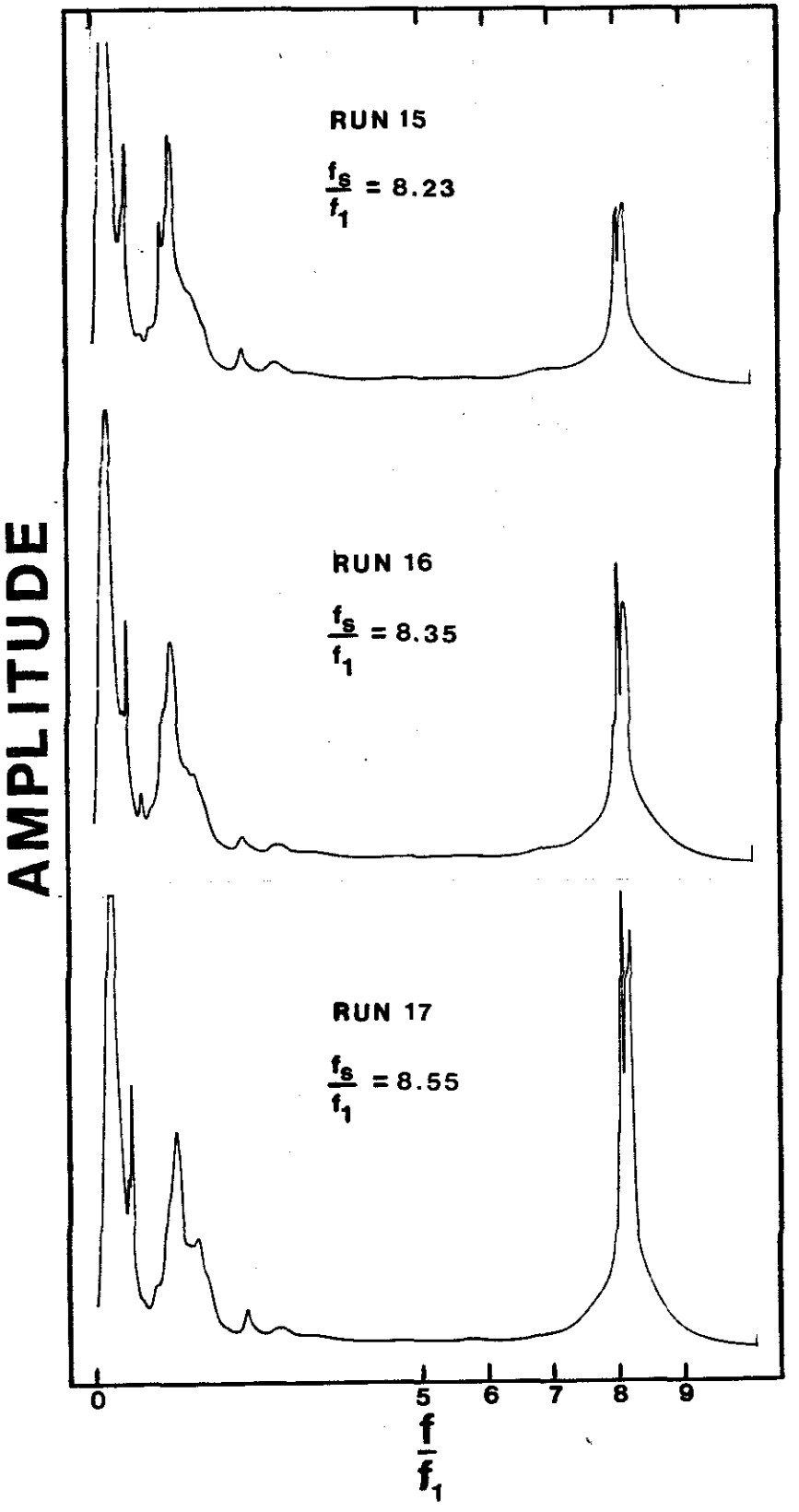

Fig. 2.5.3c: Experimental Response Spectra.

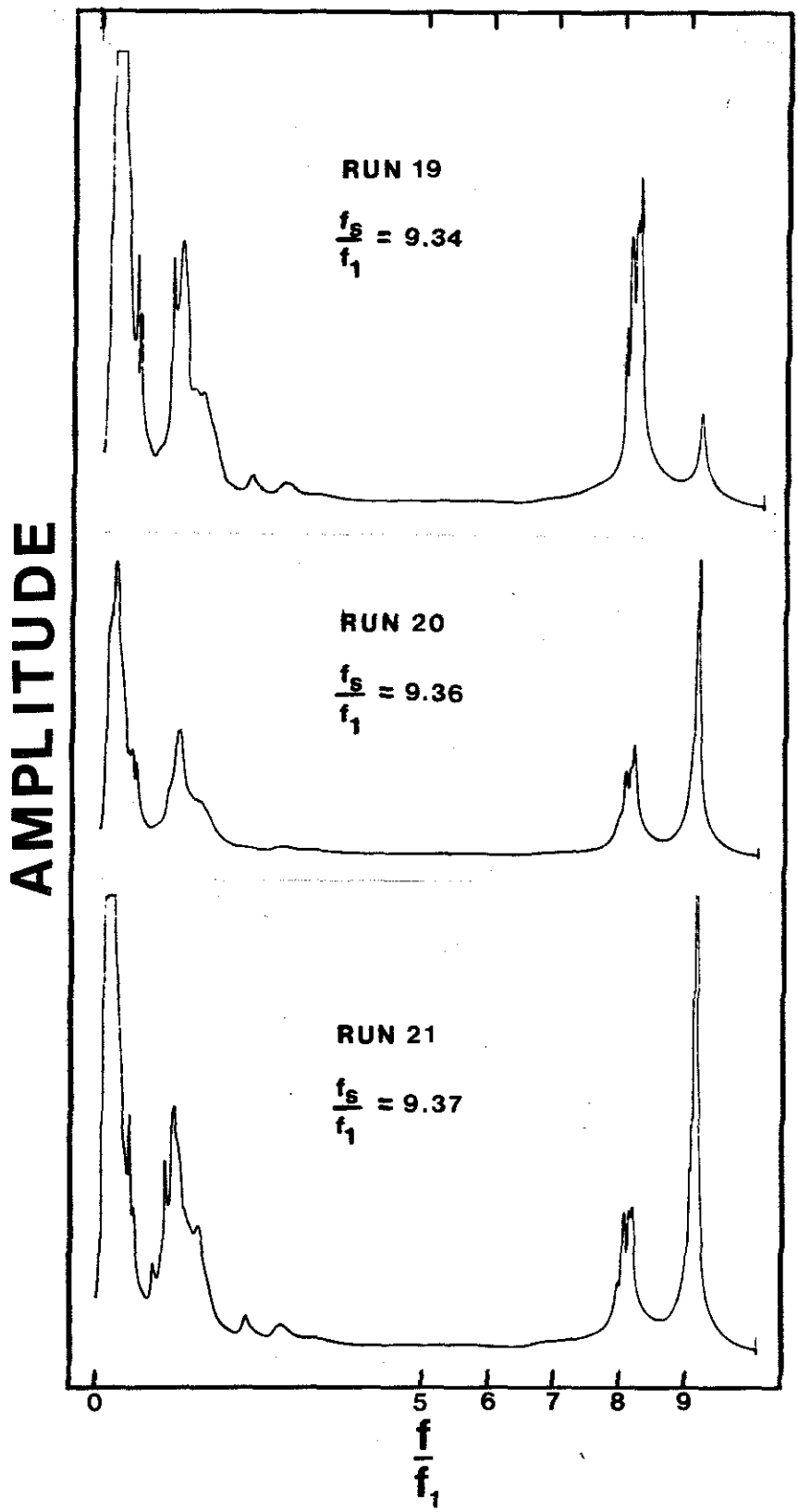

Fig. 2.5.3d: Experimental Response Spectra.

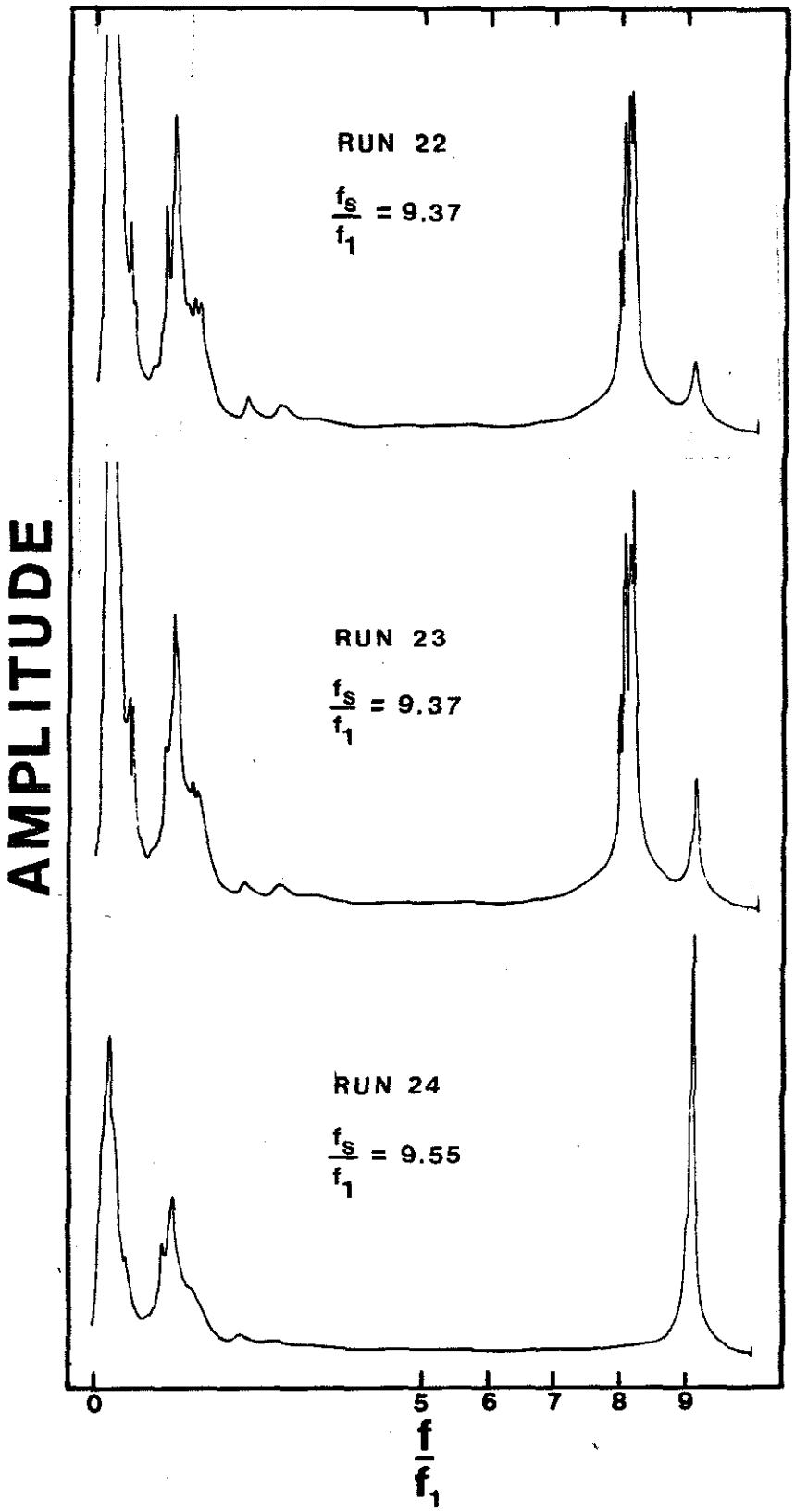

Fig. 2.5.3e: Experimental Response Spectra.

For each plot in the Figure, peaks to the left of $\frac{f}{f_1} = 5$ are merely noise, predominantly attributable to cooling fans in the experimental instruments, mentioned earlier, as well as rumble of the center-shaft in its bearing. Other peaks correspond to locked-in vibrational response of the wire, which typically was loud enough to be heard easily across a large room.

According to the discussion of Section 1.1, vortex shedding should lock onto the n^{th}-mode natural frequency of the wire at

$$\frac{f}{f_1} \approx \frac{f_n}{f_1} = n \,, \tag{2.5.5}$$

provided $\frac{f_s}{f_1}$ falls within the n^{th}-mode lock-in band. For the current experiment, modes 1-5 could not be excited; apparently the corresponding Reynolds number was too low to intiate well-established, periodic shedding capable of lock-in (see Fig. 2.2.1).

Thus, as the rotational speed was slowly increased, mode 6 was the first to respond, as illustrated in Fig 2.5.3 (Run 5), by the peak at $\frac{f}{f_1} = 6$. As the upper end of the lock-in band for $n = 6$ was reached, this amplitude peak sharply declined (Run 6, $\frac{f_s}{f_1} = 6.86$). As $\frac{f_s}{f_1}$ was further increased, the peak disappeared altogether, vortex-shedding returned to its own natural (Strouhal) frequency, and the wire was quiet (Run 7, $\frac{f_s}{f_1} = 7.14$), a situation which extended over a perceptible "dead band."

Next, lock-in for mode 7 was initiated (Run 8), and persisted over the range $7.25 < \frac{f_s}{f_1} < 8.16$ (Runs 10 and 14). As $\frac{f_s}{f_1}$ was increased to 8.23 (Run 15), response suddenly shifted from mode 7 to mode 8, with little or none of the

intervening "dead band" which occurred between modes 6 and 7. Thus mode 7 and 8 were on the verge of interfering.

Locked-in response for mode 8 (Runs 15, 16, 17) persisted from $\frac{f_s}{f_1} = 8.23$ to approximately $\frac{f_s}{f_1} = 9.3$, at which point mode 9 interfered. In the regime of interference, spectra such as Runs 19-23 were obtained, whose twin response peaks (discussed further below) indicate that modes 8 and 9 of the wire were participating simultaneously. Finally, 9^{th}-mode response established itself, free of interference from mode 8, at $\frac{f_s}{f_1} = 9.55$ (Run 24). Higher values of $\frac{f_s}{f_1}$ were unattainable, since the power demand of the motor became greater than that available from the power supply.

The above discussion is summarized in Fig. 2.5.4, which plots $\frac{f}{f_1}$ versus $\frac{f_s}{f_1}$ for each response peak, irrespective of its amplitude.[3] Using Eqs. (2.5.3) and (2.5.4), a Reynolds number scale is also provided. Data from all runs are presented, including those not shown explicitly in Fig. 2.5.3, and each data point is labeled with its associated run number. Lock-in bands appear on Fig. 2.5.4 as horizontal rows of data points at $\frac{f}{f_1} = n$, where $n = 6, 7, 8, 9$. In agreement with analogous plots for spring-mounted cylinders (Figs 2.5.2), the data points for an elastic cable (marked on Fig. 2.5.4) all lie to the right of the exact resonance points $f = f_s = f_n = nf_1$ (marked *). Thus, for both spring-mounted cylinders and elastic cables, lock-in occurs for somewhat higher values of flow speed than would be expected based on the notion of simple resonance.

---

3. In this simplified plot, a multiple (i.e. "dirty") peak, typical of mode 8, is represented by the symbol ----- (aligned vertically), where the dots indicate the locations of the lower and upper peaks. The cause of the dirty peaks at f_8 was found to be sympathetic resonance of certain structural members of the apparatus. Several experimental retrofits were attempted to alleviate this problem, without success.

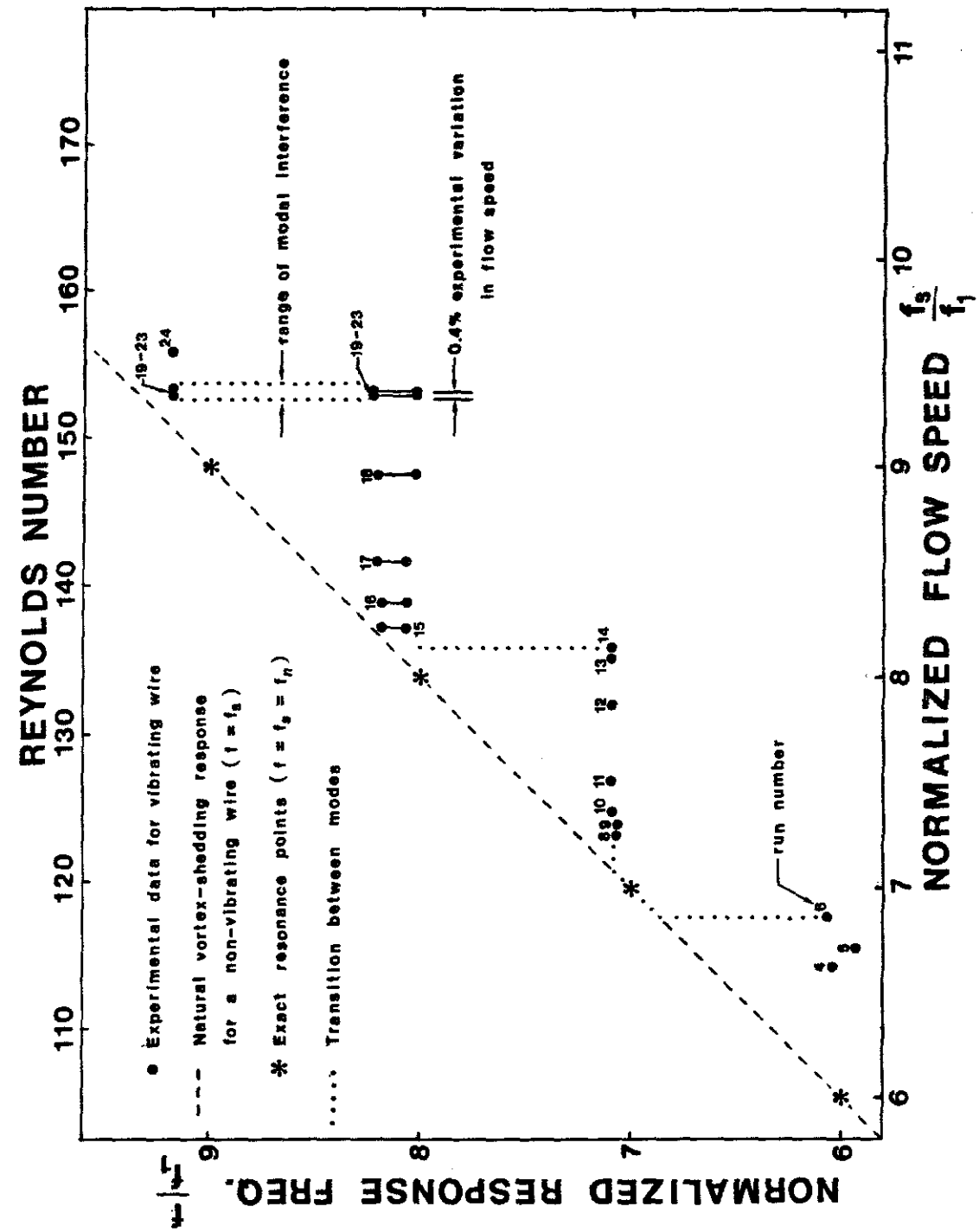

Fig. 2.5.4: Experimental Frequency Response (Peaks of the Response Spectra).

2.5.6 Modal Interaction

Further comments are in order regarding Runs 19-23, since these involve modal interaction, whose characteristics are of particular interest to the current study.

The spectra shown in Fig. 2.5.3 for these cases should not be assumed to imply steady-state response. In reality, during each run there was a very slow transient drift from 8^{th}-mode to 9^{th}-mode lock-in and vice-versa, in a seemingly random fashion. Thus the signal recorded by the spectrum analyzer (time-averaged over 7.75 seconds) shows peaks for both modes. This explains, for example, why Runs 21 and 22, despite having the same value of $\frac{f_s}{f_1}$, give very different results.

The nature of the transient drift described above suggests that at a given instant during any of the runs 19-23, only one of the two competing modes was actually being excited by vortex-shedding, while the other mode, previously excited, was dying out. This interpretation implies that vortex-shedding from the wire was at each instant monofrequency, but bistable, alternating between f_8 and f_9. The impetus to change from one frequency to the other might well have been afforded by slight changes in the rotational speed, by turbulence, or by stray air currents, none of which could be perfectly controlled with the experimental setup shown in Fig. 2.5.1. In particular, although the flow speed, and hence $\frac{f_s}{f_1}$, was held constant to within 0.4% of the value plotted,[4] this variation is still significant compared to the width of the interaction region, as shown on Fig. 2.5.4.

---

4. As discussed in Section 2.5.3.

Thus a better experimental understanding of the modal interaction phenomenon requires a more sophisticated apparatus than the one described herein. Precise regulation of the flow speed is particularly crucial. Nevertheless, the experiment described above is useful to interpret the analytical results derived in subsequent chapters.

CHAPTER III

A MODEL FOR VORTEX-INDUCED VIBRATIONS OF STRUCTURES

3.1 History and Philosophy of Empirical Modeling

In the early 1960's, Bishop and Hassan [5] demonstrated experimentally that the oscillating wake behind a forced cylinder behaves qualitatively as if it were a *single-degree-of-freedom, self-excited, nonlinear oscillator being driven by the* cylinder's motion. Their suggestion, that such a simplified mathematical system might be useful to model the complex fluid-structure interaction, has since been pursued by several authors, including Iwan and Blevins [35], whose model is based on a nonlinear fluid momentum oscillator, and Hartlen and Currie [33], whose model is based on a nonlinear lift-coefficient oscillator. The Iwan-Blevins model has been extended from rigid structures to elastic ones by Iwan [36], while the Hartlen-Currie model has been refined by Skop and Griffin [63] and extended to elastic structures by Skop [64]. Attention has been concentrated on oscillations transverse to the flow, since vortex-excited motion of a freely vibrating structure in the transverse direction is much larger than motion parallel to the flow [52], as mentioned in Section 2.1. The current discussion deals exclusively with transverse oscillations.

Common to both of the models mentioned above is the desire to use experimental knowledge of the flow field's bulk character, notably the periodic vortex-shedding, to avoid the search for detailed solutions of the flow field itself. Flow details are in fact unnecessary if, as in many applications, only the structural motion is of interest; in such cases the flow solution must merely provide expressions for the Fourier components of the overall, transverse periodic force on the structure. The equation of motion for the structure is then written with

the fluid terms as forcing functions.

Since any model of a physical phenomenon relies partially on experimental observations rather than proceeding completely from known principles, it is clear that a model must be made to fit experimental data in some way. In each of the models mentioned above, this is achieved through so-called **model constants,** which are introduced as coefficients in the fluid model equation. Values for these constants are selected to optimize the fit to some data. Unfortunately, the model constants are usually not directly measurable experimentally, so it is desirable to introduce as few of them as possible while still achieving reasonable results.

The most difficult part of the modeling problem is to concoct a fluid model which retains all essential features of the flow, particularly its interaction with the structure. Toward this end, the fluid model equation should arise from some form of the Navier-Stokes equations, for which it must serve as a substitute. By this criterion, the momentum-oscillator model of Iwan and Blevins is preferable to the lift-coefficient model of Hartlen and Currie, because the fluid oscillator equation used in the Iwan-Blevins model is based on the fluid momentum theorem, while that used in the Hartlen-Currie model is completely ad hoc. Consequently, only the Iwan-Blevins type of model is considered herein; a modified version of the original model is developed in the sequel.

It should be emphasized from the outset that the present semi-empirical model, like any of its predecessors, does not purport to "solve" the fluid-structure interaction problem, nor does it constitute a theory. Although efforts have been made to incorporate fluid mechanic principles whenever possible, there are still several ad hoc assumptions, with obscure or nonexistent physical justification, which greatly influence the results. Therefore extreme caution

should be used in extrapolating quantitative predictions beyond the range or types of data used to fit the model.

Nevertheless, qualitative results of the model may be generally useful to conceptualize the physical problem, to suggest trends, and even to lend credence to seemingly contradictory experimental data. For example, the experimental results cited in Chapter 2 are paradoxical at first glance: the lock-in band for forced circular cylinders is symmetric about the exact resonance point $f_s = f$ (*i.e.* $\sigma = 0$), as shown in Fig. 2.3.1, while the lock-in band for spring-mounted circular cylinders is highly asymmetric, occuring almost exclusively in the range $f_s > f_n$ (i.e. $d_f > 0$) as shown in Figs. 2.4.2–2.4.6. However the present model predicts just such behavior, and suggests reasons for the apparent paradox. This result casts doubt on the speculation of some investigators who, regardless of the experimental lock-in data, have postulated an analogy between the forced cylinder and the spring-mounted cylinder, and suggested experimental use of the one to understand the other [23]. The present model emphasizes the danger of such an analogy, by demonstrating, for a prototype nonlinear system, how fundamentally different the two problems are, despite their apparent similarities. Such is the usefulness of an empirical model.

In the remainder of this chapter, the present model is formulated for three types of structures, including forced and spring-mounted cylinders, as well as spanwise uniform, taut elastic cables.

3.2 Development of the Model for Spring-Mounted Cylinders

For development of the model, consider the rigid, spring-mounted cylinder sketched in Fig. 3.2.1, for which the coordinate system (x_1, x_2, x_3) is chosen with x_1 along the cylinder axis and x_3 in the direction of the free stream. Due to

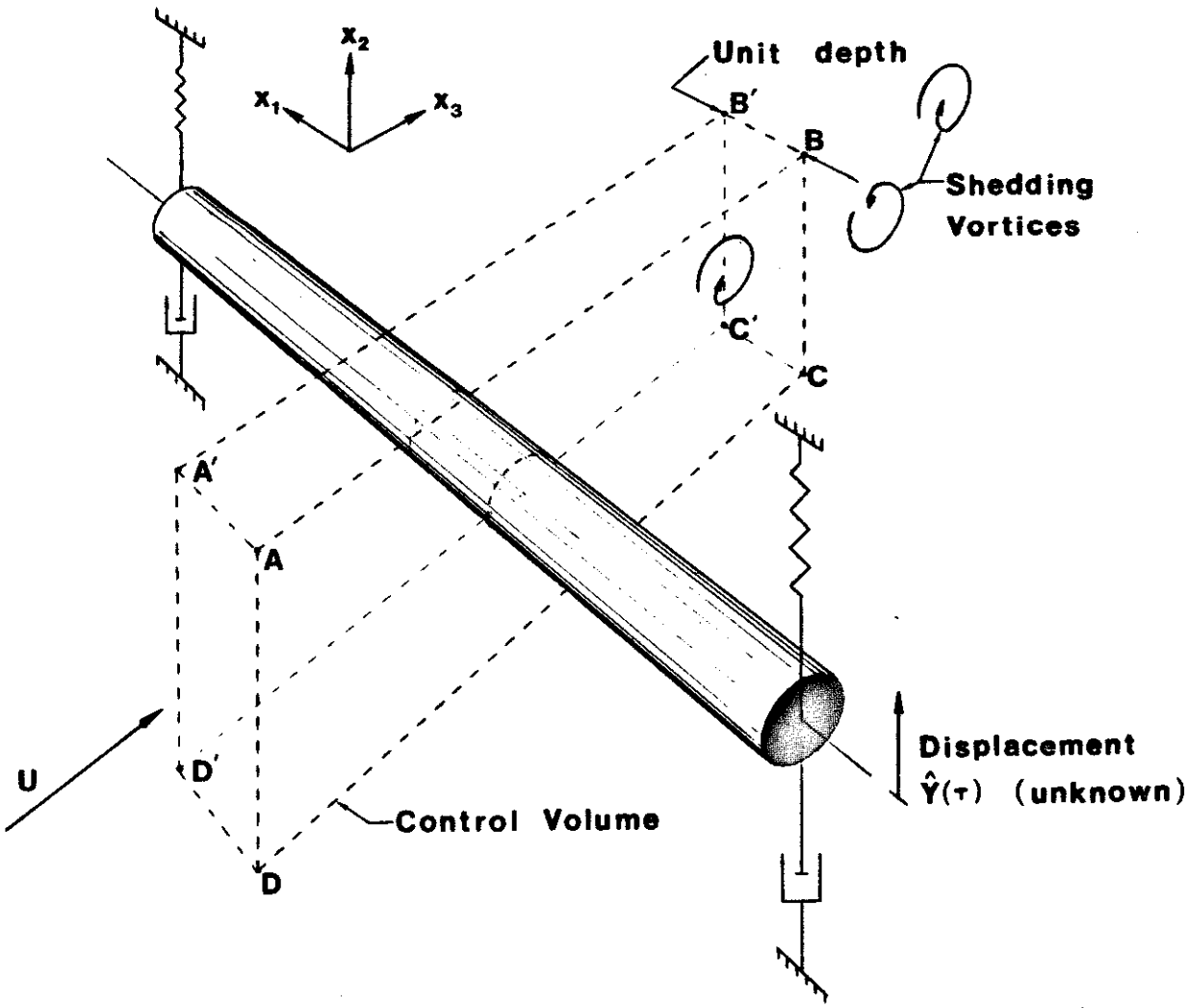

Figure 3.2.1. Control Volume Analysis for Spring-Mounted Cylinders.

spanwise rigidity of the cylinder, the problem (in particular, the vortex-shedding process) is considered two-dimensional in the (x_2, x_3) plane. This is not strictly true, but it is a reasonable approximation within the lock-in band, according to the experimental observations of Koopman [37] and Feng [16], as discussed in Chapter 2. Structural displacement in the x_2 direction, a function of time τ

only, is denoted $\hat{Y}(\tau)$, and the steady, uniform free-stream velocity is denoted U. Adopting Bishop and Hassan's concept of the flow field as a single-degree-of-freedom oscillator, the system then consists of two oscillators, one structural and one fluid, which drive each other, as depicted in Fig. 3.2.1.

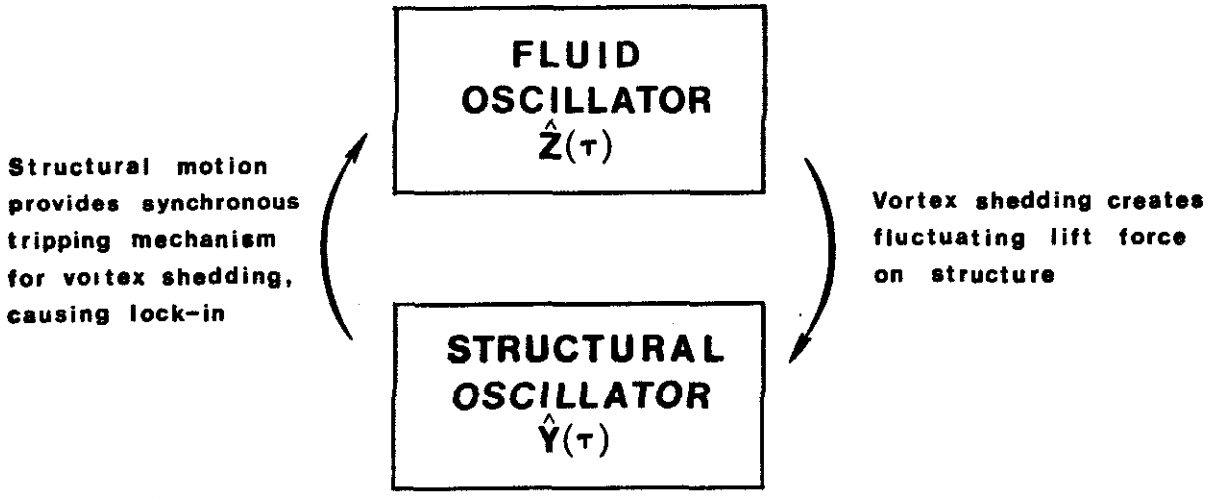

Figure 3.2.2. Fluid-Structure Coupling.

3.2.1 The Fluid Oscillator

Following Iwan and Blevins [35], a variable $\hat{Z}(\tau)$ is adopted as the fluid oscillator, whose time derivative $\hat{Z}'(\tau)$ is defined as the average vertical fluid velocity in a unit depth of control volume surrounding the cylinder:

$$\hat{Z}'(\tau) \equiv \frac{1}{\alpha_0 D^2} \int_{CV} v_2(x_2, x_3, \tau)\, dx_2\, dx_3, \tag{3.2.1}$$

where α_0 is a model constant, as discussed in Section 3.1, D is the cylinder diameter, v_2 is the x_2-component of fluid velocity, and CV is the control volume $A\,B\,C\,D\,A'B'C'D'$ of unit depth shown in Fig. 3.2.2.

The fluid oscillator equation is obtained by writing the x_2-component of the fluid momentum equation:

$$J'(\tau) + M_{flux}(\tau) = \sum F(\tau), \tag{3.2.2}$$

where $J'(\tau)$ is the time rate of change of x_2-directed momentum within the unit depth control volume, $M_{flux}(\tau)$ is the flux of x_2-directed momentum outward through the control surfaces, and $\sum F(\tau)$ is the sum of external x_2-directed forces acting on the unit depth of fluid, including pressure and viscous forces on the faces of the control volume, body forces, and the fluid-structure interaction force.

Consider first the terms in $\sum F(\tau)$ other than the interaction force. Pressures in the x_2-direction act only on the control surfaces $A\,A'B'B$ and $C\,C'D'D$, but by elongation of the control volume in the x_2-direction, these surfaces may be moved far away from the cylinder into the undisturbed fluid where the pressure is steady and equal to that of the free stream. Therefore, pressure forces on the top and bottom control surfaces cancel, except if there is a body force (gravitational field) in the x_2 -direction, in which case the pressure differential just counterbalances the body force. Consequently pressure and body forces are eliminated from consideration. Vertical viscous shears on the side control surfaces are zero by the assumed two-dimensionality; on the front and rear surfaces they are negligible according to the usual boundary layer approximation, provided the control surfaces are sufficiently far from the cylinder wall. Even though the rear surface bisects the infinite vortex street, viscosity there is negligible. Theoretical work by Rosenhead [54] and Abernathy and Kronauer [1] has shown that the role of viscosity in the vortex-shedding problem is almost entirely restricted to boundary layer separation on the cylinder and the consequent formation of vortex sheets; in the region of vortex roll-up, and certainly at the point where a vortex street is fully formed, the fluid may be considered inviscid, to a good approximation.

Therefore, all terms in $\sum F(\tau)$ other than the fluid-structure interaction force are either zero or negligible, so

$$\sum F(\tau) = -F_{int}(\tau), \tag{3.2.3}$$

where $F_{int}(\tau)$ is defined as the interaction force per unit depth of the fluid on the structure, and Eq. (3.2.2) becomes

$$J'(\tau) + M_{flux}(\tau) = -F_{int}(\tau). \tag{3.2.4}$$

Consider next the possibility of writing the terms in Eq. (3.2.4) as functions of $\hat{Y}'$, $\hat{Z}'$, and their derivatives. If the integral in Eq. (3.2.1) is multiplied by the constant fluid density ρ, the result is $J(\tau)$. Thus

$$J'(\tau) = a_0 \rho D^2 \hat{Z}''. \tag{3.2.5}$$

This expression is completely rigorous, given the definition of $\hat{Z}'$. Unfortunately, there is no equally rigorous way of deriving expressions for the momentum flux M_{flux} and the interaction force F_{int}. Expressions must merely be assumed, based on certain physical, mathematical, and heuristic grounds. The expressions assumed herein, namely

$$M_{flux}(\tau) = a_6 \rho U^2 \hat{Z} - a_1 \rho D U \hat{Z}' + a_2 \rho \frac{D}{U} \hat{Z}'^3 \tag{3.2.6}$$

$$F_{int}(\tau) = a_3 \rho D^2 (\hat{Z}'' - \hat{Y}'') + a_4 \rho D U (\hat{Z}' - \hat{Y}') + a_5 \rho D^2 \hat{Z}'' \tag{3.2.7}$$

are variants of those originally used by Blevins [6]. Factors of ρ, U, and D appearing in Eqs. (3.2.6) and (3.2.7) are chosen simply to make each term dimensionally correct, while the constants $a_1, \ldots, a_6$, like a_0 introduced previously, are model constants whose values will be selected later to fit certain experimental data.

Rationale for the selection of terms in Eqs. (3.2.6) and (3.2.7) follow:

1. *Odd functions.* If the coordinate system is turned upside down, with x_2 becoming $-x_2$, while $\hat{Z}$, $\hat{Y}$, M_{flux}, and F_{int} retain their definitions as upward-directed quantities, then the numerical values of $\hat{Z}$ and $\hat{Y}$ each chage sign, and the only effect on M_{flux} and F_{int} must likewise be a sign change. This will be the case if and only if M_{flux} and F_{int} are odd functions of $\hat{Z}'$, $\hat{Y}'$, and their derivatives.

2. *Physical Reasoning:*

   a. $\hat{Z}$ term in M_{flux}. According to a convincing pictoral argument given by Blevins [6], in which the phase relationship between $M_{flux}(\tau)$ and $\hat{Z}'(\tau)$ is examined, M_{flux} lags $\hat{Z}'$ by approximately one-quarter cycle, just as a sinusoidally-varying $\hat{Z}$ would lag $\hat{Z}'$. So it is reasonable that the principle term in M_{flux} should be proportional to $\hat{Z}$; the other terms in M_{flux} are to be viewed as corrections.

   b. $(\hat{Z}' - \hat{Y}')$ term in F_{int}. It is intuitively plausible that the interaction force should depend upon the relative velocity between the bulk of the fluid and the structure, although it is not clear that the linear dependence $(\hat{Z}' - \hat{Y}')$ is best. Perhaps a "fluid-damping" dependence $|\hat{Z}' - \hat{Y}'|(\hat{Z}' - \hat{Y}')$ would be better, but the latter is extremely difficult to handle analytically, and is therefore avoided.

   c. $(\hat{Z}'' - \hat{Y}'')$ term in F_{int}. A relative acceleration term in the interaction force attempts to model the effect of apparent fluid mass [11].

   d. $\hat{Z}''$ term in F_{int}. If the entire system (fluid + structure) is accelerated upward with a uniform acceleration $\tilde{\alpha}$, and no other motion is present, then $\tilde{\alpha} = \hat{Z}'' = \hat{Y}''$ for all time, so $\hat{Z}' = \hat{Y}'$, and the first and second terms in F_{int} are both zero. However F_{int} must not vanish in this case, because

the upward uniform acceleration is entirely equivalent to a downward gravitational field of strength $\tilde{\alpha}$, in response to which the fluid develops a hydrostatic pressure distribution, and exerts an upward bouyancy force on the structure. Therefore F_{int} must contain a third term, proportional to the bulk fluid acceleration $\tilde{\alpha} = \hat{Z}''$.

3. *Mathematical foresight.* The "correction terms" in M_{flux}, proportional to $\hat{Z}'$ and $\hat{Z}'^3$, are selected primarily on the basis of mathematical foresight, in order to produce a van der Pol type of fluid oscillator which is known to possess, at least for the forced case, the lock-in behavior observed experimentally [66]. This is the very same foresight exercised by Bishop and Hassan in their original suggestion of a nonlinear fluid oscillator.

4. *Simplicity.* While it would be possible to assume more terms in Eqs. (3.2.6) and (3.2.7), for example a $\hat{Z}'^5$ term in (3.2.6), it is desirable to minimize the number of model constants a_i as well as the complexity of the model equations. It would also be possible to model the nonlinearity into the interaction force F_{int} rather than into the momentum flux M_{flux}, and still obtain the desired van der Pol type equation. However, since F_{int} appears in both the structural and fluid oscillator equations, while M_{flux} appears only in the fluid equation, nonlinear F_{int} produces two nonlinear equations while nonlinear M_{flux} produces one nonlinear and one linear equation. The latter is of great analytical advantage.

The fluid oscillator equation is obtained by substitution of Eqs. (3.2.5), (3.2.6), and (3.2.7) into Eq. (3.2.4). Combination of $\hat{Z}''$ terms, and division by the coefficient $\rho D^2 e_1$, where

$$e_1 \equiv a_0 + a_3 + a_5, \tag{3.2.8}$$

yields

$$\hat{Z}'' - \frac{(a_1-a_4)U}{e_1 D}\hat{Z}' + \frac{a_2}{e_1 UD}\hat{Z}'^3 + \frac{a_6 U^2}{e_1 D^2}\hat{Z} = \frac{a_4 U}{e_1 D}\hat{Y}' - \frac{a_3}{e_1}\hat{Y}''. \qquad (3.2.9)$$

The model constant a_6 may be eliminated immediately according to experimental knowledge of the natural vortex-shedding frequency ω_s for a stationary cylinder ($\hat{Y} \equiv 0$), as discussed in Chapter 2. Since it is well known that the van der Pol oscillator (3.2.9) displays limit-cycle oscillations whose squared natural angular frequency equals the coefficient of the $\hat{Z}$ term [6], it follows that

$$\omega_s^2 = \frac{a_6 U^2}{e_1 D^2}. \qquad (3.2.10)$$

But according to Strouhal's relationship (1.2)

$$\omega_s \equiv 2\pi S\frac{U}{D}. \qquad (3.2.11)$$

So it follows, using Eq. (3.2.8), that

$$a_6 = 4\pi^2 S^2[a_0 + a_3 + a_5], \qquad (3.2.12)$$

which reduces the number of independent model constants to six, $a_0, \ldots, a_5$.

Time τ and the oscillator variables $\hat{Z}$ and $\hat{Y}$ are nondimensionalized as follows:

$$Z \equiv \frac{\hat{Z}}{D}; \qquad Y \equiv \frac{\hat{Y}}{D} \qquad (3.2.13a)$$

$$t \equiv \omega_s \tau \qquad (3.2.13b)$$

$$(\dot{}) \equiv \frac{d}{dt} \equiv \frac{1}{\omega_s}(\,)'. \qquad (3.2.13c)$$

Substitution of Eqs. (3.2.11) and (3.2.13) into Eq. (3.2.9) yields the **normalized fluid oscillator equation**

$$\ddot{Z} - \alpha\dot{Z} + \beta\dot{Z}^3 + Z = r\dot{Y} - \tilde{r}\ddot{Y}, \qquad (3.2.14)$$

where the coefficients α, β, r, and $\tilde{r}$ are functions of model constants and the

Strouhal number only:

$$\alpha \equiv \frac{1}{2\pi S}\frac{a_1 - a_4}{e_1} \tag{3.2.15a}$$

$$\beta \equiv 2\pi S\frac{a_2}{e_1} \tag{3.2.15b}$$

$$r \equiv \frac{1}{2\pi S}\frac{a_4}{e_1} \tag{3.2.15c}$$

$$\tilde{r} \equiv -\frac{a_3}{e_1}. \tag{3.2.15d}$$

3.2.2 The Structural Oscillator

Referring to Fig. 3.2.1, the equation of motion for the spring-mounted cylinder is

$$\hat{Y}'' + 2\zeta\omega_1\hat{Y}' + \omega_1^2 Y = \frac{F_{int}}{M} \tag{3.2.16}$$

where ζ is the fraction of critical damping

$$\zeta \equiv \frac{b}{2\sqrt{kM}}, \tag{3.2.17}$$

ω_1 is the natural frequency of the cylinder

$$\omega_1 \equiv \sqrt{\frac{k}{M}}, \tag{3.2.18}$$

and M is the cylinder mass per unit length. The dimensionless fluid-structure mass ratio η is defined as

$$\eta \equiv \frac{\rho D^2}{M}. \tag{3.2.19}$$

Substituting Eq. (3.2.7) for the interaction force F_{int} into Eq. (3.2.16), combining $\hat{Y}''$ terms, dividing by the coefficient[1]

---

1. For perspective concerning the importance of e_2, the mass ratio η is often very small for systems of engineering interest, in which case $e_2 \approx 1$.

$$e_2 \equiv 1 + a_3\eta \tag{3.2.20}$$

(assumed positive), and non-dimensionalizing as in Eqs. (3.2.13) yields the **normalized structural oscillator equation**

$$\ddot{Y} + \gamma\dot{Y} + \Omega_1^2 Y = c\ddot{Z} + \tilde{c}\ddot{Z}. \tag{3.2.21}$$

In this equation, the damping coefficient

$$\gamma \equiv \frac{1}{e_2}\left[2\zeta\frac{\omega_1}{\omega_s} + \frac{a_4}{2\pi S}\eta\right] \tag{3.2.22}$$

includes a fluid damping term as well as a structural damping term, the normalized structural frequency is

$$\Omega_1 \equiv \frac{1}{\sqrt{e_2}}\frac{\omega_1}{\omega_s}, \tag{3.2.23}$$

and the coupling coefficients are

$$c \equiv \frac{1}{e_2}\frac{a_4}{2\pi S}\eta \tag{3.2.24a}$$

$$\tilde{c} \equiv \frac{a_3 + a_5}{e_2}\eta \tag{3.2.24b}$$

3.2.3 Summary

To summarize, vortex-induced oscillations of spring-mounted cylinders are described according to the current model by the pair of differential equations (3.2.9) and (3.2.21), coefficients in which are functions of six model constants ($a_0, \ldots, a_5$) as well as four physical parameters (S, ζ, η, $\frac{\omega_1}{\omega_s}$). To obtain physically interesting information from the model, such as lock-in band location and peak structural response amplitudes, these differential equations must be solved, and the model constants selected on some rational basis. The first of these problems is addressed in Chapters 4 and 5, while the second is discussed in Chapter 6.

3.3 Application of the Model to Forced Cylinders

Consider the rigid cylinder of Fig. 2.3.1, whose normalized, transverse displacement $Y(\tau)$, typically sinusoidal, is prescribed by some external driving mechanism, as in many experiments which study vortex-induced effects on vibrating cylinders. According to the model developed above, this problem is completely described by the fluid oscillator equation (3.2.14); since the forcing functions $\dot{Y}(t)$ and $\ddot{Y}(t)$ are known, the structural oscillator equation (3.2.21) is irrelevant.

3.4 Extension of the Model to Elastic Cables

3.4.1 The Fluid Oscillator

Rigid cylinders, used above as prototype structures for development of the model, are rarely encountered in engineering practice. Extension of the model to more realistic elastic structures such as cables and beams, for which the displacement is a function of the axial coordinate x_1 as well as time, may be performed as suggested by Iwan [36], under the assumption of no spanwise coupling within the flow. That is, in applying the momentum theorem analysis of Section 3.2 to the deformed elastic structure shown in Fig. 3.4.1, the flux of vertical momentum through the lateral surfaces $A\,B\,C\,D$ and $A'B'C'D'$, as well as any vertical viscous shearing forces on these surfaces, is neglected.

Incorporation of these effects into the model would produce terms in the fluid oscillator equation involving spatial derivatives. However, experimental studies by Ramberg and Griffin [49] on vortex formation behind vibrating cables have indicated that "the shedding process is strongly dependent on the local amplitude of vibration but only weakly, if at all, dependent on the behavior of nearby cable elements [64]." Therefore it is reasonable to neglect spanwise effects in the fluid oscillator equation.

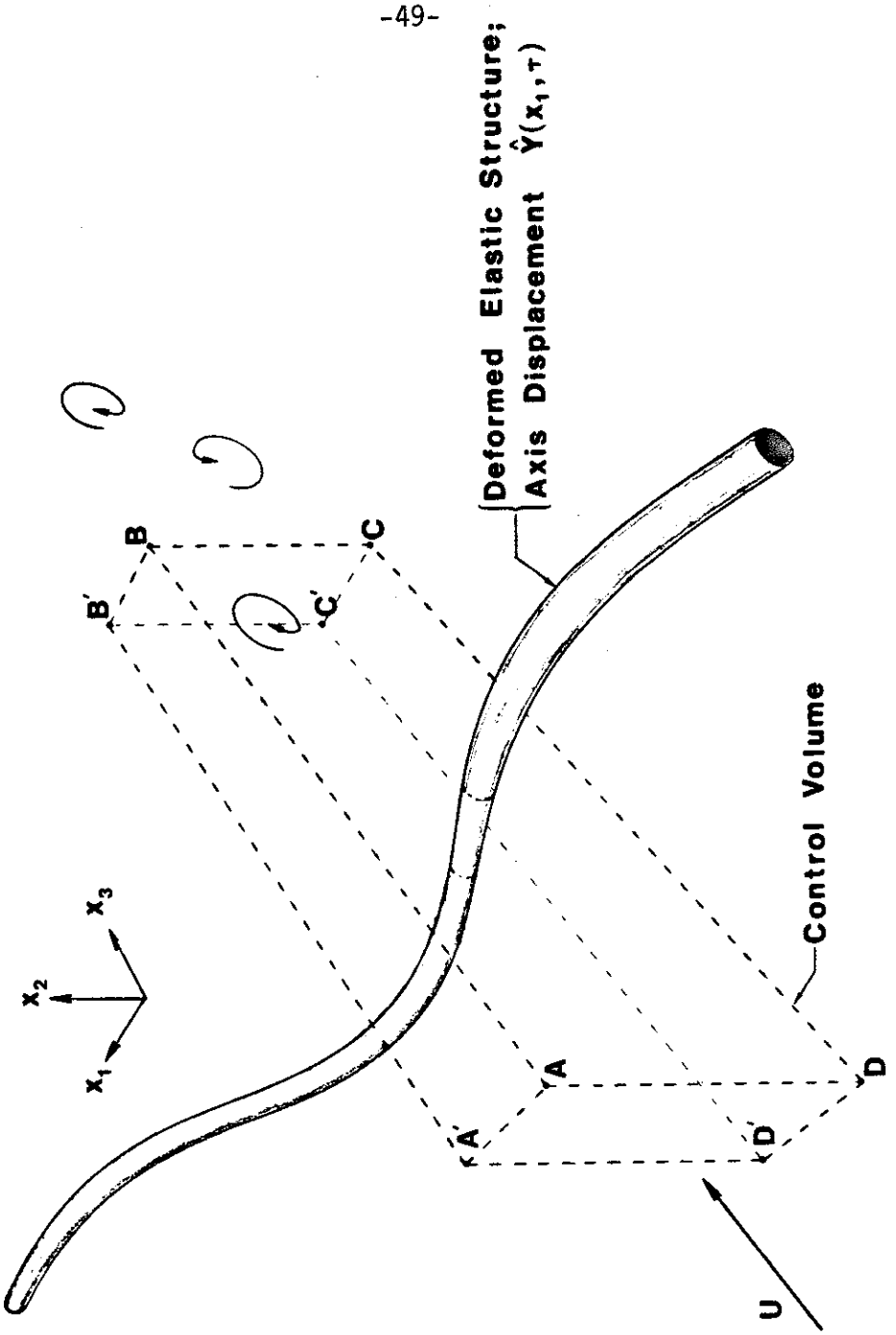

Fig. 3.4.1: Extension of the Model to Elastic Cables.

As a consequence of this approximation, all of the equations in Section 3.2 apply to the case of elastic structures, merely by reinterpreting the full time derivatives as partial derivatives. In particular, the fluid-structure interaction force per unit axial length is, upon normalization of Eq. (3.2.7),

$$F_{int} = \rho\omega_s^2 D^3 \left[a_3(Z_{tt} - Y_{tt}) + \frac{a_4}{2\pi S}(Z_t - Y_t) + a_5 Z_{tt}\right], \tag{3.4.1}$$

and the fluid oscillator equation is

$$Z_{tt} - \alpha Z_t + \beta Z_t^3 + Z = rY_t - \tilde{r}Y_{tt} \tag{3.4.2}$$

where subcript t indicates partial derivative with respect to the normalized time t. In this context,

$$Z = Z(u,t) \tag{3.4.3a}$$

$$Y = Y(u,t), \tag{3.4.3b}$$

where u is the normalized axial coordinate

$$u = \frac{x_1}{L}, \tag{3.4.4}$$

and L is the structural length.

3.4.2 The Structural Oscillator

For specificity, only spanwise uniform, taut elastic cabes with fixed ends are considered in the present analysis; a similar analysis is possible for other structures. The equation of motion for such a cable, being acted upon by the interaction force F_{int}, is

$$M\hat{Y}_{\tau\tau} = T\hat{Y}_{x_1x_1} + [C(\hat{Y})]_\tau + F_{int}, \tag{3.4.5}$$

where subscripts indicate partial derivatives, M is the structural mass per unit length, T is the cable tension, and $C(\hat{Y})$ is a linear homogeneous differential operator representing the structural damping. Normalizing according to Eqs.

(3.2.13) and (3.4.4), while noting that length scaling of $\hat{Y}$ goes through the operator C because it is linear, gives

$$Y_{tt} = \frac{1}{\omega_s^2}\frac{T}{ML^2}Y_{uu} + \frac{1}{M\omega_s}[C(Y)]_t + \frac{F_{int}}{MD\omega_s^2}. \tag{3.4.6}$$

Next, substituting Eq. (3.4.1) for F_{int}, combining Y_{tt} terms, and dividing through by e_2 as defined by Eq. (3.2.20) gives

$$Y_{tt} + \frac{1}{e_2}\left[\frac{C(Y)}{M\omega_s} + \frac{a_4}{2\pi S}\eta Y\right]_t - \frac{1}{e_2}\omega_s^2\frac{T}{ML^2}Y_{uu} = cZ_t + \tilde{c}Z_{tt}, \tag{3.4.7}$$

where the coupling coefficients c and $\tilde{c}$ have been previously defined in Eqs. (3.2.24).

3.4.3 Modal Decomposition

It is always possible to expand the spatial dependence of $Y(u,t)$ and $Z(u,t)$ in the complete set of functions $[\sin n\pi u,\ \cos n\pi u;\ n = 0, \ldots, \infty]$. However, for a cable with fixed ends, all of the cosine components of $Y(u,t)$ must be identically zero to satisfy the boundary conditions, and by spatial Fourier decompostion of Eq. (3.4.7), it may be shown that all cosine components of $Z(u,t)$ must likewise be zero. Therefore it suffices to consider only the orthonormal eigenfunctions of the cable

$$\xi_n(u) \equiv \sqrt{2}\sin n\pi u; \quad n = 1, \ldots, \infty, \tag{3.4.8}$$

expanding Z and Y as

$$Z(u,t) = \sum_{n=1}^{\infty} z_n(t)\xi_n(u) \tag{3.4.9a}$$

$$Y(u,t) = \sum_{n=1}^{\infty} y_n(t)\xi_n(u) \tag{3.4.9b}$$

where $y_n(t)$ and $z_n(t)$ are unknown time functions.

A normalized n^{th} mode natural frequency of the cable may be defined as

$$\Omega_n \equiv \frac{1}{\sqrt{e_2}} \frac{\omega_n}{\omega_s} \tag{3.4.10a}$$

where

$$\omega_n \equiv \frac{n\pi}{L}\sqrt{\frac{T}{M}}\,, \tag{3.4.10b}$$

which is exactly analagous to Eq. (3.2.23) for the spring-mounted rigid cylinder. To permit complete uncoupling of the structural equation (3.4.7), it is necessary to assume that the structural damping is expressible in classical form, whereby the operator $C[\xi_n]$ is orthogonal to ξ_m for $m \neq n$:

$$\frac{1}{\sqrt{e_2}\, M\, \omega_s}\int_0^1 \xi_m(u) C[\xi_n(u)]\, du \;=\; 2\zeta_n \Omega_n \delta_{mn}, \tag{3.4.11}$$

the symbol δ_{mn} being the Kronecker delta. Essentially, this equation defines the operator C in terms of modal damping ratios ζ_n which, for practical situations, are usually measured or estimated.

Substituting the assumed solution form (3.4.9) and (3.4.7), multiplying each by $\xi_m(u)$, integrating over u, using the orthogonality relations (3.4.11) and

$$\int_0^1 \xi_m(u)\xi_n(u)\, du \;=\; \delta_{mn}, \tag{3.4.12}$$

and finally interchanging the dummy subscripts m and n yields, for every $n = 1, \ldots, \infty$:

$$\ddot{z}_n \;-\; \alpha\dot{z}_n \;+\; \beta\int_0^1 \Big[\sum_{m=1}^{\infty} \xi_m(u)\dot{z}_m\Big]^3 \xi_n(u)\, du \;+\; z_n \;=\; r\dot{y}_n - \tilde{r}\ddot{y}_n \tag{3.4.13a}$$

and

$$\ddot{y}_n + \gamma_n\dot{y}_n + \Omega_n^2 y_n \;=\; c\dot{z}_n + \tilde{c}\ddot{z}_n. \tag{3.4.13b}$$

In the latter equation, the damping coefficient

$$\gamma_n \equiv \frac{2\zeta_n \Omega_n}{\sqrt{e_2}} + \frac{a_4}{2\pi S e_2}\eta, \tag{3.4.14}$$

includes both structural and fluid damping, in analogy to γ for the spring-mounted rigid cylinder.

Note that the above modal decomposition does not uncouple the components z_n of the fluid oscillator Z, since the nonlinear β-term in Eq. (3.4.13a) couples every z_n nonlinearly to all of the others. This difficulty precludes an analytic solution to the infinite set of equations (3.4.13).

3.4.4 One-Mode Approximation

To reduce the system (3.4.13) to a tractable from, consider a one-mode approximation for situations in which structural vibration in one particular mode, say mode k, is much greater than that in any other mode:

$$y_k \text{ large} \tag{3.4.15a}$$

$$y_n \to 0, \quad n \neq k. \tag{3.4.15b}$$

As a physical example of such a case, consider the experiment discussed in Section 2.4. In the range $\frac{f_s}{f_1} =$ 6.6 to 7.3, Figs. 2.4.2 demonstrate that the structural response is confined entirely to mode $k = 7$. It is then physicaly reasonable to presume that spatial dependence of the fluid variable $Z(u,t)$ is likewise confined to mode shape k, i.e.

$$z_n \to 0, \quad n \neq k, \tag{3.4.16}$$

since the fluid can have no knowledge of mode shapes which are absent from the structural vibration itself.

Together with Eq. (3.4.9a), Eq. (3.4.16) implies full spatial correlation of vortex shedding with the resonating cable mode shape $\xi_k(u) = \sqrt{2}\sin k\pi u$, just as

the rigid cylinder model above assumed full spatial correlation of vortex shedding with the rigid mode shape $\xi(u) = 1$. Griffin [30, p. 33] offers experimental justification of such mode-shape-correlated vortex shedding for a cable; namely, the correlation coefficient for signals from two hot-wires, located at different spanwise locations in a cable's wake, is positive if both hot-wires lie within the same half-wavelength of cable displacement, but becomes negative as soon as one hot-wire crosses a displacement node.

Based on Eqs. (3.4.16), the one-mode approximation considers only the k^{th} pair of equations (3.4.13), and truncates the infinite sum in Eq. (3.4.13a) to a single term such that the only relevant mode-shape integral is, using definition (3.4.8),

$$\int_0^1 \xi_k^4(u)\,du = \frac{3}{2}. \tag{3.4.17}$$

Therefore the one-mode-approximate equations for a cable are:

$$\ddot{z}_k - \alpha\dot{z}_k + \frac{3}{2}\beta\dot{z}_k^3 + z_k = r\ddot{y}_k - \tilde{r}\ddot{y}_k \tag{3.4.18a}$$

$$\ddot{y}_k + \gamma_k\dot{y}_k + \Omega_k^2 y_k = c\dot{z}_k + \tilde{c}\ddot{z}_k \tag{3.4.18b}$$

These equations are the same as Eqs. (3.2.14) and (3.2.21) for a rigid cylinder, with the sole exception that the coefficient of the nonlinear term, equal to β for the rigid cylinder, is here $\frac{3}{2}\beta$. The two results may easily be unified by thinking of the rigid cylinder as an elastic structure with mode shape $\xi(u) = 1$, for which the integral (3.4.17) yields 1 rather than $\frac{3}{2}$.

3.4.5 Two-Mode Approximation

Practical situations often arise in which assumptions (3.4.15) of the one-mode analysis are not valid. As demonstrated by the experiment discussed in Section 2.5, for sufficiently high mode number k, two or more adjacent natural

frequencies of a cable, say ω_k and ω_{k+1}, may lie sufficiently close to the Strouhal frequency ω_s to induce simultaneous vortex-excited oscillations of the several modes. The reason is simply that the normalized spacing between adjacent cable frequencies,

$$\frac{\omega_{k+1} - \omega_k}{\omega_k} = \frac{(k+1) - k}{k} = \frac{1}{k}, \tag{3.4.19}$$

approaches 0 as k approaches infinity. In other words, modal density increases with k such that adjacent lock-in bands may overlap, or otherwise interfere, when k is sufficiently large.

To describe such modal interference, consider a two-mode approximation of Eqs. (3.4.13), which permits y_k and y_{k+1} to be simultaneously large, but requires

$$y_n \to 0, \quad n \neq k,\ k+1. \tag{3.4.20a}$$

By extension of the argument which lead to Eq. (3.4.16), it is reasonable to assume in this case that

$$z_n \to 0, \quad n \neq k,\ k+1. \tag{3.4.20b}$$

Consequently, the infinite set of equations (3.4.13) is truncated to two pairs, one equation for each of the variables z_k, y_k, z_{k+1}, and y_{k+1}. Likewise the infinite sum in each z-equation (3.4.13b) is truncated to two terms, reducing the non-linearity for $m = k$ to

$$\int_0^1 \xi_k(u)\Big[\sum_{n=k}^{k+1} \xi_m(u)\dot{z}_m\Big]^3 du = I_{40}\dot{z}_k^3 + 3I_{31}\dot{z}_k^2\dot{z}_{k+1} + 3I_{22}\dot{z}_k\dot{z}_{k+1}^2 + I_{13}\dot{z}_{k+1}^3 \tag{3.4.22a}$$

where the integrals

$$I_{ab} \equiv \int_0^1 [\xi_k(u)]^a [\xi_{k+1}(u)]^b du \tag{3.4.22a}$$

have the following values for the mode shapes given by Eq. (3.4.8):

$$I_{40} = \frac{3}{2}; \quad I_{31} = 0; \quad I_{22} = 1; \quad I_{13} = 0. \tag{3.4.22b}$$

Substitution of Eqs (3.4.21) and (3.4.22) into the two-mode-approximate form of Eq. (3.4.13a) yields the following equation for the z_k oscillator:

$$\ddot{z}_k - \alpha\dot{z}_k + \frac{3}{2}\beta(\dot{z}_k^2 + 2\dot{z}_{k+1}^2)\dot{z}_k + z_k = ry_k - \tilde{r}\ddot{y}_k. \tag{3.4.23}$$

The equation for z_{k+1} is obtained similarly; the result is identical to Eq. (3.4.23) with subscripts k and $k + 1$ interchanged. The equation for y_k (or y_{k+1}) is identical to Eq. (3.4.13b), with subscript n replaced by k (or $k + 1$).

Symmetry in the subscripts (k, $k + 1$) may be exploited by the following convention:

For mode k equations: $i \equiv k$; $\quad j \equiv k + 1$ (3.4.24a)

For mode $(k + 1)$ equations: $i \equiv k + 1$; $\quad j \equiv k$ (3.4.24b)

The double pair of two-mode-approximate equations may then be written as a single pair:

$$\ddot{z}_i - \alpha\dot{z}_i + \frac{3}{2}\beta(\dot{z}_i^2 + 2\dot{z}_j^2)\dot{z}_i + z_i = ry_i - \tilde{r}\ddot{y}_i \tag{3.4.25a}$$

$$\ddot{y}_i + \gamma_i\dot{y}_i + \Omega_i^2 y_i = cz_i + \tilde{c}\ddot{z}_i \tag{3.4.25b}$$

where $i = k$, $k + 1$ and $j = k + 1$, k respectively, as dictated by convention (3.4.24).

3.5 Summary

In Sections 3.2--4.3 above, a modified Iwan-Blevins model for vortex-induced vibrations has been developed and applied to structures of both experimental and practical interest. For each case considered, the relevant model equations are summarized in Table 3.5.1, for ease of reference.

Table 3.5.1: Index to Chapter 3

Type of Structure	Fluid Oscillator Equation	Structural Oscillator Equation	Oscillators Involed	Number of Diff. Eqs.
Elastically Mounted Cylinder	(3.2.14)	(3.2.21)	Z, Y	2
Forced Cylinder	(3.2.14)	None; $Y(t)$ prescribed	Z	1
Cable	(3.4.13a)	(3.4.13b)	z_1, z_2,...; y_1, y_2,...	∞
One-Mode Cable Approximation	(3.4.18a)	(3.4.18b)	z_k, y_k	2
Two-Mode Cable Approximation	(3.4.25a)	(3.4.25b)	z_k, z_{k+1} ; y_k, y_{k+1}	4

CHAPTER IV

MATHEMATICAL ANALYSIS OF MODEL EQUATIONS

4.1 Generalized Model Equations

All sets of equations listed in Table 3.5.1 are so similar that it is desirable to unify the mathematical treatment as far as possible. In each case the general form of the equations is

$$\ddot{\mathbf{x}} + \mathbf{x} = \varepsilon \mathbf{F}(\mathbf{x}, \dot{\mathbf{x}}, \ddot{\mathbf{x}}), \tag{4.1.1}$$

where $\varepsilon << 1$,[1] and $\mathbf{x}$ is the vector of component oscillators; e.g. $\mathbf{x} = (z_k, z_{k+1}, y_k, y_{k+1})$ for the two-mode-approximate cable.

To write the structural oscillator equations, for example Eq. (3.4.25b), in the form (4.1.1), it is necessary to add $(1 - \Omega_i^2)y_i$ to both sides, thereby introducing this term in the function $\varepsilon\mathbf{F}$. Implicit in such a procedure is the assumption

$$1 - \Omega_i^2 = O(\varepsilon). \tag{4.1.2}$$

For the spring-mounted cylinder and the one-mode cable approximation this assumption is valid in the vicinity of lock-in (Ω_s near Ω_i, where $\Omega_s \equiv 1$), which is the region of greatest interest from a physical viewpoint. Likewise, for the two-mode cable approximation, assumption (4.1.2) is valid for both i ($i = k, k+1$) in the region where modal lock-in bands are likely to interfere, which is again the region of greatest physical interest. Consequently, assumption (4.1.2) will be adopted henceforth.

If the analysis is carried out to order ε only, then the appearance of $\ddot{\mathbf{x}}$ on the right-hand side of Eq. (4.1.1) may be eliminated as follows. According to Eq. (4.1.1),

---

1. See the comment following Eqs. (4.1.8).

$$\ddot{\mathbf{x}} = -\mathbf{x} + \varepsilon\mathbf{F}. \tag{4.1.3}$$

Therefore

$$\ddot{\mathbf{x}} + \mathbf{x} = \varepsilon\mathbf{F}(\mathbf{x}, \dot{\mathbf{x}}, -\mathbf{x} + \varepsilon\mathbf{F}). \tag{4.1.4}$$

Expanding $\varepsilon\mathbf{F}$ in a Taylor's series of its third argument about $-\mathbf{x}$,

$$\ddot{\mathbf{x}} + \mathbf{x} = \varepsilon\mathbf{F}(\mathbf{x}, \dot{\mathbf{x}}, -\mathbf{x}) + O(\varepsilon^2). \tag{4.1.5}$$

Defining

$$\varepsilon\mathbf{f}(\mathbf{x}, \dot{\mathbf{x}}) \equiv \varepsilon\mathbf{F}(\mathbf{x}, \dot{\mathbf{x}}, -\mathbf{x}), \tag{4.1.6}$$

this may be written more simply, to order ε, as

$$\ddot{\mathbf{x}} + \mathbf{x} = \varepsilon\mathbf{f}(\mathbf{x}, \dot{\mathbf{x}}). \tag{4.1.7}$$

Therefore, apart from the infinite set of equations for the elastic cable, each set of equations listed in Table 3.5.1 is, to order ε, a special case of the following set of **generalized model equations:**

$$\ddot{y}_1 + y_1 = -\gamma_1\dot{y}_1 + (1 - \Omega_1^2)y_1 + c\dot{z}_1 - \tilde{c}z_1 \tag{4.1.8a}$$

$$\ddot{y}_2 + y_2 = -\gamma_2\dot{y}_2 + (1 - \Omega_2^2)y_2 + c\dot{z}_2 - \tilde{c}z_2 \tag{4.1.8b}$$

$$\ddot{z}_1 + z_1 = \alpha\dot{z}_1 - p\dot{z}_1^3 - q\dot{z}_2^2\dot{z}_1 + r\dot{y}_1 + \tilde{r}y_1 \tag{4.1.8c}$$

$$\ddot{z}_2 + z_2 = \alpha\dot{z}_2 - p\dot{z}_2^3 - q\dot{z}_1^2\dot{z}_2 + r\dot{y}_2 + \tilde{r}y_2. \tag{4.1.8d}$$

These equations have the form (4.1.7) if each of the terms on the right-hand side is an order of magnitude smaller than the terms on the left-hand side; that is, for each of the four component equations,

$$\frac{O(\varepsilon f_m)}{O(x_m)} \approx O(\varepsilon); \qquad m = 1, \ldots, 4. \tag{4.1.9}$$

For $i = 1, 2$ this requires that the products [2] $p\,|z_i^2|$, $q\,|z_i^2|$ and the coefficients α,

---

2. In this context, $|\ |$ indicates the amplitude of an oscillating quantity.

γ_i, c, $\tilde{c}$, r, $\tilde{r}$, as well as the quantity $1 - \Omega_i^2$ discussed above, must be order ε.

Eqs. (4.1.8) correspond to the various equations listed in Table 3.5.1 according to the following conventions:

1. *Subscript Values.* The generic subscript values $i = 1, 2$ are employed in place of $i = k, k + 1$, merely for convenience. With these generic subscripts, convention (3.4.24) becomes:

   For "mode–1" equations: i = 1, j = 2 (4.1.10a)

   For "mode–2" equations: i = 2, j = 1 (4.1.10b)

   By the quotation marks in convention (4.1.10), it is emphasized that subscripts 1 and 2 in this context do **not** refer necessarily to modes 1 and 2 of an elastic structure, but to *any* two adjacent modes k and $k + 1$.

2. *Coefficients of nonlinear terms.* The generic parameters p and q appearing in Eqs. (4.1.8) are employed to represent certain multiples of β, as indicated in Table 4.1.1.

3. *Variable Identification.* The generic variables (z_1, z_2, y_1, y_2) are employed to represent the oscillator variables Z, Y, z_k, y_k, etc. as indicated in Table 4.1.1 . Some of the generic variables have no counterparts in certain cases, as represented by dashes in the Table. In such instances the associated oscillator equations are ignored.

The asymptotic method to be used for analysis of equations (4.1.8) is developed in the following section.

4.2 An Asymptotic Method Using Two Time Scales

Consider a set of N coupled, nonlinear, autonomous, ordinary differential equations of the form[3]

Table 4.1.1: Reduction of Generalized Equations (4.1.1)

Type of Structure	Parameter Values		Variable Identification				Number of Differential Eqs. Involved	Comments
	p	q	z_1	z_2	y_1	y_2		
Forced Cylinder	β	0	Z	-	Y	-	1	Y(t) is Prescribed
Spring-Mounted Cylinder	β	0	Z	-	Y	-	2	
One-Mode Cable Approximation	$\frac{3}{2}\beta$	0	Z_k	-	yk	-	2	Identical to Spring-Mounted Cylinder Except for value of p
Two-Mode Cable Approximation	$\frac{3}{2}\beta$	3β	Z_k	Z_{k+1}	yk	y_{k+1}	4	

$$\ddot{\mathbf{x}} + [\Lambda]^2\mathbf{x} = \varepsilon \mathbf{f}(\mathbf{x}, \dot{\mathbf{x}}), \tag{4.2.1}$$

where

$$\mathbf{x} \equiv (x_1, \ldots, x_N), \tag{4.2.2a}$$

$$[\Lambda] \equiv \text{diag}(\lambda_1, \ldots, \lambda_N), \tag{4.2.2b}$$

$$(\dot{}) \equiv \frac{d}{dt}, \tag{4.2.2c}$$

and

$$\varepsilon << 1. \tag{4.2.2d}$$

Analysis of this system may be carried out using a variation of the method of multiple time scales, as given in Nayfeh [46, pp. 228-230], and further illustrated in Nayfeh and Mook [47, pp. 388-390]. *Specifics of the method as used herein* are presented below.

Let the solution $\mathbf{x}$ be expanded as a power series in ε, which for the current discussion is truncated to two terms:

$$\mathbf{x} = \mathbf{x}^{(0)}(T_0, T_1) + \varepsilon \mathbf{x}^{(1)}(T_0, T_1) + \cdots \tag{4.2.3}$$

The independent time scales T_0 and T_1 are defined as

$$T_0 \equiv t; \qquad T_1 \equiv \varepsilon t, \tag{4.2.4}$$

so by the chain rule,

$$(\dot{}) = D_0 + \varepsilon D_1, \tag{4.2.5}$$

where the operators D_0 and D_1 are defined as

---

3. This system is more general than is necessary for the present purposes, since the system of interest (4.1.8) has the form (4.1.7), for which $[\Lambda] = [I]$ (the identity matrix). Consequently, the asymptotic method presented in this section would be capable of handling, for example, Eqs. (4.1.8) in the case where Eq. (4.1.2) is not satisfied.

$$D_0 \equiv \frac{\partial}{\partial T_0}; \qquad D_1 \equiv \frac{\partial}{\partial T_1}. \tag{4.2.6}$$

Consequently,

$$\dot{\mathbf{x}} = D_0\mathbf{x}^{(0)} + \varepsilon(D_0\mathbf{x}^{(1)} + D_1\mathbf{x}^{(0)}) + \cdots \tag{4.2.7a}$$

$$\ddot{\mathbf{x}} = D_0^2\mathbf{x}^{(0)} + \varepsilon(D_0^2\mathbf{x}^{(1)} + 2D_0D_1\mathbf{x}^{(0)}) + \cdots \tag{4.2.7b}$$

where

$$D_0^2 \equiv \frac{\partial^2}{\partial T_0^2}. \tag{4.2.8}$$

Furthermore, expansion of the right-hand side of Eq. (4.2.1) about the zeroth order solution $\mathbf{x}^{(0)}$ gives

$$\begin{aligned} \varepsilon\mathbf{f}(\mathbf{x}, \dot{\mathbf{x}}) &= \varepsilon\mathbf{f}[\mathbf{x}^{(0)} + \varepsilon\mathbf{x}^{(1)},\ D_0\mathbf{x}^{(0)} + \varepsilon(D_1\mathbf{x}^{(0)} + D_0\mathbf{x}^{(1)})] \\ &= \varepsilon\mathbf{f}[\mathbf{x}^{(0)}, D_0\mathbf{x}^{(0)}] + \cdots \end{aligned} \tag{4.2.9}$$

Therefore, substituting Eqs. (4.2.3), (4.2.7b), and (4.2.9) into Eq. (4.2.1) and equating coefficients of like powers of ε:

$$\varepsilon^0: \qquad D_0^2\mathbf{x}^{(0)} + [\Lambda]^2\mathbf{x}^{(0)} = 0 \tag{4.2.10a}$$

$$\varepsilon^1: \qquad \varepsilon(D_0\mathbf{x}^{(1)} + [\Lambda]^2\mathbf{x}^{(1)}) = -2\varepsilon D_0D_1\mathbf{x}^{(0)} + \varepsilon\mathbf{f}(\mathbf{x}^{(0)}, D_0\mathbf{x}^{(0)}). \tag{4.2.10b}$$

The ε^0 equation is satisfied by

$$x_m^{(0)} = H_m(T_1)e^{i\lambda_m T_0} + \overline{H_m}(T_1)e^{-i\lambda_m T_0}, \qquad m = 1, \ldots, N \tag{4.2.11}$$

where H_m is a slowly-varying complex amplitude whose conjugate is $\overline{H_m}$, and $i \equiv \sqrt{-1}$. Consequently the ε^1 equation becomes

$$\varepsilon(D_0^2x_m^{(1)} + \lambda_m^2x_m^{(1)}) = -2i\lambda_m(\varepsilon H_m'e^{i\lambda_m T_0} - \varepsilon\overline{H_m}'e^{i\lambda_m T_0}) + \varepsilon f_m(\mathbf{x}^{(0)}, D_0\mathbf{x}^{(0)}), \tag{4.2.12}$$

in which H_m' denotes differentiation of H_m with respect to its argument, the "slow time" T_1.

To proceed further, it is necessary to specify constants λ_m and functions εf_m in the system (4.2.1). The objective is then to generate first order differential equations for the H_m by identifying the secular terms in εf_m, and requiring that these, together with the explicit secular terms in Eq. (4.2.12), vanish.[4] This process is carried out in the next section, where the system (4.2.1) is specified to be the set of model equations (4.1.8).

4.3 Application of the Asymptotic Method to the Model Equations

4.3.1 Introduction

The generalized model equations (4.1.8) may be written in the language of Eqs. (4.2.1) by letting $N = 4$,

$$\mathbf{x} \equiv (y_1,\ y_2,\ z_1,\ z_2), \tag{4.3.1}$$

$$\varepsilon f_1(\mathbf{x},\ \dot{\mathbf{x}}) = -\gamma_1 \dot{y}_1 + \delta_1 y_1 + c\dot{z}_1 - \tilde{c} z_1 \tag{4.3.2a}$$

$$\varepsilon f_2(\mathbf{x},\ \dot{\mathbf{x}}) = -\gamma_2 \dot{y}_2 + \delta_2 y_2 + c\dot{z}_2 - \tilde{c} z_2 \tag{4.3.2b}$$

$$\varepsilon f_3(\mathbf{x},\ \dot{\mathbf{x}}) = a\dot{z}_1 - p\dot{z}_1^3 - q\dot{z}_2^2\dot{z}_1 + r\dot{y}_1 + \tilde{r} y_1 \tag{4.3.2c}$$

$$\varepsilon f_4(\mathbf{x},\ \dot{\mathbf{x}}) = a\dot{z}_2 - p\dot{z}_2^3 - q\dot{z}_1^2\dot{z}_2 + r\dot{y}_2 + \tilde{r} y_2, \tag{4.3.2d}$$

and, as indicated in the footnote to Eq. (4.2.1),

$$\lambda_1 = \lambda_2 = \lambda_3 = \lambda_4 = 1. \tag{4.3.3}$$

For brevity, the symbol[5]

$$\delta_i \equiv 1 - \Omega_i^2; \quad i = 1,\ 2 \tag{4.3.4}$$

has been introduced in Eqs. (4.3.2).

---

4. The rationale for this procedure is well known: if the secular $e^{\pm i\lambda_m T_0}$ terms on the right-hand side of Eq. (4.2.12) did not vanish, unbounded resonance of the undamped harmonic oscillator $x_m^{(1)}$ would result, thereby destroying the order of magnitude assumption in the expansion (4.2.3).
5. Throughout Section 4.3, $i \equiv \sqrt{-1}$ whenever i is used explicitly, except as noted in Eqs. (4.3.4) and (4.3.20b), where i is an index.

4.3.2 Determination of Secular Terms

Consider the determination of secular terms on the right-hand side of Eq. (4.2.12). The functions $\varepsilon f_m(\mathbf{x}^{(0)}, D_0\mathbf{x}^{(0)})$, are, for $m = 1, 3$:

$$\varepsilon f_1(\mathbf{x}^{(0)}, D_0\mathbf{x}^{(0)}) = -\gamma_1[D_0x_1^{(0)}] + \delta_1 x_1^{(0)} + c[D_0x_3^{(0)}] - \tilde{c}x_3^{(0)} \tag{4.3.5a}$$

$$\varepsilon f_3(\mathbf{x}^{(0)}, D_0\mathbf{x}^{(0)}) = \alpha[D_0x_3^{(0)}] - p[D_0x_3^{(0)}]^3 - q[D_0x_4^{(0)}]^2[D_0x_3^{(0)}] + r[D_0x_1^{(0)}] + \tilde{r}x_1^{(0)} . \tag{4.3.5b}$$

Companion expressions for εf_2 and εf_4 are obtained by interchanging subscripts as follows

$$1 \leftrightarrow 2, \qquad 3 \leftrightarrow 4, \tag{4.3.6}$$

Differentiation of the solution form (4.2.11) gives, in view of Eq. (4.3.3),

$$D_0x_m^{(0)} = i(H_m e^{iT_0} - \overline{H}_m e^{-iT_0}). \tag{4.3.7}$$

Calculation of the nonlinear terms in Eq. (4.3.5b) yields

$$[D_0x_3^{(0)}]^3 = -i(H_3^3 e^{3iT_0} - 3H_3^2\overline{H}_3 e^{iT_0}) + c.c. \tag{4.3.8a}$$

$$[D_0x_4^{(0)}]^2[D_0x_3^{(0)}] = -i[H_3H_4^2 e^{3iT_0} - (\overline{H}_3H_4^2 + 2H_3H_4\overline{H}_4)e^{iT_0}] + c.c. \tag{4.3.8b}$$

where "c.c." indicates the complex conjugate of all preceding terms. Substitution of Eqs. (4.2.11), (4.3.7), and (4.3.8) into Eqs. (4.3.5) produces:

$$\varepsilon f_1[\mathbf{x}^{(0)}, D_0\mathbf{x}^{(0)}] = C_1 e^{iT_0} + c.c. \tag{4.3.9a}$$

$$\varepsilon f_3[\mathbf{x}^{(0)}, D_0\mathbf{x}^{(0)}] = C_3 e^{iT_0} + K_3 e^{3iT_0} + c.c. \tag{4.3.9b}$$

where

$$C_1 \equiv (\delta_1 - i\gamma_1)H_1 + (ic - \tilde{c})H_3 \tag{4.3.10a}$$

$$C_3 \equiv (ir + \tilde{r})H_1 + i\alpha H_3 - 3ipH_3^2\overline{H_3} - 2iqH_3H_4\overline{H_4} - iq\overline{H_3}H_4^2 \quad (4.3.10b)$$

$$K_3 \equiv iH_3(qH_4^2 + pH_3^2) \quad (4.3.10c)$$

Again, companion expressions for εf_2 and εf_4 are obtained merely by interchanging subscripts according to (4.3.6).

Substitution of Eqs. (4.3.10) into Eq. (4.2.12) produces, for $m = 1, 3$,

$$\varepsilon[D_0^2 x_1^{(1)} + {}^2x_1^{(1)}] = (C_1 - 2i\varepsilon H_1')e^{iT_0} + c.c. \quad (4.3.11a)$$

$$\varepsilon[D_0^2 x_3^{(1)} + x_3^{(1)}] = (C_3 - 2i\varepsilon H_3')e^{iT_0} + K_3 e^{3iT_0} + c.c. \quad (4.3.11b)$$

On the right-hand side of each equation (4.3.11), the e^{iT_0} term is secular, while the e^{3iT_0} term in Eq. (4.3.11b) is not. Using (4.3.16), the situation is analagous for the companion equations. The "*c.c.*" notation emphasizes that the set of equations generated by secular e^{-iT_0} terms is always equivalent to that generated by e^{iT_0} terms, since the one set is just the complex conjugate of the other.

4.3.3 Amplitude/Phase Equations

The requirement that secular terms vanish in Eqs. (4.3.11) gives, for $m = 1, 3$,

$$-2i\varepsilon H_1' + (1 - \Omega_1^2 - i\gamma_1)H_1 + (ic - \tilde{c})H_3 = 0 \quad (4.3.12a)$$

$$-2i\varepsilon H_3' + i\alpha H_3 - 3ipH_3^2\overline{H_3} - 2iqH_3H_4\overline{H_4} - iq\overline{H_3}H_4^2 + (ir + \tilde{r})H_1 = 0, \quad (4.3.12b)$$

and companion equations for $m = 2, 4$. These equations are satisfied by the following solution form for the complex amplitudes H_m :

$$H_m(T_1) = \frac{1}{2}B_m(T_1)e^{i\theta_m(T_1)}. \quad (4.3.13)$$

The unknown real quantities B_m and θ_m, which depend on the slow time T_1, may be identified respectively as slowly-varying amplitudes and phases for the four

component oscillators (y_1, y_2, z_1, z_2). That is, by substituting Eq. (4.3.13) into Eq. (4.2.11),

$$x_m^{(0)} = B_m \cos(\lambda_m T_0 + \Theta_m). \tag{4.3.14}$$

Thus, recalling equations (4.3.1), and (4.3.3), explicit representations for the approximate component oscillators are found to be

$$y_1^{(0)} = B_1 \cos(T_0 + \Theta_1); \qquad z_1^{(0)} = A_1 \cos(T_0 + \Phi_1) \tag{4.3.15a}$$

$$y_2^{(0)} = B_2 \cos(T_0 + \Theta_2); \qquad z_2^{(0)} = A_2 \cos(T_0 + \Phi_2), \tag{4.3.15b}$$

where

$$A_1 \equiv B_3; \quad \Phi_1 \equiv \Theta_3 \tag{4.3.16a}$$

$$A_2 \equiv B_4; \quad \Phi_2 \equiv \Theta_4 \tag{4.3.16b}$$

have been introduced for convenience in the sequel.

Substitution of Eqs. (4.3.13) and (4.3.14) into Eqs. (4.3.12), while noting

$$(\ )' \equiv \frac{d}{dT_1} \equiv \frac{1}{\varepsilon}\frac{d}{dt} \equiv \frac{1}{\varepsilon}(\dot{}), \tag{4.3.17}$$

gives

$$-2i(\dot{B}_1 + iB_1\dot{\Theta}_1) + (ic - \tilde{c})A_1 e^{-i(\Theta_1 - \Phi_1)} + (1 - \Omega_1^2 - i\gamma_1)B_1 = 0 \tag{4.3.18a}$$

$$-2i(\dot{A}_1 + iA_1\dot{\Phi}_1) + i\alpha A_1 - \frac{3}{4}ipA_1^3 - \frac{1}{2}iqA_2^2A_1$$
$$- \frac{1}{4}qA_2^2A_1 e^{2i(\Phi_2 - \Phi_1)} + (ir + \tilde{r})B_1 e^{i(\Theta_1 - \Phi_1)} = 0 \tag{4.3.18b}$$

As before, companion equations also hold, as obtained by interchanging subscripts 1 and 2.

Separating real and imaginary parts gives, upon rearrangement, the following set of first-order, nonlinear differential equations in the amplitudes and phases:

$$\dot{A}_1 = \frac{1}{2}\alpha A_1 - \frac{3}{8}pA_1^3 - \frac{1}{8}qA_2^2A_1(2+\cos 2\varphi) + \frac{1}{2}B_1(r\cos\mu_1 + \tilde{r}\sin\mu_2) \tag{4.3.19a}$$

$$\dot{A}_2 = \frac{1}{2}\alpha A_2 - \frac{3}{8}pA_2^3 - \frac{1}{8}qA_1^2A_2(2+\cos 2\varphi) + \frac{1}{2}B_2(r\cos\mu_2 + \tilde{r}\sin\mu_2) \tag{4.3.19b}$$

$$\dot{B}_1 = -\frac{1}{2}\gamma_1 B_1 + \frac{1}{2}A_1(c\cos\mu_1 + \tilde{c}\sin\mu_1) \tag{4.3.19c}$$

$$\dot{B}_2 = -\frac{1}{2}\gamma_2 B_2 + \frac{1}{2}A_2(c\cos\mu_2 + \tilde{c}\sin\mu_2) \tag{4.3.19d}$$

$$\dot{\Phi}_1 = -\frac{1}{8}qA_2^2\sin 2\varphi - \frac{B_1}{2A_1}(\tilde{r}\cos\mu_1 - r\sin\mu_1) \tag{4.3.19e}$$

$$\dot{\Phi}_2 = +\frac{1}{8}qA_1^2\sin 2\varphi - \frac{B_2}{2A_2}(\tilde{r}\cos\mu_2 - r\sin\mu_2) \tag{4.3.19f}$$

$$\dot{\Theta}_1 = -\frac{1}{2}(1-\Omega_1^2) - \frac{A_1}{2B_1}(-\tilde{c}\cos\mu_1 + c\sin\mu_1) \tag{4.3.19g}$$

$$\dot{\Theta}_2 = -\frac{1}{2}(1-\Omega_2^2) - \frac{A_2}{2B_2}(-\tilde{c}\cos\mu_2 + c\sin\mu_2) \tag{4.3.19h}$$

Here the companion equations have been written explicitly, and the phase differences

$$\varphi \equiv \Phi_2 - \Phi_1 \tag{4.3.20a}$$

$$\mu_i \equiv \Theta_i - \Phi_i, \quad i = 1, 2 \tag{4.3.20b}$$

have been introduced. Eqs. (4.3.19) will be referred to hereafter as the amplitude/phase equations.

4.4 Summary

In this chapter, Eqs. (4.1.8) have been proposed as generalized model equations which contain each of the entries in Table 4.1.1 as a special case. An asymptotic method developed in Section 4.2 has been applied to the generalized equations in Section 4.3, the result being a set of differential equations in the amplitudes and phases of the original oscillator variables y_i and z_i.

CHAPTER V

STEADY-STATE MONOFREQUENCY SOLUTIONS

5.1 Introduction

As indicated in Figs. 2.4.2, vortex-induced structural vibrations reach maximum amplitude during lock-in, when the fluid and structural oscillators vibrate steadily at a common frequency. Such steady-state, monofrequency oscillations are therefore of great practical interest, and should rightfully be emphasized in an analysis of the empirical model. In this chapter, approximate monofrequency solutions are found analyitically, based on results of the previous chapter, for each of the cases listed in Table 4.1.1. The unified analysis of Chapter 4 is continued in Section 5.2, after which separate, specific results are obtained for each case.

5.2 General Analysis

Consider the following expressions for the approximate oscillator variables $(z_i^{(0)},\ y_i^{(0)})$, $i = 1,\ 2$:

$$z_i^{(0)}(t) = A_i(t)\cos[\Omega t + \varphi_i(t)] \tag{5.2.1a}$$

$$y_i^{(0)}(t) = B_i(t)\cos[\Omega t + \vartheta_i(t)]. \tag{5.2.1b}$$

Although this form is slightly different than Eqs. (4.3.15) dictated by the asymptotic method, the equivalence of the two forms is recognized by identifying

$$\theta_i(t) \equiv \vartheta_i(t) + (\Omega - 1)t \tag{5.2.2a}$$

$$\Phi_i(t) \equiv \varphi_i(t) + (\Omega - 1)t \tag{5.2.2b}$$

and recalling $T_0 \equiv t$. Simply stated, Eqs. (4.3.15) interpret as a uniform phase drift what Eqs. (5.2.1) interpret as a frequency shift.

For steady-state, monofrequency oscillations at the (unknown) frequency Ω,

the amplitudes and phases in Eqs. (5.2.1) must be constant:

$$\dot{A}_i = \dot{B}_i = 0 \tag{5.2.3a}$$

$$\dot{\varphi}_i = \dot{\vartheta}_i = 0. \tag{5.2.3b}$$

Thus, according to Eqs. (5.3.2), the phases Φ_i and Θ_i must, in the steady state, all drift at the same, constant rate

$$\dot{\Phi}_i = \dot{\Theta}_i = \Omega - 1, \quad i = 1, 2. \tag{5.2.4}$$

Substitution of Eqs. (5.2.3) and (5.2.4) into the amplitude/phase equations (4.3.19) yields the following equations for approximate, steady-state, monofrequency oscillations of the system (4.1.8):

$$\alpha A_i - \frac{3}{4}pA_i^3 - \frac{1}{4}qA_j^2A_i(2 + \cos 2\varphi_{ji}) + B_i(r\cos\mu_i + \tilde{r}\sin\mu_i) = 0 \tag{5.2.5a}$$

$$-\gamma_i B_i + A_i(c\cos\mu_i + \tilde{c}\sin\mu_i) = 0 \tag{5.2.5b}$$

$$2\sigma A_i + \frac{1}{4}qA_j^2A_i\sin 2\varphi_{ji} + B_i(\tilde{r}\cos\mu_i - r\sin\mu_i) = 0 \tag{5.2.5c}$$

$$(1 - \Omega_i^2 + 2\sigma)B_i + A_i(-\tilde{c}\cos\mu_i + c\sin\mu_i) = 0, \tag{5.2.5d}$$

where $i = 1, 2$, and convention (4.1.10) applies for subscripts i and j. The frequency unknown

$$\sigma \equiv \Omega - 1 \sim O(\varepsilon) \tag{5.2.6}$$

has been introduced here, as well as the phases φ_{21} and φ_{12}, where

$$\varphi_{21} \equiv \varphi \equiv \varphi_2 - \varphi_1 \equiv -\varphi_{12}. \tag{5.2.7}$$

The latter series of definition is necessary to preserve the (1, 2) subscript symmetry of the two sets of equations represented by (5.2.5).

The system (5.2.5) comprises eight nonlinear algebraic equations for the steady-state values of the eight unknowns (A_1, A_2, B_1, B_2, μ_1, μ_2, φ, σ). The method of solution depends strongly upon which of the cases listed in Table 4.1.1 is considered. Consequently, in the following sections, a separate analysis is performed for each case.

5.3 Forced Cylinder

5.3.1 Amplitude Solution

According to Table 4.1.1, there is only one unknown oscillator variable in this case,

$$z_1 \equiv Z, \tag{5.3.1}$$

satisfying the generalized model equation

$$\ddot{Z} - \alpha\dot{Z} + p\dot{Z}^3 + Z = r\dot{Y}(t) + \tilde{r}Y(t) \tag{5.3.2}$$

where $p = \beta$. The cylinder displacement

$$y_1 \equiv Y(t), \tag{5.3.3}$$

assumed to be harmonic with frequency Ω and amplitude B_1, is known. Therefore, with the help of Eqs. (4.3.20) and (5.2.2), Eqs. (5.2.1) give

$$Z^{(0)} = A_1\cos(\Omega t + \varphi_1) \tag{5.3.4a}$$

$$Y(t) \equiv Y^{(0)} = B_1\cos(\Omega t + \varphi_1 + \mu_1). \tag{5.3.4b}$$

Since the phase of the forcing function $Y^{(0)}$ may be arbitrarily prescribed, let

$$\varphi_1 + \mu_1 = 0, \tag{5.3.5}$$

such that

$$Z^{(0)} = A\cos(\Omega t + \varphi_1) \tag{5.3.6a}$$

$$Y^{(0)} = B\cos\Omega t. \tag{5.3.6b}$$

Subscripts on A and B have been dropped here for simplicity, without ambiguity. The forcing frequency $\Omega = 1 + \sigma$ and the forcing amplitude B are both known, so there remain only two unknowns, A and φ_1.

Of Eqs. (5.2.5), only Eqs. (5.2.5a) and (5.2.5c) for $i = 1$ are relevant, having been obtained from the differential equations for $z_1^{(0)}$. Reduction of these two equations according to Table 4.1.1 and Eq. (5.3.5) yields

$$\alpha A - \frac{3}{4}pA^3 + B(r\cos\varphi_1 - \tilde{r}\sin\varphi_1) = 0 \tag{5.3.7a}$$

$$2\sigma A + B(\tilde{r}\cos\varphi_1 + r\sin\varphi_1) = 0, \tag{5.3.7b}$$

which may be solved as a linear, inhomogeneous algebraic system in the unknowns $\cos\varphi_1$ and $\sin\varphi_1$:

$$\cos\varphi_1 = -\frac{A}{B}\frac{r(\alpha - \frac{3}{4}pA^2) + 2\tilde{r}\sigma}{r^2 + \tilde{r}^2} \tag{5.3.8a}$$

$$\sin\varphi_1 = +\frac{A}{B}\frac{\tilde{r}(\alpha - \frac{3}{4}pA^2) - 2r\sigma}{r^2 + \tilde{r}^2}. \tag{5.3.8b}$$

Squaring and adding gives a single equation in the unknown amplitude A:

$$\left(\frac{B}{A}\right)^2 = \frac{(\alpha - \frac{3}{4}pA^2)^2 + 4\sigma^2}{r^2 + \tilde{r}^2}. \tag{5.3.9}$$

It is useful in the sequel to introduce the constants

$$c_1 \equiv \frac{2}{\alpha} \tag{5.3.10a}$$

$$c_2 \equiv \sqrt{\frac{3(r^2 + \tilde{r}^2)p}{4\alpha^3}} \tag{5.3.10b}$$

and the normalizations

$$\sigma^* \equiv c_1\sigma = c_1(\Omega - 1) \tag{5.3.11a}$$

$$B^* \equiv c_2 B \tag{5.3.11b}$$

$$A^* \equiv \frac{3}{4}\frac{pA^2}{\alpha}, \tag{5.3.11c}$$

in terms of which the solution (5.3.9) relating A, B, and σ becomes

$$B^{*2} = A^*[(1 - A^*)^2 + \sigma^{*2}]. \tag{5.3.12}$$

The quantities (c_1, c_2) may be regarded as **axis-stretching constants** which transform the physical variables (σ, B) into the canonical variables (σ^*, B^*). Eq. (5.3.12) is quadratic in σ^*, so

$$\sigma^* = \pm \left[\frac{B^{*2} - A^*(1 - A^*)^2}{A^*} \right]^{\frac{1}{2}}, \tag{5.3.13}$$

from which the solution curves on Fig. 5.3.1 have been generated. This is a well-known result for the single degree-of-freedom van der Pol oscillator equation (5.3.2) [66]. With B^* and σ^* fixed there may be either one or three real solutions for A^*, which is not surprising since Eq. (5.3.12) may be alternatively regarded as a cubic in A^*. Stability of solutions shown in Fig. 5.3.1 is considered below; lettered points in the Figure are discussed in Section 6.2.

5.3.2 Stability

To investigate stability of the above solutions, it is necessary to return to the amplitude/phase equations of Chapter 4, prior to assumption of the steady-state. Using Eqs. (4.3.19a) and (4.3.19e), with the help of Eqs. (5.2.2) and (5.2.6), the two variables (A_1, φ_1) are found to satisfy a pair of first-order differential equations of the form

$$\dot{\mathbf{X}} = \mathbf{J}(\mathbf{X}), \tag{5.3.14}$$

where, recalling $A_1 \equiv A$ and $B_1 \equiv B$,

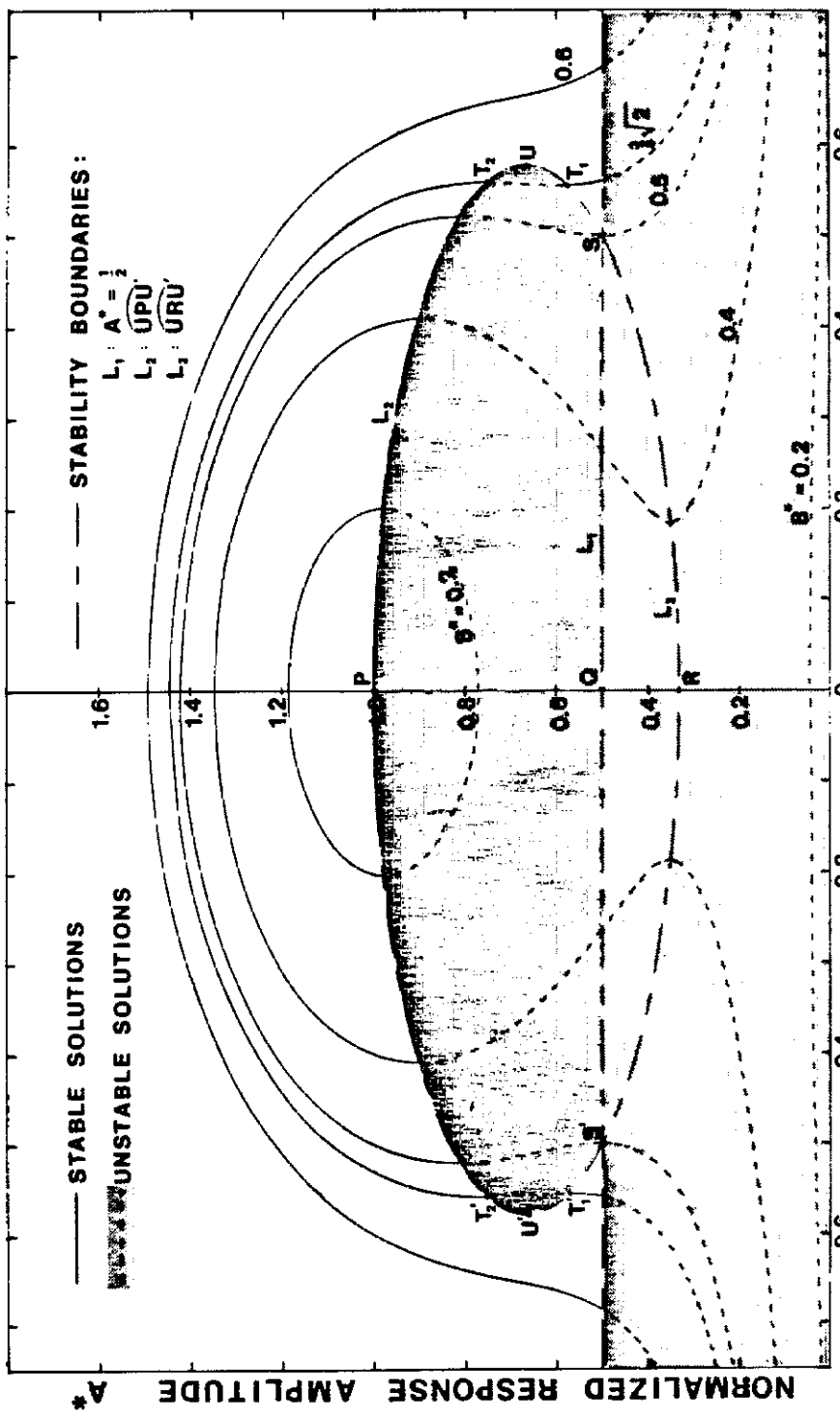

Fig. 5.3.1: Solutions to the Forced van der Pol Equation (5.3.2).

$$\mathbf{X} \equiv \begin{Bmatrix} A \\ \varphi_1 \end{Bmatrix} \tag{5.3.15}$$

and

$$\mathbf{J}(\mathbf{X}) \equiv \begin{Bmatrix} \dot{A} \\ \dot{\varphi}_1 \end{Bmatrix} = \frac{1}{2} \begin{Bmatrix} A(\alpha - \frac{3}{4}pA^2) + B(r\cos\varphi_1 - \tilde{r}\sin\varphi_1) \\ -2\sigma - \frac{B}{A}(\tilde{r}\cos\varphi_1 + r\sin\varphi_1) \end{Bmatrix} \tag{5.3.16}$$

The steady-state solution $\mathbf{X}_0$ satisfies

$$\mathbf{J}(\mathbf{X}_0) = 0, \tag{5.3.17}$$

so if $\mathbf{X}$ is perturbed sightly away from $\mathbf{X}_0$, i.e.

$$\mathbf{X} = \mathbf{X}_0 + \varepsilon\hat{\mathbf{X}}, \tag{5.3.18}$$

the perturbation $\hat{\mathbf{X}}$ satisfies, to first order in ε,

$$\dot{\hat{\mathbf{X}}} = [J']_0\hat{\mathbf{X}}, \tag{5.3.19}$$

where $[J']_0$ is an abbreviation for the Jacobian matrix evaluated in the steady state $\left[\frac{\partial \mathbf{J}}{\partial \mathbf{X}}\right]\Big|_{\mathbf{X}=\mathbf{X}_0}$.

Differentiating Eq. (5.3.16), using the steady-state equations (5.3.7) in the form

$$\frac{B}{A}(\tilde{r}\sin\varphi_1 - r\cos\varphi_1)\Big|_{\mathbf{X}=\mathbf{X}_0} = \alpha - \frac{3}{4}pA^2 \tag{5.3.20a}$$

$$B(\tilde{r}\cos\varphi_1 + r\sin\varphi_1)\Big|_{\mathbf{X}=\mathbf{X}_0} = -2\sigma A, \tag{5.3.20b}$$

and normalizing according to Eqs. (5.3.11) gives

$$[J']_0 = \alpha \begin{bmatrix} 1 - 3A^* & A\sigma^* \\ -\dfrac{\sigma^*}{A} & 1 - A^* \end{bmatrix}. \qquad (5.3.21)$$

By a well-known property of two-dimensional linear systems of the form (5.3.19), the perturbation $\hat{\mathbf{X}}$ decays with time, and hence the steady-state solution $\mathbf{X}_0$ is stable, if and only if the trace of $[J']_0$ is negative and the determinant is positive [44]. *Consequently the stability conditions are*

$$A^* > \frac{1}{2} \qquad (straight\text{-}line\ boundary) \qquad (5.3.22a)$$

$$(1 - 3A^*)(1 - A^*) + \sigma^{*2} > 0 \qquad (elliptical\ boundary) \qquad (5.3.22b)$$

In other words, if a stability boundary in the (σ^*, A^*) plane is denoted by the locus of points

$$A^* = L_k(\sigma^*), \qquad (5.3.23)$$

where k is an index, then according to Eqs (5.3.22), a solution of (5.3.13) is stable if and only if the point (σ^*, A^*) lies above the straight line given by

$$L_1(\sigma^*) \equiv \frac{1}{2}, \qquad (5.3.24a)$$

and outside the ellipse whose upper half is given by

$$L_2(\sigma^*) \equiv \frac{2}{3}\left\{1 + \sqrt{1 - \frac{3}{4}(1 + \sigma^{*2})}\right\} \qquad (5.3.24b)$$

and whose lower half is given by

$$L_3(\sigma^*) \equiv \frac{2}{3}\left\{1 - \sqrt{1 - \frac{3}{4}(1 + \sigma^{*2})}\right\}. \qquad (5.3.24c)$$

On Fig. (5.3.1) these loci are shown as dashed lines, marking the limits beyond

which real stable solutions of the assumed form (5.3.6) fail to exist. In the unstable regions, solutions of a more complex nature prevail.

The stability boundaries are important for comparison of the mathematical model with experimental results. Physically, the stability boundaries imply that, according to the model, vortex-shedding is synchronized with the forcing frequency (i.e. locked-in) only within a certain range of σ^* bracketing $\sigma^* = 0$. For example, with $B^* = 0.6$ in Fig. 5.3.1, the solution curve is stable for $|\sigma^*| < \frac{1}{10}\sqrt{47} \approx 0.686$,[1] and unstable otherwise. Moreover, this range of stability increases in width as B^* is increased. The truth of such qualitative model predictions is well-documented experimentaly, as shown in Fig. 2.3.2. This agreement is not surprising; in fact, as discussed in Sections 3.1 and 3.2, such qualitative agreement was anticipated by experimentalists Bishop and Hassan [5] when they first proposed the idea of modeling vortex wakes as nonlinear oscillators.

It is emphasized that the present model predicts the forced-cylinder lock-in band to be symmetrically located about the exact resonance point $\sigma^* = 0$, regardless of what values are selected for the model constants. This qualitative result appears to agree with Koopman's data (Fig. 2.3.2). Quantitatively, the agreement obtainable with the present model depends on judicious selection of the model constants, to be carried out in Chapter 6.

---

1. This value is obtained using Eq. (5.3.13) with $A^* = \frac{1}{2}$, since, according to Fig. 5.3.1, stability boundary L_1 is relevant for this case.

5.4 Spring-Mounted Cylinder

5.4.1 Amplitude and Frequency Solution

According to Table 4.1.1, there are two unknown oscillator variables in this case,

$$z_1 = Z \tag{5.4.1a}$$

$$y_1 = Y, \tag{5.4.1b}$$

satisfying the generalized model equations

$$\ddot{Z} - a\dot{Z} + p\dot{Z}^3 + Z = r\dot{Y} + \tilde{r}Y \tag{5.4.2a}$$

$$\ddot{Y} + \gamma\dot{Y} + \Omega_1^2 Y = c\dot{Z} - \tilde{c}Z \tag{5.4.2b}$$

where $p = \beta$ and $\gamma = \gamma_1$. As in Section 5.3, Eqs. (5.2.1) give

$$Z^{(0)} = A_1\cos(\Omega t + \varphi_1) \tag{5.4.3a}$$

$$Y^{(0)} = B_1\cos(\Omega t + \varphi_1 + \mu_1). \tag{5.4.3b}$$

However, in this case $Y^{(0)}$ is unknown rather than prescribed, so the differential equations (5.4.2) are autonomous, and the origin of time is arbitrary. Consequently one arbitrary condition may be imposed on the phases (φ_1, μ_1). Eq. (5.3.5) would be one possibility, but the ensuing analysis has been carried out instead with

$$\varphi_1 = 0. \tag{5.4.4}$$

Therefore

$$Z^{(0)} = A\cos\Omega t \tag{5.4.5a}$$

$$Y^{(0)} = B\cos(\Omega t + \mu), \tag{5.4.5b}$$

where subscripts on A, B, and μ have been dropped for simplicity.[1]

---

1. The subscript on Ω_1 is retained in order to distinguish the natural structural frequency Ω_1 from the response frequency Ω.

Steady-state equations for the four unknowns A, B, μ, and $\sigma \equiv \Omega - 1$ are generated by application of Eqs. (5.2.5) with $i = 1$, $\gamma = \gamma_1$, and $q = 0$ (see Table 4.1.1):

$$\alpha A - \frac{3}{4}pA^3 + B(r\cos\mu + \tilde{r}\sin\mu) = 0 \tag{5.4.6a}$$

$$-\gamma B + A(c\cos\mu + \tilde{c}\sin\mu) = 0 \tag{5.4.6b}$$

$$2\sigma A + B(\tilde{r}\cos\mu - r\sin\mu) = 0 \tag{5.4.6c}$$

$$(1 - \Omega_1^2 + 2\sigma)B + A(-\tilde{c}\cos\mu + c\sin\mu) = 0 \tag{5.4.6d}$$

Solving Eqs. (5.4.6b) and (5.4.6d) as a linear, inhomogeneous, algebraic system in the unknowns $\cos\mu$ and $\sin\mu$ yields

$$\cos\mu = \frac{c\gamma + \tilde{c}(1 - \Omega_1^2 + 2\sigma)}{c^2 + \tilde{c}^2}\frac{B}{A} \tag{5.4.7a}$$

$$\sin\mu = \frac{\tilde{c}\gamma - c(1 - \Omega_1^2 + 2\sigma)}{c^2 + \tilde{c}^2}\frac{B}{A}. \tag{5.4.7b}$$

Squaring and adding gives

$$(\frac{B}{A})^2 = \frac{c^2 + \tilde{c}^2}{(1 - \Omega_1^2 + 2\sigma)^2 + \gamma^2}. \tag{5.4.8}$$

Substitution of Eqs. (5.4.7) into Eqs. (5.4.6a) and (5.4.6c) followed by substitution of Eq. (5.4.8) to eliminate $(\frac{B}{A})^2$ produces a frequency equation and an amplitude equation,

$$F(\sigma) = 0 \tag{5.4.9a}$$

$$G(\sigma) = A^2, \tag{5.4.9a}$$

where the functions F and G are defined as

$$F(\sigma) \equiv \frac{4}{3p}\left[-2\sigma - \frac{k_b(1-\Omega_1^2+2\sigma)+k_a\gamma}{(1-\Omega_1^2+2\sigma)^2+\gamma^2} \right] \tag{5.4.10a}$$

$$G(\sigma) \equiv \frac{4}{3p}\left[\alpha + \frac{-k_a(1-\Omega_1^2+2\sigma)+k_b\gamma}{(1-\Omega_1^2+2\sigma)^2+\gamma^2} \right], \tag{5.4.10b}$$

and

$$k_a \equiv \tilde{r}c - r\tilde{c} \tag{5.4.11a}$$

$$k_b \equiv rc + \tilde{r}\tilde{c}. \tag{5.4.11b}$$

5.4.2 Detuning Variables

Since σ is the only unknown appearing in the functions F and G, Eq. (5.4.9a) might be used to solve for σ, and the result inserted into Eq. (5.4.9b) to solve for amplitude A. However, upon clearing of fractions in Eq. (5.4.9a), a cubic in σ is obtained, yielding either one or three real solutions, which must be found numerically or by the relatively complicated analytical formulas for a cubic.

A simpler result is obtained by replacing the pair of frequency variables (σ, Ω_1) appearing in Eqs. (5.4.10) with *detuning variables*

$$\Delta_r \equiv \frac{1}{2}(1-\Omega_1^2+2\sigma) \tag{5.4.12a}$$

$$\Delta_f \equiv \frac{1}{2}(1-\Omega_1^2). \tag{5.4.12b}$$

The subscripts "r " and "f" on (Δ_r, Δ_f) are mnemonic for response-structure detuning and fluid-structure detuning respectively, although the Δ's are "detunings" only in an approximate sense. Assuming $e_2 \approx 1$ [as explained in the footnote to Eq. (3.2.20)],[2] the exact detunings

$$d_r \equiv \Omega - \sqrt{e_2}\,\Omega_1 \quad \text{(Response–structure detuning)} \tag{5.4.13a}$$

---

2. The factors of $\sqrt{e_2}$ appearing in Eqs. (5.4.13) are necessary to achieve consistency with the physically motivated definitions of (d_r, d_f) given in Section 2.4; see Eqs. (2.4.4), (2.4.5), and (3.2.20).

$$d_f \equiv 1 - \sqrt{e_2}\,\Omega_1 \quad \text{(Fluid–structure detuning)} \tag{5.4.13b}$$

are equivalent, respectively, to (Δ_r, Δ_f) only in the limit $d_f \to 0$, which is apparent upon substitution of Eqs. (5.4.13) into Eqs. (5.4.12):[3]

$$\Delta_r \approx d_r - \tfrac{1}{2} d_f^2 \tag{5.4.14a}$$

$$\Delta_f \approx d_f - \tfrac{1}{2} d_f^2. \tag{5.4.14b}$$

The relationship between frequencies, normlaized frequencies, and detuning variables (d_r, d_f) is diagrammed on Fig. 5.4.1 for the case $e_2 = 1$.

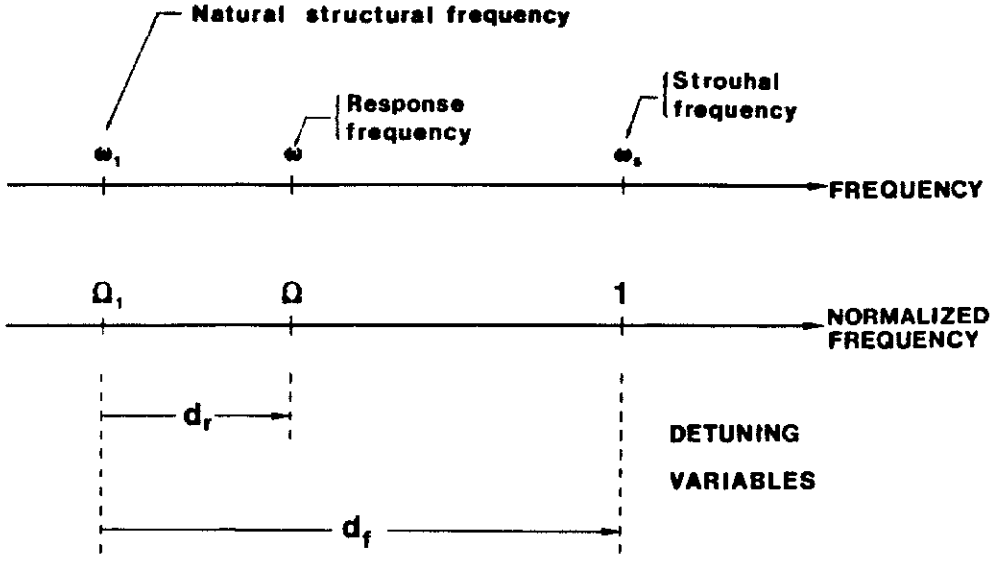

Figure 5.4.1. One-Mode Interpretation of d–Variables.

According to the order of magnitude assumptions (4.1.2) and (5.2.6), d_f is order ε; hence, to the order of accuracy of the asymptotic method, terms of order d_f^2 may theoretically be neglected; that is, it would be permissible to approximate Δ_r as d_r, and Δ_f as d_f. Pracitically however, the comparison between analytical and numerical solutions to Eqs. (5.4.2) is somewhat better if

---

3. The relations (5.4.14) are exact if $e_2 = 1$.

these approximations are not made. Therefore the distinctions between (Δ_r, Δ_f) and (d_r, d_f), which cause no analytical difficulty, will be retained in the sequel, according to definitions (5.4.12) and (5.4.13). Nevertheless, for conceptual purposes, the Δ's and the d's may be thought of as equivalent. Typically, solutions are obtained in terms of (Δ_r, Δ_f) and then converted to (d_r, d_f) for plotting.

5.4.3 Solution in Detuning Variables

Recasting the frequency and amplitude equations (5.4.9) in terms of Δ-variables gives

$$\hat{F}(\Delta_r) = 0 \tag{5.4.15a}$$

$$\hat{C}(\Delta_r) = A^2, \tag{5.4.15b}$$

where

$$\hat{F}(\Delta_r) \equiv \frac{4}{3p}\left[\, 2(\Delta_f - \Delta_r) - \frac{2k_b\Delta_r + k_a\gamma}{4\Delta_r^2 + \gamma^2} \,\right] \tag{5.4.16a}$$

$$\hat{C}(\Delta_r) \equiv \frac{4}{3p}\left[\, \alpha + \frac{-2k_a\Delta_r + k_b\gamma}{4\Delta_r^2 + \gamma^2} \,\right]. \tag{5.4.16b}$$

This form of solution is not useful unless Δ_r and Δ_f are the only frequency variables in the problem. Therefore it is necessary to make a slight approximation; namely, the quantity γ, defined according to Eqs. (3.2.22) and (3.2.23) as

$$\gamma \equiv \frac{2\zeta\Omega_1}{\sqrt{e_2}} + \frac{\alpha_4}{2\pi S e_2}\eta, \tag{5.4.17}$$

is approximated as

$$\gamma \approx \frac{2\zeta}{\sqrt{e_2}} + \frac{\alpha_4}{2\pi S e_2}\eta, \tag{5.4.18}$$

thereby eliminating the appearance of the structural frequency Ω_1. This is permissible because of condition (4.1.2); since γ itself is $O(\varepsilon)$, the error associated

with approximation (5.4.18) is $O(\varepsilon^2)$.

In the solution (5.4.15), the response detuning Δ_r would normally be considered the dependent variable, with Δ_f independent. However, upon clearing fractions, $\widehat{F} = 0$ is cubic in Δ_r, hence the solution would be either single or triple valued, and not expressible in simple form. Therefore it is advantageous to reverse the roles of Δ_r and Δ_f, considering Δ_r independent and Δ_f dependent. Then, using $\widehat{F} = 0$, the explicit, single-valued expression for Δ_f is

$$\Delta_f = \Delta_r + \frac{1}{2}\left[\frac{2k_b\Delta_r + k_a\gamma}{4\Delta_r^2 + \gamma^2}\right]. \qquad (5.4.19)$$

A typical example of this relationship is shown as the solid line in Fig. 5.4.2.

5.4.4 Interpretation of the Frequency Solution

The general nature of the frequency solution (5.4.19), as exemplified by Fig. 5.4.2, may be readily interpreted. When the independent variable Δ_r is far from 0, the denominator of the second term is large, so the first term predominates, giving $\Delta_f \approx \Delta_r$; thus Δ_f is likewise far from zero. According to definitions (5.4.12), the latter implies that Ω_1 is far away from 1, while $\Delta_f \approx \Delta_r$ implies $\sigma \approx 0$, i.e. $\Omega \approx 1$. Hence, according to the model, when the natural frequency Ω_1 of the spring-mounted cylinder is far from the natural vortex-shedding frequency ($\Omega_s \equiv 1$), the system response frequency Ω is very near Ω_s; that is, vortices shed nearly at their natural frequency. This is a physically correct result.

Conversely, when $\Delta_r \approx 0$, the second term on the right of Eq. (5.4.19) may become large, especially for light damping (γ small), producing $\Delta_f \neq \Delta_r$ such that $\Delta_f \neq 0$. Hence in this case $\Omega \approx \Omega_1 \neq 1$, which describes lock-in. These qualitative observations are quantified in Chapter 6, where simple, analytical expressions for model lock-in characteristics are derived and compared to experimental data.

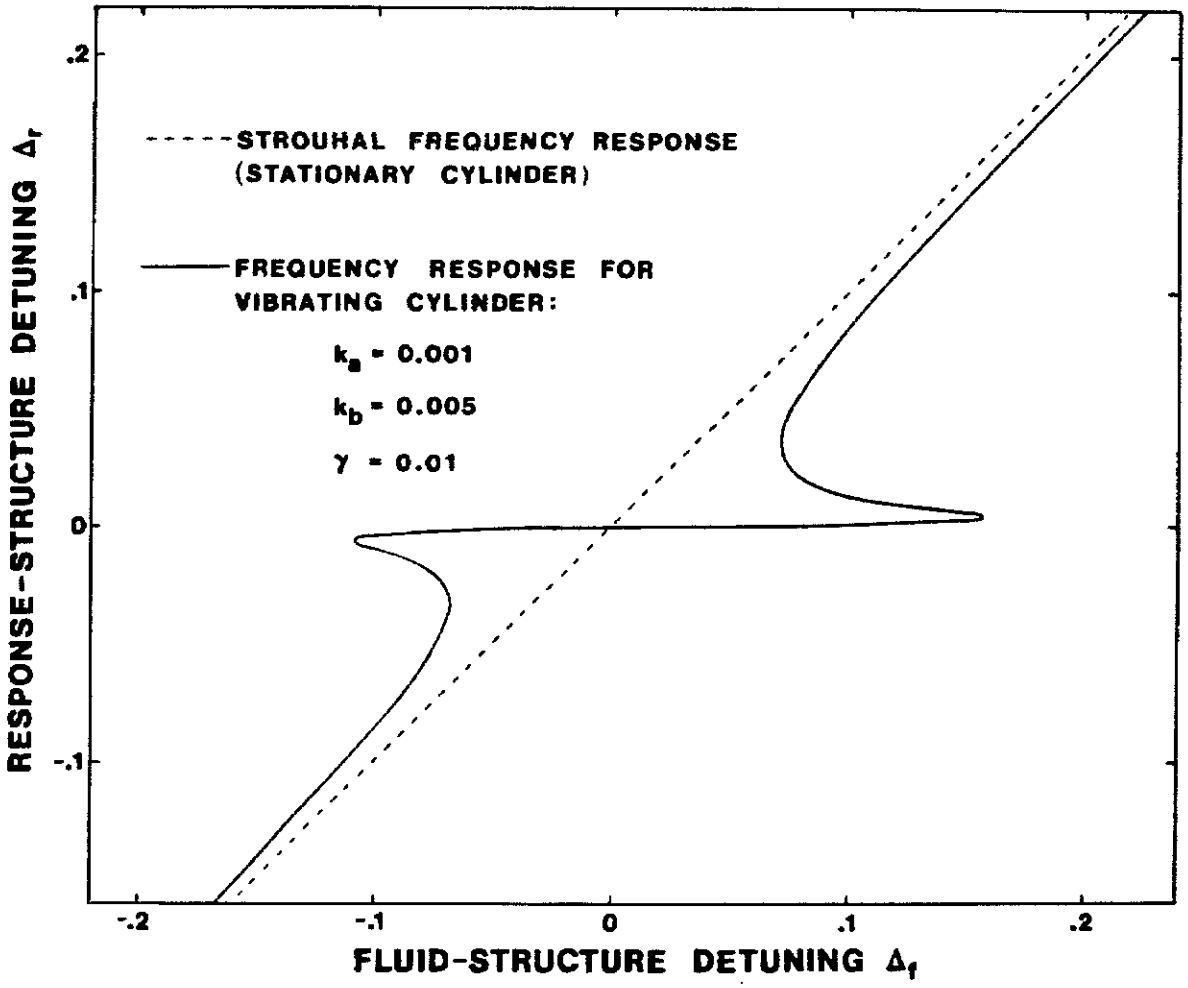

Figure 5.4.2. Typical Model Solution, Prior to Stability Considerations.

5.4.5 Classes of Solution: The Boundary of Real Amplitudes

For each value of Δ_r, the amplitude A is given by Eqs (5.4.15b) and (5.4.16b), but there is no guarantee that A is real since $\hat{G}(\Delta_r)$ may be negative. Specifically, setting $\hat{G}(\Delta_r) = 0$ to find the boundary of real solutions, it follows that A is imaginary in the range

$$\frac{k_a - \sqrt{\Gamma}}{4\alpha} < \Delta_r < \frac{k_a + \sqrt{\Gamma}}{4\alpha} \tag{5.4.20}$$

provided the discriminant

$$\Gamma \equiv k_a^2 - 4\alpha\gamma(\alpha\gamma + k_b) \tag{5.4.21}$$

is positive. If Γ is negative, A is real for all values of Δ_r. Whenever A is real, the structural amplitude B and phase μ may be recovered using Eqs. (5.4.8) and (5.4.7) respectively, with the help of definition (5.4.12a).

Further, whenever A is real, stability of the solution may be investigated as discussed below (Section 5.4.6). Therefore, three classes of solution are possible:

(1) Non-real (A imaginary)

(2) Real but unstable

(3) Real and stable.

5.4.6 Stability

As in Section 5.3, stability of the steady-state, monofrequency solutions above may be investigated using the amplitude/phase equations (4.3.19), assuming the solution under consideration is real, as discussed in Section 5.4.4. Since $q = 0$ for this case while $\gamma \equiv \gamma_1$ and $\mu \equiv \mu_1 \equiv \Theta_1 - \Phi_1$ by definition, the following system of three first order differential equations is obtained:

$$\dot{\mathbf{X}} = \mathbf{J}(\mathbf{X}), \tag{5.4.22}$$

where

$$\mathbf{X} \equiv (A, B, \mu) \tag{5.4.23}$$

and

$$J(X) \equiv \frac{1}{2}\begin{Bmatrix} \alpha A - \frac{3}{4}pA^3 + B(r\cos\mu + \tilde{r}\sin\mu) \\ -\gamma B + A(c\cos\mu + \tilde{c}\sin\mu) \\ -(1-\Omega_1^2) - \frac{A}{B}(-\tilde{c}\cos\mu + c\sin\mu) + \frac{B}{A}(\tilde{r}\cos\mu - r\sin\mu) \end{Bmatrix} \quad (5.4.24)$$

Repeating the argument preceding Eq. (5.3.19), a perturbation $\hat{X}$ satisfying

$$\dot{\hat{X}} \equiv [J']_0\hat{X} \quad (5.4.25)$$

will decay with time, and hence the steady-state solution X_0 will be stable, if and only if all eigenvalues of $[J']_0$ have negative real parts.

The Jacobian $[J']_0$ may be found as a function of constants and the independent variable Δ_r only. That is, after differentiating $J(X)$, the steady-state equations (5.4.6) may be used to replace trigonometric functions of μ with functions of A, B, Δ_f, and Δ_r, after which Eqs. (5.4.9b), (5.4.8), and (5.4.19) may be substituted to eliminate A, B, and Δ_f in favor of Δ_r:

$$A\Big|_{X=X_0} = \sqrt{\hat{G}(\Delta_r)} \quad (5.4.26a)$$

$$\frac{B}{A}\Big|_{X=X_0} = \sqrt{\frac{c^2+\tilde{c}^2}{4\Delta_r^2+\gamma^2}} \equiv R(\Delta_r) \quad (5.4.26b)$$

$$\Delta_f = \Delta_f(\Delta_r). \quad (5.4.26c)$$

Without writing $\Delta_f(\Delta_r)$ explicitly, the result is

$$[J']_0 = \frac{1}{2}\begin{bmatrix} \alpha - \frac{9}{4}p\hat{C} & -\frac{\alpha - \frac{3}{4}p\hat{C}}{R} & -2(\Delta_r - \Delta_f)\sqrt{\hat{C}} \\ \gamma R & -\gamma & 2\Delta_r R\sqrt{\hat{C}} \\ \frac{2}{\sqrt{\hat{C}}}(2\Delta_r - \Delta_f) & \frac{-2(2\Delta_r - \Delta_f)}{R\sqrt{\hat{C}}} & \alpha - \gamma - \frac{3}{4}p\hat{C} \end{bmatrix} \tag{5.4.27}$$

The eigenvalues λ of $[J']_0$, satisfying

$$\det(\lambda[I] - [J']_0) = 0 \quad ([I] = \text{the identity matrix}), \tag{5.4.28}$$

are found to be roots of the cubic

$$\lambda^3 + k_2\lambda^2 + k_1\lambda + k_0 = 0, \tag{5.4.29}$$

where

$$k_2 \equiv 3p\hat{C} + 2(\gamma - \alpha) \tag{5.4.30a}$$

$$k_1 \equiv (\alpha - \gamma)^2 + \frac{3}{2}p\hat{C}(3\gamma - 2\alpha) + \frac{27}{16}p^2\hat{C}^2 + 4(2\Delta_r - \Delta_f)^2 \tag{5.4.30b}$$

$$k_0 \equiv 6p\hat{C}\Delta_r(2\Delta_r - \Delta_f) - \frac{3}{2}\gamma p\hat{C}(\alpha - \gamma - \frac{3}{4}p\hat{C}). \tag{5.4.30c}$$

The well-known Routh conditions [9]

$$(i)\ k_m > 0,\ m = 0,\ 1,\ 2 \tag{5.4.31a}$$

$$(ii)\ k_2k_1 - k_0 > 0 \tag{5.4.31b}$$

are necessary and sufficient to insure that all solutions λ of Eq. (5.4.29) have negative real parts.

Therefore, a given value of the independent variable Δ_r produces a stable, steady-state solution $\mathbf{X}_0$ if and only if conditions (5.4.31) hold. In general, only certain portions of a solution curve such as Fig. 5.4.2 will be stable; instability indicates that the steady-state solution under consideration is in fact not physically meaningful.

5.5 One-Mode Cable Approximation

As indicated in Table 4.1.1, the model equations for this case are identical to those for the previous case (Section 5.4), except for the identification of variables and the value of p. Thus, adopting the subscript convention (4.1.10), the oscillator variables ($z_1^{(0)}$, $y_1^{(0)}$) replace ($Z^{(0)}$, $Y^{(0)}$) in Eqs. (5.4.5):

$$z_1^{(0)} = A\cos\Omega t \tag{5.5.1a}$$

$$y_1^{(0)} = B\cos(\Omega t + \mu). \tag{5.5.1b}$$

All of the equations in Section 5.4 are valid here; p merely assumes the value $\frac{3}{2}\beta$ rather than β, which does not affect the frequency solution (5.4.19) at all, affects the amplitude solution (5.4.15b) by a constant factor

$$(A)_{\substack{one-mode\\ cable\\ approximation}} = \sqrt{\frac{2}{3}}\,(A)_{\substack{spring-\\ mounted\\ cylinder}} \tag{5.5.2a}$$

$$(B)_{\substack{one-mode\\ cable\\ approximation}} = \sqrt{\frac{2}{3}}\,(B)_{\substack{spring-\\ mounted\\ cylinder}}. \tag{5.5.2b}$$

Any solution which is stable (unstable) for the spring-mounted cylinder will likewise be stable (unstable) for the one-mode cable approximation, because the stability equations (5.4.31) do not involve the altered values of the amplitudes (Eqs. 5.5.2), while the altered parameter p always appears in the combination $p\hat{C}$, which according to Eq. (5.4.16b) is only a function of α, γ, k_a, k_b, and Δ_r, irrespective of p itself.

In short, the spring-mounted cylinder and the one-mode cable approximation have identical solutions, except that the amplitudes are smaller in the latter case by a factor of $\sqrt{\frac{2}{3}}$.

5.6 Two-Mode Cable Approximation

5.6.1 General Remarks

According to Table 4.1.1, all four of the generalized model equations (4.1.8) apply to this case. Using Eqs. (5.2.1), the approximate solutions are

$$z_i^{(0)} = A_i \cos(\Omega t + \varphi_i) \tag{5.6.1a}$$

$$y_i^{(0)} = B_i \cos(\Omega t + \vartheta_i), \tag{5.6.1b}$$

where $i = 1, 2$.

Since Eqs. (4.1.8) are autonomous, only the three phase differences

$$\mu_i \equiv \vartheta_i - \varphi_i \tag{5.6.2}$$

and

$$\varphi \equiv \varphi_{21} \equiv \varphi_2 - \varphi_1 \equiv -\varphi_{12} \tag{5.6.3}$$

rather than the four phases (φ_i, ϑ_i) themselves, are independent.[1] Thus, as in Section 5.4, one arbitrary condition may be imposed on the four phases, for example $\varphi_1 = 0$.

Upon inspection of Eqs. (4.1.8) it is clear that two entirely different brands of nontrivial solution are possible, namely

1. **Case 1: Non-degenerate solutions,** for which both z_i and both y_i are non-zero

2. **Case 2: Degenerate solutions,** which are of two types:

   - $z_1, y_1 \neq 0$ and $z_2 = y_2 = 0$ (Type 1)

   - $z_2, y_2 \neq 0$ and $z_1 = y_1 = 0$ (Type 2).

For any given set of parameters (α, p, q, r, $\tilde{r}$, etc.), it is not clear *a priori*

---

1. These definitions are consistent with previous equations (4.3.20), (5.2.2), and (5.2.7).

which type of steady-state solution (if any) will actually prevail. In analogy to Section 5.3, existence demands not only a real algebraic solution to the steady-state equations (5.2.5), but also the stability of that solution against arbitrary, small disturbances. These questions are discussed in subsections 5.6.2 and 5.6.3 for non-degenerate and degenerate solutions respectively. Reasons for handling the two types of solution separately will become clear in the course of the analysis.

5.6.2 Non-Degenerate Solutions

5.6.2.1 Algebraic Solutions of Equations (5.2.5)

Initially, solution of the eight steady-state equations (5.2.5) in eight unknowns (A_1, A_2, B_1, B_2, μ_1, μ_2, φ, σ) proceeds in direct analogy to the solution of the reduced one-mode system (5.4.6). By definition of non-degenerate solutions (Section 5.6.1), $A_i \neq 0$ for both values of i, so it is permissible to write:

$$\cos\mu_i = \frac{c\gamma_i + \tilde{c}(1 - \Omega_i^2 + 2\sigma)}{c^2 + \tilde{c}^2}\frac{B_i}{A_i} \tag{5.6.4a}$$

$$\sin\mu_i = \frac{\tilde{c}\gamma_i - c(1 - \Omega_i^2 + 2\sigma)}{c^2 + \tilde{c}^2}\frac{B_i}{A_i} \tag{5.6.4b}$$

$$\left(\frac{B_i}{A_i}\right)^2 = \frac{c^2 + \tilde{c}^2}{(1 - \Omega_i^2 + 2\sigma)^2 + \gamma_i^2} \tag{5.6.5}$$

At this point, the analogy to Section 5.4 becomes less direct because, for the present case $q \neq 0$. Substitution of Eqs. (5.6.4) into Eqs. (5.2.5a) and (5.2.5c), followed by substitution of Eq. (5.6.5) to eliminate $\left(\frac{B_i}{A_i}\right)^2$, produces a set of four equations ($i = 1, 2$) in the four unknowns (A_1, A_2, φ, σ):

$$QA_j^2 \sin 2\varphi_{ji} = F_i(\sigma) \tag{5.6.6a}$$

$$A_i^2 + QA_j^2(2 + \cos 2\varphi_{ji}) = G_i(\sigma), \tag{5.6.6b}$$

where, in analogy to Eqs. (5.4.10),

$$F_i(\sigma) \equiv \frac{4}{3p}\left[2\sigma + \frac{k_b(1 - \Omega_i^2 + 2\sigma) + k_a\gamma_i}{(1 - \Omega_i^2 + 2\sigma)^2 + \gamma_i^2}\right] \tag{5.6.7a}$$

$$G_i(\sigma) \equiv \frac{4}{3p}\left[\alpha + \frac{-k_a(1 - \Omega_i^2 + 2\sigma) + k_b\gamma_i}{(1 - \Omega_i^2 + 2\sigma)^2 + \gamma_i^2}\right], \tag{5.6.7b}$$

while

$$Q \equiv \frac{q}{3p}, \tag{5.6.8}$$

and convention (4.1.10) holds for subscripts $i = 1, 2$ and $j = 2, 1$, as always. It should be noted that each pair of equations represented by (5.6.6) reduces correctly to Eqs. (5.4.9) for the special case $Q = 0$. However, division of both sides by A_i^2 is necessary to obtain Eq. (5.6.6a), which consequently is valid in a two-mode context only for the non-degenerate case, where $A_i \neq 0$ for both i. This is one of the motivations for the separate discussion of degenerate solutions in Section 5.6.3. Another motivation occurs in the stability analysis (see Section 5.6.3.2).

Eqs. (5.6.6) are next reduced to two equations in two unknowns (φ, σ) by elimination of the A_i. Multiplying Eq. (5.6.6b) by $\sin 2\varphi_{ji}$, Eq. (5.6.6a) by $(2 + \cos 2\varphi_{ji})$, and subtracting yields

$$A_i^2 \sin 2\varphi_{ji} = G_i \sin 2\varphi_{ji} - F_i(2 + \cos 2\varphi_{ji}). \tag{5.6.9}$$

Interchanging the indices (i, j) in Eq. (5.6.6a) and recalling $\varphi_{ij} = -\varphi_{ji}$ gives

$$-QA_i^2 \sin 2\varphi_{ji} = F_j. \tag{5.6.10}$$

Multiplying Eq. (5.6.9) by Q and adding Eq. (5.6.10) accomplishes elimination of the A_i:

$$Q[F_i(2 + \cos 2\varphi_{jk}) - G_i \sin 2\varphi_{jk}] = F_j. \tag{5.6.11}$$

Again, this result correctly reduces to Eq. (5.4.9a) for the special case $Q = 0$.

Elimination of φ is achieved by writing Eq. (5.6.11) for $i = 1, 2$ as a linear system in the trigonometric functions $Q(2 + \cos 2\varphi)$ and $Q \sin 2\varphi$, where $\varphi \equiv \varphi_{21} \equiv -\varphi_{12}$ is recalled from Eq. (5.6.3):

$$\begin{bmatrix} F_1 & G_1 \\ F_2 & G_2 \end{bmatrix} \begin{Bmatrix} Q(2 + \cos 2\varphi) \\ Q \sin 2\varphi \end{Bmatrix} = \begin{Bmatrix} F_2 \\ F_1 \end{Bmatrix}. \tag{5.6.12}$$

Solving:

$$Q \cos 2\varphi = \frac{F_1 G_1 + F_2 G_2}{F_1 G_2 + F_2 G_1} - 2Q \tag{5.6.13a}$$

$$Q \sin 2\varphi = \frac{F_1^2 - F_2^2}{F_1 G_2 + F_2 G_1}. \tag{5.6.13b}$$

Squaring and adding yields

$$\begin{aligned} (F_1^2 - F_2^2)^2 + [(F_1 G_1 + F_2 G_2) - 2Q(F_1 G_2 + F_2 G_1)]^2 \\ = Q^2 (F_1 G_2 + F_2 G_1)^2, \end{aligned} \tag{5.6.14}$$

which is a single equation in the unknown σ.

5.6.2.2 Detuning Variables

Substitution of Eqs. (5.6.7) into (5.6.14) would produce, upon clearing of fractions and cancellation of terms, a tenth-order polynomial equation in σ. The analogous equation for the one-mode case is the cubic (5.4.9). As in Section 5.4, detuning variables are introduced here to recast the frequency equation in simpler form.

Eqs. (5.4.12) for the approximate detunings (Δ_r, Δ_f) are generalized so as to preserve the modal (1, 2) symmetry of the problem:

$$\Delta_r \equiv \frac{1}{2}[1 - \frac{\Omega_2^2 + \Omega_1^2}{2} + 2\sigma] \tag{5.6.15a}$$

$$\Delta_f \equiv \frac{1}{2}[1 - \frac{\Omega_2^2 + \Omega_1^2}{2}]. \tag{5.6.15b}$$

Attempting to write the functions F_i and G_i in terms of these variables (Δ_r, Δ_f) reveals that a third variable is needed to measure the separation between structural frequencies Ω_1 and Ω_2:

$$\Delta_{21} \equiv \frac{1}{2}(\Omega_2^2 - \Omega_1^2) \equiv -\Delta_{12}. \tag{5.6.15c}$$

As in Section 5.4, the Δ's are "detunings" only in an approximate sense. In analogy to Eqs. (5.4.13), the exact **mode-averaged response-structure detuning** is

$$d_r \equiv \frac{\omega - \frac{1}{2}(\omega_1 + \omega_2)}{\omega_s} = \Omega - \sqrt{e_2}\frac{\Omega_1 + \Omega_2}{2}, \tag{5.6.16a}$$

the exact **mode-averaged fluid-structure detuning** is

$$d_f \equiv \frac{\omega_s - \frac{1}{2}(\omega_1 + \omega_2)}{\omega_s} = 1 - \sqrt{e_2}\frac{\Omega_1 + \Omega_2}{2}, \tag{5.6.16b}$$

and the exact **intermodal detuning** is

$$d_{21} \equiv \frac{\omega_2 - \omega_1}{\omega_s} = \sqrt{e_2}(\Omega_2 - \Omega_1). \tag{5.6.16c}$$

The relationships between frequencies, normalized frequencies, and detuning variables are diagrammed on Fig. 5.6.1 for the case $e_2 = 1$.[2] This Figure is analogous to Fig. 5.4.1.

Assuming $e_2 \approx 1$, these quantities (d_r, d_f, d_{21}) are equivalent, respectively, to (Δ_r, Δ_f, Δ_{21}) only in the limit as d_f and d_{21} approach zero, which is apparent

---

2. See the footnote to Eqs. (3.2.20).

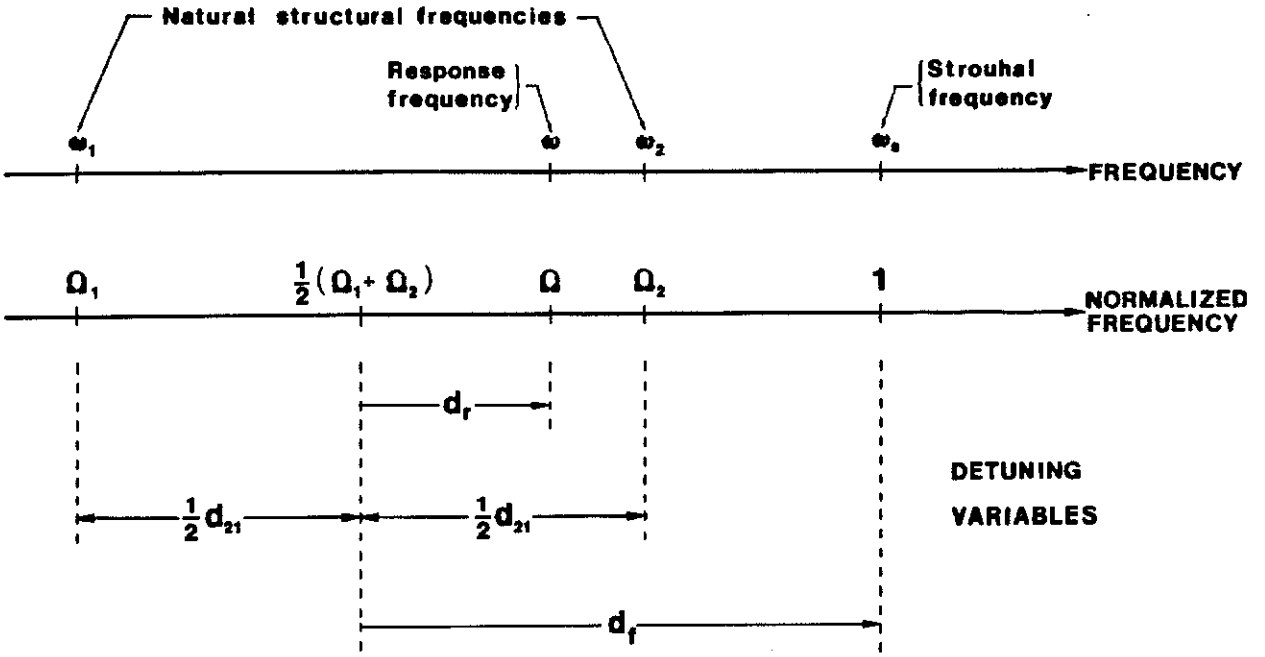

Figure 5.6.1. Two-Mode Interpretation of d–Variables.

upon substitution of Eqs. (5.6.16) into Eqs. (5.6.15):[1]

$$\Delta_r \approx d_r - \tfrac{1}{2}[d_f^2 + (\tfrac{1}{2}d_{21})^2] \tag{5.6.17a}$$

$$\Delta_f \approx d_f - \tfrac{1}{2}[d_f^2 + (\tfrac{1}{2}d_{21})^2] \tag{5.6.17b}$$

$$\Delta_{21} \approx d_{21} - d_f d_{21}. \tag{5.6.17c}$$

The discussion following Eqs. (5.4.14), which argues in favor of distinguishing between the Δ's and the d's even though the difference is order ε^2, goes through analogously in this case.

5.6.2.3 Solution in Detuning Variables

Recasting the frequency equation (5.6.14) in terms of Δ-variables gives

1. The relations (5.6.17) are exact for $e_s = 1$.

$$(\hat{F}_1^2 - \hat{F}_2^2)^2 + [(\hat{F}_1\hat{G}_1 + \hat{F}_2\hat{G}_2) - 2Q(\hat{F}_1\hat{G}_2 + \hat{F}_2\hat{G}_1)]^2 = Q^2(\hat{F}_1\hat{G}_2 + \hat{F}_2\hat{G}_1)^2, \tag{5.6.18}$$

where

$$\hat{F}_i(\Delta_r) \equiv \frac{4}{3p}\left[2(\Delta_f - \Delta_r) - \frac{k_b(2\Delta_r + \Delta_{fi}) + k_a\gamma_i}{(2\Delta_r + \Delta_{fi})^2 + \gamma_i^2}\right] \tag{5.6.19a}$$

$$\hat{G}_i(\Delta_r) \equiv \frac{4}{3p}\left[\alpha + \frac{-k_a(2\Delta_r + \Delta_{fi}) + k_b\gamma_i}{(2\Delta_r + \Delta_{fi})^2 + \gamma_i^2}\right]. \tag{5.6.19b}$$

Some algebra reveals that Eq. (5.6.18) may be written

$$u^2 + (v - 3Qw)(v - Qw) = 0 \tag{5.6.20}$$

where

$$u(\Delta_r) \equiv \left(\frac{3p}{4}\right)^2(\hat{F}_1^2 - \hat{F}_2^2) \tag{5.6.21a}$$

$$v(\Delta_r) \equiv \left(\frac{3p}{4}\right)^2(\hat{F}_1\hat{G}_1 + \hat{F}_2\hat{G}_2) \tag{5.6.21b}$$

$$w(\Delta_r) \equiv \left(\frac{3p}{4}\right)^2(\hat{F}_1\hat{G}_2 + \hat{F}_2\hat{G}_1). \tag{5.6.21c}$$

As in Section 5.4, this form of solution is not useful unless $(\Delta_r, \Delta_f, \Delta_{fi})$ are the only frequency variables in the problem. Therefore it is necessary to replace definition (3.4.14)

$$\gamma_i \equiv \frac{2\zeta_i\Omega_i}{\sqrt{e_2}} + \frac{a_4}{2\pi Se_2}\eta \tag{5.6.22a}$$

with the approximation

$$\gamma_i \approx \frac{2\zeta_i}{\sqrt{e_2}} + \frac{a_4}{2\pi Se_2}\eta, \tag{5.6.22b}$$

which is permissible on account of Eq. (4.1.2).

Also in analogy to Section 5.4, Δ_f is chosen as the dependent variable in Eq. (5.6.20), with Δ_r independent. Substitution of Eqs. (5.6.19) into Eqs. (5.6.21) produces

$$u = u_0 + \Delta_f u_1 \tag{5.6.23a}$$

$$v = v_0 + \Delta_f v_1 \tag{5.6.23b}$$

$$w = w_0 + \Delta_f w_1 \tag{5.6.23c}$$

where

$$u_0 \equiv f_1^2 - f_2^2 ; \qquad u_1 \equiv 4(f_1 - f_2) \tag{5.6.24a}$$

$$v_0 \equiv f_1 g_1 + f_2 g_2 ; \qquad v_1 \equiv 2(g_1 + g_2) \tag{5.6.24b}$$

$$w_0 \equiv f_1 g_2 + f_2 g_1 ; \qquad w_1 \equiv 2(g_1 + g_2) \tag{5.6.24c}$$

and

$$f_i(\Delta_r) \equiv -2\Delta_r - \frac{k_b(2\Delta_r + \Delta_{fi}) + k_a\gamma_i}{(2\Delta_r + \Delta_{fi})^2 + \gamma_i^2} \tag{5.6.25}$$

$$g_i(\Delta_r) \equiv \alpha + \frac{-k_a(2\Delta_r + \Delta_{fi}) + k_b\gamma_i}{(2\Delta_r + \Delta_{fi})^2 + \gamma_i^2} \tag{5.6.26}$$

Consequently, the frequency equation (5.6.20) is quadratic in Δ_f,

$$\kappa_2\Delta_f^2 + \kappa_1\Delta_f + \kappa_0 = 0, \tag{5.6.27}$$

where

$$\kappa_2(\Delta_r) \equiv u_1^2 + (v_1 - 3Qw_1)(v_1 - Qw_1) \tag{5.6.28a}$$

$$\kappa_1(\Delta_r) \equiv 2u_0u_1 + (v_1 - 3Qw_1)(v_0 - Qw_0) + (v_0 - 3Qw_0)(v_1 - Qw_1) \tag{5.6.28b}$$

$$\kappa_0(\Delta_r) \equiv u_0^2 + (v_0 - 3Qw_0)(v_0 - Qw_0). \tag{5.6.28c}$$

Hence for each value of Δ_r there are two solutions Δ_f:

$$\Delta_f(\Delta_r) = \frac{-\kappa_1 \pm \sqrt{\kappa_1^2 - 4\kappa_2\kappa_0}}{2\kappa_2}, \tag{5.6.29}$$

which are either both real or both non-real, depending on the sign of the discriminant. The latter equation is analogous to Eq. (5.4.19) of the one-mode analysis, where the solution Δ_f was single-valued rather than double-valued.

For each real solution Δ_f, the amplitudes and phases (A_i, B_i, μ_i, φ) may be recovered by back-substitution. First, with the help of Eqs. (5.6.21), Eqs. (5.6.13) give, for $Q \neq 0$:

$$\varphi = \frac{1}{2}\tan^{-1}\left\{\frac{\frac{v}{w} - 2Q}{\frac{u}{w}}\right\}. \tag{5.6.30}$$

Next, using Eqs. (5.6.21) and (5.6.13b), Eq. (5.6.10) gives

$$A_1^2 = \frac{-F_2 w}{Qu} \tag{5.6.31a}$$

$$A_2^2 = \frac{+F_1 w}{Qu}. \tag{5.6.31b}$$

Finally, from Eqs. (5.6.5) and (5.6.4),

$$B_i^2 = \frac{c^2 + \tilde{c}^2}{(2\Delta_r + \Delta_{fi})^2 + \gamma_i^2} A_i^2 \tag{5.6.32}$$

and

$$\mu_i = \tan^{-1}\left\{\frac{\tilde{c}\gamma_i - c(2\Delta_r + \Delta_{fi})}{c\gamma_i + \tilde{c}(2\Delta_r + \Delta_{fi})}\right\}. \tag{5.6.33}$$

5.6.2.4 Classes of Solution

Stability of real steady-state solutions is considered in the next sub-section. However, from the above discussion it is clear that for certain values of Δ_r, a real steady-state solution may fail to exist altogether. First, if the discriminant is negative in Eq. (5.6.29), no real frequency solution exists. Second, even if a

pair of real values for Δ_f is found, either or both may fail to generate real amplitudes κ_i in Eqs. (5.6.31). To summarize, four classes of solution are possible:

(0) Δ_f non-real

(1) Δ_f real but one or both A_i imaginary

(2) Δ_f real and A_i real, but unstable

(3) Δ_f real, A_i real, stable.

Each class, except (0), has its analogy in the one-mode analysis; see Section 5.4.4. Only class (3), of course, is physically meaningful.

5.6.2.5 Stability

As in Sections 5.4 and 5.5, stability of the above solutions is investigated using the amplitude/phase equations (4.3.19). By subtraction of Eq. (4.3.19c) from each of the equations (4.3.19f) and (4.3.16g), and by subtraction of Eq. (4.3.19f) from Eq. (4.3.19h), the following set of seven first-order differential equations is obtained in the four amplitudes and three phase differences:

$$\dot{\mathbf{X}} = \mathbf{J}(\mathbf{X}) \tag{5.6.34}$$

where

$$\mathbf{X} \equiv (A_1, A_2, B_1, B_2, \mu_1, \mu_2, \varphi), \tag{5.6.35}$$

and the functions

$$J_1 \equiv \dot{A}_1(\mathbf{X}) \tag{5.6.36a}$$

$$J_2 \equiv \dot{A}_2(\mathbf{X}) \tag{5.6.36b}$$

$$J_3 \equiv \dot{B}_1(\mathbf{X}) \tag{5.6.36c}$$

$$J_4 \equiv \dot{B}_2(\mathbf{X}) \tag{5.6.36d}$$

$$J_5 \equiv \dot{\Theta}_1(\mathbf{X}) - \dot{\Phi}_1(\mathbf{X}) \tag{5.6.36e}$$

$$J_6 \equiv \dot{\Theta}_2(\mathbf{X}) - \dot{\Phi}_2(\mathbf{X}) \tag{5.6.36f}$$

$$J_7 \equiv \dot{\Phi}_2(\mathbf{X}) - \dot{\Phi}_1(\mathbf{X}) \tag{5.6.36g}$$

are given explicitly by substitution of Eqs. (4.3.19).

As in the stability analyses of Sections 5.3 and 5.4, the steady-state solution $\mathbf{X}_0$ is stable if and only if all eigenvalues of the Jacobian matrix $[J']_0$ have negative real parts. However, unlike the previous cases, the 7 x 7 Jacobian of the present case is too large to permit a convenient analytical determination of specific stability conditions. The stability results given in Chapter 7 were obtained by numerical determination of eigenvalues for the analytically differentiated matrix $[J']_0$.

5.6.3 Degenerate Solutions

5.6.3.1 The Steady State

According to the discussion of Section 5.6.1, solutions to the set of four differential equations (4.1.8) are called "degenerate" if either

$$z_1,\ y_1 \neq 0 \quad \text{and} \quad z_2 = y_2 = 0 \quad \text{(Type 1)} \tag{5.6.37a}$$

or

$$z_2,\ y_2 \neq 0 \quad \text{and} \quad z_1 = y_1 = 0 \quad \text{(Type 2).} \tag{5.6.37b}$$

Type 1 solutions are treated below. However, as should be clear from the differential equations (4.1.8), Type 2 solutions may be obtained analogously, merely by interchanging all subscripts 1 and 2. This observation will be referred to henceforth as **subscript symmetry.**

Considering Type 1 solutions, the steady-state equations (5.2.5) reduce, for the non-degenerating degrees of freedom $(z_1,\ y_1)$, to Eqs. (5.4.6).[1] The same equations reduce, for the degenerating degrees of freedom $(z_2,\ y_2)$, to the identity 0 = 0, since Eq. (5.6.37a) implies $A_2 = B_2 = 0$. Therefore, steady-state degenerate solutions for the two-mode-approximate cable reduce to the solutions developed in Section 5.4, provided $p = \frac{3}{2}\beta$ (Table 4.1.1).

To clarify this result in a two-mode context, the one-mode detunings previously defined by Eqs. (5.4.12) must be embellished by a subscript indicating the generic mode number[2] of the non-degenerating mode. Thus for Type 1:

$$\Delta_{r1} \equiv \tfrac{1}{2}(1 - \Omega_1^2 + 2\sigma). \tag{5.6.38a}$$

---

1. Provided $A \equiv A_1$, $B \equiv B_1$, $\mu \equiv \mu_1$ and $\gamma \equiv \gamma_1$.
2. Recall convention (4.1.10).

$$\Delta_{f1} \equiv \frac{1}{2}(1 - \Omega_1^2) \tag{5.6.38b}$$

The relationships connecting the two-mode detunings (Δ_f, Δ_r, Δ_{21}) defined by Eqs. (5.6.15) and the one-mode detunings (Δ_{f1}, Δ_{r1}) are:

$$\Delta_{f1} = \Delta_f + \frac{1}{2}\Delta_{21} \tag{5.6.39a}$$

$$\Delta_{r1} = \Delta_r + \frac{1}{2}\Delta_{21}. \tag{5.6.39b}$$

This coordinate transformation is shown in Fig. 5.6.2, together with the analogous transformation for Type 2,

$$\Delta_{f2} = \Delta_f - \frac{1}{2}\Delta_{21} \tag{5.6.40a}$$

$$\Delta_{r2} = \Delta_r - \frac{1}{2}\Delta_{21}, \tag{5.6.40b}$$

obtained from Eqs. (5.6.39) using subscript symmetry and Eq. (5.6.15c).

Hence Type-1 solutions for frequency and amplitude response, obtained by rewriting Eqs. (5.4.15b), (5.4.16b) and (5.4.19) in a two-mode context, are given by

$$\Delta_{f1} = \Delta_{r1} + \frac{1}{2}\left[\frac{2k_b\Delta_{r1} + k_a\gamma_1}{4\Delta_{r1}^2 + \gamma_1^2}\right] \tag{5.6.41a}$$

$$\frac{3}{4}pA_1^2 = \alpha + \frac{-2k_a\Delta_{r1} + k_b\gamma_1}{4\Delta_{r1}^2 + \gamma_1^2}. \tag{5.6.41b}$$

Using subscript symmetry, analogous equations hold for Type 2 solutions. Figure 5.6.3 exemplifies Type 1 and Type 2 frequency solutions. Since the parameter values used here are the same as for Fig 5.4.2, each curve is identical to Fig. 5.4.2, except for the simple coordinate shifts (5.6.39) and (5.6.40). Thus solution Types 1 and 2 exhibit lock-in for the lower mode and the upper mode respectively. It remains to investigate which portions of these solution curves

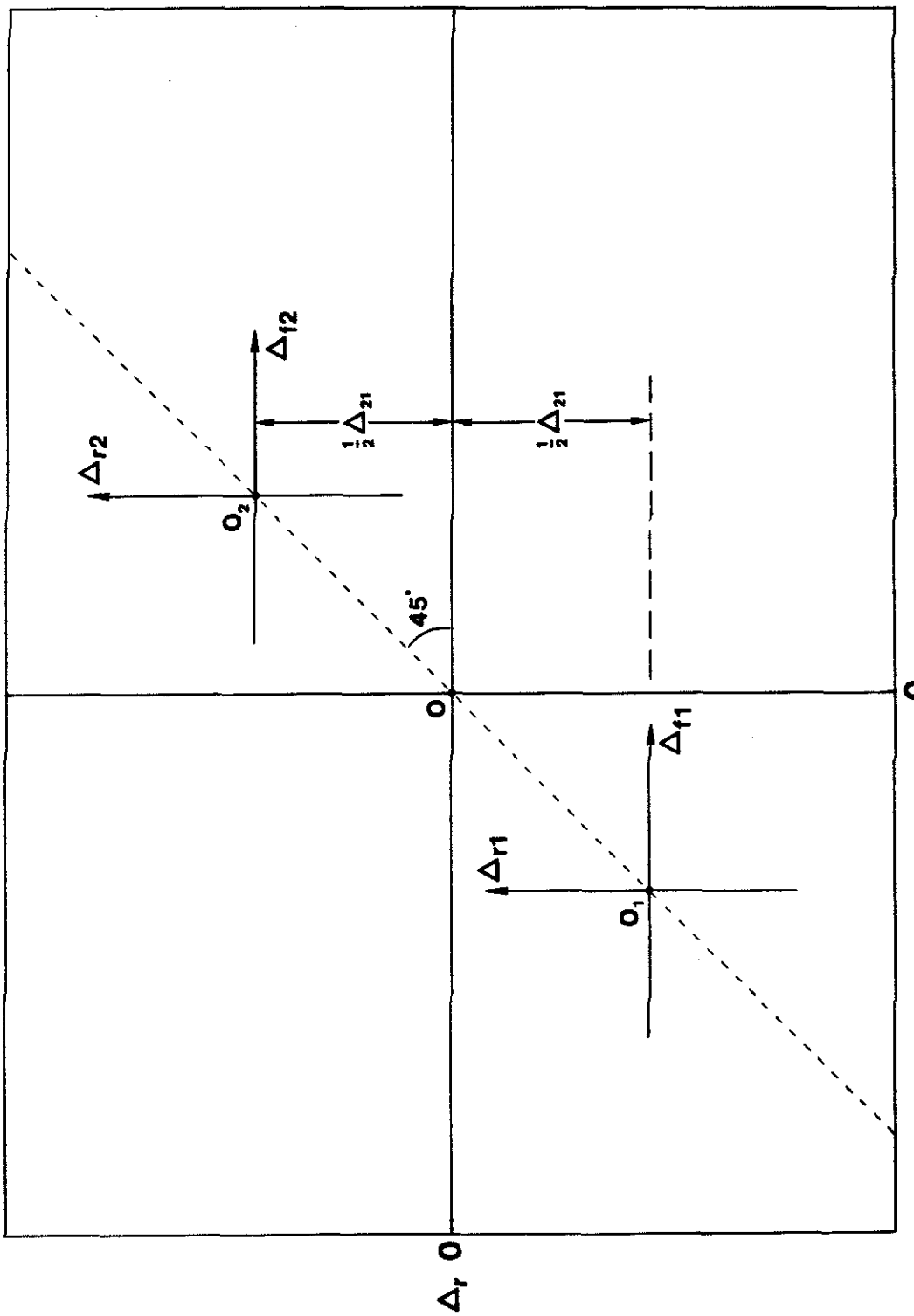

Fig. 5.6.2: Coordinate Transformations for One-Mode Variables in a Two-Mode Context.

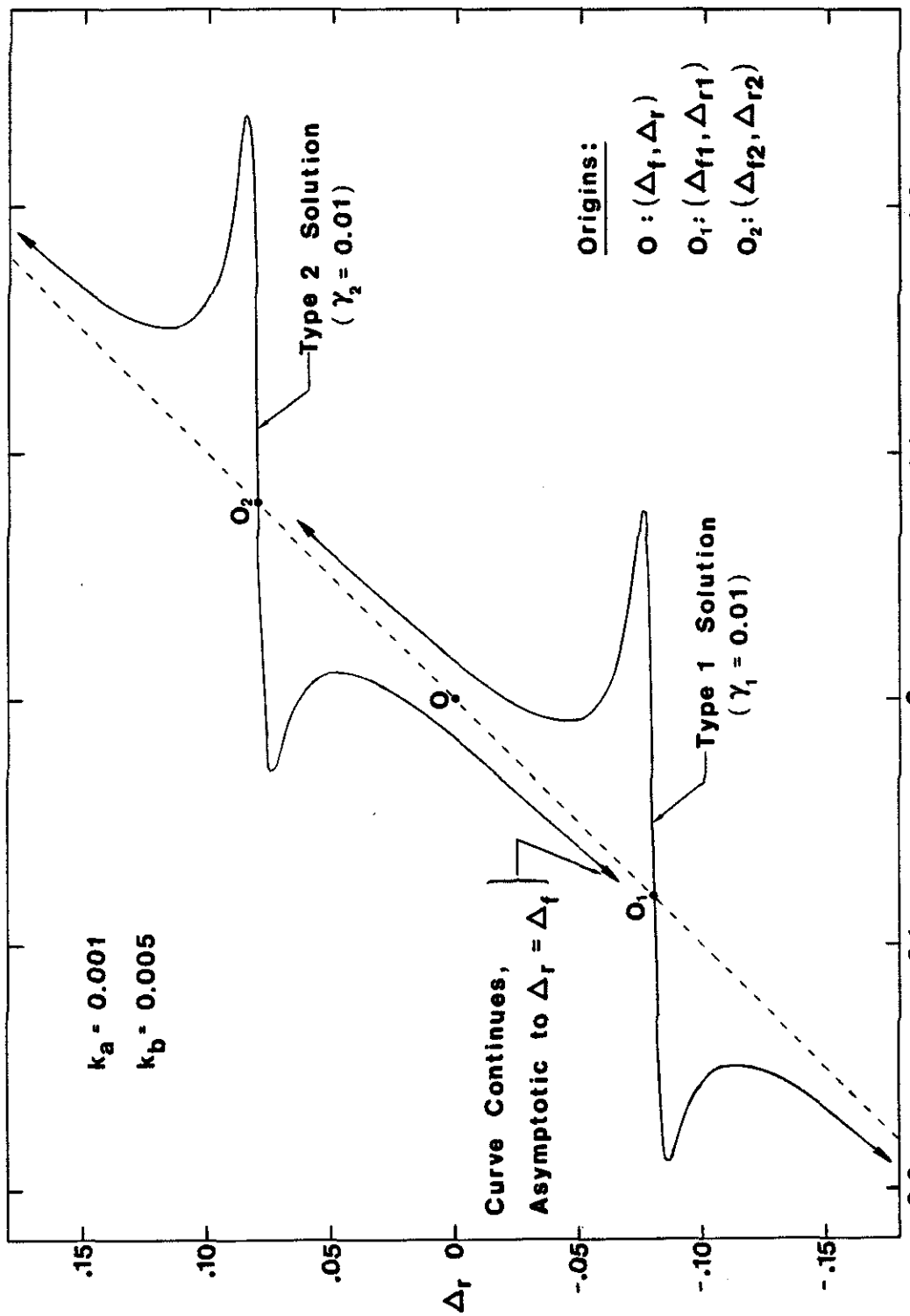

Fig. 5.6.3: Typical Degenerate Solutions, Prior to Stability Considerations.

are stable.

5.6.3.2 A Difficulty with the Stability Analysis Used Previously.

Although the above steady-state solutions are identical to those for the one-mode case, the corresponding stability analysis is quite different. Consider Type 1 solutions (as usual, Type 2 is analogous). Since arbitrary perturbations about the steady-state may, in a two-mode context, include perturbed values of the degenerating amplitudes A_2 and B_2 which are non-zero, the full system of eight amplitude/phase equations (4.3.19) must be considered, involving all four amplitudes (A_1, A_2, B_1, B_2) and three phase differences (μ_1, μ_2, φ).

However, a problem arises; namely, since the steady-state amplitudes of z_2 and y_2 are zero, it is meaningless to speak of the corresponding phases, and steady-state values of the phase differences μ_2 and φ are not well-defined. Consequently a stability analysis based on the amplitude/phase equations, which requires well-defined A's, B's, μ's and φ, must be abandoned in the degenerate case.

5.6.3.3 An Alternative Approach to Stability

Still considering Type 1 solutions, an alternative stability method is to perturb the original, second-order differential equations (4.1.8) about the exact, degenerate steady-state (designated by an (e) superscript):

$$z_1 = z_1^{(e)} + \varepsilon u_1 \qquad (5.6.42a)$$

$$y_1 = y_1^{(e)} + \varepsilon v_1 \qquad (5.6.42b)$$

$$z_2 = 0 + \varepsilon u_2 \qquad (5.6.42c)$$

$$y_2 = 0 + \varepsilon v_2. \qquad (5.6.42d)$$

In such a method the concept of phases for the degenerating degrees of freedom is absent, so the problem discussed above does not arise. Substituting Eqs.

(5.6.42) into Eqs. (4.1.8), subtracting the exact steady-state, and retaining terms to first order in ε yields a pair of parametrically excited equations for the perturbations of the non-degenerating degrees of freedom,

$$\ddot{u}_1 - \alpha\dot{u}_1 + 3p[\dot{z}_1^{(e)}(t)]^2\dot{u}_1 + u_1 = r\dot{v}_1 + \tilde{r}v_1 \tag{5.6.43a}$$

$$\ddot{v}_1 + \gamma_1\dot{v}_1 + \Omega_1^2 v_1 = c\dot{u}_1 - \tilde{c}u_1, \tag{5.6.43b}$$

and a corresponding pair for the perturbations of the degenerating degrees of freedom,

$$\ddot{u}_2 - \alpha\dot{u}_2 + q[\dot{z}_1^{(e)}(t)]^2\dot{u}_2 + u_2 = r\dot{v}_2 + \tilde{r}v_2 \tag{5.6.44a}$$

$$\ddot{v}_2 + \gamma_2\dot{v}_2 + \Omega_2^2 v_2 = c\dot{u}_2 - \tilde{c}u_2. \tag{5.6.44b}$$

Therefore, the stability of a Type-1, steady-state solution to Eqs. (4.1.8) depends on the mutual stability of the two systems (5.6.43) and (5.6.44), which fortunately are completely uncoupled. If either system has unbounded response, then the steady-state solution ($z_1^{(e)}$, $y_1^{(e)}$; $z_2^{(e)} = y_2^{(e)} = 0$) is unstable.

5.6.3.4 Stability of the Non-Degenerating Degrees of Freedom

The stability characteristics of Eqs. (5.6.43) may be inferred from work previously presented. That is, consider perturbing the one-mode variables (Z, Y) of Section 5.4, which satisfy the differential equations (5.4.2):

$$Z = Z^{(e)} + \varepsilon U \tag{5.6.45a}$$

$$Y = Y^{(e)} + \varepsilon V. \tag{5.6.45b}$$

These equations are analogous to Eqs. (5.6.42); as before, superscript (e) denotes the exact steady-state solution. Substituting Eqs. (5.6.45) into Eqs. (5.4.2) and subtracting the exact steady-state yields, to order ε:

$$\ddot{U} - \alpha\dot{U} + 3p[\dot{Z}^{(e)}(t)]^2\dot{U} + U = r\dot{V} + \tilde{r}V \tag{5.6.46a}$$

$$\ddot{V} + \gamma\dot{V} + \Omega_1^2 V = c\dot{U} - \tilde{c}U. \tag{5.6.46b}$$

Upon identifying (U, V, γ, Ω_1) as $(u_1, v_1, \gamma_1, \Omega_1)$ respectively, and noting[3]

$$z_1^{(e)}(t) = Z^{(e)}(t), \tag{5.6.47}$$

it follows that Eqs. (5.6.43) are identical to Eqs. (5.6.46), and therefore the stability characteristics of these two systems are identical. But the stability characteristics of Eqs. (5.6.46) are implicitly known, since the present perturbation approach to stability must give the same results as the amplitude/phase approach of Section 5.4.6, to the accuracy of the asymptotic method. It follows then that the stability of the system (5.6.43) may likewise be inferred from Section 5.4.6, upon substituting $(\gamma_1, A_1, B_1, \mu_1)$ for (γ, A, B, μ).

Specifically, stability conditions for the non-degenerating degrees of freedom (z_1, y_1) are given by rewriting Eqs. (5.4.30) and (5.4.31) in the notation of this section:

$$(i)\ k_m > 0; \qquad m = 0, 1, 2 \tag{5.6.48a}$$

$$(ii)\ k_2 k_1 - k_0 > 0 \tag{5.6.48b}$$

where, using Eqs. (5.4.15b) and (5.4.16b),

$$k_2 \equiv 3pA_1^2 + 2(\gamma_1 - \alpha) \tag{5.6.49a}$$

$$k_1 \equiv (\alpha - \gamma_1)^2 + \frac{3}{2}pA_1^2(3\gamma_1 - 2\alpha) + \frac{27}{16}p^2A_1^2 + 4(2\Delta_{r1} - \Delta_{f1})^2 \tag{5.6.49b}$$

$$k_0 \equiv 6pA_1^2\Delta_{r1}(2\Delta_{r1} - \Delta_{f1}) - \frac{3}{2}\gamma_1 pA_1^2(\alpha - \gamma_1 - \frac{3}{4}pA_1^2). \tag{5.6.49c}$$

Using Eqs. (5.6.41), it is clear that these conditions depend only on the parameters α, k_a, k_b, γ_1, and the independent variable Δ_{r1}. In particular, there is no dependence on the modal separation Δ_{21}.

---

3. Since, $z_2^{(e)}(t) \equiv 0$ in the degenerate steady-state (Type 1), the differential equations (4.1.8a,c) governing (z_1, y_1) are identical to Eqs. (5.4.2) governing (Z, Y).

5.6.3.5 Stability of the Degenerating Degrees of Freedom

The stability characteristics of Eqs. (5.6.44), unlike Eqs. (5.6.43), cannot be inferred from previous work. However, if the exact parametric excitation $[\dot{z}_1^{(e)}(t)]^2$ in Eq. (5.6.44a) is replaced by the approximate value given by the asymptotic method,

$$\dot{z}_1^{(e)}(t) \approx \dot{z}_1^{(0)}(t) = -\Omega A_1 \sin(\Omega t + \varphi_1), \tag{5.6.50}$$

then stability characteristics may be deduced using Floquet theory. Toward this end the system (5.6.44) is written in matrix form as

$$\dot{\mathbf{x}} = [P(t)]\mathbf{x} \tag{5.6.51}$$

where

$$\mathbf{x} \equiv (u_2,\ \dot{u}_2,\ v_2,\ \dot{v}_2) \tag{5.6.52a}$$

and

$$[P(t)] \equiv \begin{bmatrix} 0 & 1 & 0 & 0 \\ -1 & \hat{a}_1 + 2\hat{b}_1\cos 2\Omega t & \tilde{r} & r \\ 0 & 0 & 0 & 1 \\ -\tilde{c} & c & -\Omega_2^2 & -\gamma_2 \end{bmatrix}. \tag{5.6.52b}$$

The above expression for P_{22} has been obtained by replacing the time function $\sin(\Omega t + \varphi_1)$ in Eq. (5.6.45) with $\sin \Omega t$ through a simple shift of the time scale,. and by introducing (for brevity) the coefficients $\hat{a}_1$ and $\hat{b}_1$, whose definitions arise from Eq. (5.6.41b) and the two-mode identity $q = 2p$ (see Table 4.1.1):

$$\hat{a}_1 \equiv \alpha - \frac{4}{3}\Omega^2(\alpha + \Gamma_1) \tag{5.6.53a}$$

$$\hat{b}_1 \equiv \frac{2}{3}\Omega^2(\alpha + \Gamma_1). \tag{5.6.53b}$$

The quantity Γ_1 is defined by

$$\Gamma_1 \equiv \frac{-2k_a\Delta_{r1} + k_b\gamma_1}{4\Delta_{r1}^2 + \gamma_1^2}, \tag{5.6.54}$$

and the response frequency Ω is given by definitions (5.6.39) and (5.2.6) as

$$\Omega = 1 + \Delta_{r1} - \Delta_{f1}(\Delta_{r1}). \tag{5.6.55}$$

Thus the matrix $[P(t)]$ is periodic with a known period T,

$$[P(t+T)] = [P(t)]; \qquad T \equiv \frac{\pi}{\Omega}, \tag{5.6.56}$$

so Eq. (5.6.51) may be treated with Floquet theory, a summary of which is given below.

According to the theory of differential equations, there exists for Eq. (5.6.51) a set of $N \equiv 4$ linearly independent solutions $\mathbf{x}^{(k)}$ $(k = 1, \ldots, N)$ called *principle solutions*, which, when arranged as columns of a matrix denoted $[X]$, satisfy

$$[\dot{X}(t)] = [P(t)][X(t)] \tag{5.6.57}$$

and

$$[X(0)] = [I] \quad \text{(the identity matrix)}. \tag{5.6.58}$$

$[X(t)]$ is called the *principle matrix solution*. In general, the principle solution vectors in $[X]$ are related to any alternative set of N independent solutions $\mathbf{w}^{(k)}(t)$ by

$$[X(t)] = [W(t)][R]^{-1}, \tag{5.6.59}$$

where the $\mathbf{w}^{(k)}$ are columns of $[W]$, and $[R]$ is a constant, nonsingular transformation matrix. In particular, since $[P(t)]$ is periodic, the columns of $[X(t+T)]$ are solutions of Eq. (5.6.51), so the vectors $\mathbf{x}^{(k)}(t+T)$ must be related to the $\mathbf{x}^{(k)}(t)$ by

$$[X(t+T)] = [X(t)][M]. \tag{5.6.60}$$

where $[M]$ is a constant matrix. From Eqs. (5.6.59) and (5.6.60) it follows that

$$[W(t+T)] = [W(t)][R]^{-1}[M][R]. \tag{5.6.61}$$

If [R] is chosen such that[4]

$$[R]^{-1}[M][R] = [\Lambda] = \text{diag}(\lambda_1, \ldots, \lambda_N), \tag{5.6.62}$$

then each of the solutions $\mathbf{w}^{(k)}(t)$ satisfies

$$\mathbf{w}^{(k)}(t+T) = \lambda_k \mathbf{w}^{(k)}(t), \tag{5.6.63}$$

the multipliers λ_k being constants, complex in general. Thus the λ_k are eigenvalues of the matrix $[M]$, and $[R]$ is the matrix of eigenvectors. The vectors $\mathbf{w}^{(k)}$ are usually called *normal solutions*.

The eigenvalues may be found using the following algorithm:

- Numerically integrate N systems of equations $\dot{\mathbf{x}}^{(k)} = [P(t)]\mathbf{x}^{(k)}$ $(k = 1, \ldots, N)$ over one period $(0 \leq t \leq T)$, using the N columns of initial conditions (5.6.58). Then according to Eq. (5.6.60),

$$[X(T)] = [M]. \tag{5.6.64}$$

- Numerically determine the eigenvalues λ_k of $[M]$. In particular, find the complex moduli $|\lambda_k|$.

According to Eq. (5.6.63), the perturbations represented by the $\mathbf{w}^{(k)}$ will decay with time, and hence the system (5.6.51) [i.e. Eqs. (5.6.44)] will be stable, if and only if

---

4. To be completely general, the possibility of $[M]$ possessing indistinct eigenvalues with less than a full complement of independent eignevectors should be considered. In such a case $[\Lambda]$ cannot be made diagonal. However practicaly (i.e. numerically) speaking, this is a very special case; in fact, for random values of $(\hat{a}_1, \hat{b}_1, r, \tilde{r}, c, \tilde{c}, \gamma_2, \Omega_2)$ in the matrix $[P(t)]$, the probability of such an occurance is nil.

$$|\lambda_k| < 1 \quad \text{for every } k = 1, \ldots, N. \tag{5.6.65}$$

Unlike conditions (5.6.48), the stability condition (5.6.65) *does* depend on the intermodal spacing Δ_{21}, since the quantity Ω_2 appearing in $[P(t)]$ must be calculated according to definitions (5.6.39) and (5.2.6) as

$$\Omega_2^2 = \Omega_1^2 + 2\Delta_{21}, \tag{5.6.66a}$$

where Ω_1 is given by definition (5.6.39a) and the frequency solution (5.6.41a):

$$\Omega_1^2 = 1 - 2\Delta_{f1}(\Delta_{r1}). \tag{5.6.66b}$$

Stability condition (5.6.65) depends additionally on the parameters α, γ_2, r, $\tilde{r}$, c, and $\tilde{c}$.

5.6.3.6 Summary and Interpretation

For Type 1, a degenerate steady-state solution (5.6.37a) is stable if and only if

- Conditions (5.6.48), which do not depend on Δ_{21}, hold for the non-degenerating degrees of freedom (z_1, y_1)
- Condition (5.6.65), which does depend on Δ_{21}, holds for the degenerating degrees of freedom (z_2, y_2).

The situation is analogous for Type 2 solutions, upon interchanging subscripts 1 and 2, and recalling $\Delta_{12} = -\Delta_{21}$.

The first condition above is equivalent to the one-mode stability condition, thus segments of a solution curve (e.g. either of the curves on Fig. 5.6.3) which are unstable in the one-mode case are also unstable in the two-mode case.

The second condition, depending on Δ_{21}, can only restrict the range of stability further. From a physical viewpoint (in analogy to the experiment discussed in Section 2.5), the second condition should cause modal interference for small Δ_{21}; that is, the lock-in bands are likely to overlap, and/or be suppressed, as the

two modes compete for control of the response frequency Ω. For example, it is reasonable to expect that the lock-in band for Type 1 (representing the lower mode) will become unstable at the upper end in deference to Type 2 (representing the upper mode); and conversely, that the lock-in band for Type 2 will become unstable at the lower end in deference to Type 1. Numerical results presented in Chapter 7 display just such behavior.

5.7 Summary

For each case listed in Table 4.1.1, steady-state monofrequency solutions to the amplitude/phase equations (4.3.19) have been found analytically, and the stability of solutions has been investigated by a combination of analytical and numerical techniques. An index to the results is given in Table 5.7.1.

Table 5.7.1: Steady State Solution Index

Type of Structure		Differential Equations Involved		Approximate Steady-State Solution Assumed	Algebraic Equations Involved		Frequency Solution Given by	Amplitude and Phase Solution Given by	Stability Conditions Given by
		Where in Text	How Many		Where in Text	How Many			
Forced Cylinder (§5.3)		(5.3.2)	1	(5.3.6)	(5.3.7)	2	Frequency Prescribed	(5.3.8) (5.3.9) (5.3.13)	(5.3.24)
Elastically Mounted Cylinder (§5.4)		(5.4.2)	2	(5.4.3)	(5.4.6)	4	(5.4.19)	(5.4.7) (5.4.8) (5.4.15b)	(5.4.31)
One-Mode Cable Approx. (§5.5)		(5.4.2) $Z^{(0)} \leftarrow Z_1^{(0)}$ $y^{(0)} \leftarrow y_1^{(0)}$	2	(5.5.1)	(5.4.6)	4	(5.4.19)	(5.5.2)	(5.4.31)
Two-Mode Cable Approx. (§5.6)	Case 1	(4.1.8)	4	(5.6.1)	(5.2.5)	8	(5.6.29)	(5.6.30) through (5.6.33)	§5.6.2.5
	Case 2	(4.1.8)	4	(5.6.1) (5.6.37)	(5.4.6)	4	(5.6.41a)	(5.6.41b)	(5.6.49) (5.6.65)

CHAPTER VI

METHODS OF FITTING THE MODEL TO EXPERIMENTAL DATA

6.1 Introduction

In this chapter, certain important characteristics of the model solutions for rigid cylinders, distilled from the analyses of Sections 5.3 and 5.4, are found to depend on a set of six parameters, denoted P_k, $k = 0, 1, \ldots, 5$, from which the six model constants a_k may be recovered. Simple, easily implemented methods are developed for selecting numerical values of the P_k which optimally fit the model to experimental data.

To be more specific, Table 6.1.1 summarizes the chapter by listing the solution characteristics considered, the pertinent experimental data, and the relevant parameters P_k, whose definitions arise naturally in the sequel. The sixth parameter P_5 does not appear in the Table, for reasons explained in Section 6.4.

Table 6.1.1: An Overview of Chapter 6

Structure	Section	Solution Characteristic	Exp'l Data	Parameter(s) Optimized
Forced Cylinder	6.2	Dependence of lock-in band-width on forcing amplitude	Fig. 2.3.2	P_0
Spring-Mounted Cylinder	6.3	Lock-in band-center C, bandwidth W, and the dependence of C and W on "reduced damping".	Fig. 2.4.2	P_1, P_2, P_3
	6.4	Peak structural amplitude	Fig. 2.4.2	P_4

The above criteria for selecting model constants are considered superior to those previously used in a similar model by Blevins [6], for two reasons. First, the previous work relied heavily on experimental data for stationary cylinders. Here, on the contrary, stationary-cylinder data has been deliberately avoided,[1] since Koopman's photographs (Figs. 2.3.3) show clearly that the assumption of two-dimensionality, inherent in the fluid model, is strongly violated for the stationary cylinder. Second, Blevins' method does little to clarify the dependence of physically measurable quantities on a set of model parameters. Here, on the contrary, some simple formulas are developed which make such relationships transparent.

For comparison of the current model with Skop and Griffin's lift-coefficient model [63], previously discussed at the opening of Chapter 3, it is emphasized that here the parameters P_k are restricted to be constant. In contrast, the parameters of the lift-coefficient model, as determined for spring-mounted cylinders, are allowed to vary with the reduced damping $\frac{\zeta}{\eta}$, which gives an illusion of good model/experimental agreement. Indeed, if such variation were permitted in the present model, the agreement with experiment would be greatly enhanced. However, the fluid oscillator, which depends upon the P_k, can in reality have no knowledge of the structural damping ratio – the fluid reacts only to motion of the structure, not to parameters internal to the structural oscillator. Consequently it is physically incorrect to allow model parameters to vary with $\frac{\zeta}{\eta}$, and the temptation to do so, in order to improve the appearance of results, has been resisted in the current work.

---

1. Except for the previous determination of model constant a_6 using the stationary-cylinder shedding frequency ω_s; see Eqs. (3.2.11) and (3.2.12).

6.2 Lock-in Band-Width for Forced Cylinders

6.2.1 Experimental Data

Experimental measurements by Koopman [37] of lock-in band-width versus forcing amplitude have been discussed in Section 2.3; the results are shown in Fig. 2.3.1 for Reynolds numbers of 100, 200, and 300. Of these three values, Re = 300 best represents the fully turbulent vortex street which prevails for the entire Reynolds number range from 300 to 3×10^5 (see Fig. 2.2.1). Therefore only the Re = 300 data, as digitized in Table 6.2.1, is considered in the current analysis.

Table 6.2.1: Koopman Experimental Data for Re = 300

σ	-0.294	-0.242	-0.199	-0.099	-0.062	0.094	0.150
B	0.273	0.186	0.150	0.073	0.050	0.057	0.105

6.2.2 Model Stability Boundaries in the (σ^*, B^*) Plane

As discussed in Section 5.3, the theoretical equivalent of experimental lock-in boundaries are the model-predicted stability boundaries. As given by Eqs. (5.3.24) and shown in Fig. 5.3.1, the stability boundaries

$$A^* = L_k(\sigma^*) \tag{6.2.1}$$

are loci in the (σ^*, A^*) plane; however, the normalized squared-amplitude A^* of the fluid oscillator cannot be measured experimentally. Therefore, to compare the model with experiment directly, it is necessary to eliminate A^* from the expressions for the stability boundaries, obtaining instead explicit relationships between the normalized forcing amplitude B^* and the normalized detuning σ^*.

To accomplish this objective, each of the boundaries (5.3.24) is substituted into the solution (5.3.12), yielding

$$[B^*]_{\substack{\text{stability} \\ \text{boundary } k}} = \sqrt{L_k(\sigma^*)\{[1 - L_k(\sigma^*)]^2 + \sigma^{*2}\}}\,, \qquad (6.2.2)$$

where $k = 1, 2, 3$. Each of these loci in the (σ^*, B^*) plane may be readily calculated; the results are shown in Figs. 6.2.1, with lettered points corresponding to those in Fig. 5.3.1.

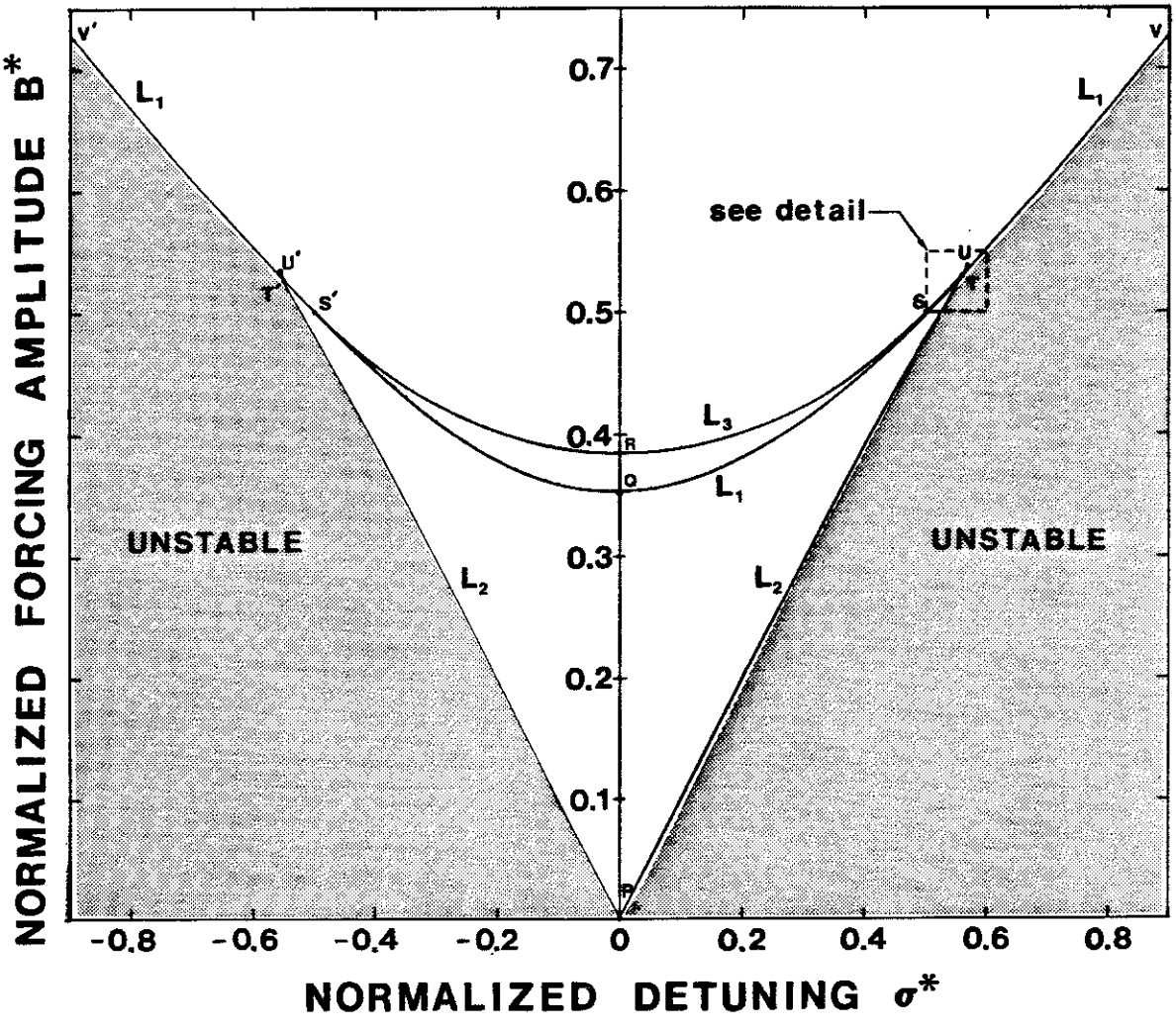

Figure 6.2.1a. Transformed Stability Boundaries (cf. Fig. 5.3.1).

Interpretation of the various stability boundaries in Figs. 6.2.1 to determine the overall boundary requires some care, because the regions of stability and instability do not map simply from the (σ^*, A^*) plane to the (σ^*, B^*) plane. For fixed σ^*, the transformation $B^*(A^*)$ given by Eq. (5.3.12) is sometimes one-to-

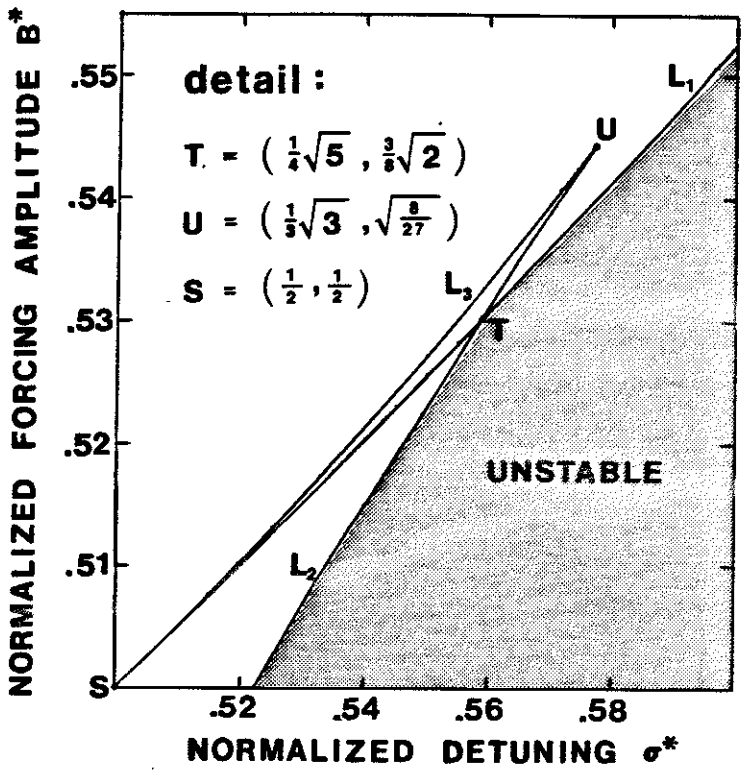

Figure 6.2.1b. Magnified View of Region Indicated on Fig. 6.2.1a.

one, sometimes three-to-one, and, in the special situation where two of the three roots A^* coalesce (i.e. at the point of vertical tangency), two-to-one. The many-to-one mappings invalidate the notion of regions mapping into regions.

To infer the overall stability boundary for Fig. 6.2.1 from the boundaries of Fig. 5.3.1, attention is focused on the solution for $B^* = \frac{3}{8}\sqrt{2}$, shown explicitly in Fig. 5.3.1, and occurring at points T and T' in Figs. 6.2.1. This particular solution is special because it represents the dividing line between two types of behavior; that is, for $B^* < \frac{3}{8}\sqrt{2}$ (e.g. $B^* = 0.4$) each solution crosses L_1 (the straight-line stability boundary $A^* = \frac{1}{2}$) at a lower value of $|\sigma^*|$ than it crosses L_2 (the half-elliptical boundary UPU'), while for $B^* > \frac{3}{8}\sqrt{2}$ (e.g. $B^* = 0.6$), the opposite is true. The solution for $B^* = \frac{3}{8}\sqrt{2}$ crosses both stability boundaries L_1 and L_2 at the same value of $|\sigma^*|$,[1] namely

$$\sigma_T^* = \sigma_T^{*\prime} = \frac{1}{4}\sqrt{5}. \tag{6.2.3}$$

Consequently if B^* is fixed and it is desired to know the maximum value of $|\sigma^*|$ which will produce a stable solution, L_2 is the relevant boundary if $B^* < \frac{3}{8}\sqrt{2}$, while L_1 is the relevant boundary otherwise. In other words, the overall stability boundary in Fig. 6.2.1a is $V'T'P\,T\,V$, and the region above is stable.[2]

Using Eq. (6.2.2), this result is stated mathematically as

$$[B^*]_{\substack{model\\ stability\\ boundary}} = \begin{cases} \sqrt{L_2[(1-L_2)^2 + \sigma^{*2}]}\,; & |\sigma^*| \leq \sigma_T^* \\ \sqrt{L_1[(1-L_1)^2 + \sigma^{*2}]}\,; & |\sigma^*| > \sigma_T^* \end{cases} \tag{6.2.4}$$

where $L_k \equiv L_k(\sigma^*)$, as given by Eqs. (5.3.24), and σ_T^* is given by Eq. (6.2.3).

6.2.3 Optimizing Model Lock-in With Respect to Experiment

The analysis above has determined a fixed set of model stability boundaries in the normalized (σ^*, B^*) plane. Therefore, recalling the definitions

$$\sigma^* \equiv c_1\sigma\,; \quad c_1 \equiv \frac{2}{\alpha} \tag{6.2.5a}$$

$$B^* \equiv c_2 B\,; \quad c_2 \equiv \sqrt{\frac{3(r^2 + \tilde{r}^2)p}{4\alpha^3}}\,, \tag{6.2.5b}$$

it follows that the location of the model stability boundaries in the (σ, B) plane of Fig. 2.3.2 depends only on the axis-stretching constants c_1 and c_2. The goal of this Section is to determine positive numerical values for c_1 and c_2, or equivalently c_1 and $\frac{c_1}{c_2}$, which best fit the experimental data (σ_i, B_i) listed in

---

1. In fact, this condition was used to arrive at the special values $\sigma_T^* = \frac{1}{4}\sqrt{5}$ and $B^* = \frac{3}{8}\sqrt{2}$.
2. Since the mapping $B^*(A^*)$ is three to one in the region bounded by $U'P\,U\,R$, that region represents not only the unstable interior of the ellipse (L_2, L_3), but also some of the stable exterior.

Table 6.2.1.

The optimum values of $(c_1, \frac{c_1}{c_2})$ are defined to be those which minimize the squared-error E_1 between the experimental data and the model,

$$E_1 \equiv \sum_{i:|\sigma_i|<\frac{\sigma_T^*}{c_1}} \left\{ B_i - \frac{1}{c_2}\sqrt{L_{2i}[(1-L_{2i})^2 + (c_1\sigma_i)^2]} \right\}^2 + \sum_{i:|\sigma_i|>\frac{\sigma_T^*}{c_1}} \left\{ B_i - \frac{1}{c_2}\sqrt{L_{1i}[(1-L_{1i})^2 + (c_1\sigma_i)^2]} \right\}^2 , \qquad (6.2.6)$$

where the quantities L_{ki} are defined by

$$L_{ki} \equiv L_k(\sigma_i^*) = L_k(c_1\sigma_i), \quad k = 1, 2, 3 \qquad (6.2.7)$$

and the second term within each pair of curly brackets is obtained from Eq. (6.2.4).

At first it may seem that minimization of E_1 with respect to c_1 and c_2 must be carried out by trial and error; however, calculations reveal a considerable simplification. For the data of Table 6.2.1, E_1 versus c_1 is plotted in Fig. 6.2.2 with $\frac{c_1}{c_2}$ as parameter. On the plateaus at left ($c_1, c_2 << 1$, $\frac{c_1}{c_2}$ fixed), only the first summation in Eq. (6.2.6) contributes since $|\sigma_i| \leq \frac{\sigma_T^*}{c_1}$ holds for all the data points. In other words, c_1 and c_2 are so small that all of the data (σ_i, B_i) lie very near the origin of the normalized (σ^*, B^*) plane (Fig. 6.2.1), such that only stability boundary L_2 is relevant. Conversely, on the plateaus at the right of Fig. 6.2.2 ($c_1, c_2 >> 1$, $\frac{c_1}{c_2}$ fixed), only the second summation in Eq. (6.2.6) contributes since $|\sigma_i| > \frac{\sigma_T^*}{c_1}$ holds for all the data points. In other words, the axis-stretching constants are so large that points T and T' of Fig. 6.2.1 appear, on the scale of the data, to be virtually at the origin, such that only stability boun-

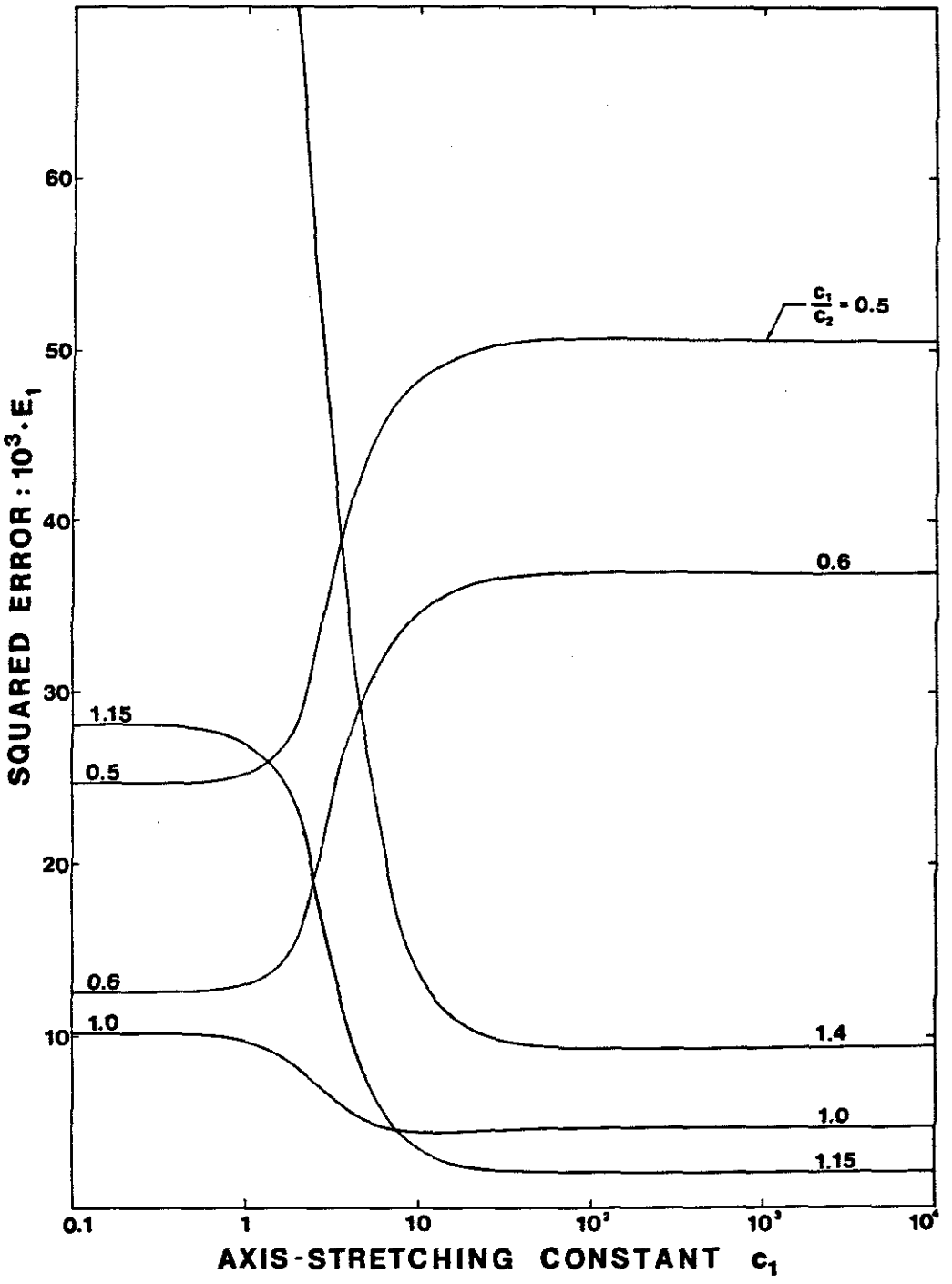

Fig. 6.2.2: Model/Experimental Error vs. Axis-Stretching Constants (Re = 300).

dary L_1 is relevant.

From Fig 6.2.2 it is apparent that the least-squares solution occurs either for $c_1 << 1$ or for $c_1 >> 1$. But $c_1 << 1$ must be ruled out on the basis of the assumption

$$\alpha \equiv \frac{2}{c_1} \sim O(\varepsilon), \tag{6.2.8}$$

which is inherent in the asymptotic method of Chapter 4; see Eq. (4.1.9). Hence the least squares solution of interest lies at $c_1 >> 1$, and only stability boundary L_1 is relevant.

With the help of definitions (5.3.24) and (6.2.5), consideration of the second line of Eq. (6.2.4) in the limit $c_1 >> 1$ with $\frac{c_1}{c_2}$ fixed gives[3]

$$\lim_{\substack{c_1 \to \infty \\ \frac{c_1}{c_2}\ finite}} B_{\substack{model \\ stability \\ boundary}} = \frac{1}{\sqrt{2}} \frac{c_1}{c_2} |\sigma| \tag{6.2.9}$$

Therefore, minimization of E_1, occurring at $c_1 \to \infty$, is equivalent to finding the best straight line[4]

$$B = P_0 |\sigma| \tag{6.2.10}$$

to fit the stability boundary data $(|\sigma_i|, B_i)$ given in Table 6.1.1, where

$$P_0 \equiv \frac{1}{\sqrt{2}} \frac{c_1}{c_2}. \tag{6.2.11}$$

Substituting definitions (6.2.5) and (3.2.15), while identifying $p = \beta$ for the

---

3. It has been assumed here that $\sigma^* = c_1 \sigma >> 1$ so that only Eq. (6.2.4b) need be considered, with σ^* dominating under the radical. These assumptions might be questioned on the grounds that c_1 is not actually infinite, while the detuning σ may actually be zero, in which case σ^* goes to zero rather than infinity. Experimentally, however, the value of σ on the lock-in boundaries never actually approaches zero, due to the threshold displacement level shown in Fig. 2.3.2. This threshold level, although not predicted by the present model, demonstrates that the behavior of the model stability boundaries near $\sigma = 0$, including whatever distortions of them are inherent in the limiting process (6.2.9), is irrelevant from a physical viewpoint.
4. Eq. (6.2.10) represents a V-shaped line in the (σ, B) plane, a straight line in the $(|\sigma|, B)$ plane.

forced case (Table 4.1.1), yields

$$P_0 = 2\left\{\frac{2\alpha}{3\beta(\bar{r}^2+\bar{r}'^2)}\right\}^{\frac{1}{2}} = \left\{\frac{2(a_1-a_4)e_1^2}{3\pi^2S^2a_2[\,(\frac{a_4}{2\pi S})^2+a_3^2\,]}\right\}^{\frac{1}{2}} \qquad (6.2.12)$$

In view of the definition (3.2.8) of e_1, the latter expression is a function of S and the a_i only, hence P_0 is a proper candidate for the set of model parameters P_i discussed in Section 6.1.

The optimum value for the stability boundary slope P_0 is defined to be that which minimizes the squared error

$$E_2 \equiv \sum_i (B_i - P_0|\sigma_i|)^2 \qquad (6.2.13)$$

between the experimental lock-in-boundary values B_i in Table 6.2.1 and the corresponding model values given by Eq. (6.2.10). Minimization of E_2 with respect to P_0 gives

$$P_0 = \frac{\sum_i B_i|\sigma_i|}{\sum_i |\sigma_i|^2}. \qquad (6.2.14)$$

Performing these summations using Table 6.2.1 yields the optimum value

$$P_0 = 0.813, \qquad (6.2.15)$$

which corresponds to the curve $\frac{c_1}{c_2} = 1.15$ in Fig. 6.2.2.

6.3 Lock-in for Spring-Mounted Cylinders

6.3.1 Frequency Variables for Comparing Model to Experiment

For comparison with experimental plots such as Fig. 2.4.2, model predictions for frequency response (e.g. Fig. 5.4.2) must be converted from the (Δ_f, Δ_r) plane to the (d_f, d_r) plane, using the inverted form of approximations (5.4.14),

$$d_f \approx 1 - \sqrt{1 - 2\Delta_f} \,. \tag{6.3.1a}$$

$$d_r \approx \Delta_r - \Delta_f + 1 - \sqrt{1 - 2\Delta_f} \,, \tag{6.3.1b}$$

which are exact for $e_2 = 1$. Such a conversion has been applied to Fig. 5.4.2 (duplicated here as Fig. 6.3.1a), the result being Fig. 6.3.1b. Two features of the transformation should be noted:

i. A 45° line, $\Delta_r - \Delta_f = K$, where K is a constant, transforms to the 45° line $d_r - d_f = K$. In particular, portions of the frequency solution satisfying $\Delta_r \approx \Delta_f$ transform to $d_r \approx d_f$.

ii. The horizontal line $\Delta_r = 0$ transforms to the parabola $d_r = \frac{1}{2} d_f^2$. This explains the slight upward curl in the horizontal (locked-in) portion of the transformed solution, Fig. 6.3.1b. Thus, while the function $\Delta_f(\Delta_r)$ is one-to-one [Eq. (5.4.19)], the function $d_f(d_r)$ is not.

6.3.2 Model Lock-in Characteristics

The objective of this subsection is to develop simple expressions for the position and width of the model lock-in band, delimited by the points l^+ and l^- on Fig. 6.3.1a.[1] The easiest way to describe the position and width of this band is to define a new coordinate x in the (Δ_f, Δ_r) plane as

$$x \equiv \Delta_f - \Delta_r \tag{6.3.2}$$

---

1. It is assumed throughout that all solutions in the lock-in band are stable. As shown in Chapter 7, this is a justifiable assumption for the parameter values selected herein.

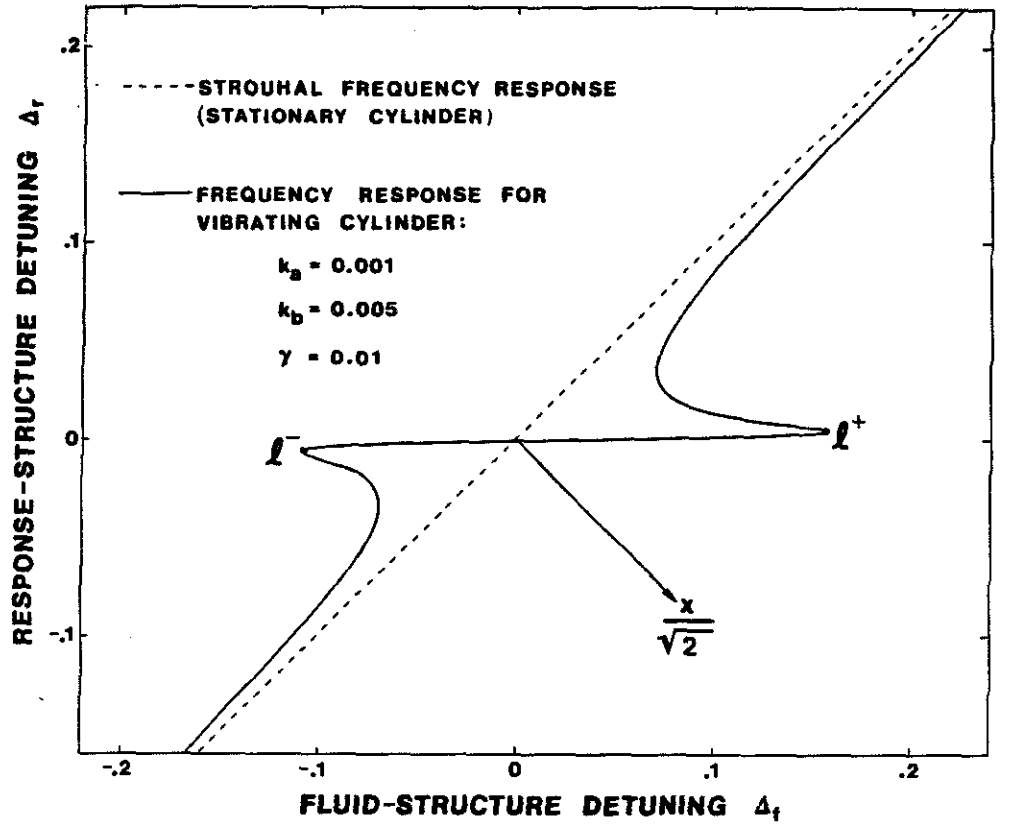

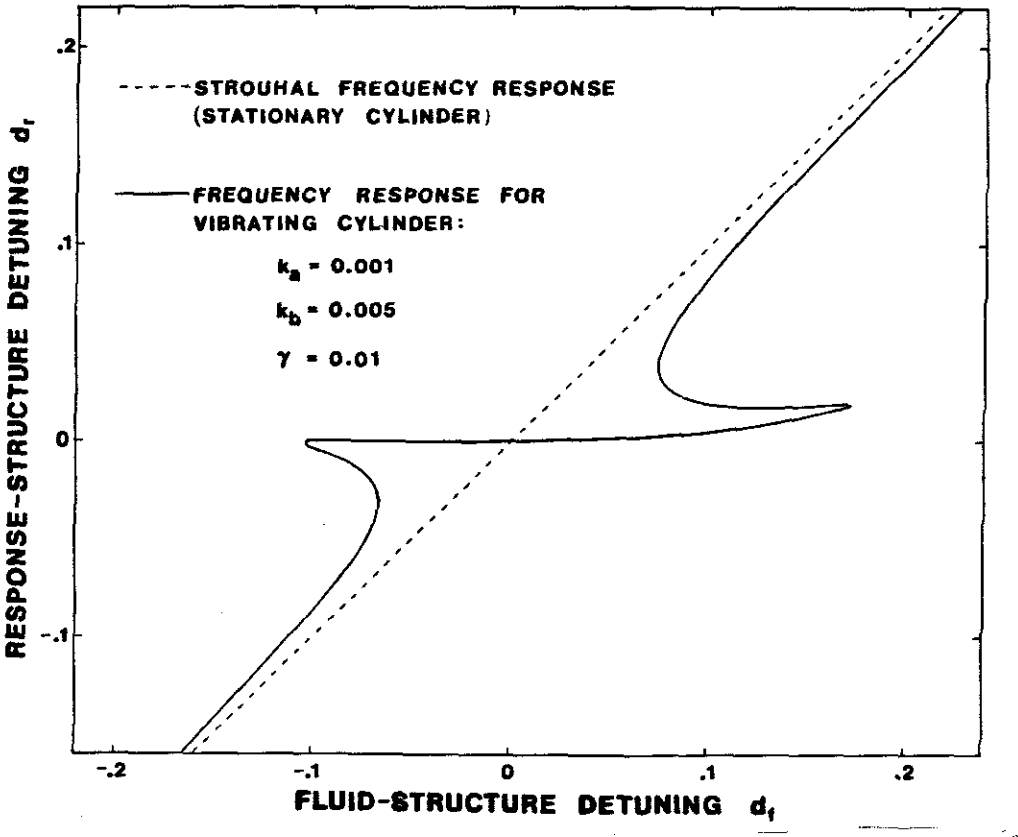

Fig. 6.3.1: Comparison of Detuning Coordinates

which has the advantage of reducing the frequency equation (5.4.19) to a quadratic in the response detuning Δ_r:

$$2x[4\Delta_r^2 + \gamma^2] = 2k_b\Delta_r + k_a\gamma. \tag{6.3.3}$$

Solving,

$$\Delta_r = \frac{k_b}{8x} \pm \sqrt{(\frac{k_b}{8x})^2 + \frac{k_a\gamma}{8x} - \frac{\gamma^2}{4}}. \tag{6.3.4}$$

Viewed in (x, Δ_r) coordinates, the endpoints $x_l^{\pm}$ of the lock-in band correspond almost exactly to the limits of real solution Δ_r, where the two roots (6.3.4) of the quadratic coalecse. Therefore, setting the radical in Eq. (6.3.4) equal to zero:

$$16\gamma^2 x_l^{\pm 2} - 8k_a\gamma x_l^{\pm} - k_b^2 = 0 \tag{6.3.5}$$

Solving,

$$x_l^{\pm} = \frac{1}{4\gamma}[k_a \pm \sqrt{k_a^2 + k_b^2}\,]. \tag{6.3.6}$$

Therefore the center of the lock-in band,

$$C \equiv \frac{x_l^+ + x_l^-}{2}, \tag{6.3.7a}$$

and the width of the lock-in band,

$$W \equiv x_l^+ - x_l^-, \tag{6.3.7b}$$

are given by the following simple expressions:

$$\textbf{Model Band-Center: } C = \frac{k_a}{4\gamma} \tag{6.3.8a}$$

$$\textbf{Model Band-Width: } W = \frac{1}{2\gamma}\sqrt{k_a^2 + k_b^2}. \tag{6.3.8b}$$

Since the damping coefficient γ in Eqs. (6.3.8) is positive, symmetry of the lock-in band about the exact resonance point $\Delta_f = 0$ depends entirely on the parameter k_a. In particular, if $k_a > 0$, then the lock-in band is skewed to the right, in qualitative agreement with experimental data (see Fig. 2.4.2).

To fit the above result to experimental data, it is necessary to isolate the dependence of k_a, k_b, and γ on the mass ratio η and structural damping ratio ζ. Substitution of Eqs. (3.2.15c,d) and (3.2.24a,b) into definitions (5.4.11) gives

$$k_a = \frac{-\eta}{e_1 e_2}\left(\frac{a_4}{2\pi S}\right)(2a_3 + a_5) \tag{6.3.9a}$$

$$k_b = \frac{\eta}{e_1 e_2}\left[\left(\frac{a_4}{2\pi S}\right)^2 - a_3(a_3 + a_5)\right] \tag{6.3.9b}$$

Also, recalling approximation (5.4.17b):

$$\gamma \approx \frac{2\zeta}{\sqrt{e_2}} + \frac{a_4}{2\pi S e_2}\eta. \tag{6.3.10}$$

Although the previously defined quantity

$$e_2 \equiv 1 + a_3\eta \tag{6.3.11}$$

is strictly a function of η, the value of η for the experiments under consideration is so small ($\eta = 0.00514$) that

$$e_2 \approx 1 \tag{6.3.12}$$

is assumed, the validity of which must be verified *a posteriori* when a value for a_3 is known. Assumption (6.3.12) does not invalidate results of the model for large values of η; it merely implies that the current procedure for selecting model constants is not generally applicable.[2]

Under assumption (6.3.12), the parameters (k_a, k_b, γ) may be written as

$$k_a \approx P_1\eta \tag{6.3.13a}$$

$$k_b \approx P_2\eta \tag{6.3.13b}$$

$$\gamma \approx 2\zeta + P_3\eta, \tag{6.3.13c}$$

where the P_k, discussed in Section 6.1, are functions of Strouhal number S and the a_k only:

---

2. As previously indicated, the accuracy of the approximate conversions (5.4.14) and (6.3.1), which relate the solution coordinates (Δ_f, Δ_τ) in a simple way to the physical coordinates (d_f, d_τ), also depends on assumption (6.3.12).

$$P_1 \equiv -\frac{1}{e_1}\left(\frac{a_4}{2\pi S}\right)(2a_3 + a_5) \tag{6.3.14a}$$

$$P_2 \equiv \frac{1}{e_1}\left[\left(\frac{a_4}{2\pi S}\right)^2 - a_3(a_3 + a_5)\right] \tag{6.3.14b}$$

$$P_3 \equiv \frac{a_4}{2\pi S}. \tag{6.3.14c}$$

Substitution of approximations (6.3.13) into Eqs. (6.3.8) produces the following expressions for model lock-in band-center C and band-width W:

$$\textbf{Model Band-Center:}\quad C \approx \frac{P_1}{4(2\hat{\zeta} + P_3)} \tag{6.3.15a}$$

$$\textbf{Model Band-Width:}\quad W \approx \frac{\sqrt{P_1^2 + P_2^2}}{2(2\hat{\zeta} + P_3)}, \tag{6.3.15b}$$

where the *reduced damping* $\hat{\zeta}$ is defined as

$$\hat{\zeta} \equiv \frac{\zeta}{\eta}. \tag{6.3.16}$$

Hence for small η, C and W are function of reduced damping only. It remains to select values for P_1, P_2, and P_3 to optimize this result with respect to experimental data.

6.3.3 Experimental Lock-in Characteristics

Experimental values of lock-in band-center and band-width, denoted C_i and W_i respectively ($i = 1, \ldots, 5$), may be calculated for the five frequency response curves shown in Fig. 2.4.2 by the method illustrated in Fig. 6.3.2. Since

$$x \equiv \Delta_r - \Delta_f = d_r - d_f, \tag{6.3.17}$$

values of x may be read directly from the original (d_r, d_f) plots. Results of these calculations are given in Table 6.3.1.

6.3.4 Optimizing Model Lock-in With Respect to Experiment

The optimal values of model parameters P_1, P_2, and P_3 are defined to be those which minimize the squared error E_3 between the experimental values

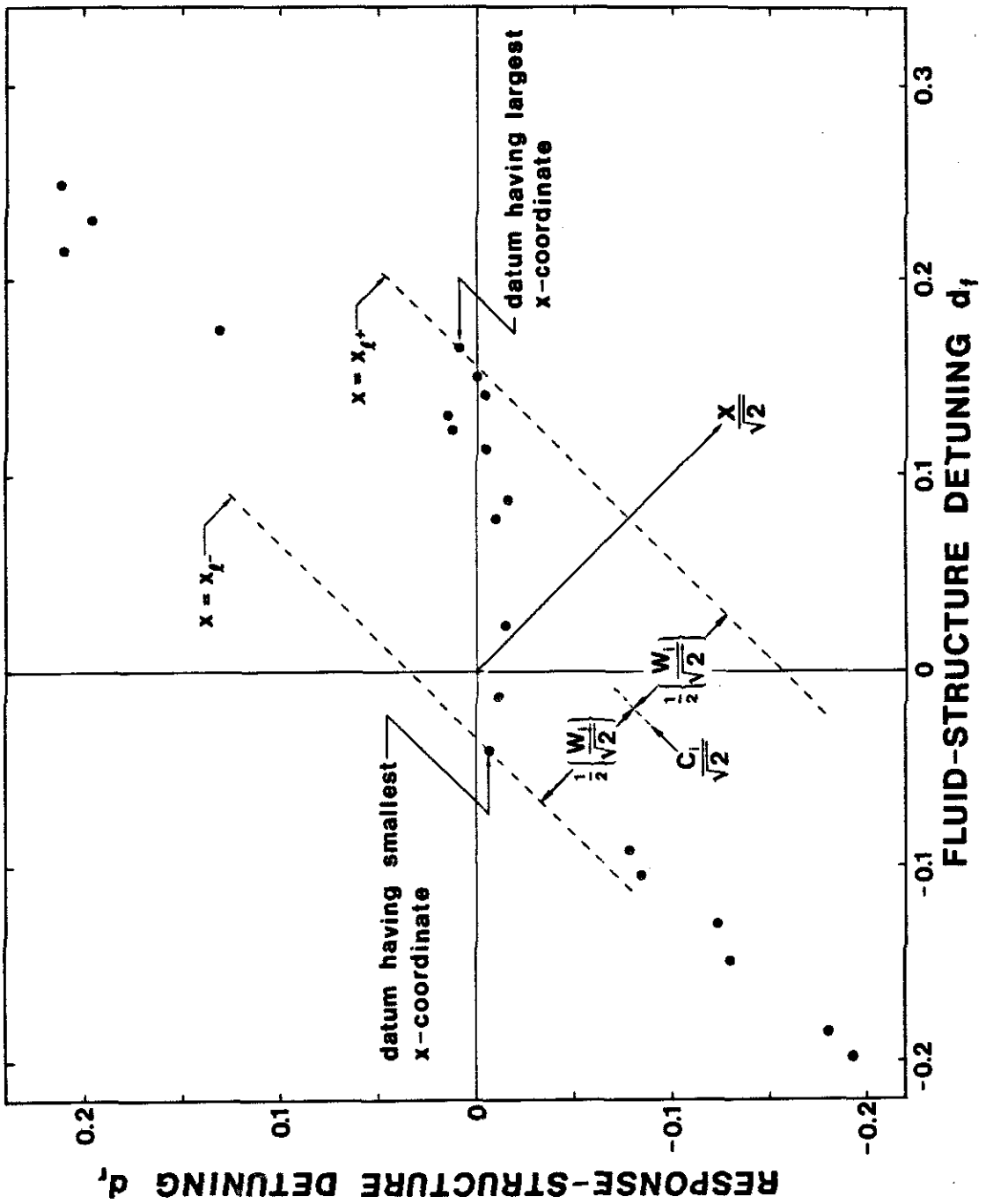

Fig. 6.3.2: Determination of Experimental Lock-In Characteristics.

Table 6.3.1: Experimental Lock-in Characteristics							
i	η_i	ζ_i	$\hat{\zeta}$	$(x_l^-)_i$	$(x_l^+)_i$	C_i	W_i
1	0.00514	0.00103	0.200	0.000	0.314	0.157	0.314
2	0.00514	0.00145	0.282	0.000	0.257	0.1285	0.257
3	0.00514	0.00181	0.352	0.000	0.225	0.1125	0.225
4	0.00514	0.00257	0.500	-0.021	0.156	0.067	0.177
5	0.00514	0.00324	0.630	0.000	0.106	0.053	0.106

$(C_i,\ W_i)$ and the model predictions $(C,\ W)$:

$$E_3 \equiv \sum_{i=1}^{5} [\ (C_i - C)^2 + (W_i - W)^2\ ]. \tag{6.3.18}$$

Defining for convenience

$$Q_1 \equiv \frac{P_1}{8} \tag{6.3.19a}$$

$$Q_2 = \frac{1}{4}\sqrt{P_1^2 + P_2^2} \tag{6.3.19b}$$

$$Q_3 \equiv \frac{P_3}{2}, \tag{6.3.19c}$$

it follows from Eqs. (6.3.15) that

$$E_3(Q_1,\ Q_2,\ Q_3) = \sum_{i=1}^{5} [C_i - \frac{Q_1}{\hat{\zeta}_i + Q_3}]^2 + [W_i - \frac{Q_2}{\hat{\zeta}_i + Q_3}]^2 . \tag{6.3.20}$$

Error minimization with respect to Q_1 and Q_2 requires that at the optimal point $(Q_1^*,\ Q_2^*)$

$$\frac{\partial E_3}{\partial Q_1} = -2 \sum_{i=1}^{5} [C_i - \frac{Q_1^*}{\hat{\zeta}_i + Q_3}][\frac{1}{\hat{\zeta}_i + Q_3}] = 0 \tag{6.3.21a}$$

$$\frac{\partial E_3}{\partial Q_2} = -2 \sum_{i=1}^{5} [W_i - \frac{Q_2^*}{\hat{\zeta}_i + Q_3}][\frac{1}{\hat{\zeta}_i + Q_3}] = 0, \tag{6.3.21b}$$

which yields

$$Q_1^* = \frac{\sum_{i=1}^{5} \frac{C_i}{\hat{\zeta}_i + Q_3}}{\sum_{i=1}^{5} \frac{1}{(\hat{\zeta}_i + Q_3)^2}} \tag{6.3.22a}$$

$$Q_2^* = \frac{\sum_{i=1}^{5} \frac{W_i}{\hat{\zeta}_i + Q_3}}{\sum_{i=1}^{5} \frac{1}{(\hat{\zeta}_i + Q_3)^2}}. \tag{6.3.22b}$$

For fixed Q_3, optimal values (Q_1^*, Q_2^*) may easily be found by performing the indicated summations using Table 6.3.1. Complete optimization is achieved by tabulating the (Q_1, Q_2)-minimized error $E_3(Q_1^*, Q_2^*, Q_3)$ versus Q_3, and seeking the minimum at Q_3^*. The result is

$$Q_1^* = 0.04641; \qquad Q_2^* = 0.09556; \qquad Q_3^* = 0.096. \tag{6.3.23}$$

By inverting Eqs. (6.3.19), and substituting Eqs. (6.3.23), the optimum values of P_1, P_2, P_3 are found to be

$$P_1 = 0.371 \tag{6.3.24a}$$

$$P_2 = \pm 0.0909 \tag{6.3.24b}$$

$$P_3 = 0.192. \tag{6.3.24c}$$

The ambiguous result for P_2, to be resolved in Section 6.4, is natural here since expressions (6.3.15) for C and W depend on P_2^2 rather than on P_2 itself.

6.4 Peak Structural Amplitude for Spring-Mounted Cylinders

6.4.1 Model Predictions for Peak Amplitude

An explicit formula for the model-predicted structural amplitude B is obtained in terms of Δ_r by substitution of Eqs. (5.4.15b) and (5.4.16b) into Eq. (5.4.8):

$$B^2 = \frac{4}{3p}(c^2 + \tilde{c}^2)\frac{4\alpha\Delta_r^2 - 2k_a\Delta_r + \alpha\gamma^2 + k_b\gamma}{(4\Delta_r^2 + \gamma^2)^2}. \tag{6.4.1}$$

For comparison with the experimental curves (Figs. 2.4.2), the maximum of B^2 with respect to d_f is sought,

$$\frac{dB^2}{d(d_f)} = 0. \tag{6.4.2}$$

According to Eqs. *(6.3.1)* and *(5.4.19)*,

$$d_f = d_f[\Delta_f(\Delta_r)], \tag{6.4.3}$$

so according to the chain rule

$$\frac{dB^2}{d\Delta_r} = \frac{dB^2}{d(d_f)}\frac{d(d_f)}{d\Delta_f}\frac{d\Delta_f}{d\Delta_r}. \tag{6.4.4}$$

Differentiation of Eqs. (6.3.1a) and (5.4.19) demonstrates that each of the latter two derivatives is bounded,[1] so that every solution of Eq. (6.4.2) is also a solution of

$$\frac{dB^2}{d\Delta_r} = 0. \tag{6.4.5}$$

Therefore, the latter condition may be used to deduce the peak amplitude $\hat{B}$ and the corresponding value $\hat{\Delta}_r$ of Δ_r.

Differentiating Eq. (6.4.1) and evaluating at the peak gives

---

1. $\frac{d(d_f)}{d\Delta_f}$ is infinite at $\Delta_f = \frac{1}{2}$, but such large values of Δ_f are not permitted.

$$\frac{d}{d\Delta_r}[B^2(4\Delta_r^2+\gamma^2)^2]\bigg|_{peak} = \frac{4}{3p}(c^2+\tilde{c}^2)(8\alpha\hat{\Delta}_r - 2k_a). \qquad (6.4.6)$$

On the other hand, by direct differentiation of the product $B^2(4\Delta_r^2+\gamma^2)^2$ and evaluation at the peak [condition (6.4.5)]:

$$\frac{d}{d\Delta_r}[B^2(4\Delta_r^2+\gamma^2)^2]\bigg|_{peak} = 16\hat{\Delta}_r(4\hat{\Delta}_r{}^2+\gamma^2)\hat{B}^2 \qquad (6.4.7)$$

Thus the peak amplitude is given by

$$\hat{B}^2 = \frac{4}{3p}(c^2+\tilde{c}^2)\frac{4\alpha\hat{\Delta}_r - k_a}{8\hat{\Delta}_r(4\hat{\Delta}_r{}^2+\gamma^2)}. \qquad (6.4.8)$$

$\hat{\Delta}_r$ is given by equating the specific expression (6.4.8) for $\hat{B}^2$ to the general expression (6.4.1) for B^2 evaluated at $\Delta_r = \hat{\Delta}_r$, the result being

$$16\alpha\hat{\Delta}_r{}^3 - 12k_a\hat{\Delta}_r{}^2 - 4\gamma(\alpha\gamma+2k_b)\hat{\Delta}_r + k_a\gamma^2 = 0. \qquad (6.4.9)$$

Whenever this cubic yields more than one real root, Eq. (6.4.8) may be applied for each to determine which root actually corresponds to the peak.

6.4.2 Experimental Data for Peak Amplitude

Experimental values of peak structural response, read from Figs. 2.4.2, are tabulated below.

Table 6.4.1: Experimental Peak Amplitudes

i	η_i	ζ_i	$\hat{B}_i$
1	0.00514	0.00103	0.524
2	0.00514	0.00145	0.396
3	0.00514	0.00181	0.204
4	0.00514	0.00257	0.146
5	0.00514	0.00324	0.082

6.4.3 Optimizing Model Peak Amplitude Predictions With Respect to Experiment

Recapping the selection of model parameters so far: P_0 has been chosen to optimize model/experimental agreement for lock-in of forced cylinders, while

P_1, P_2, and P_3 have been chosen to optimize such agreement for spring-mounted cylinders. Since there are a total of 6 parameters ($P_0, \ldots, P_5$) available to fit the model, P_4 and P_5 remain free for optimization of peak-amplitude predictions.

Identification of a pair of parameters P_4 and P_5 may be attempted by writing the equations for $\hat{B}$ and $\hat{\Delta}_r$ [Eqs. (6.4.8) and (6.4.9)] as functions of ζ, η, and $P_0, \ldots, P_3$ only; whatever additional parameter groups remain are candidates for P_4 and P_5. Toward this end, the quantities k_a, k_b, and γ are written as in Eqs. (6.3.13), which utilize the small-η approximation (6.3.12), while the quantity $\frac{4}{3p}(c^2 + \tilde{c}^2)$ is rewritten using Eq. (6.2.12) and the identity

$$(c^2 + \tilde{c}^2)(r^2 + \tilde{r}^2) = k_a^2 + k_b^2, \tag{6.4.10}$$

the result being

$$\frac{4}{3p}(c^2 + \tilde{c}^2) = \frac{\eta^2}{2\alpha} P_0^2 (P_1^2 + P_2^2). \tag{6.4.11}$$

It is apparent then that, instead of two additional parameters (P_4, P_5), only one, namely

$$P_4 \equiv \alpha \equiv \frac{1}{2\pi S} \frac{a_1 - a_4}{e_1}, \tag{6.4.12}$$

will appear in the equations for $\hat{B}$ and $\hat{\Delta}_r$.

Some reflection reveals that the sixth model parameter P_5 has actually been discarded by the small-η approximation (6.3.12). Comparing Eqs. (6.3.11) and (6.3.12) it is therefore appropriate to take

$$P_5 \equiv -a_3, \tag{6.4.13}$$

with the realization that this parameter cannot be numerically determined using the data or the analysis presented herein. Determination of P_5 requires

additional experimental data on spring-mounted cylinders for which η is sufficiently large that the product ηP_5 is likely to be comparable to 1.[2]

To find the optimum value for P_4 (assuming $P_0, \ldots, P_3$ are fixed), Eq. (6.4.8) for the model-predicted peak amplitude $\hat{B}^2$ is written as

$$\hat{B}(P_4, \eta, \zeta) = \frac{\eta}{4} P_0 \sqrt{P_1^2 + P_2^2} \left\{ \frac{4\hat{\Delta}_r - \frac{P_1}{P_4}\eta}{\hat{\Delta}_r [4\hat{\Delta}_r^2 + (2\zeta + P_3\eta)^2]} \right\}^{\frac{1}{2}} \tag{6.4.14}$$

where

$$\hat{\Delta}_r = \hat{\Delta}_r(P_4, \eta, \zeta) \tag{6.4.15}$$

according to Eq. (6.4.9).

The optimum value of P_4 is defined as that which minimizes the squared error

$$E_4(P_4) \equiv \sum_i [\hat{B}_i - \hat{B}(P_4, \eta_i, \zeta_i)]^2 \tag{6.4.16}$$

between the experimental peaks $\hat{B}_i$ listed in Table 6.4.1 and the corresponding model predictions $\hat{B}(P_4, \eta_i, \zeta_i)$. Substitution of the previously optimized values of P_0, P_1, and P_3 [Eqs. (6.2.15) and (6.3.25a,c)], as well as the two alternative values for P_2 [Eq. (6.3.25b)] yields Table 6.4.2.

Table 6.4.2: Two Alternative Solutions

Solution #	P_2	Optimum P_4	Minimized Error E_4
I	+0.0909	0.385	0.02283
II	-0.0909	0.126	0.01973

Of the two possibilities tabulated,

---

2. Recall that the value $\eta = 0.00514$ is used herein for comparison to experimental data (Table 6.4.1).

$$P_2 = -0.0909 \tag{6.4.17a}$$

is better for several reasons. Firstly, the error E_4 is lower in that case. Secondly, the corresponding value

$$P_4 = 0.126 \tag{6.4.17b}$$

yields $c_1 = \frac{2}{\alpha} = \frac{2}{P_4} = 15.75$, whereas $P_4 = 0.385$ yields $c_1 = 5.19$. The former value is sufficiently large to achieve the least-squares plateau for $c_1 \to \infty$ and $\frac{c_1}{c_2} = 1.149$ on Fig 6.2.2, whereas the latter value is not. Thirdly, the smaller value of $P_4 \equiv \alpha$ is more consistent with the order of magnitude assumption (4.1.9).

6.5 Recovering Model Constants from the Parameters P_k

6.5.1 Algebraic Expressions

The functions

$$P_k = P_k(a_0, \ldots, a_5, S), \quad k = 0, \ldots, 5, \tag{6.5.1}$$

as given by definitions (6.2.12), (6.3.14a,b,c), (6.4.12), and (6.4.13), may be inverted by algebraic manipulation to yield

$$a_k = a_k(P_0, \ldots, P_5, S). \tag{6.5.2}$$

It should be emphasized however that the a_k are model constants and do not actually depend on the Strouhal number S. The parameters P_k do depend on S, and their numerical values have been determined in Sections 6.2, 6.3, and 6.4 for $S = 0.20$. Consequently, when these numerical values are substituted into equations of the form (6.6.2), $S = 0.20$ must again be used.

Algebraic manipulation of the equations represented by (6.5.1) begins by solving for e_1, a function of a_0, a_3, and a_5 previously defined by Eq. (3.2.8). Using Eqs. (6.3.14), (6.4.12), and (6.4.13), the result is

$$e_1 = \frac{2P_3P_5}{P_1}. \tag{6.5.3}$$

Back substitution into the same equations yields

$$\alpha_0 = \frac{(P_1 + P_3)(P_3^2 + P_5^2)}{P_1P_5 + P_2P_3} - P_5 \tag{6.5.4a}$$

$$\alpha_1 = 2\pi SP_3[1 + \frac{P_4(P_3^2 + P_5^2)}{P_1P_5 + P_2P_3}] \tag{6.5.4b}$$

$$\alpha_2 = \frac{4}{3\pi S} \frac{P_3^3P_4(P_3^2 + P_5^2)^2}{P_0^2(P_1P_5 + P_2P_3)^3} \tag{6.5.4c}$$

$$\alpha_3 = -P_5 \tag{6.5.4d}$$

$$\alpha_4 = 2\pi SP_3 \tag{6.5.4e}$$

$$\alpha_5 = \frac{-P_1(P_3^2 + P_5^2)}{P_1P_5 + P_2P_3} + 2P_5. \tag{6.5.4f}$$

6.5.2 Sign Restrictions

The physical arguments used to develop the model in Chapter 3 imply that α_0 and α_4 must be positive, for the following reasons:

- α_0 is a proportionality constant relating the bulk fluid velocity and the integrated fluid momentum, which makes sense if and only if

$$\alpha_0 > 0. \tag{6.5.5a}$$

- In the expression (3.2.7) for the fluid-structure interaction force F_{int}, α_4 multiplies the term proportional to the relative velocity between fluid and structure, and this force properly opposes the relative motion if and only if

$$\alpha_4 > 0. \tag{6.5.5b}$$

Other physical arguments in Chapter 3, of a more nebulous nature, suggest that α_3 and α_5 should also be positive, for the following reasons:

- In the expression for F_{int}, α_3 multiplies the term representing apparent fluid mass, and the apparent mass is positive if and only if

$$\alpha_3 > 0. \tag{6.5.5c}$$

- In the expression for F_{int}, α_5 multiplies the term representing a bouyancy force, whose sign is physically correct if and only if

$$\alpha_5 > 0. \tag{6.5.5d}$$

6.5.3 Numerical Values

In Fig. 6.5.1, the model constants α_k are plotted versus the undetermined[3] model parameter P_5 using Eqs. (6.5.4) and the optimal values for $P_0, \ldots, P_4$ given by Eqs. (6.2.15), (6.3.25a,c), and (6.4.18a,b). According to Eqs. (6.5.4), there is a singularity at $P_5 = -\dfrac{P_2 P_3}{P_1}$. Unfortunately, there is no value of P_5 in Fig. 6.5.1 which simultaneously satisfies all four of the sign restrictions above, α_3 being negative whenever α_0 is positive, and vice-versa.

If compromising the desired conditions is unavoidable, it should at least be minimal. Since conditions (6.5.5a,b) are deemed more important than conditions (6.5.5c,d),

$$P_5 = 0.30 \tag{6.5.6}$$

is selected as the best value, since α_0 α_4 and α_5 are then positive in Fig. 6.5.1, while α_3 is minimally negative.

For this value, the small-η approximation

$$e_2 = 1 - P_6\eta \approx 1, \tag{6.5.7}$$

upon which the analyses of Sections 6.3 and 6.4 are based, is certainly justified for the value $\eta = 0.00514$ used therein.

---

3. As mentioned in Section 6.4, an optimum value of P_5 cannot be deduced from the experimental data presented in Chapter 2.

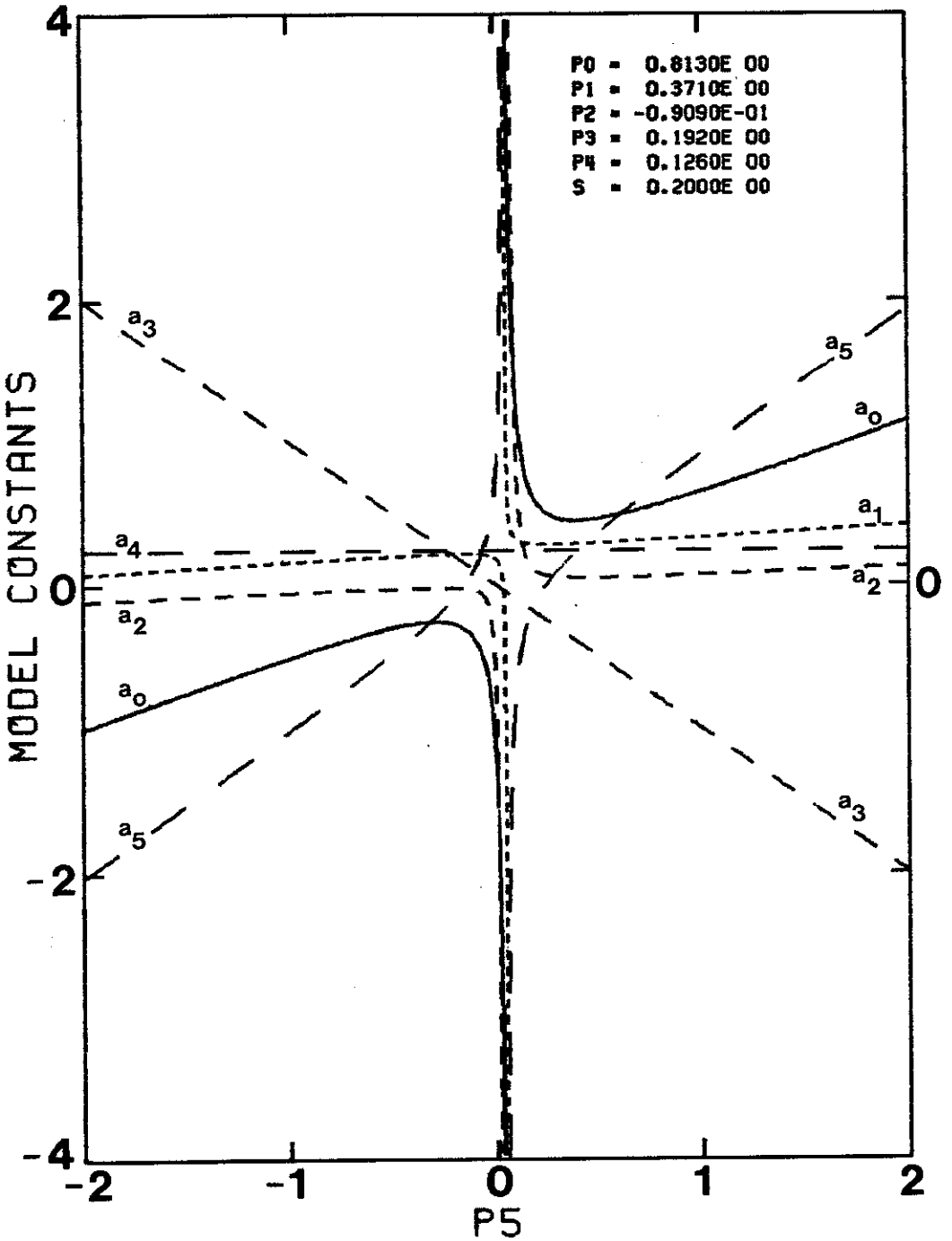

Fig. 6.5.1: Model Constants Corresponding to the Optimal P_k.

CHAPTER VII

RESULTS

7.1 Introduction

Fig. 7.1.1 summarizes the thesis: the description of vortex-shedding phenomena in Chapters 1 and 2 is represented by boxes A and A' of the Figure, while the mathematical development in Chapters 3–6 is outlined by the sequence $A \rightarrow B \rightarrow C \rightarrow D \rightarrow E \rightarrow$. Boxes F, G, B', C', and H diagram the contents of this chapter, including

- Analytic results for each type of structure considered (box F), and a comparison to experimental results (circle G).
- A comparison (circle H) between numerical solutions to the differential equations (B'), numerical solutions to the amplitude/phase equations (C'), and analytic results F.

Comparison H serves two purposes:

1. To check the mathematical analysis represented by $B \rightarrow C \rightarrow D \rightarrow E \rightarrow$.
2. To isolate the effect of model assumptions ($A \rightarrow B$) from mathematical assumptions ($B \rightarrow C \rightarrow D$). If comparison H reveals that analytic results F match numerical results B' fairly well, then whatever discrepancies appear in the comparison G are directly attributable to the model assumptions $A \rightarrow B$.

All of the model results presented in this chapter have been obtained using the parameter values P_k selected in Chapter 6, summarized here for ease of reference,

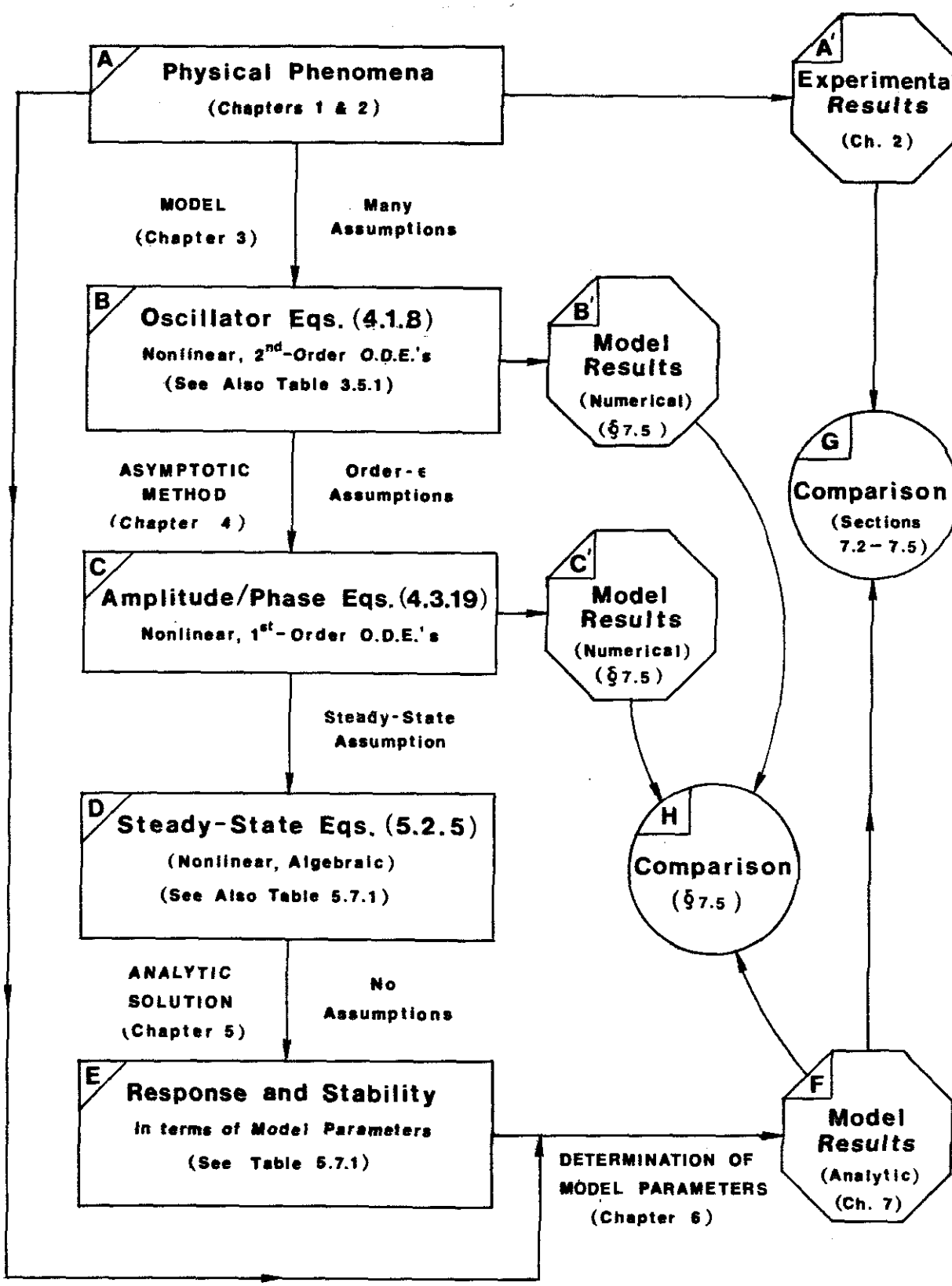

Fig. 7.1.1: Thesis Summary; the Role of Chapter 7.

$$P_0 = 0.813; \qquad P_1 = 0.371; \qquad P_2 = -0.0909 \tag{7.1.1a}$$

$$P_3 = 0.192; \qquad P_4 = 0.126; \qquad P_5 = 0.30. \tag{7.1.1b}$$

and hereafter referred to as **Parameter Set I.**

7.2 Forced Cylinders

Model versus experimental stability boundaries are shown in Fig. 7.2.1. Values of P_0 and P_4 used for the model calculations are those given by Eqs. (7.1.1). The calculations have been performed according to Eqs. (6.2.4) and (6.2.5), where the axis-stretching constants c_1 and c_2 are given in terms of P_0 and P_4 by definitions (6.2.11), (6.2.8), and (6.4.12). Points T and T' on Fig. 7.2.1 correspond to those discussed at some length in Section 6.2 (see Fig. 6.2.1).

The relatively good agreement between model and experiment is attributable to the small value of P_4 (large value of c_1) determined in Section 6.4, since large c_1 has the effect of placing points T and T' close to the origin, as assumed in Section 6.2.3 during the determination of P_0.

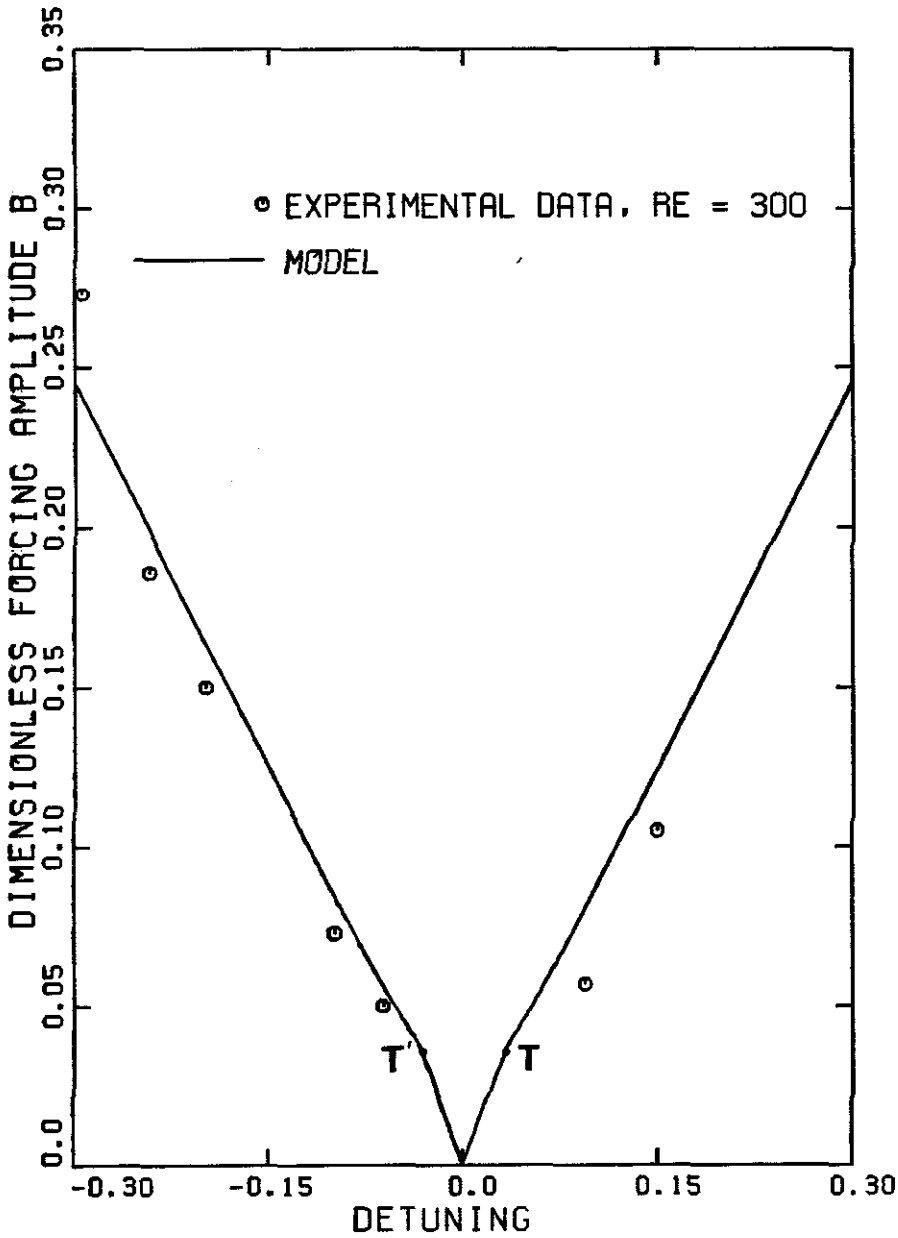

FIG. 7.2.1: EXPERIMENTAL VS. MODEL LOCK-IN BOUNDARIES FOR A FORCED CYLINDER

7.3 Spring-Mounted Cylinders

Experimental measurements of amplitude and frequency response for spring-mounted cylinders, previously given in Fig. 2.4.2, are compared to the corresponding model predictions [Eqs. (5.4.19) and (6.4.1)] in Figs. 7.3.1–7.3.5. Parameter Set I is used throughout, together with the experimental value of mass ratio

$$\eta = 0.00514 \tag{7.3.1}$$

and the Strouhal number $S = 0.20$. The structural damping ratio ζ is given on each plot.

Recalling the discussion following Eq. (5.4.19), there are three types of solution for spring-mounted cylinders, denoted on subsequent Figures as follows:

1. *Short-dashed lines:* Non-real amplitudes
2. *Long-dashed lines:* Real amplitudes, but unstable
3. *Solid lines:* Real amplitudes, stable.

Therefore, **only the solid line segments are physically meaningful.**

7.3.1 Frequency Response (Figs. 7.3.1a–7.3.5a)

The discussion of model-predicted frequency response is facillitated by the annotation of Fig. 7.3.2a, the other frequency curves being similar. Non-locked-in freqency response $\omega \approx \omega_s$ (i.e. $d_r \approx d_f$), typical of the experimental data far from resonance (d_r far from 0), is well approximated by the nearly straight segments $\overline{AB}$ and $\overline{FC'D'G}$. Likewise, locked-in response $\omega_n \approx \omega \neq \omega_s$ (i.e. $d_r \approx 0 \neq d_f$), typical of the experimental data near resonance, is well-approximated by the nearly horizontal, hair-pin-shaped segment $BCDEF$. The upward curl of the hair-pin segment at large values of d_f has been explained previously in the discussion following Eqs. (6.3.1).

Solutions generated by the underside of the hair-pin segment are real and

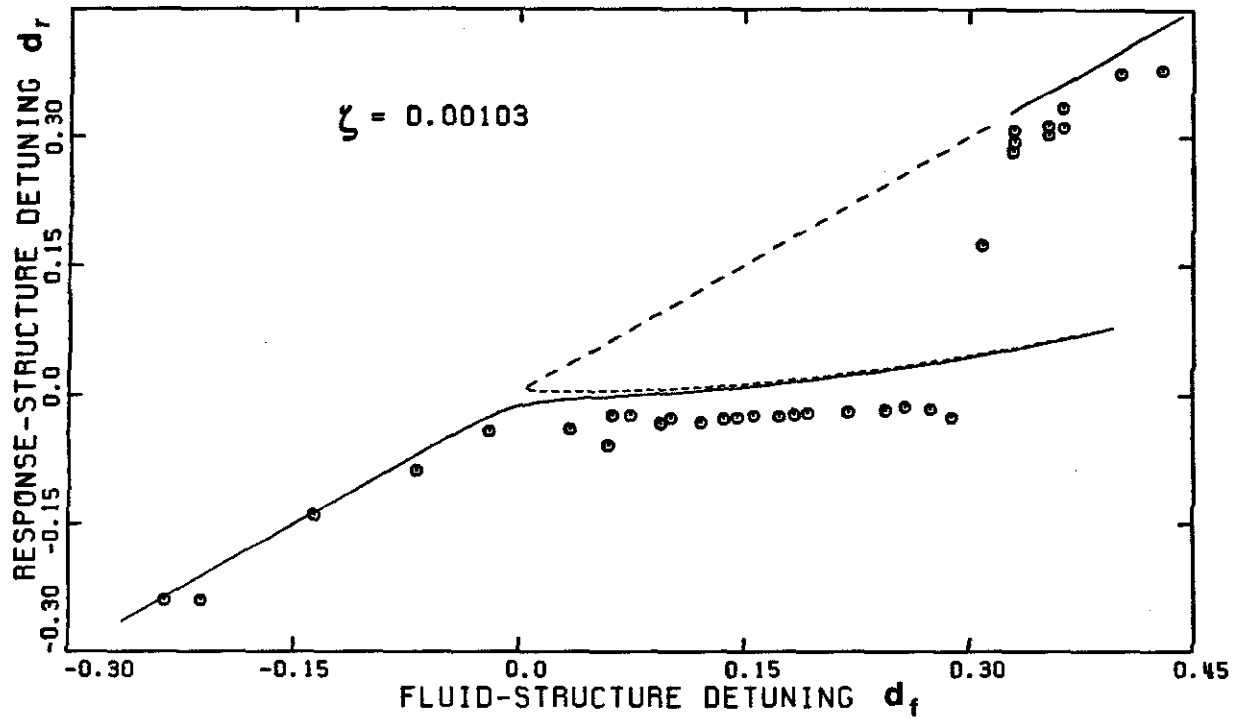

FIG. 7.3.1A: MODEL VS. EXPERIMENTAL FREQUENCY RESPONSE

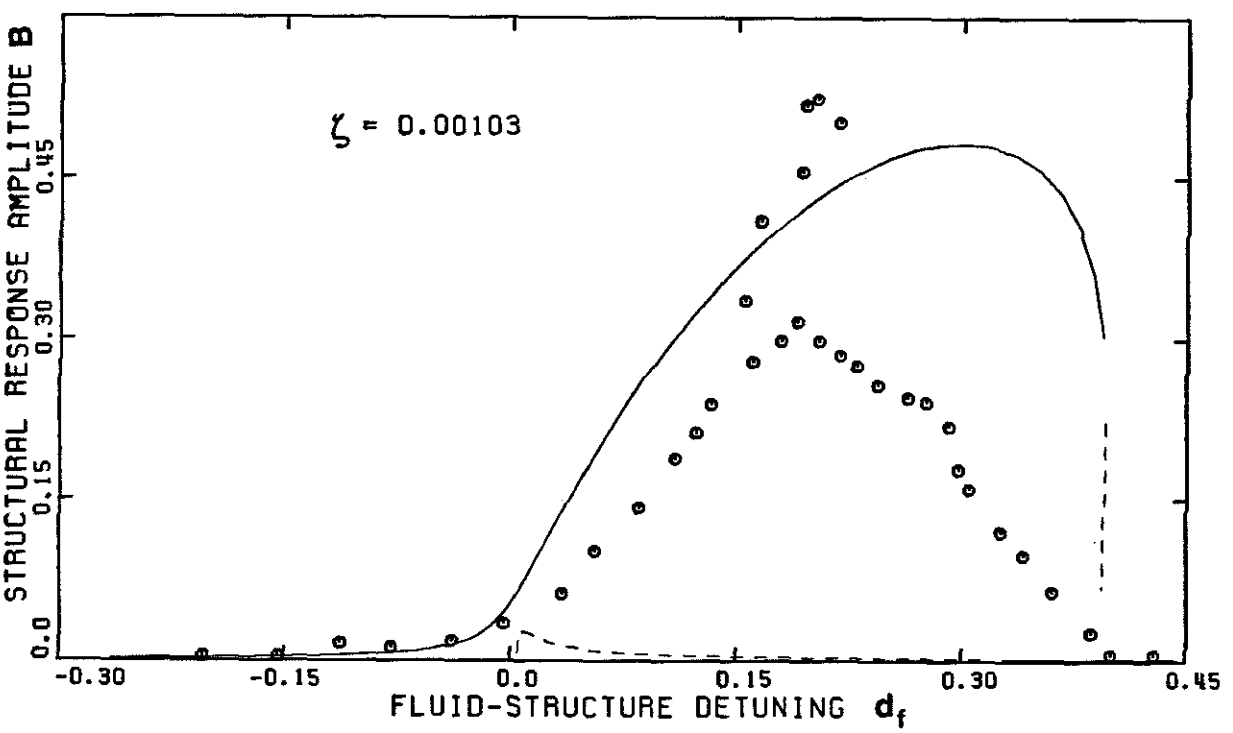

FIG. 7.3.1B: MODEL VS. EXPERIMENTAL AMPLITUDE RESPONSE

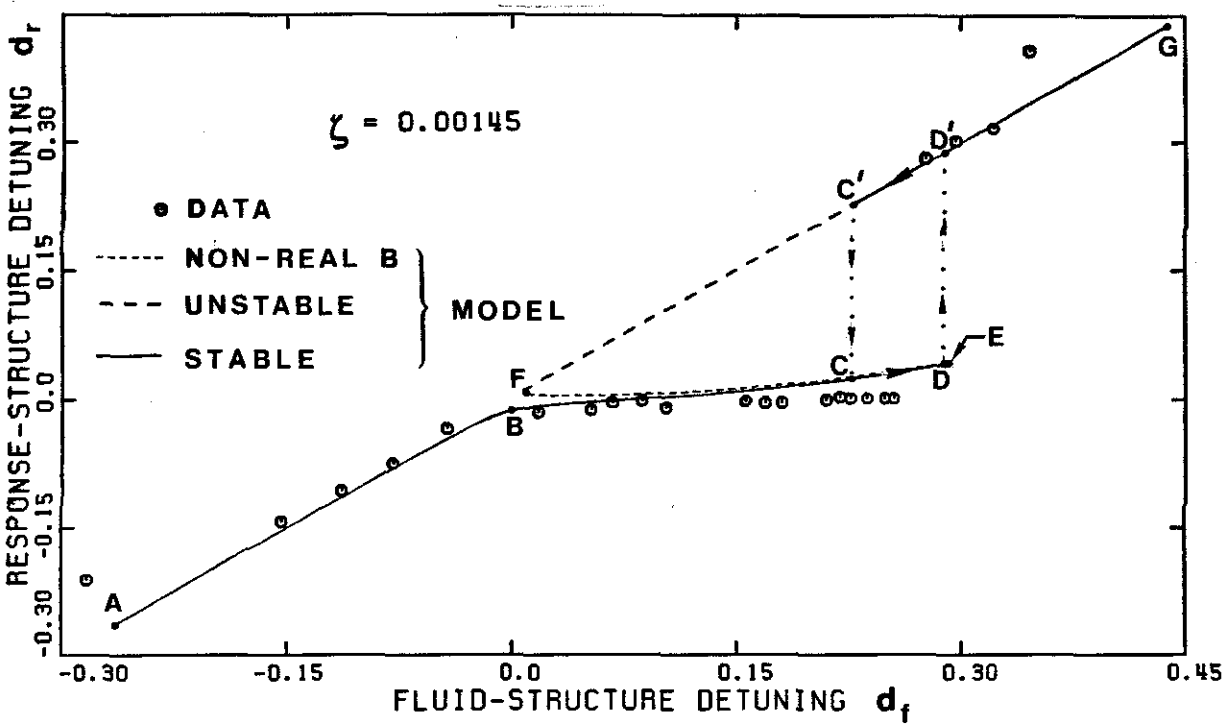

FIG. 7.3.2A: MODEL VS. EXPERIMENTAL FREQUENCY RESPONSE

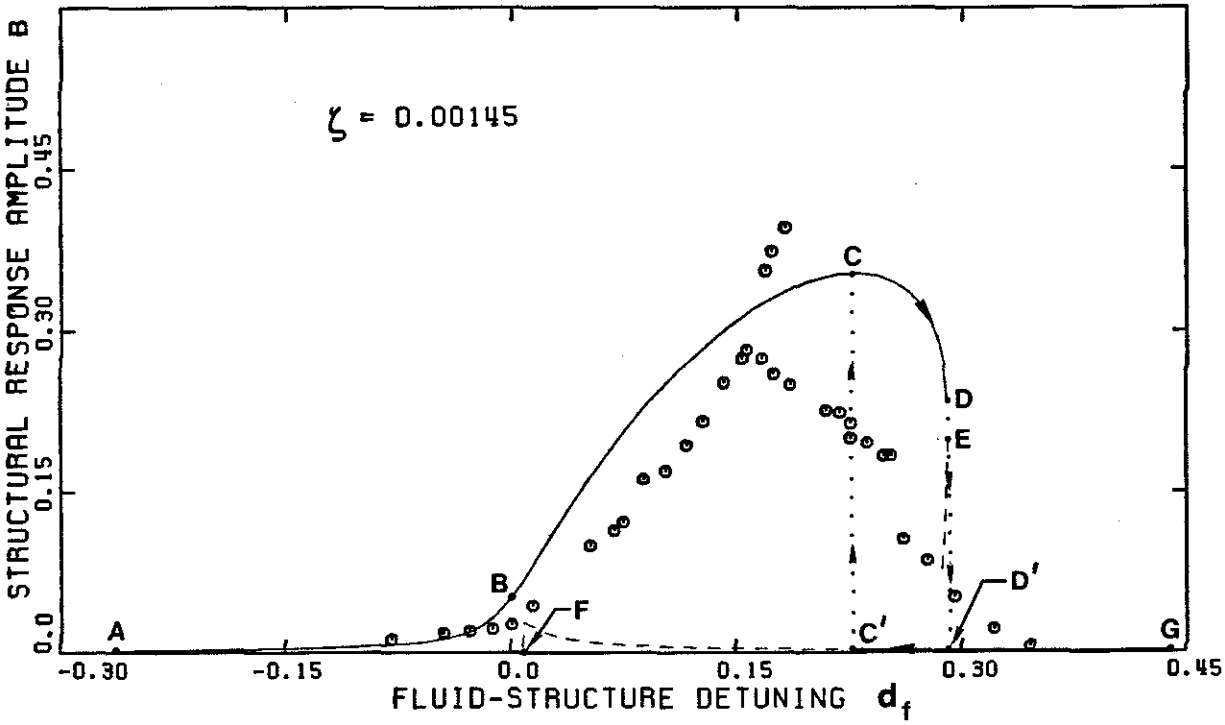

FIG. 7.3.2B: MODEL VS. EXPERIMENTAL AMPLITUDE RESPONSE

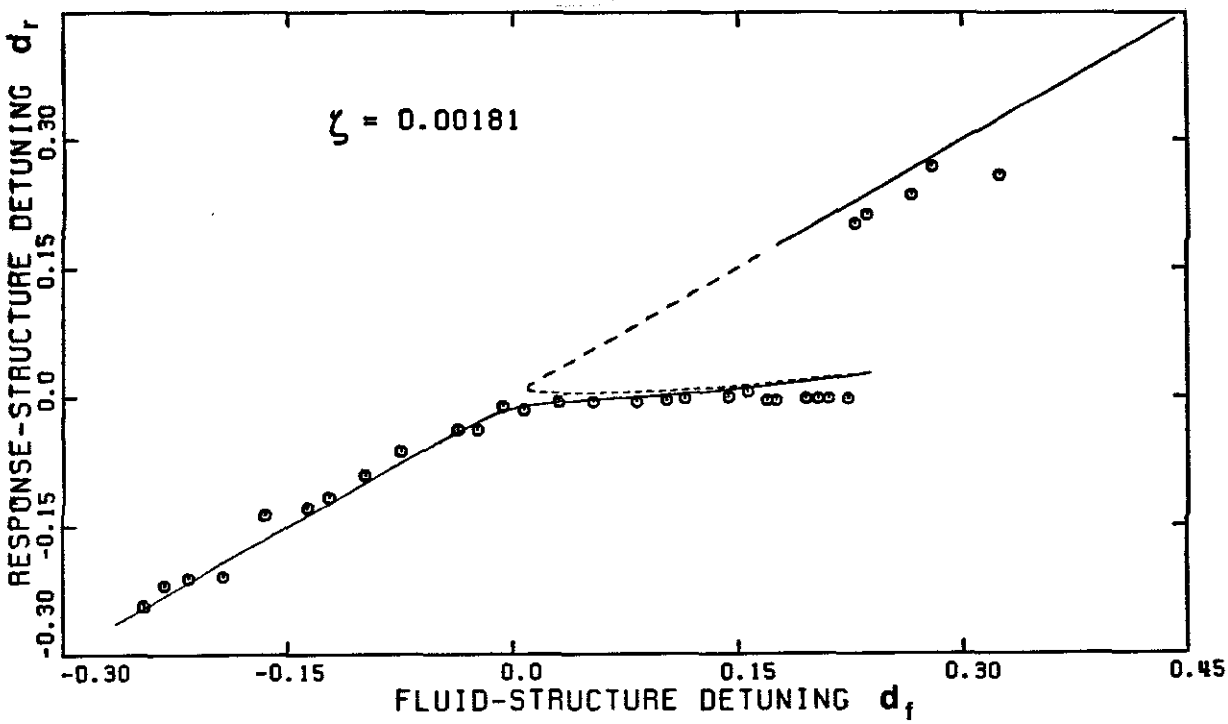

FIG. 7.3.3A: MODEL VS. EXPERIMENTAL FREQUENCY RESPONSE

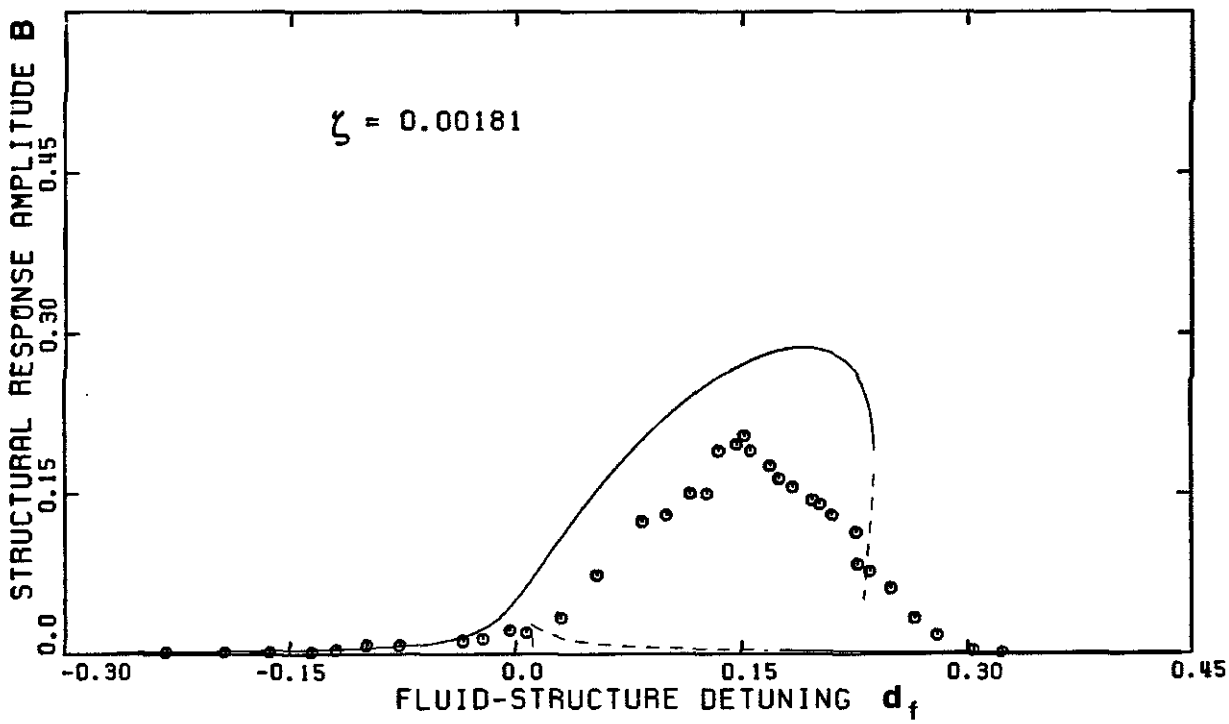

FIG. 7.3.3B: MODEL VS. EXPERIMENTAL AMPLITUDE RESPONSE

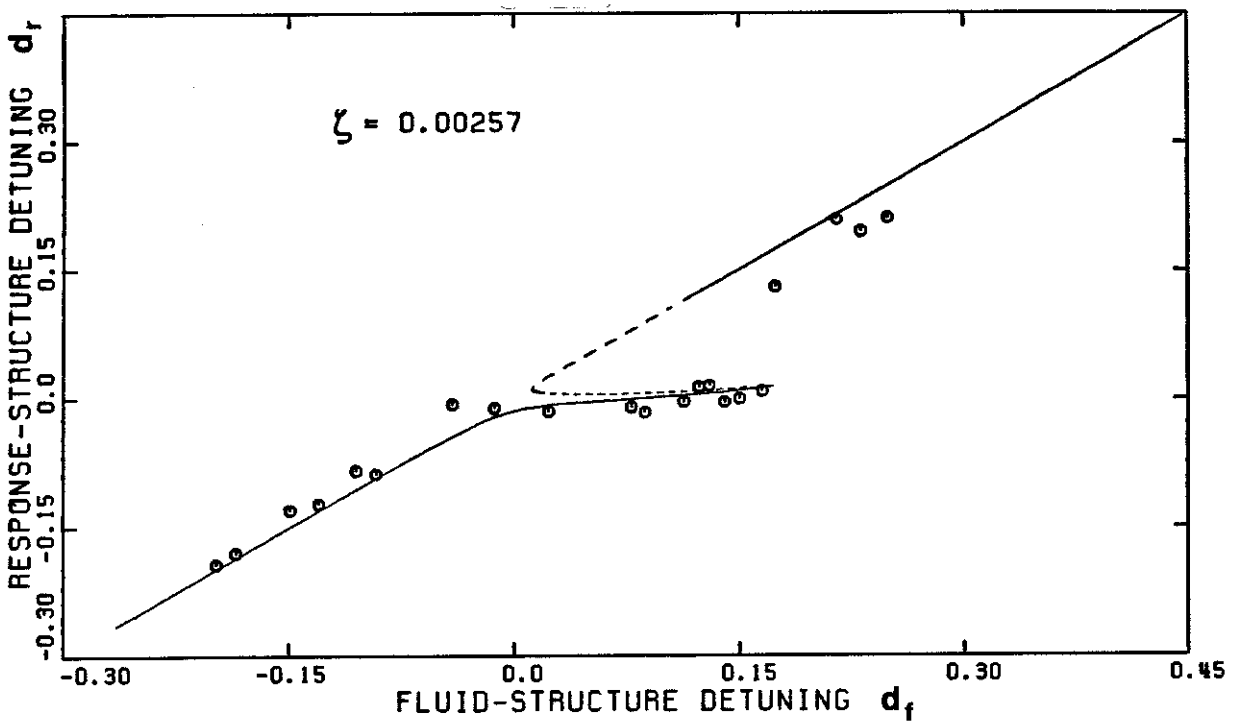

FIG. 7.3.4A: MODEL VS. EXPERIMENTAL FREQUENCY RESPONSE

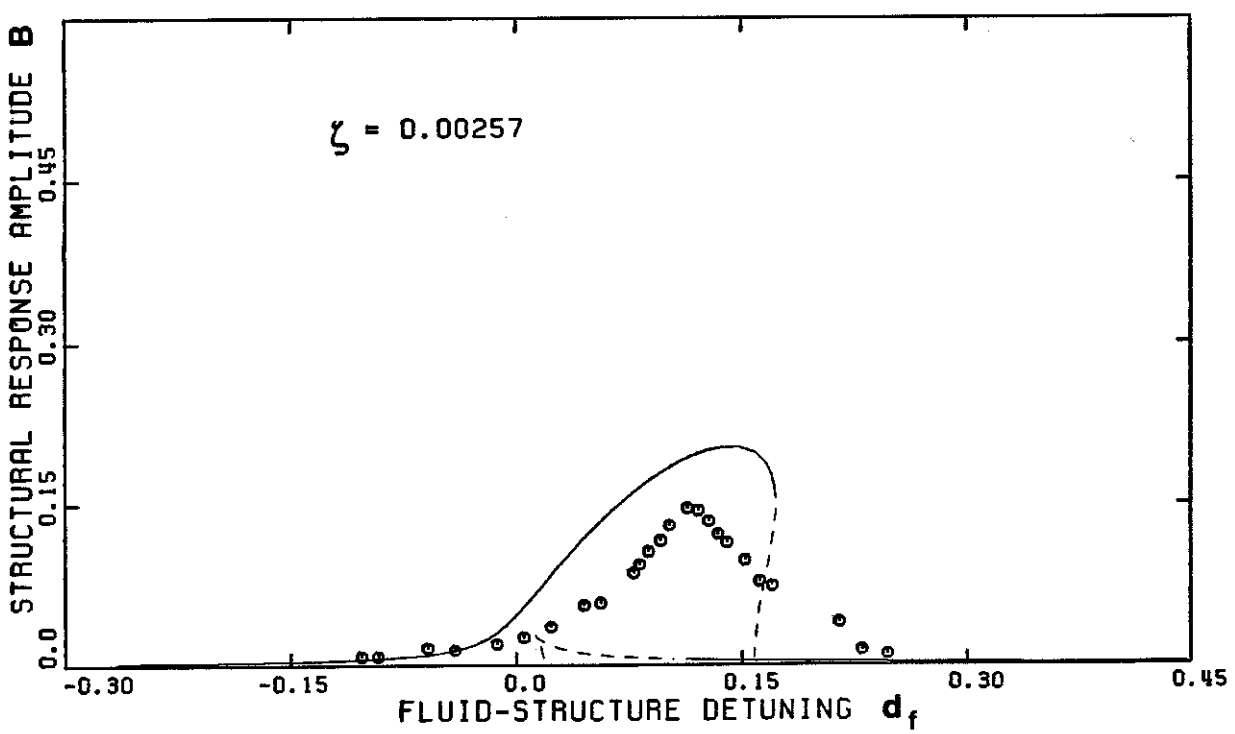

FIG. 7.3.4B: MODEL VS. EXPERIMENTAL AMPLITUDE RESPONSE

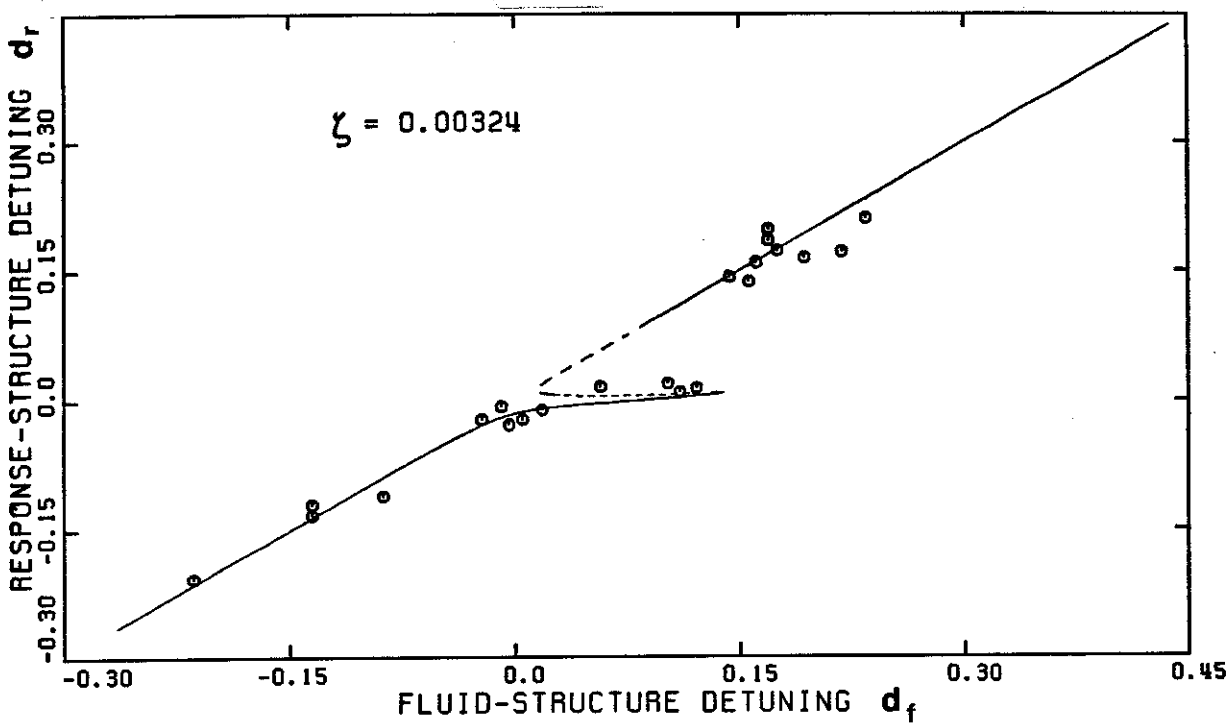

FIG. 7.3.5A: MODEL VS. EXPERIMENTAL FREQUENCY RESPONSE

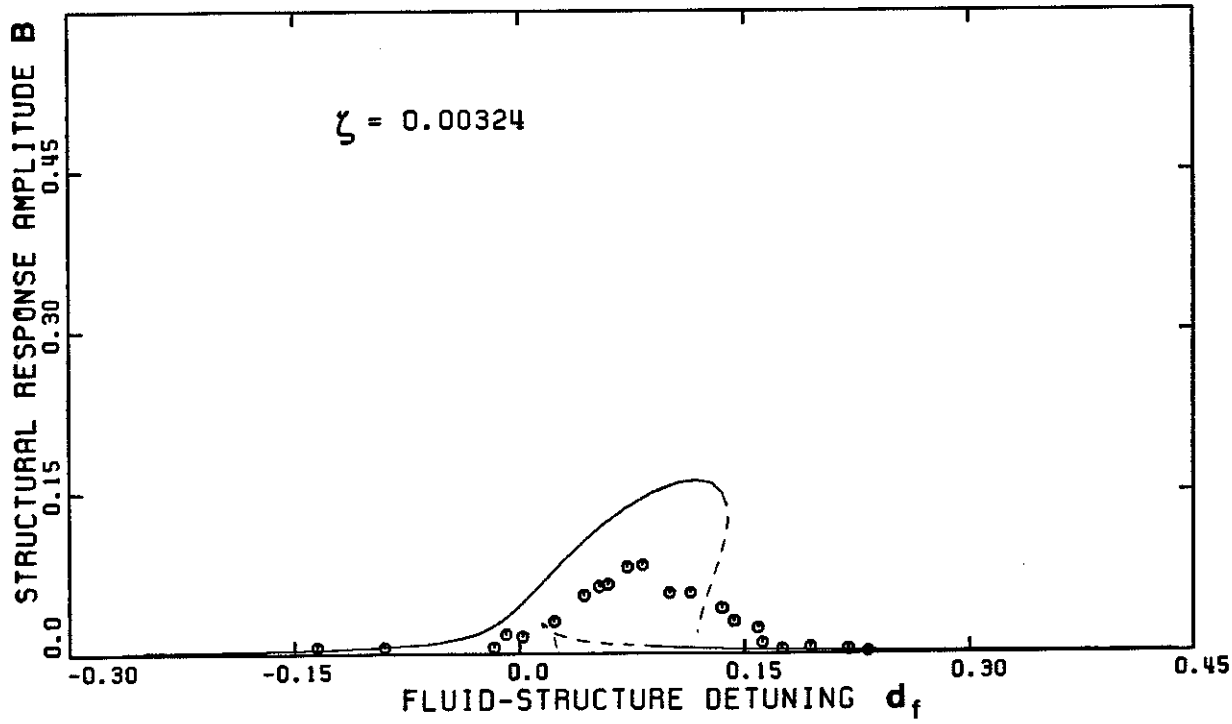

FIG. 7.3.5B: MODEL VS. EXPERIMENTAL AMPLITUDE RESPONSE

stable (i.e. the curve is a solid line) virtually all the way out to the cusp E, except for a very small distance between D and E. Stability of the entire lock-in band $BCDE$ was assumed in the regression analysis of Section 6.3, without any guarantee that it would actually be true. However, since it is virtually true for the parameter values under consideration (Eqs. 7.1.1), the design of Section 6.3 succeeds, producing model predictions for lock-in band width, position, and dependence on damping ratio which compare well to the experimental data.

Thus, according to the model, as d_f (i.e. flow speed U) is increased, there is initially a smooth transition from natural vortex-shedding response to lock-in along the curve $ABCD$, but at D the solution jumps suddenly to D', marking the end of the lock-in band and a return to natural vortex-shedding. As d_f is further increased, the solution proceeds along $D'G$. Conversely, as d_f (i.e. U) is decreased, the solution at first proceeds along $GD'C'$, then jumps from C' to C, and finally proceeds along CBA. This behavior agrees qualitatively with the experimental data, except that the model-predicted jump upward from D to D' occurs at a higher value of d_f than the jump downward from C' to C – a hysteretic effect typical of nonlinear systems, but not exhibited by the frequency response data.

7.3.2 Amplitude Response (Figs. 7.3.1b–7.3.5b)

The discussion of model amplitude response is facillitated by the annotation of Fig. 7.3.2b, the other amplitude curves being similar. Lettered points on Figs. 7.3.2a and 7.3.2b correspond respectively, such that a discussion of the model-predicted hysteresis loop need not be repeated. However, in contrast to the frequency data, it should be noted that the amplitude data, like the model, *does* exhibit hysteresis, as indicated by the arrows in Fig. 2.4.2. [1]

The curious smaller branch $FC'D'G$ of each amplitude curve is easily

---

1. For clarity, the arrows have been omitted from Figs. 7.3.1b and 7.3.2b.

explained by plotting the squared amplitude B^2, as obtained from Eq. (6.4.1), rather than the amplitude B itself. For $\zeta = 0.00145$, the result is Fig. 7.3.6, with lettered points corresponding to those in Figs. 7.3.2. It is clear then that points E and F connect through the region $B^2 < 0$, which of course is imaginary in the (d_f, B) plane of Fig. 7.3.2b.

Quantitatively, model/experimental agreement is not nearly as good for amplitude response as for frequency response. This is natural however, since three model parameters (P_1, P_2, P_3) were devoted to fitting the frequency data, whereas only one parameter (P_4) was allotted to fit the amplitude data.

7.3.3 Numerical Implementation

Considerable care was required to obtain Figs. 7.3.1–7.3.5, since the one-to-one functions $\Delta_f(\Delta_r)$ [Eq. (5.4.19)] and $B(\Delta_r)$ [Eq. (6.4.1)] are *extremely* sensitive in the locked-in region, at least for the parameter values used herein. This sensitivity is somewhat masked by the conversion to (d_f, d_r) coordinates, which causes the hair-pin segment of the frequency response to curl upward at the right (see Section 6.3.1 and Fig. 6.3.1).

To allow for this sensitivity, the increment in the "independent variable" [2] Δ_r was selected at each step such that the next stepwise element of arclength along either of the curves Δ_r vs. Δ_f or B vs. Δ_f would be no greater than some prescribed maximum. For example, to produce Fig. 7.3.1a, Δ_r-steps on the order of 10^{-4} were required in the hair-pin segment, while steps on the order of 10^{-2} were possible in the straight segments. Additionally, a step-size control based on the second derivative $\Delta_f''(\Delta_r)$ was incorporated as an override, to guard against taking too large a step near a point of vertical tangency $\Delta_f'(\Delta_r) \to 0$.

---

2. See the discussion of Section 5.4.2.

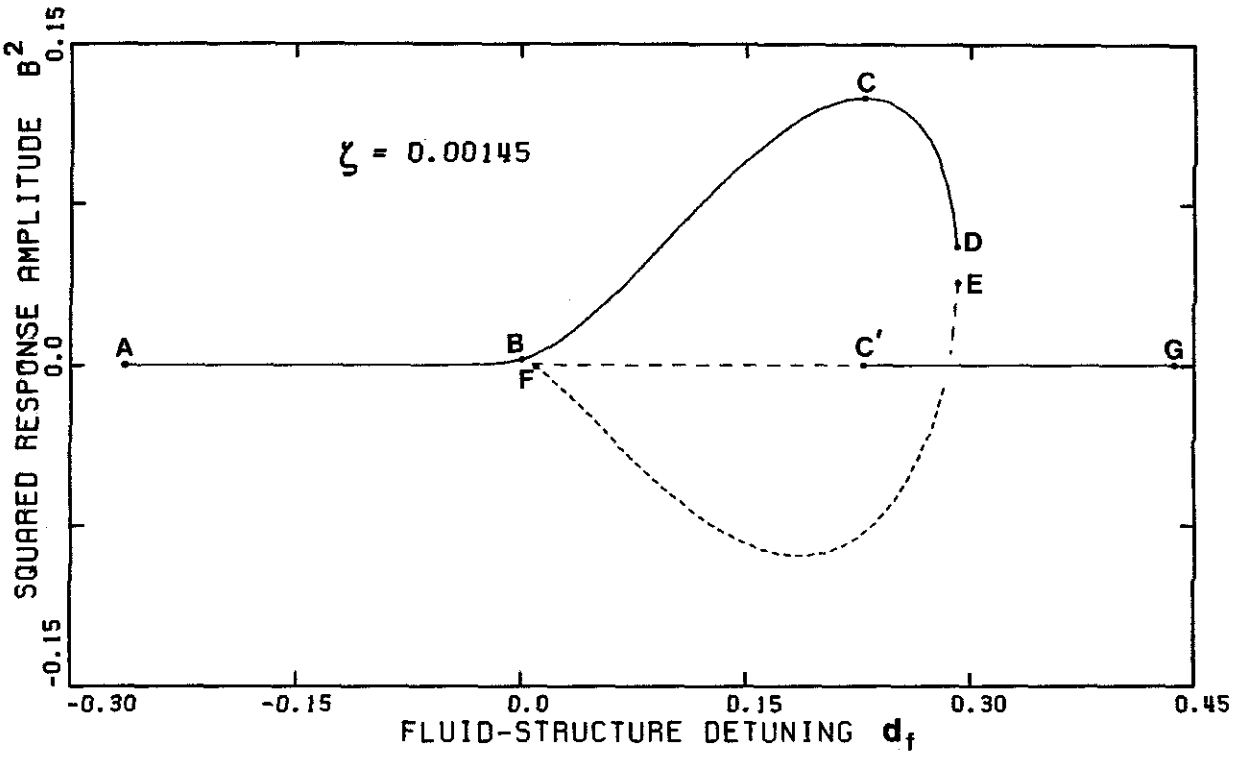

FIG. 7.3.6: IMAGINARY CONNECTION BETWEEN POINTS E AND F ($B^2 < 0$)

7.4 One-Mode Cable Approximation

As discussed in Section 5.5, the solutions for this case are identical to those for the spring-mounted cylinder (Section 7.3), except that all amplitudes are smaller by a factor of $\sqrt{\frac{2}{3}}$. In particular, the lock-in band characteristics are identical to those of a rigid cylinder having the same mass ratio and damping ratio. Thus Eq. (6.3.15b), plotted in Fig. 7.4.1 using Parameter Set I, predicts the model lock-in band-width $W(\hat{\zeta})$ for vibrating wires or cables, provided that the one-mode approximation is valid and the mass ratio η is small.

Both of these conditions hold for mode 7 of the steel wire examined in Section 2.5,[1] for which the experimental value of band-width is $W = 0.106$.[2] Thus, for model/experimental agreement in this regard, the experimental structural damping ratio would have to be $\zeta \approx 1.6 \times 10^{-4}$. Realistically, it is unlikely that ζ is so small, since even the slightest amount of structural slippage – notably between the vibrating wire and the pins around which its ends are wrapped (cf. Fig. 2.5.2) – is capable of dissipating energy at a rate corresponding to $\zeta \sim 0.001$ or greater [32, p. 31-11]. For such a realistic value of damping, Parameter Set I seriously under-predicts the width of the lock-in band, by a factor of about 5.

The source of this difficulty is easily ascertained: the model parameters (P_1, P_2, P_3) were selected in Section 6.3 to produce model values of bandwidth agreeing optimally with Feng's data (also shown in Fig. 7.5.1), for which the levels of reduced damping are much smaller than those appropriate for a steel wire in air. Ideally, of course, the model should extrapolate correctly to larger values of $\hat{\zeta}$. However, it fails to do so, at least for Parameter Set I. Improved results for large $\hat{\zeta}$ may be possible by re-selecting (P_1, P_2, P_3) based on experimental results which incorporate a wider range of $\hat{\zeta}$. Unfortunately, such data is una-

---

1. The mass ratio for steel in air is 1.94×10^{-4}.
2. In terms of the coordinates used on Fig. 2.5.4, values of x [Eq. (6.3.17)] are given by $x = 1 - \frac{f/f_1}{f_s/f_1}$.

vilable at the present time.

Consequently, as the two-mode cable approximation analysis is discussed in the next section, Parameter Set I is used, and no further attempt is made to relate model results *quantitatively* to the experimental data of Section 2.5. Rather, the mass ratio and damping ratios typical of Feng's rigid-cylinder experiments are selected, and *qualitative* features of the experimental data are sought in the model solutions.

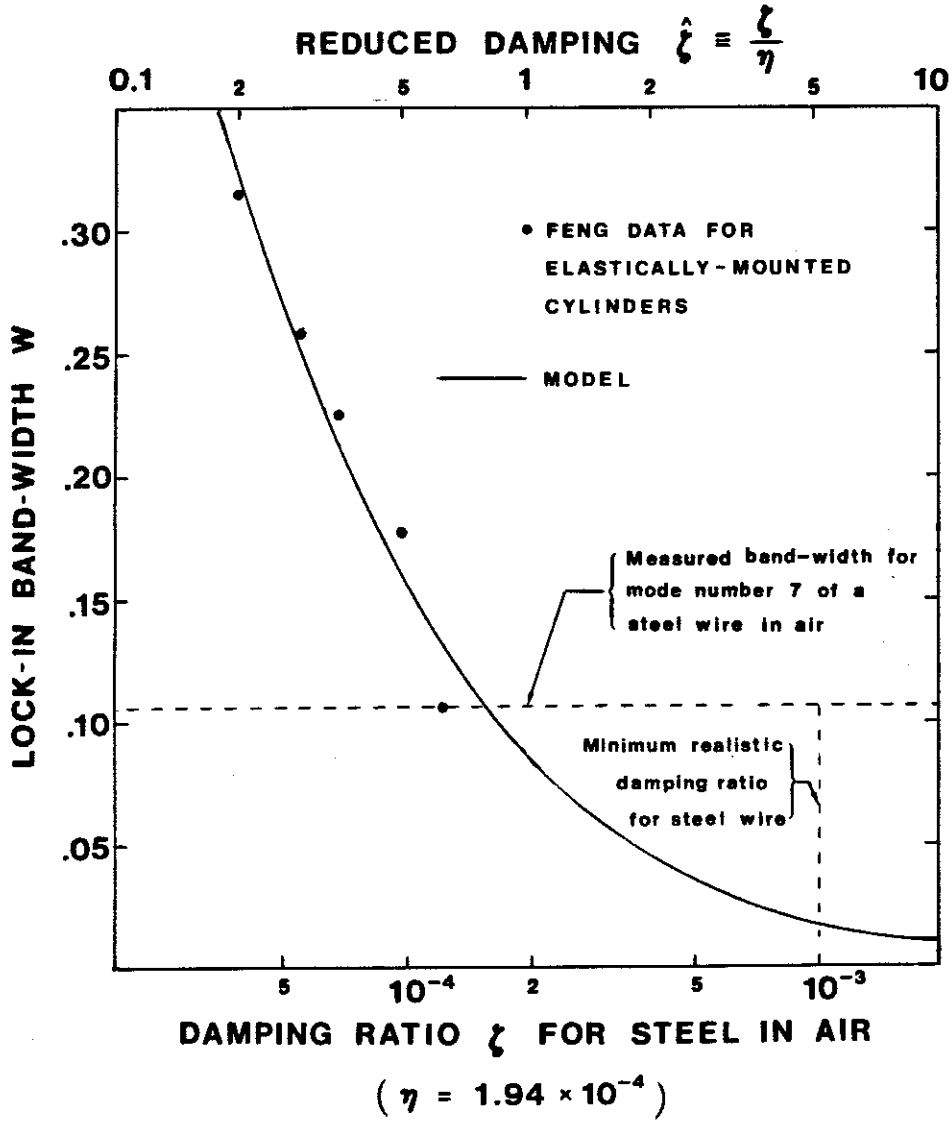

Figure 7.4.1. Model vs. Experimental Lock-In Band-Width

7.5 Two-Mode Cable Approximation

7.5.1 General Remarks

In this Section, the analytic, steady-state solutions developed in Section 5.6 are presented graphically. The foremost objective of the presentation is to demonstrate the nature of modal interaction for small values of the intermodal detuning Δ_{21}. These model results may then be compared qualitatively to the experimental observations of Section 2.5. Additionally, the reasonableness of two-mode solutions is sought by comparison to one-mode results; for large Δ_{21} the two-mode problem should resolve into two one-mode problems.

For such purposes, the dependence on the mass ratio η and on damping ratios ζ_i is of secondary importance. Thus, the fixed values

$$\eta = 0.00514, \tag{7.5.1a}$$

$$\zeta_1 = \zeta_2 = 0.00257 \tag{7.5.1b}$$

are used throughout Section 7.5, together with the Strouhal number $S = 0.20$ and Parameter Set I (Eqs. 7.1.1).

The results are plotted using the approximate detunings $(\Delta_f, \Delta_\tau, \Delta_{21})$,[1] which

---

1. In contrast, d-variables (the exact detunings) rather than Δ-variables were used to present one-mode results in Section 7.3. There are good reasons for this:
   - The Δ's may be regarded as natural variables for solution of the mathematical problem, while the d's are natural from a physical viewpoint. Thus in Section 7.3, the use of (d_τ, d_f) [defined by Eqs. (5.4.13)] was advantageous for quantitative comparison with experimental data. In this Section on the other hand, quantitative conparisons with experimental data are never made, so the use of (d_f, d_τ) [defined by Eqs. (5.6.16)] holds no particular advantage.
   - The use of (d_τ, d_f) in Section 7.3 was convenient because the conversion from (Δ_f, Δ_τ) to (d_f, d_τ) was easily accomplished for the one-mode problem [cf. Eqs. (5.3.1)]. In this Section on the other hand, there is no easy way, for the non-degenerate case, of converting the function $\Delta_f(\Delta_\tau)$ (Δ_{21} fixed) [Eq. (5.6.29)] to the function $d_f(d_\tau)$ (d_{21} fixed), since the conversion from Δ_{21} to d_{21} involves the unknown Δ_f [cf. Eqs. (5.6.17)].

   Therefore, Δ-variables are preferable for Section 7.5, and will be used exclusively throughtout. In any case, the small distinction between Δ's and d's should not cause undue concern. The results look much the same in either set of variables, except for a slight, upward curl of the lock-in bands in the (d_f, d_τ) plane (see Fig. 6.3.1; the

are defined by Eqs. (5.6.15). These variables are to be interpreted as shown on Fig. 7.5.1, which is exactly analogous to Fig. 5.6.1.[2] Thus Δ_f, plotted below as the abscissa, measures the normalized free-stream velocity U, while Δ_{21}, treated below as a parameter, measures the separation between the two adjacent structural frequencies Ω_1 and Ω_2.[3] The frequency solution $\Delta_f(\Delta_r)$ is expected to exhibit locked-in behavior near $\Delta_r \approx \pm\frac{1}{2}\Delta_{21}$, since these values correspond to $\Omega = \Omega_1$ and $\Omega = \Omega_2$.

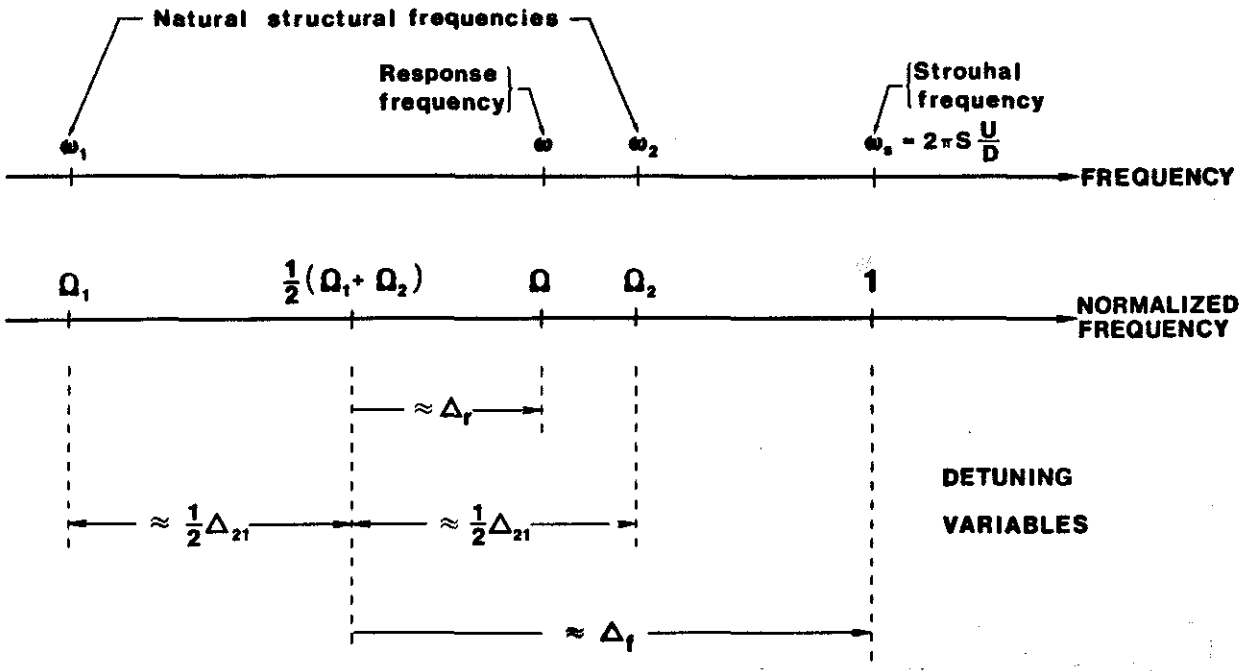

Figure 7.5.1. Interpretation of Δ–Variables

As indicated in Fig. 7.5.2, the solutions developed in Sections 5.6.2 and 5.6.3 must be pieced together to form the composite solution. Non-degenerate solutions are denoted "Plus" or "Minus" in reference to the quadratic formula (5.6.29), while degenerate solutions are denoted by "Type" as discussed in Sec-

---

two–mode case is analogous).

2. The approximations "≈" indicated in Fig. 7.5.1 are attributable to the $O(\varepsilon^2)$ difference between the Δ's and the d's [Eqs. (5.6.17)].
3. See the discussion concerning generic subscripts, Eqs.(4.1.10).

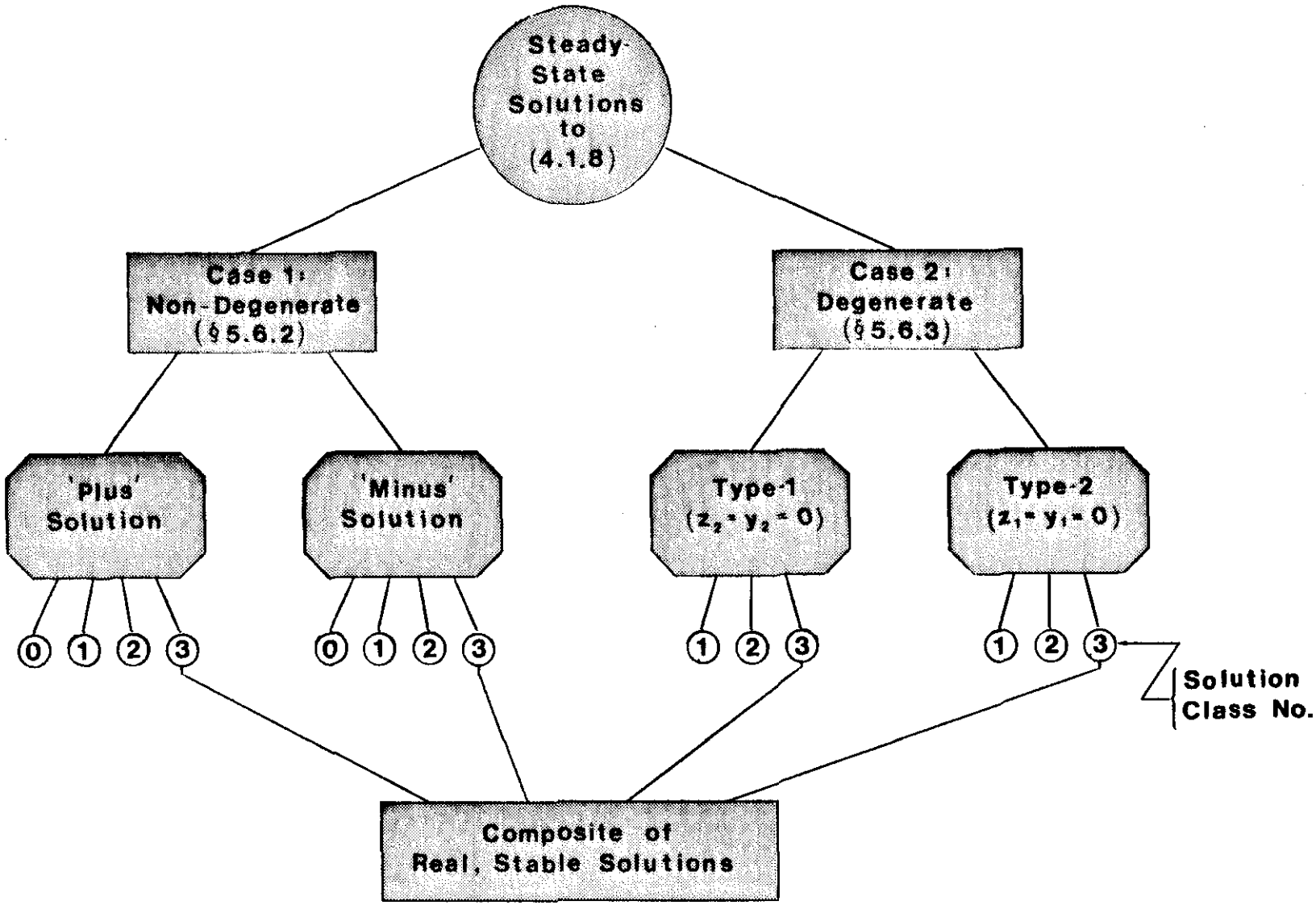

Fig. 7.5.2: Classification of Steady-State Solutions.

tion 5.6.1. Each kind of solution is further distinguished by its "Class," as discussed in Section 5.4.5 (applicable to the degenerate case) and again in Section 5.6.2.4 (applicable to the non-degenerate case). Solution Classes are indicated on plots as follows:

(0) *No line:* Frequency solution Δ_f not real (non-degenerate case only)

(1) *Short-dashed line:* Δ_f real but one or both amplitudes non-real

(2) *Long-dashed line:* Δ_f real and ampltidues real, but unstable

(3) *Solid line:* Real, stable solution.

Only Class (3) is physically meaningful, thus the composite steady-state solution is the union of Class (3) results.

7.5.2 Case 1: Non-Degenerate Solutions

Frequency response and structural amplitude response are plotted in Figures 7.5.3, 7.5.4, and 7.5.5 for Δ_{21} = 0.05, 0.10, and 0.20 respectively.[4] For each value of Δ_{21}, the "Plus" and "Minus" frequency solutions are plotted separately for clarity. However, for the parameters under consideration, "Plus" solutions are never Class (3), so the corresponding amplitude plots are omitted. "Minus" solutions are Class (3) over the segments $\overline{AB}$ and $\overline{EF}$, and additionally over the segment $\overline{CD}$ when the intermodal detuning Δ_{21} is large enough (Fig. 7.5.5). In each instance, points A–F on the frequency plot correspond respectively to those on the amplitude plots.

---

4. The arclength controls used to adjust the Δ_τ step size in Figs. 7.5.3–5, although similar to those described in Section 7.3.3, were not refined enough to capture all the details. In particular, the denominator κ_2 in Eq. (5.6.29) goes through zero near each of the values $\Delta_\tau = \pm\frac{1}{2}\Delta_{21}$. Therefore the long, dashed, horizontal lines on the frequency plots should properly extend to the edge of the graph; their truncation is attributable to the particular numerical algorithm used. On the other hand, the apparent vertical gaps in the frequency solution (e.g. Fig. 7.5.3a, near $\Delta_\tau = \frac{1}{2}\Delta_{21}$) are not attributable to oversized steps, but rather to the occurance of non-real frequency solutions [Class (0)].

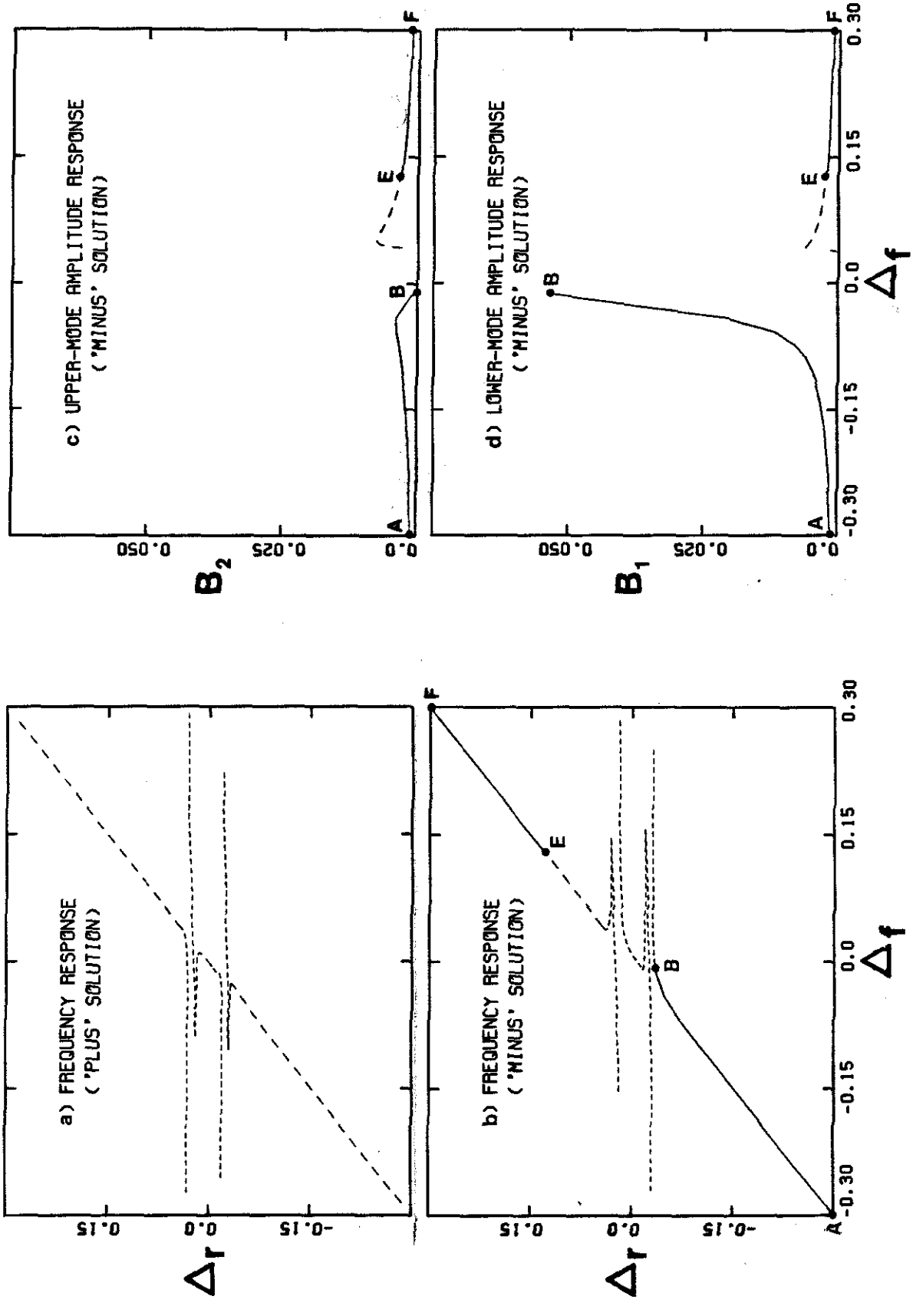

Fig. 7.5.3: Non-Degenerate Solutions, $\Delta_{21} = 0.05$.

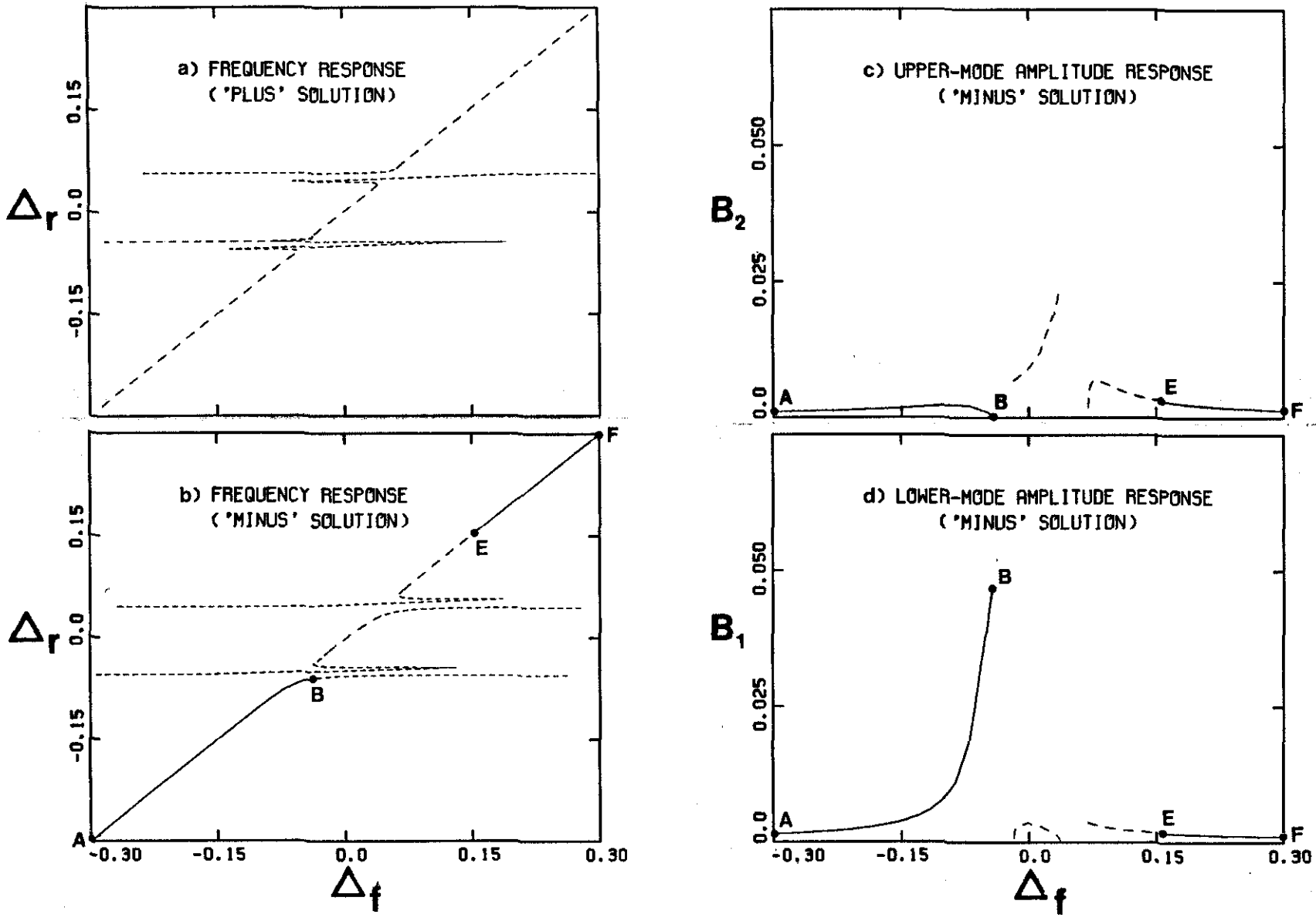

Fig. 7.5.4: Non-Degenerate Solutions, $\Delta_{21} = 0.10$.

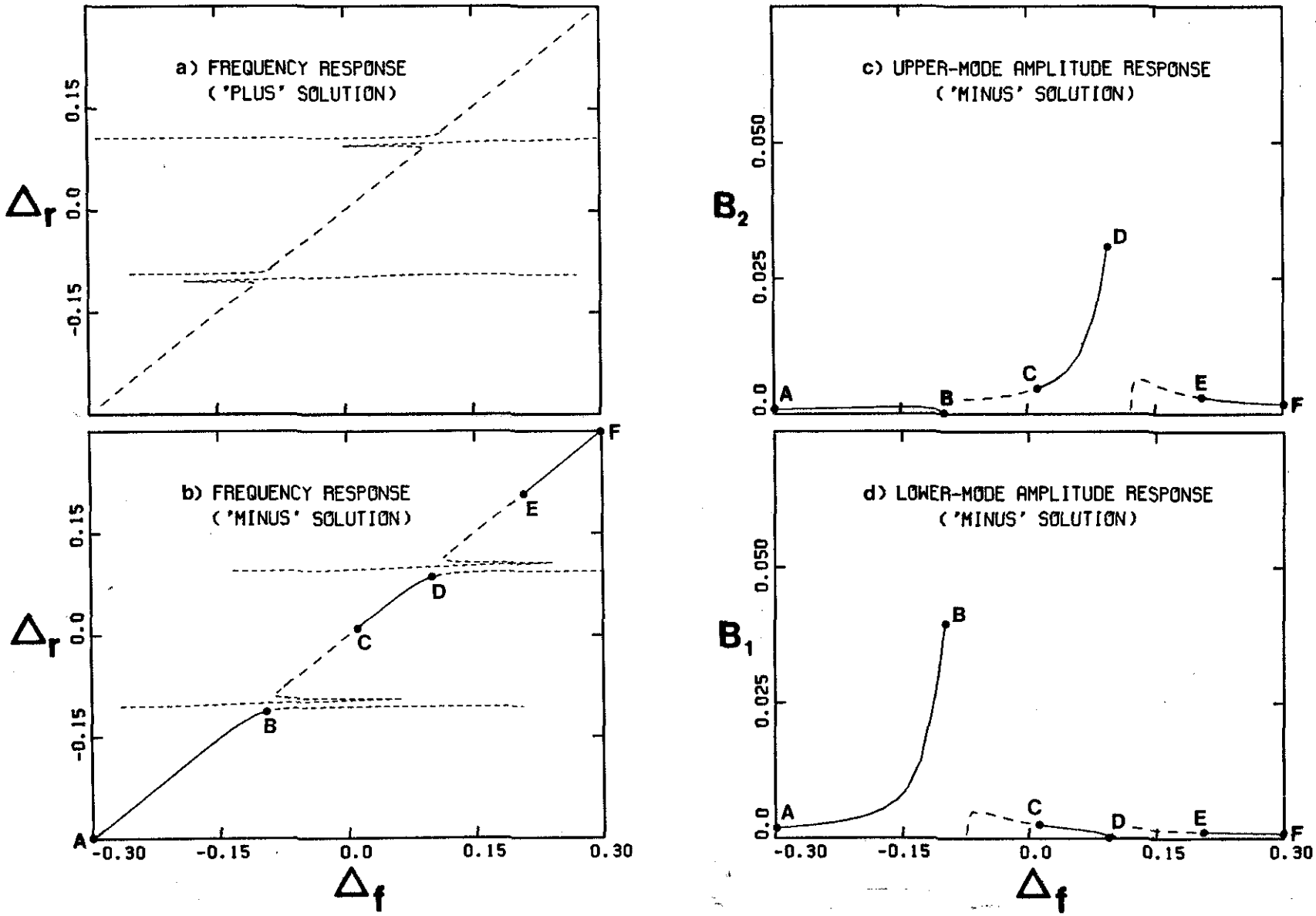

Fig. 7.5.5: Non-Degenerate Solutions, $\Delta_{21} = 0.20$.

Points B and D have a special significance. At B, the upper mode amplitudes B_2 and A_2 vanish,[5] so point B must represent the borderline between non-degenerate solutions and degenerate solutions of Type 1. Likewise, at D, the lower mode amplitudes B_1 and A_1 vanish, so point D must represent the borderline between non-degenerate solutions and degenerate solutions of Type 2. These observations will be discussed further in connection with the composite solution (Section 7.5.4).

For the set of parameters under consideration, non-degenerate solutions apparently do not exhibit lock-in to any great degree. This is by no means true in general; for alternative sets of models parameters, "locked-in" portions of the frequency solution have been found which are real and stable. Such solutions typically involve large amplitudes for one of the structural variables y_i and for *both* of the fluid variables z_i, which persist even for large values of the modal separation Δ_{21}. This is unacceptable from a physical viewpoint, since it is then impossible for the two-mode problem to resolve into two one-mode problems for large Δ_{21}, inasmuch as assumption (3.4.16) of the one-mode approximation is violated by one of the z_i. It is fortunate – or perhaps significant – that Parameter Set I, selected herein in accordance with experimental data, does not produce such physically unacceptable results.

7.5.3 Case 2: Degenerate Solutions

As for Case 1, frequency response and structural amplitude response for the degenerate case are plotted on Figs. 7.5.6, 7.5.7, and 7.5.8 for $\Delta_{21} = 0.05$, 0.10, and 0.20 respectively. In each instance, Type 1 and Type 2 frequency solutions are plotted on a single set of axes (similar to Fig. 5.6.3). As indicated by arrows, each frequency curve is truncated so as not to obscure the other, but the trun-

---

5. Referring to Eq. (5.6.5), A_i must go to zero whenever B_i does.

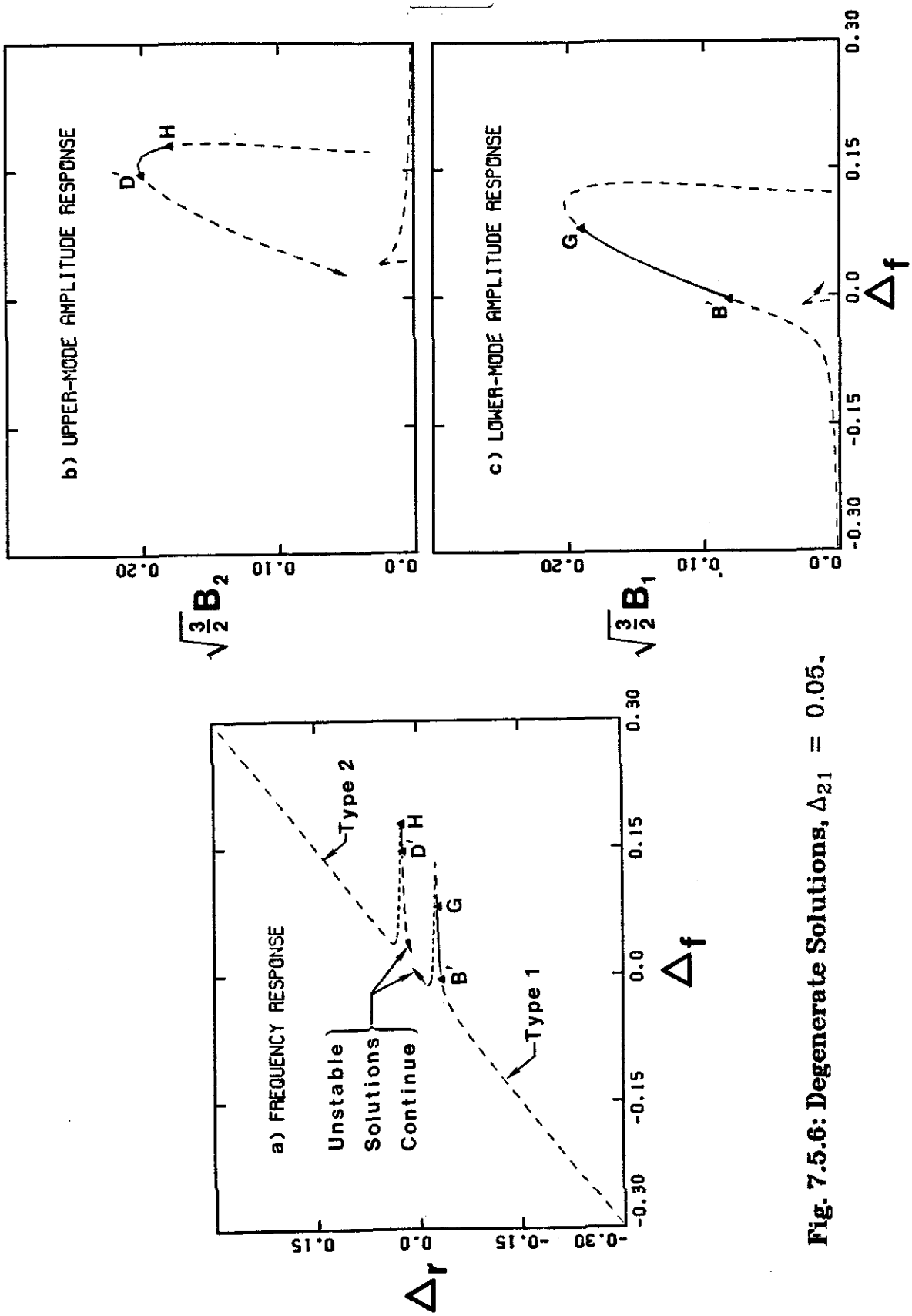

Fig. 7.5.6: Degenerate Solutions, $\Delta_{21} = 0.05$.

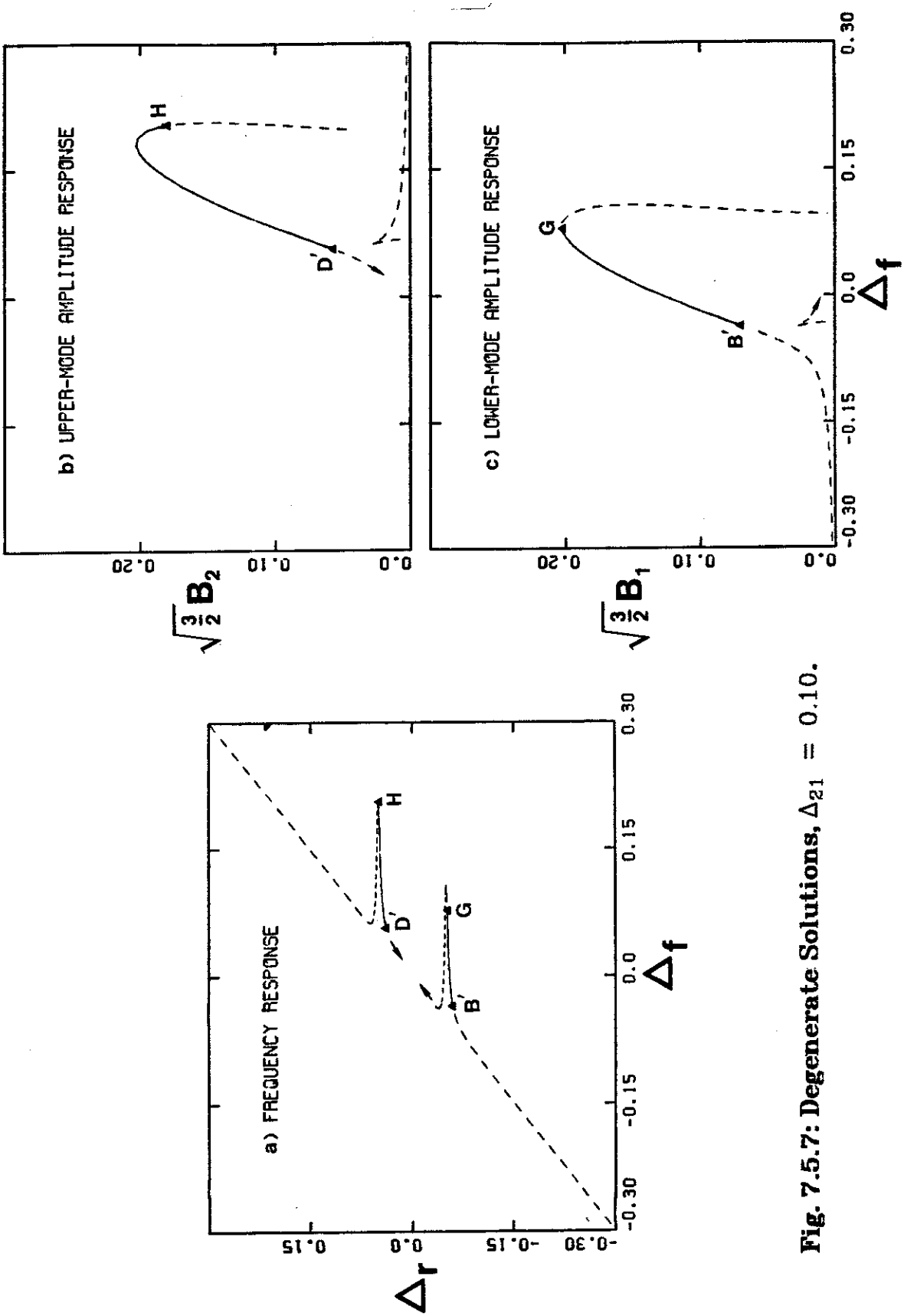

Fig. 7.5.7: Degenerate Solutions, $\Delta_{21} = 0.10$.

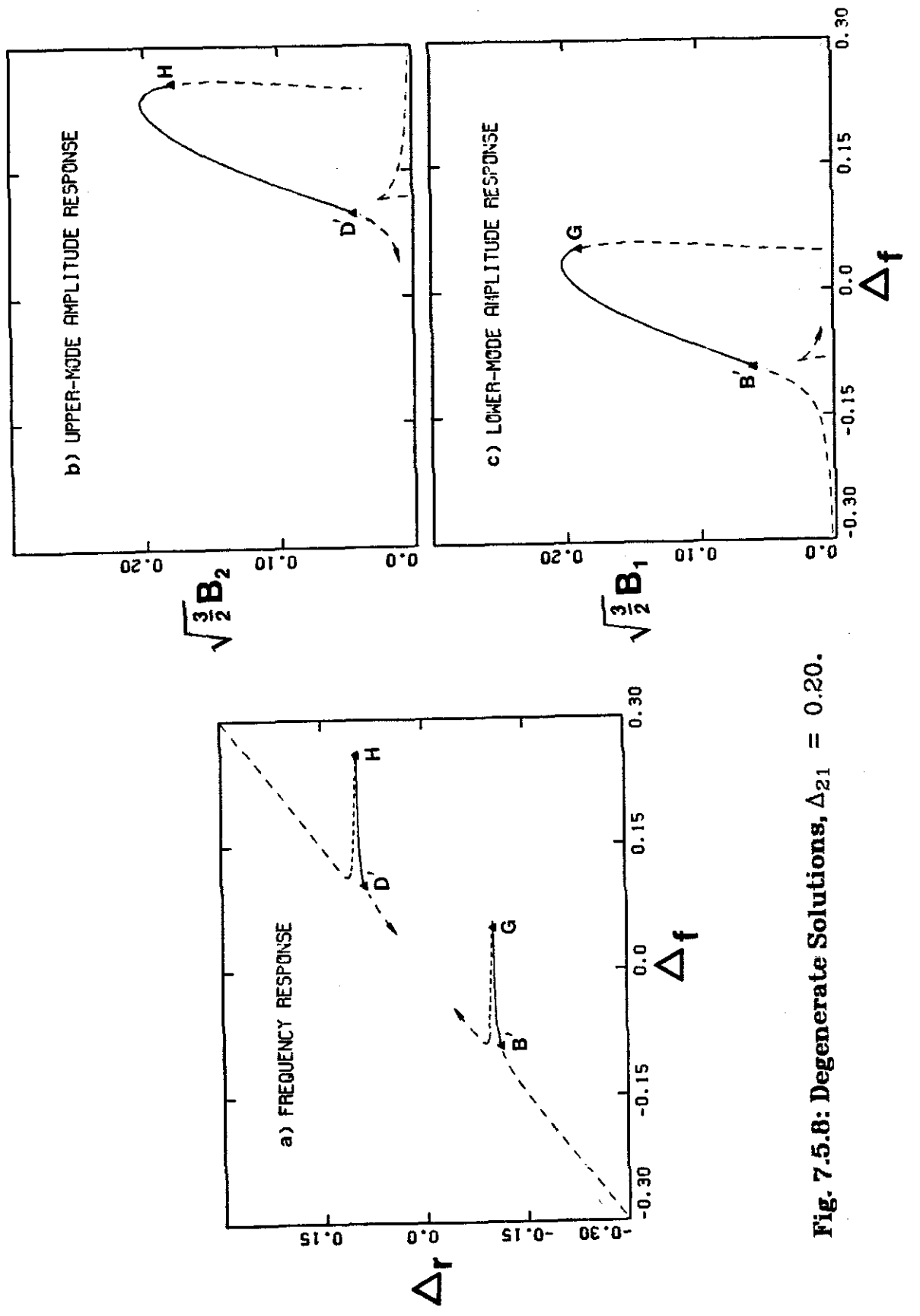

Fig. 7.5.8: Degenerate Solutions, $\Delta_{21} = 0.20$.

cated portions contain only unstable solutions. The Type 1 solution generates an amplitude curve for B_1 (plot c of each Figure), while Type 2 generates a curve for B_2 (plot b of each Figure).[6] Apparently, real stable solutions [Class (3)] occur for the degenerate case only in the locked-in segments $\overline{B'C}$ and $\overline{D'H}$. It is clear that these lock-in bands are suppressed as the modal separation Δ_{21} decreases; the presence of the upper mode causes instability of the right end of the mode-1 lock-in band, and likewise, the presence of the lower mode causes instability of the left end of the mode-2 lock-in band.

7.5.4 Composite Solutions

By piecing together the Class (3) results from Figs. 7.5.3–7.5.8, the composite solutions shown in Figs. 7.5.9–7.5.11 are obtained, with lettered points corresponding to the previous Figures. Although not shown, similar composite graphs might be constructed for the structural amplitudes.

The frequency composites reveal certain features of modal interaction:

- *Complex solutions for small values of* Δ_{21}. In Fig. 7.5.9 ($\Delta_{21} = 0.05$), the suppression of lock-in bands discussed above is evident. As a result, in the range of Δ_f between points C and E, no solution of the assumed form (5.6.1) exists, thus some other, more complex form of solution must prevail. An example of such a solution is given in Section 7.5.4.

- *Lock-in overlap for intermediate values of* Δ_{21}. In Fig. 7.5.10 ($\Delta_{21} = 0.10$), a hysteresis loop involving both lock-in bands appears. Thus, for intermediate values of modal separation, the model predicts the possibility of lock-in for both modes at the same value of flow

---

6. The factor of $\sqrt{\frac{3}{2}}$ appearing on the axis scales is that discussed in Section 5.5. The computer code which generated the amplitude plots was adapted from a routine originally written for rigid cylinders; the amplitude scaling by $\sqrt{\frac{2}{3}}$ was neglected in the plotting.

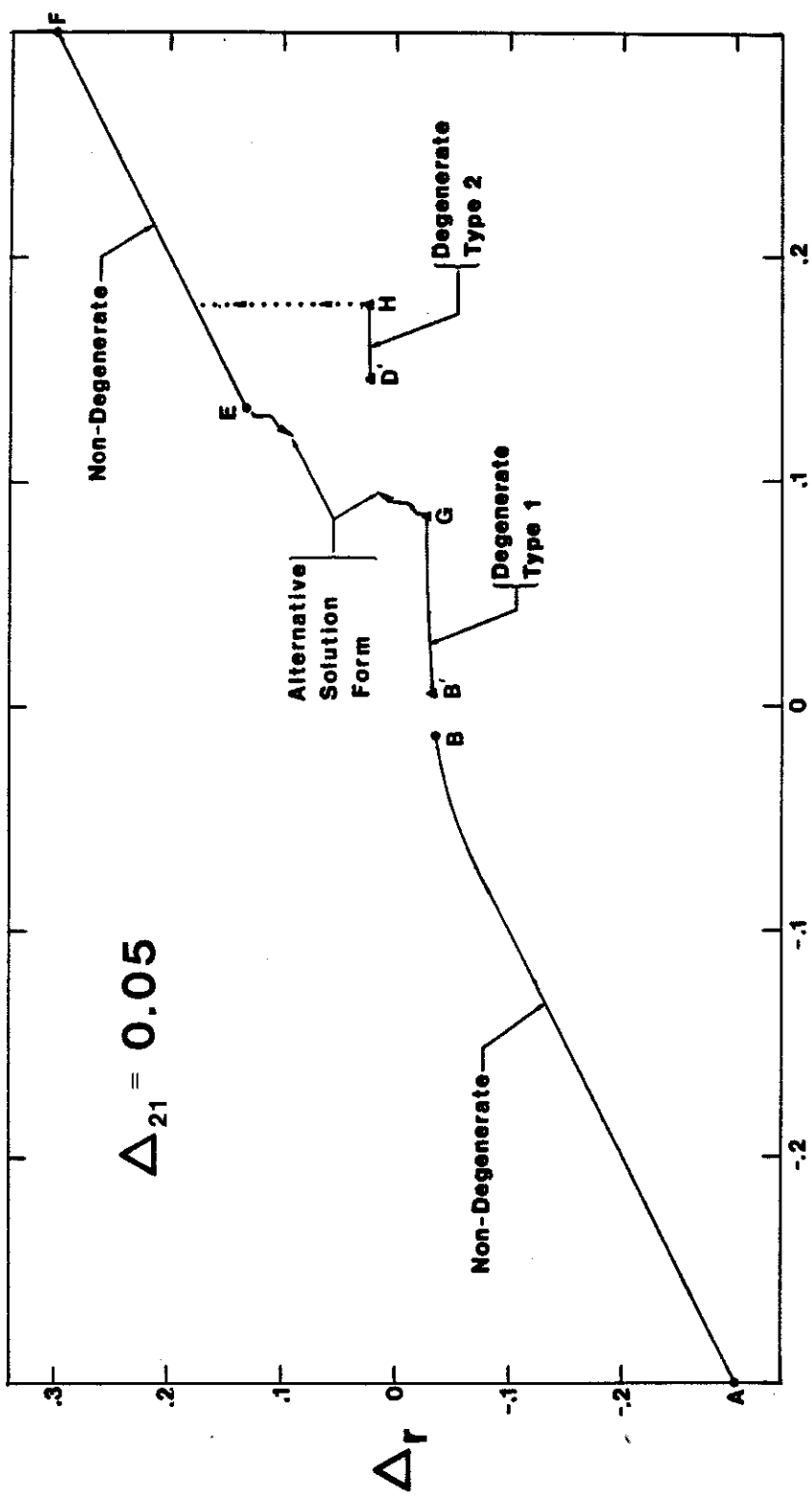

Fig. 7.5.9: Composite Solution, Δ_{21} = 0.05.

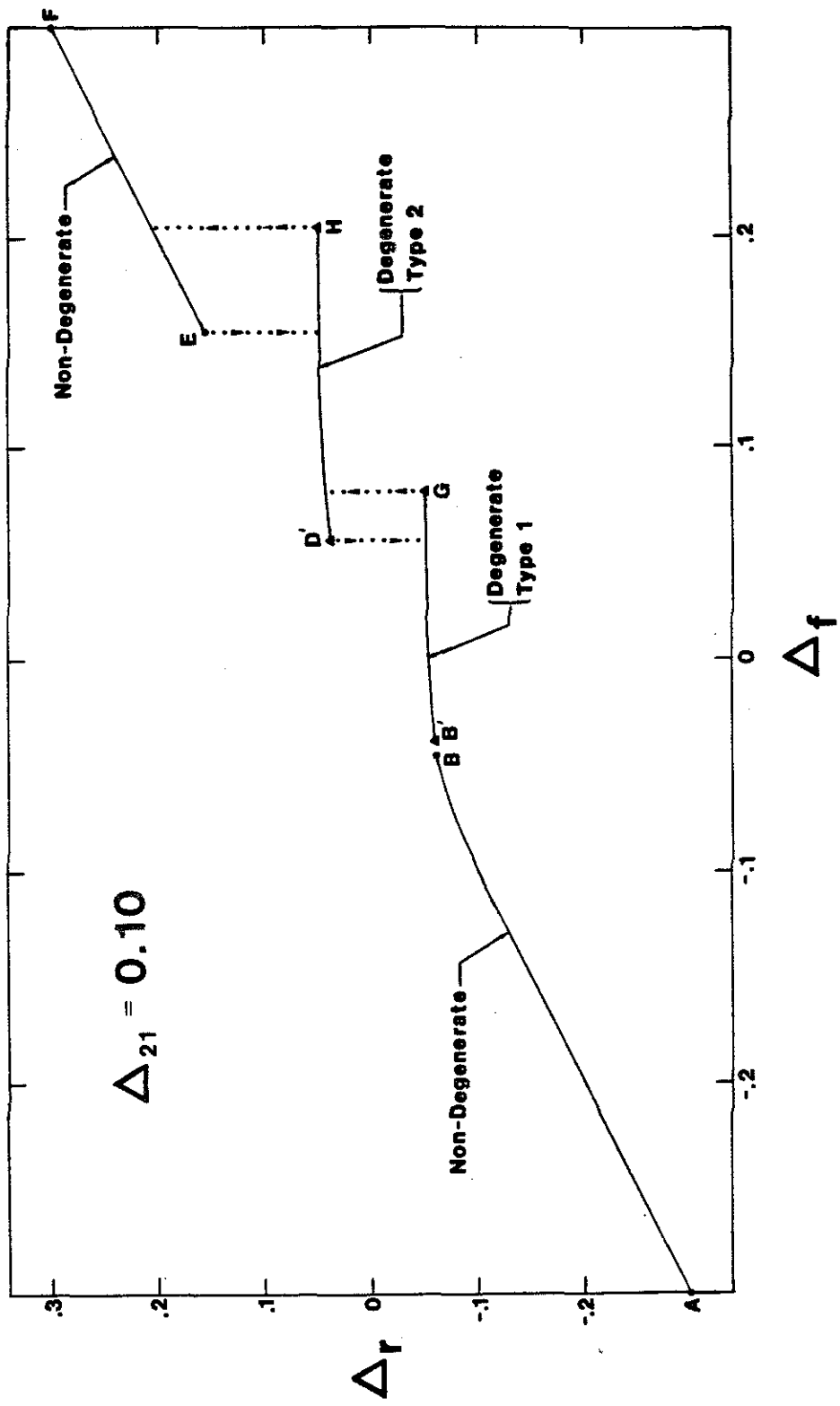

Fig. 7.5.10: Composite Solution, $\Delta_{21} = 0.10$.

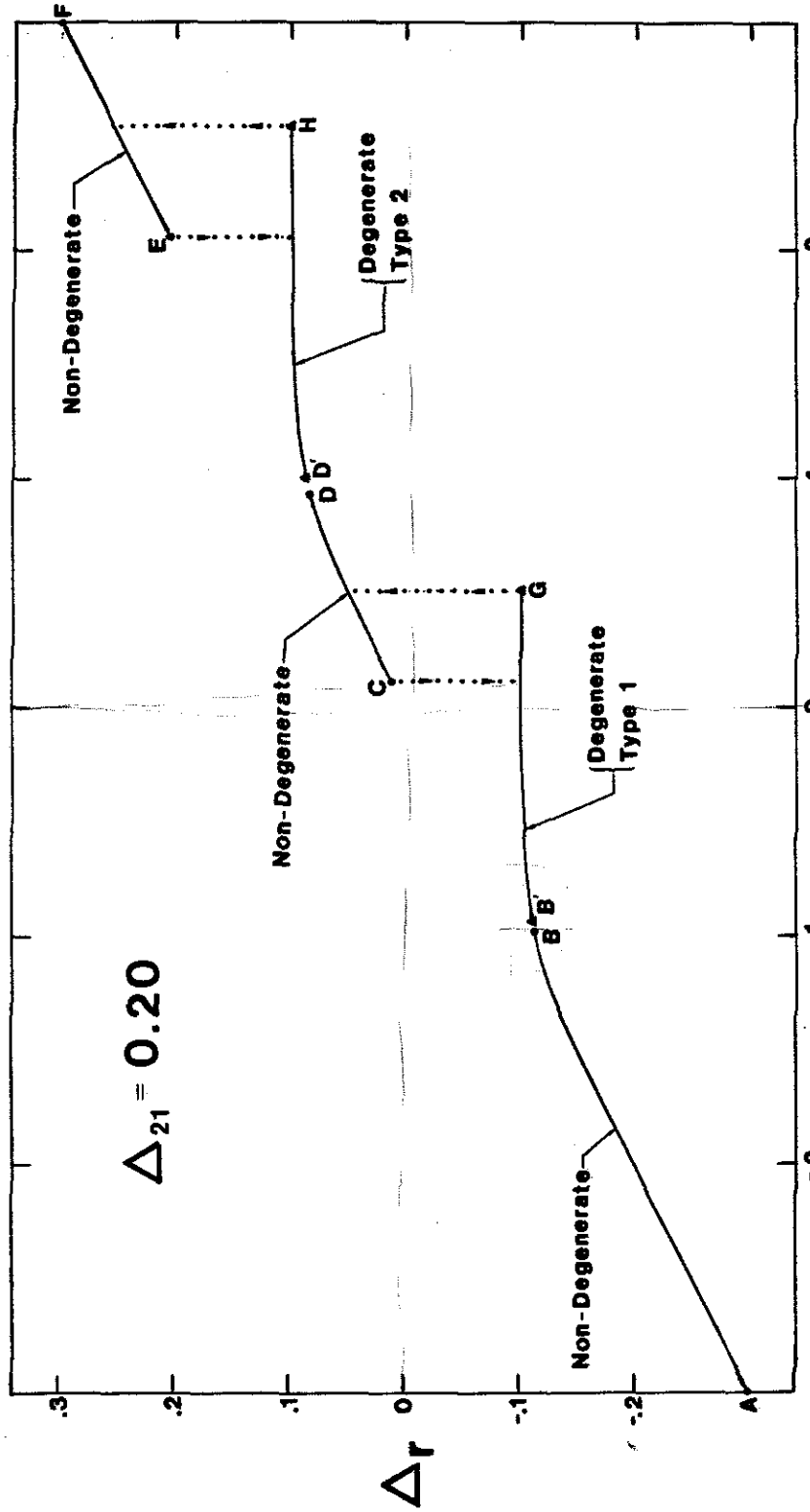

Fig. 7.5.11: Composite Solution, $\Delta_{21} = 0.20$.

speed (Δ_f); one mode or the other prevails depending on initial conditions. This result is qualitatively similar to the experimental observations discussed in Section 2.5.6, where lock-in "drifted" between modes 8 and 9 despite a virtually constant flow speed. It is quite possible that, in this crude experiment, various "initial conditions" were imposed randomly by factors not under strict experimental control (e.g. extraneous air currents).

- *Resolution of the two-mode problem into two one-mode problems for large values of* Δ_{21}. In Fig. 7.5.11 ($\Delta_{21} = 0.20$), the two modes are well separated, there is an intervening "dead-band" between them, and each of the hysteresis loops is similar to that discussed previously for the one-mode case (Section 7.5.3). Again, this result resembles experimentally observed behavior of the lower modes having larger Δ_{21}, for example modes 6 and 7 discussed in Section 2.5.5.

It is clear that non-degenerate and degenerate solutions "fit together" at points $B-B'$ and $D-D'$. This makes perfect sense since, as previously noted (Section 7.5.2), the "non-degenerate" solutions at B ad D are in fact borderline-degenerate. Thus B and D are bifurcation points. But what are the small gaps between B and B' and between D and D'? Ideally there should be no gaps; $B-B'$ should be a single point, as should $D-D'$. The gaps are attributable to the fact that the analysis which obtained points B and D (Section 5.6.2) is entirely different from that which obtained points B' and D' (Section 5.6.3). In particular, points (B, D) arise from the asymptotic method, which includes certain order-ε approximations, while points (B', D') arise from a direct perturbation of the differential equations and a stability analysis based on Floquet theory, which include only some of these approximations. Thus, the "primed" points are

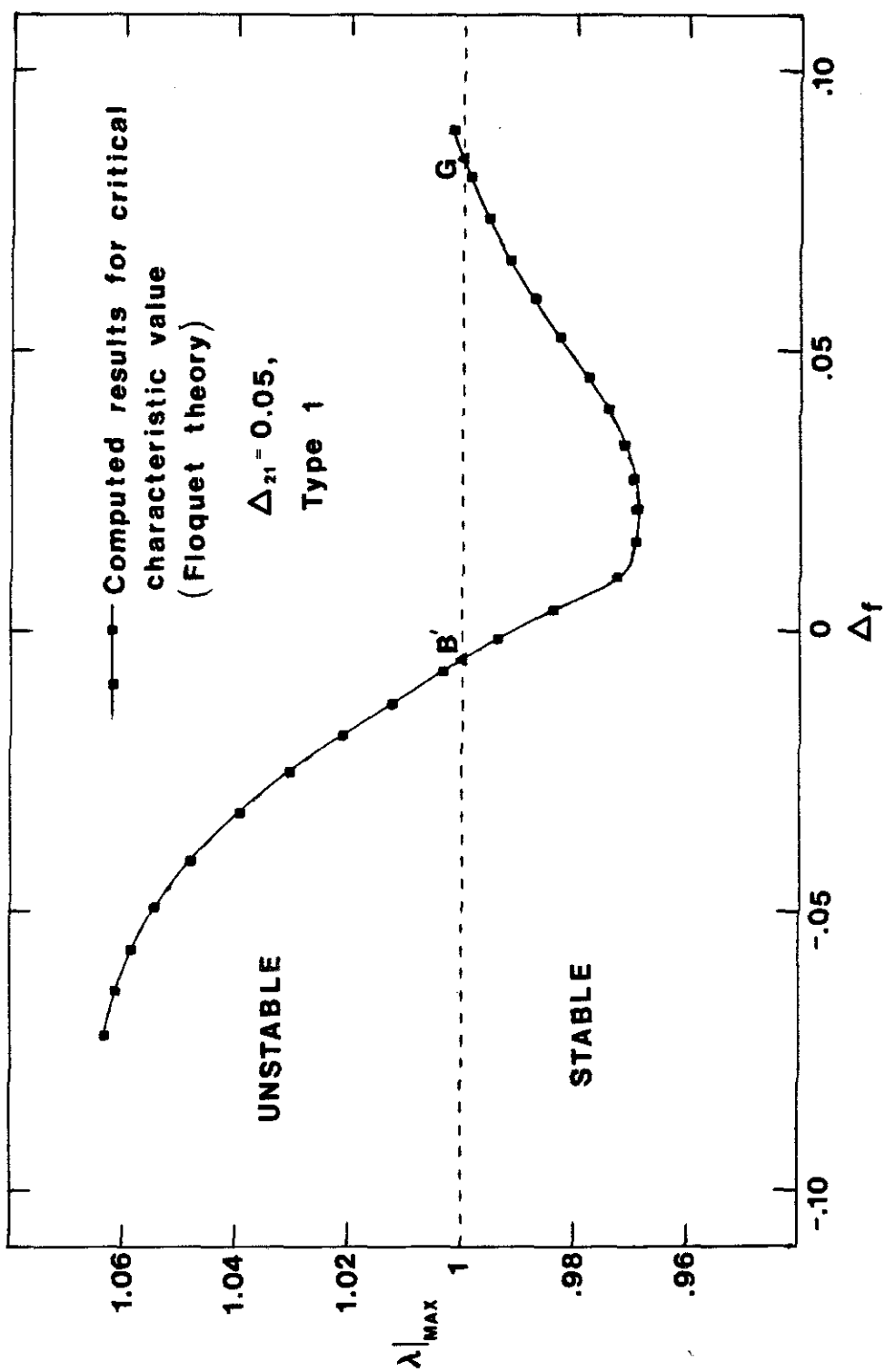

Fig. 7.5.12: Typical Eigenvalue Behavior for Degenerate Solutions.

probably more accurate, but this speculation is uncertain. As exemplified by Fig. 7.5.12, the largest modulus of the eigenvalues arising from Floquet theory (Section 5.6.3.5) is very close to the critical value $|\lambda| = 1$, such that numerical error in the integration routine used to obtain the matrix $X(T)$ may be a factor in determining the precise location of the stability boundaries B' and D'.[7]

Fig. 7.5.13 is a map of the composite solutions, which has been obtained by computing the various boundaries B, B', G, C, D, D', H, E for a number of values of Δ_{21}. Thus, the lettered points at $\Delta_{21} = 0.20$ correspond to those on Fig. 7.5.11. Non-degenerate solutions exist in the three shaded regions, while degenerate solutions exist in the hatched regions. The white gaps between the $B-B'$ boundaries and between the $D-D'$ boundaries are artificial, as discussed in the previous paragraph. On the other hand, the large white area is real; in this region the differential equations fail to admit simple-harmonic solutions of any sort, as mentioned previously in connection with Fig. 7.5.9. Overlapping regions indicate hysteretic behavior; in particular, lock-in overlap occurs in the region where Type 1 and Type 2 degenerate solutions coexist. The lettered points $T_1, \ldots, T_4$ are test points for numerical solutions, as discussed in Section 7.5.4.

The phenomenon of lock-in suppression, particularly of the upper mode,[8] is clearly displayed by the solution map. Lock-in suppresion has two effects: first, it reduces the extent of lock-in overlap, and second, it gives rise to the region of complex solutions (the white region of Fig. 7.5.13), discussed above.

Decomposition of the two-mode problem into two one-mode problems at large

---

7. Double precision (IBM 370) was used exclusively in the numerical work. Numerical integrations were performed with the Adams–Moulton predictor–corrector method, with starting values obtained by the method of Runge–Kutta–Gill. This routine incorporated automatic step–size refinement to control the local truncation error. The tolerance for this error was set at 10^{-5}.
8. This asymmetry is attributable to the same factor which causes the skewness of lock-in bands, namely, $k_a \neq 0$.

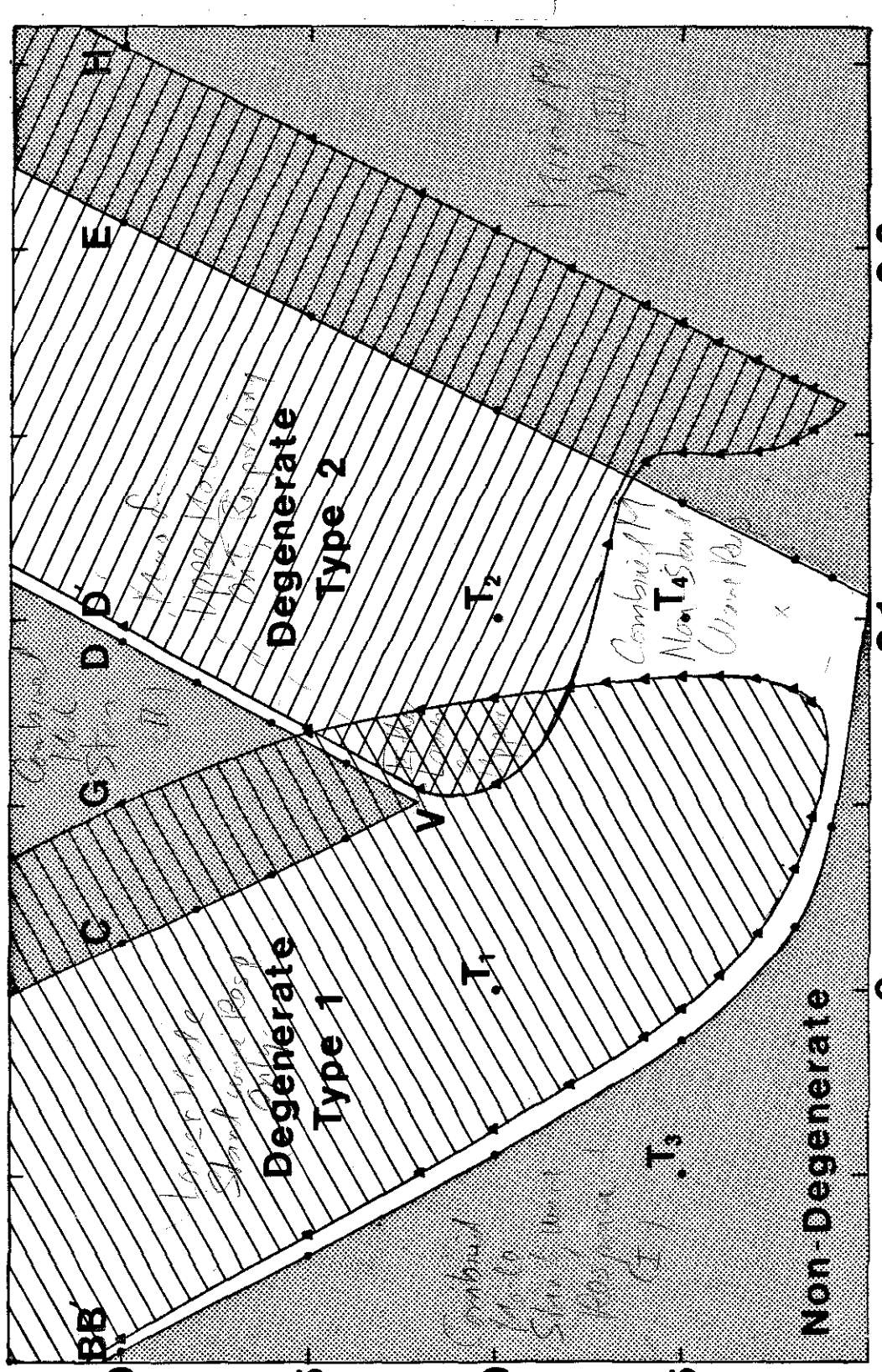

Fig. 7.5.13: Composite Solution Map.

values of Δ_{21} is also depicted by the solution map. The shaded, triangular "wedge" of non-degenerate solutions near the center of the map represents the "dead" area between modes, where both structural amplitudes B_i are relatively small (cf. Figs. 7.5.5c,d and Fig. 7.5.11). Thus the two modes are "well-separated" – and hence the one-mode approximation is adequate for each – if Δ_{21} is sufficiently large that this wedge is intersected during a traverse of the flow-speed variable Δ_f.[9] *Thus the value of modal separation Δ_{21} at the vertex V may be regarded as the minimum value for which the one-mode approximation is permissible.* The location of this point will of course vary with the parameters which have been fixed throughout this Section, notably the mass ratio η and the structural damping ratios ζ_i.

7.5.5 Numerical Checks

As previously indicated in Fig. 7.1.1, the mathematical analysis of Chapters 4 and 5 may be checked by solving the differential equations (4.1.8) numerically. In Figs. 7.5.14–7.5.17, such solutions are shown for four combinations of (Δ_f, Δ_{21}), as itemized in Table 7.5.1. These test points have been selected to represent the four types of solution predicted analytically by the composite solution map, Fig. 7.5.13.

Table 7.5.1: Test Points for Numerical Solution

Figure	Δ_f	Δ_{21}	*Point on Fig. 7.5.13*	*Analytical Prediction*
7.5.14	0	0.10	T_1	Degenerate, Type 1
7.5.15	0.10	0.10	T_2	Degenerate, Type 2
7.5.16	-0.05	0.05	T_3	Non-Degenerate
7.5.17	0.10	0.05	T_4	Not Simple Harmonic

9. Solutions in the "degenerate" regions of Fig. 7.5.13 are *precisely* those of the one-mode approximation, while solutions in the "non-degenerate" regions differ somewhat, since the other mode is participating.

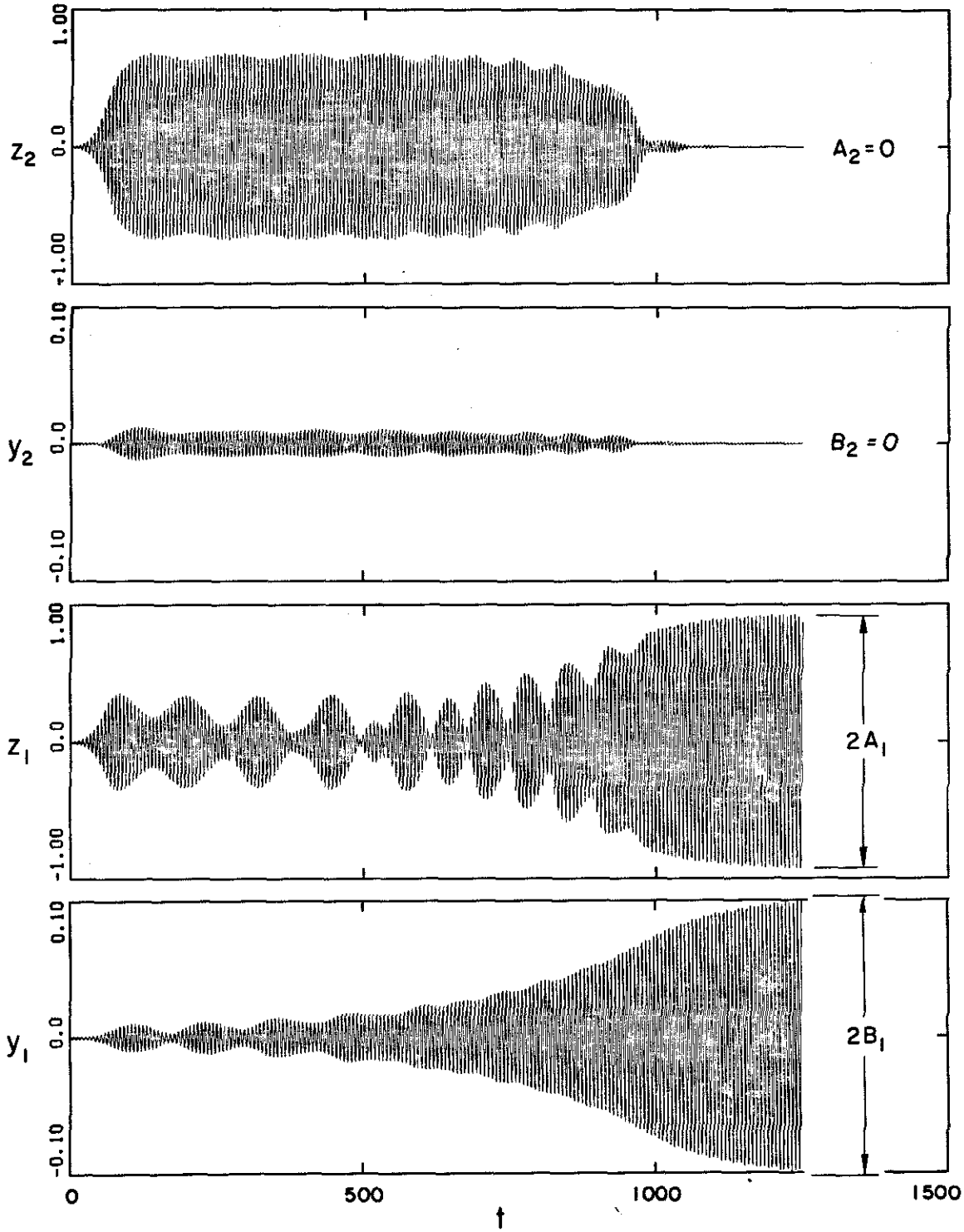

Fig. 7.5.14: Numerical Solution vs. Asymptotic Prediction for Test Point T_1.

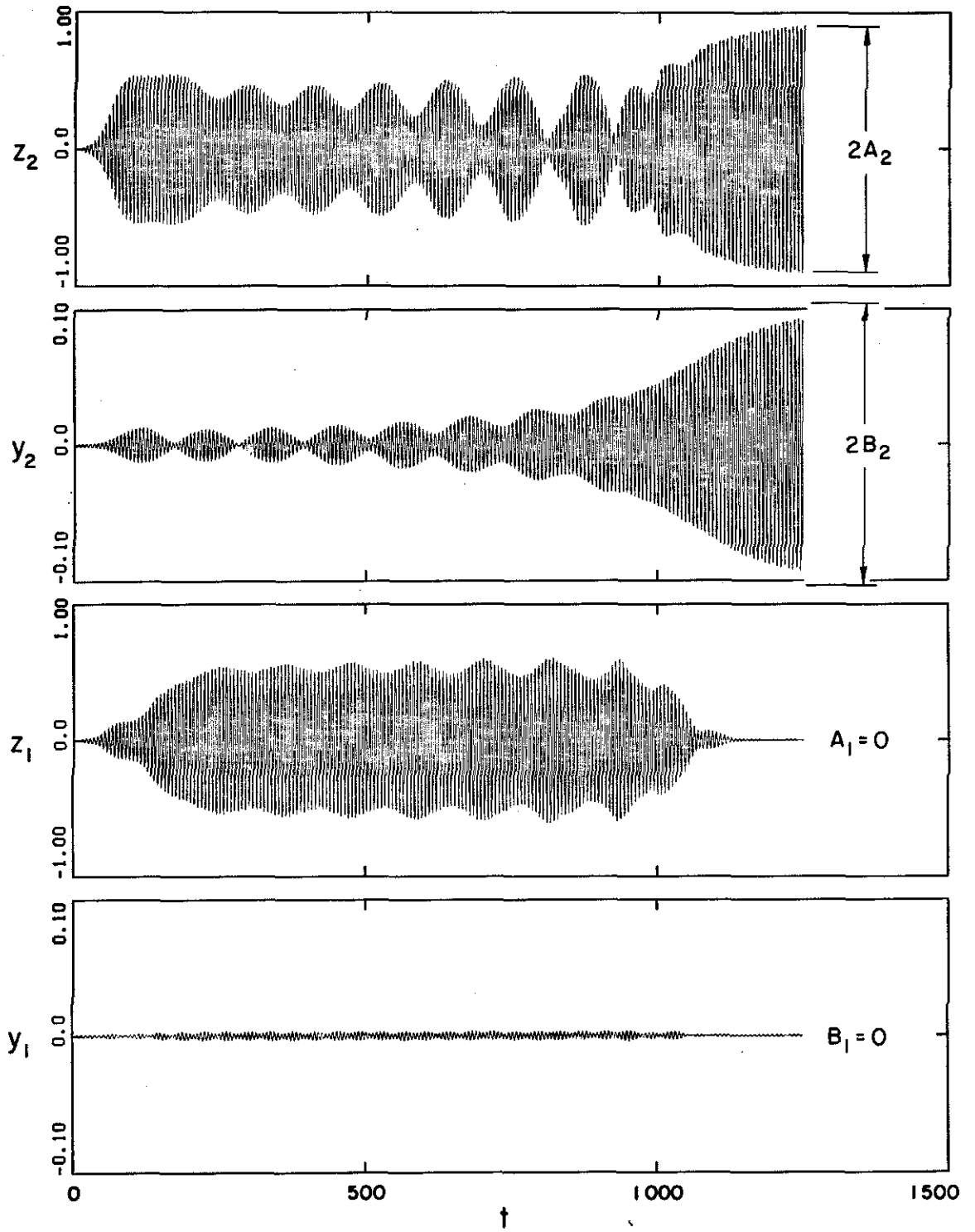

Fig. 7.5.15: Numerical Solution vs. Asymptotic Prediction for Test Point T_2.

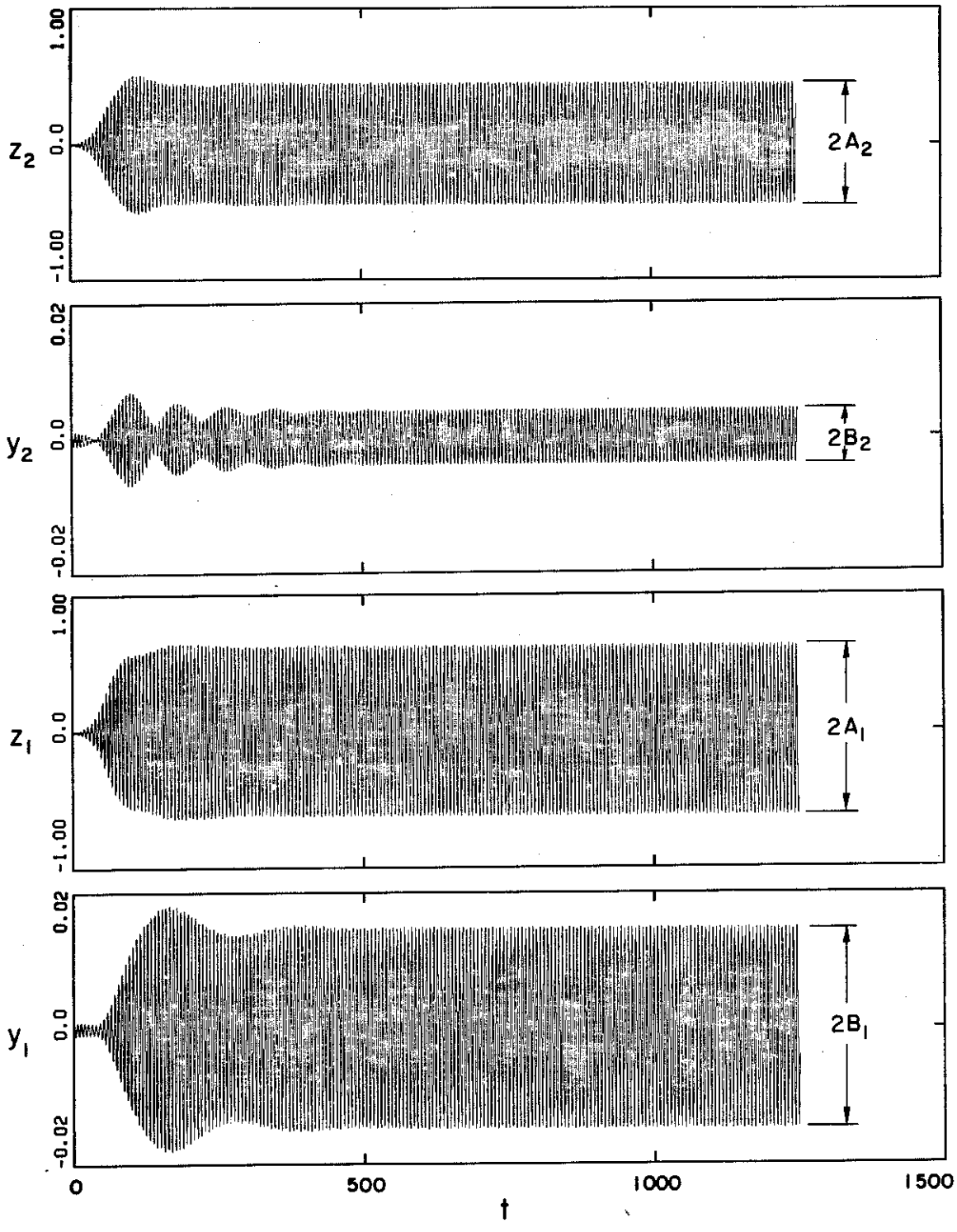

Fig. 7.5.16: Numerical Solution vs. Asymptotic Prediction for Test Point T_3.

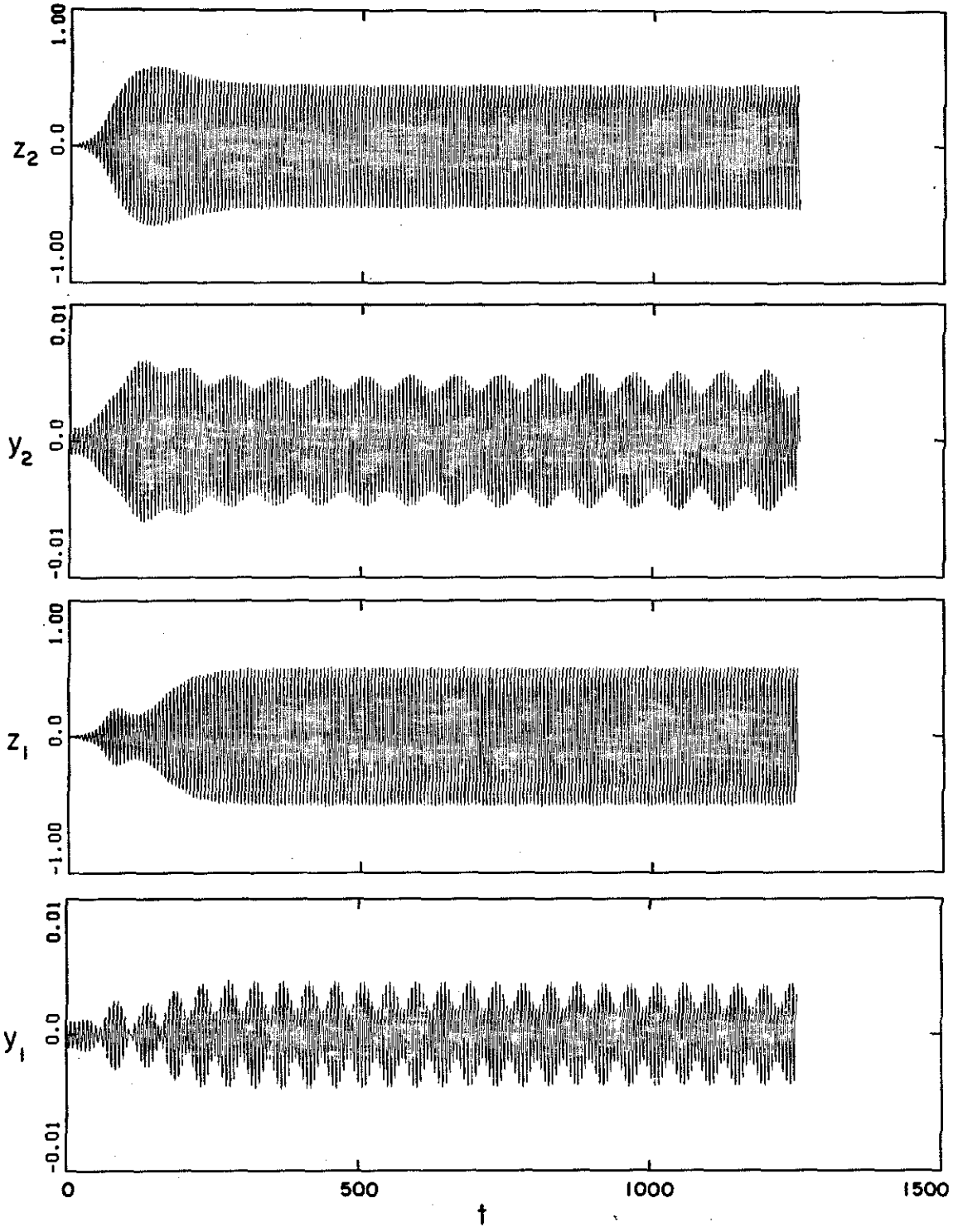

Fig. 7.5.17: Numerical Solution for Test Point T_4.

The numerical solutions are plotted for $0 < t < 1250$, each integration starting from the perturbed rest state

$$z_1(0) = z_2(0) = y_1(0) = y_2(0) = 0.001 \tag{7.5.2a}$$

$$\dot{z}_1(0) = \dot{z}_2(0) = \dot{y}_1(0) = \dot{y}_2(0) = 0. \tag{7.5.2b}$$

Footnote 7 of Section 7.5 describes the details of the numerical integration procedure, except that the local truncation error tolerance was set to 10^{-4} in this case. The time step for the plots is $\Delta t = 0.5$; thus, since $\Omega = 1 + 0(\varepsilon)$, there are approximately 12 points plotted per cycle.

In Figs. 7.5.14–7.5.16, the steady-state amplitudes (A_i, B_i) predicted by the asymptotic method are given at the right of each plot. Clearly, the analytical predictions are very good – qualitatively, each solution is of the type predicted by Fig. 7.5.13, and quantitatively, the amplitude predictions are accurate. The quantitative agreement is somewhat surprising, since Parameter Set I produces $r = 0.7398$, $\tilde{r} = 1.156$, $p = 0.405$, and $q = 0.810$, which violate the order-ε assumption (4.1.9). Apparently, the asymptotic method continues to perform well in spite of this.

As predicted by the steady-state stability analysis, the solution shown in Fig. 7.5.17 is not simple harmonic. Although the steady-state equations yield no further information for such a case, the asymptotic method itself, prior to the assumption of steady state, *does* yield such information, as shown by Fig. 7.5.18. The latter Figure was obtained by numerical integration of the amplitude/phase equations (4.3.19), with initial conditions

$$A_1 = A_2 = B_1 = B_2 = 0.001 \tag{7.5.3a}$$

$$\mu_1 = \mu_2 = \varphi = 0, \tag{7.5.3b}$$

which are the amplitude/phase equivalents of (7.5.2). Envelope plots were

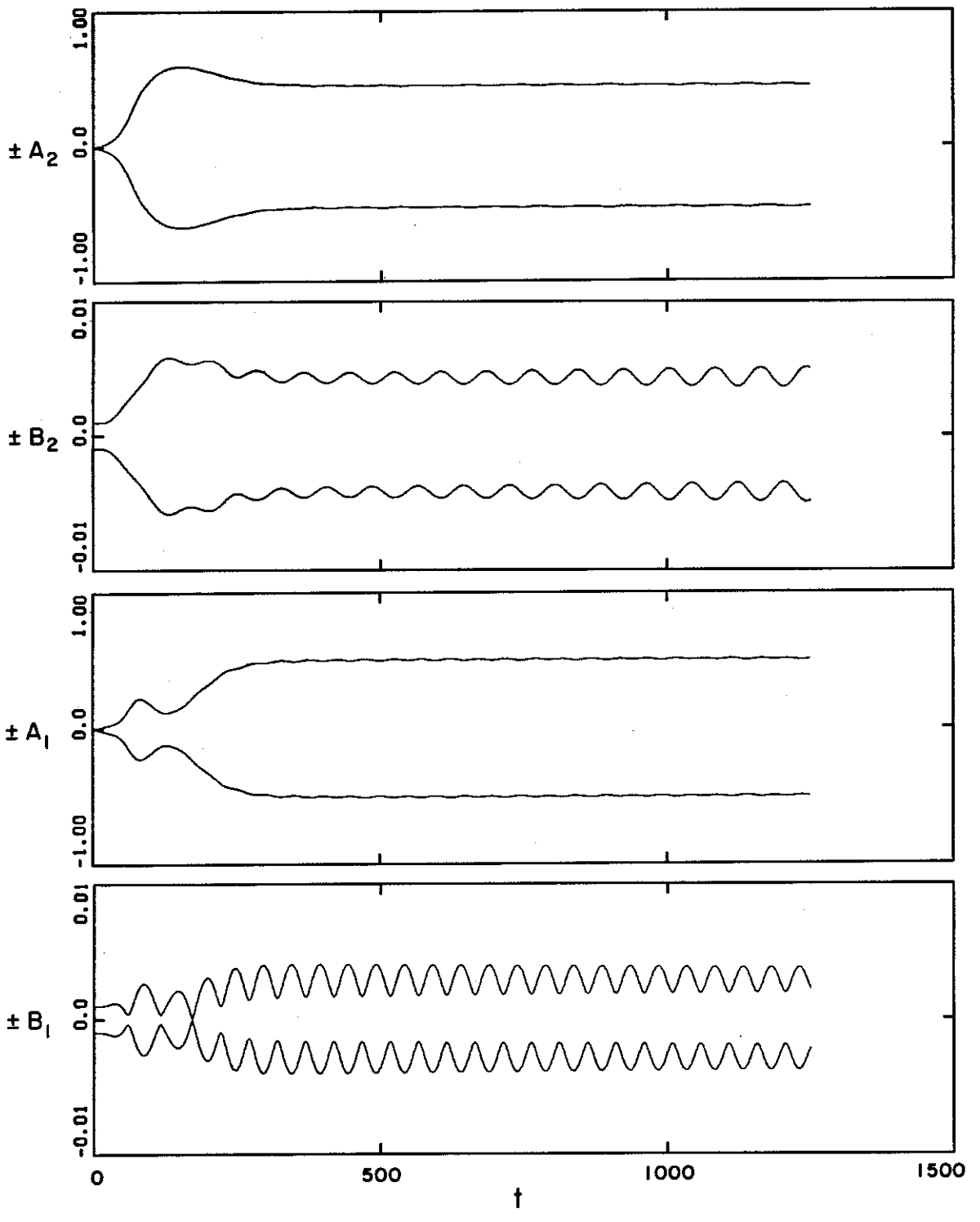

Fig. 7.5.18: Asymptotic Prediction for Test Point T_4 (compare to Fig. 7.5.17).

produced by plotting $\pm A_i(t)$ and $\pm B_i(t)$, as indicated on the vertical axes.

Comparison of Fig. 7.5.18 to Fig. 7.5.17 reveals that the asymptotic method continues to predict accurately even when the solution is not steady-state. On account of order-ε approximations in the asymptotic method, the comparison is of course not perfect; for example, the predicted number of envelope maxima for each of the y_i (Fig. 7.5.18) is slightly lower than the actual number (Fig. 7.5.17). However, if such inaccuracies are acceptable, the asymptotic results are very valuable in such cases, since an integration such as Fig. 7.5.18 is computationally far less costly than Fig. 7.5.17.

CHAPTER VIII

SUMMARY AND CONCLUSIONS

8.1 Overview

In this investigation, vortex-induced structural oscillations have been considered using a semi-empirical modeling approach, the results of which have been compared to experimental data. In the Introduction, the mechanisms of vortex-shedding and lock-in have been discussed from a physical viewpoint, and attention has been focused on three types of structures having circular cross-section, including forced and spring-mounted rigid cylinders, as well as taut elastic cables.

The development of the thesis, diagrammed by Fig. 7.1.1 above, has proceeded in a parallel fashion for these three types of structures, but the emphasis throughout has been on elastic cables, and particularly on the associated problem of modal interaction.

8.2 Synopsis of Chapter 2

Experimental results have lead to several conclusions regarding the nature of lock-in, all of which may be understood in terms of the mathematical model developed in later Chapters:

- For circular cylinders, lock-in is somewhat different if the structural vibrations are externally forced rather than vortex-induced: forced vibrations produce lock-in bands symmetrically disposed about resonance (Fig. 2.3.1), while vortex-induced vibrations produce lock-in bands skewed entirely to the right side of resonance (Fig. 2.4.1).[1]

1. Skewness of lock-in bands depends on other factors as well, notably the structure's cross sectional shape. For example, lock- in for spring- mounted, D- section cylinders is skewed almost entirely to the *left* side of resonance, in direct contrast to

- For lower modes of elastic cables, lock-in occurs as for a spring-mounted cylinders (Fig. 2.5.4, modes 6 and 7).
- For higher modes of elastic cables, lock-in overlap exists, in which either of two modes may prevail depending on initial conditions. (Fig. 2.5.4, modes 8 and 9).

8.3 Synopsis of Chapter 3

A mathematical model for vibrations of vortex-shedding structures has been developed. The model contains a series of bold assumptions which succeed in reducing the complex flow problem to a tractable form, but which are hardly rigorous. Moreover, there are a half-dozen empirical constants in the model whose numerical values must be determined by comparison to experimental data. Nevertheless, the differential equations generated by the model may be regarded as prototype nonlinear systems for studying the physical processes involved.

As summarized by Table 3.5.1, the model yields a pair of coupled, nonlinear oscillator equations for spring-mounted cylinders, which reduce to a single equation for forced cylinders, and generalize, using modal decomposition, to an infinite set of coupled equations for elastic cables (one pair per mode). The infinite set of equations for cables have been truncated to one pair (the one-mode approximation) and to two pairs (the two-mode approximation) based on a physical understanding of lock-in and modal participation. One of the goals of the ensuing analysis has been to assess the validity of such finite-mode approximations by a comparison of one-mode and two-mode results.

---

circular cylinders [16]. The present model cannot explain this, since the only parameter in the model which depends on cross-sectional shape is the Strouhal number S, but variation of S does not change the sign of k_e; see item 2 of Section 8.6.

8.4 Synopsis of Chapter 4

The introduction of order-ε approximations has permitted the development of generalized model equations (4.1.8), which contain each of the problems of interest as a special case (Table 4.1.1). Moreover, Eqs. (4.1.8) are amenable to analysis by well-known asymptotic methods, one of which is described in Section 4.2. In this method, each of the structural variables y_i and fluid variables z_i is assumed to perform sinusoidal oscillations with slowly varying amplitude and phase. The result of the analysis is a set of first order differential equations for the amplitudes and phases, Eqs. (4.3.19).

8.5 Synopsis of Chapter 5

The steady state has been assumed for the structural and fluid oscillators, thereby reducing the nonlinear differential equations (4.3.19) to nonlinear algebraic equations (5.2.5). The latter equations have been specialized to the various structures of interest; the two-mode approximation involves the full set of equations. In each case, the algebraic equations have been solved analytically, and the stability of steady-state solutions has been investigated. These analyses have led to a number of observations, cataloged below.

A. Forced cylinder:

1. *Mathematical analog of lock-in.* For the forced case, monofrequency oscillations automatically satisfy the condition (2.3.1) for forced lock-in. Thus, boundaries of stability for the assumed solution form are the model analogs of experimentally observed lock-in boundaries. In agreement with experiment, the stability boundaries are found to be symmetric about resonance, irrespective of model parameter values.

2. *Lock-in band-width.* Band-width increases with forcing amplitude, a

dependence which is made more explicit in Chapter 6.

B. Spring mounted cylinder:

1. *Mathematical analog of lock-in.* For induced oscillations, monofrequency solutions do not necessarily satisfy the condition (1.4) for lock-in; condition (1.3) may be satisfied instead. Thus, from a mathematical viewpoint, lock-in for spring-mounted cylinders is not delimited by stability boundaries (as in the forced case) but by the peculiar shape of the frequency respsonse curve. This calls for a special definition to define uniquely the endpoints of the lock-in band; see item 2 of Section 8.6.

2. *Lock-in symmetry and band-width.* Steady-state solutions and stability depend on two groupings (k_a, k_b) of the fluid-structure coupling coefficients (r, $\tilde{r}$, c, $\tilde{c}$) rather than on the four coefficients themselves. In Chapter 6, these same two groupings are found to control the extent and symmetry of lock-in; see item 2 of Section 8.6.

3. *Detuning variables.* There exist frequency detuning variables (Δ_f, Δ_r) which are natural for the solution of the mathematical problem, such that the inverted form of the frequency solution, $\Delta_f(\Delta_r)$, is single-valued. The exact detuning variables (d_f, d_r), which are natural for a description of the physical problem, differ from (Δ_f, Δ_r) by quantities of order ε^2.

4. *Solution Classes.* Only solutions which are real and stable [Class (3)] are of interest.

C. One-mode cable approximation:

1. *Similarity to spring-mounted cylinder.* Solutions and stability are identical to those for the spring-mounted cylinder, except that all amplitudes for the cable are smaller by the mode-shape factor $\sqrt{\frac{2}{3}}$.

D. Two-mode cable approximation:

1. *Identification of two Cases.* Solutions to the two-mode equations (4.1.8) may be either non-degenerate (Case 1) or degenerate (Case 2). The two Cases require separate analyses. For both Cases, natural detuning variables (Δ_f, Δ_r, Δ_{21}) exist for solution of the mathematical problem; (Δ_f, Δ_r) are two-mode generalizations of the variables discussed in item B3 above, while Δ_{21} measures the separation between the two natural structural frequencies under consideration (Fig. 7.5.1).

2. *The Non-degenerate Case.* In Case 1, the solution is quite different than for the one-mode case. For example, the inverted frequency solution $\Delta_f(\Delta_r)$ is double-valued, whereas it was single valued for the one-mode problem. Solutions Classes exist as for the one-mode problem, with the additional possibility that $\Delta_f(\Delta_r)$ is non-real [Class (0)].

3. *The Degenerate Case.* In Case 2, two sub-cases ("Types") are identified; either "mode-1" variables[2] are non-zero while "mode-2" variables are zero (Type 1), or vice-versa (Type 2). For each Type, the one-mode-approximate solution is applicable for the non-degenerating mode, provided the results are shifted according to Eqs. (5.6.39) and (5.6.40). However, for each Type, the presence of the degenerating mode gives rise to extra stability conditions, which destabalize many portions of

---

2. See convention (4.1.10) regarding the use of generic mode numbers (1,2).

the solution curves, notably causing the supression of lock-in bands as the structural frequencies approach each other. This is one of the mechanisms of modal interaction, as discussed further in Section 8.8.

8.6 Synopsis of Chapter 6

Model predictions are largely dependent on the values selected for the model constants $a_0, \ldots, a_5$. A series of regression techniques have been developed to fit the model optimally to experimental data on rigid cylinders. In the course of this development, some important properties of the model solutions have emerged:

1. *Lock-in boundaries for forced cylinders.* Stability boundaries for the forced van der Pol equation, traditionally plotted in the (σ, A) plane (where A is the response amplitude), are replotted in the (σ, B) plane (where B is the forcing amplitude). Qualtitatively, this representation clearly demonstrates the similarity between the model and experimental data. Quanitatively, it permits the development of a simple regression scheme to optimize this similarity.

2. *Lock-in characteristics for spring-mounted cylinders.* By defining a new coordinate in the (Δ_f, Δ_r) plane, a simplified description of the frequency-response curve is possible in terms of the lock-in band-center C and band-width W. The band-center C, and hence the symmetry of lock-in about resonance, is simply proportional to k_a, while W depends on k_a and k_b. These observations permit the development of a regression scheme to fit the model to experimental frequency-response data.

3. *Peak structural amplitude for spring-mounted cylinders.* A formula

for peak cylinder amplitude has been derived. This permits a regression scheme to fit the model to experimental amplitude-response data.

8.7 Synopsis of Chapter 7

Using the model parameter values selected in Chapter 6, model/experimental comparisons for rigid cylinders have been presented graphically. A similar comparison for elastic cables (using the one-mode approximation) has demonstrated the need for refitting the model over a wider range of the ratio $\frac{\zeta}{\eta}$. Subsequently, results of the two-mode approximation have been presented to describe modal interaction mechanisms in a qualitative sense.

8.8 General Conclusions

In Fig. 8.1, the thesis is diagrammed in a manner similar to Fig. 7.1.1, but in less detail.

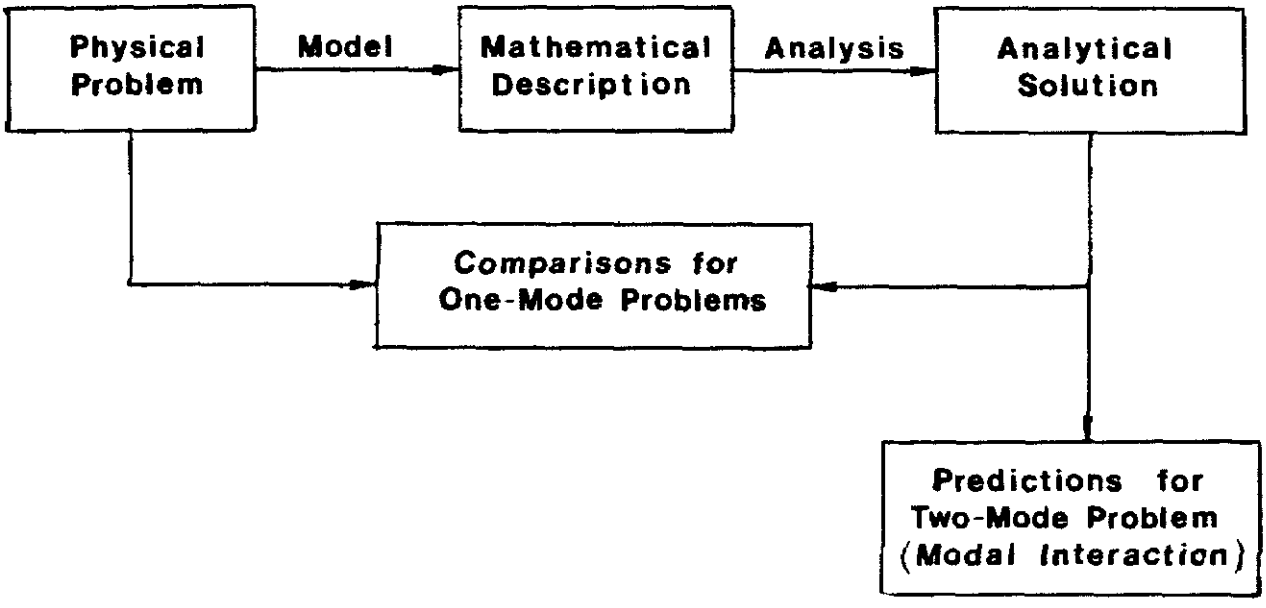

Figure 8.1. Thesis Summary

On the basis of this diagram, conclusions may be conveniently catagorized into three areas:

I. *Evaluation of analytical methods.* The results are excellent, as demonstrated by the agreement of the approximate analytic solutions with direct numerical solutions of the differential equations (Section 7.5). As an additional check, two entirely different analytical approaches to stability for the two-mode problem yield very similar results (Section 7.5.4).

II. *Evaluation of the model.* Since the analytical methods are accurate, analytical/experimental comparisons reflect wholly on the model. The results are mixed. On the one hand, the mathematical solutions exhibit certain features which resemble experimentally observed behavior:

1. For forced circular cylinders, the lock-in band is symmetric about resonance (irrespective of model parameters), and grows wider as the forcing amplitude is increased.

2. For spring-mounted circular cylinders, the lock-in band is skewed with respect to resonance (in contrast to the forced case). Moreover, the transition between lock-in and non-lock-in is discontinuous at the upper end of the lock-in band, while it is smooth at the lower end.

3. For elastic cables, structural response in the vicinity of each natural frequency is similar to that of spring-mounted cylinders, provided that the mode number is sufficiently small (i.e. Δ_{21} sufficiently large). For high mode numbers, the complexities of modal interaction become important, as discussed in item III below.

On the other hand, the model also displays a number of short-comings:

1. There are serious discrepancies between model predictions and experimental data regarding amplitude response for spring-mounted cylinders (Figs. 7.3.1b–7.3.5b).

2. For the "optimal" model parameters selected herein, the dependence of lock-in band-width on reduced damping $\frac{\zeta}{\eta}$ is far too strong (Section 7.4).

3. For the "optimal" parameters, it is impossible to satisfy all of the sign restrictions on the model constants, which are dictated by physical reasoning (Section 6.5.2).

In general, although the present model can fit certain experimental features very well, it seems to be unable to fit all the data adequately with a single set of model parameters. For example, when an attempt was made, for forced cylinders, to reconcile model predictions of the fluid-structure interaction force with experimental data [19, 51, 58, 59, 60] using regression techniques, the optimum parameter values thus generated were incompatible with the optimal values selected in Chapter 6. Attempts to fit interaction-force data were subsequently abandoned. Another example, discussed in footnote 1 of Section 8.2, is that the model cannot simultaneously predict right-skewed lock-in for spring-mounted circular cylinders and left-skewed lock-in for D-section cylinders, although it can predict either if the model parameter P_1 is appropriately selected. Other vortex-shedding models are plagued with the same problems. Some authors have dealt with this difficulty by allowing the model parameters to vary with the ratio $\frac{\zeta}{\eta}$ [63],[3] or even with the independent flow variable (i.e. Δ_f) [4]. Although such treatments are of course capable of obtaining improved results, the cost is greater empiricism, and the benefit in terms of understand-

---

3. See the discussion in Section 6.1.

ing basic mechanisms is questionable.

III. *Predictions concerning modal interaction.* If the model is accepted, regardless of its shortcomings, for its ability to describe qualitative features of lock-in, then the following description of modal interaction may be postulated, some of which has been verified by experimental evidence. The discussion is based on the analysis of Section 5.6 and the results of Section 7.5, with particular references to the composite solution map, Fig. 7.5.13.

For mathematical comparison, consider first the one-mode approximation, in which modal interaction is completely ignored. This is equivalent to setting $q = 0$ in Eqs. (4.1.8), such that a monofrequency solution may exist for each mode independently of the other, regardless of the modal frequency separation $\omega_2 - \omega_1$ (i.e. Δ_{21}). Thus at a given flow speed (i.e. Δ_f), the response frequency ω (i.e. Δ_r) for each of the independent solutions may be different.

When the interaction of "mode 1" and "mode 2" is considered[4] using the two-mode approximation ($q \neq 0$), the situation is entirely different, because the coupled modes may no longer establish independent monofrequency solutions. Instead, there are three possibilities:

- *Case 1. Non-degenerate solutions.* The two competing modes are able to "compromise" on a single value of ω, and thereby achieve mutual, monofrequency response. This typically occurs when the compromise response frequency is not too close to either of the modal frequencies (ω_1, ω_2).

- *Case 2. Degenerate solutions.* One mode dominates, drives the other mode to zero, and establishes monofrequency respsonse at the value of ω which it would assume if the other mode were totally absent. That is,

4. See convention (4.1.10) regarding the use of generic mode numbers (1,2).

the dominant mode reverts to the one-mode approximation. Typically, "mode 1" dominates when the would-be solution for ω in the non-degenerate case is very much closer to ω_1 than to ω_2, and conversely for "mode 2".

- *Case 3. Complex solutions.* The two modes are unable to "agree" on a compromise value of ω for monofrequency response, and at the same time, neither mode is able to dominate the other. This typically occurs when the modal separation Δ_{21} is very small, but ω lies neither very near ω_1 nor very near ω_2.

As exemplified by Fig. 7.5.13, the interplay between these three possibilities produces the following phenomena:

- *Degnerate/Non-degenerate bifurcation.* The smooth transition from Case 1 to Case 2 occurs along certain loci in the (Δ_f, Δ_{21}) plane.
- *Degenerate/Non-degenerate overlap.* Regions exist in the (Δ_f, Δ_{21}) plane where either kind of solution may occur, depending on initial conditions. "Jump" phenomena occur at the edges of the overlap.
- *Degenerate/Degenerate overlap (or "lock-in overlap").* A region exists in the (Δ_f, Δ_{21}) plane where either mode may dominate, depending on initial conditions. "Jump" phenomena occur at the edges of the overlap. This phenomenon has been observed experimentally.
- *Lock-in suppression.* As Δ_{21} becomes small, each mode suppresses the region of dominance of the other. If it were not for lock-in suppression, the region of lock-in overlap would be much larger, and complex solutions would not occur.

As a practical consequence of this investigation, it may be concluded that the one-mode approximation is adequate (and in fact *precise* whenever degenerate solutions prevail) provided that the modal separation Δ_{21} is greater than some minimum value which depends on the mass ratio and the structural damping.

8.9 Suggestions for Futher Research

Extensions of the above work are immediately obvious. First, the dependence of the two-mode solution map (Fig. 7.5.13) on mass ratio and damping ratios should be considered. In particular, such dependence of the vertex V is of interest, as a guide to the adequacy of the one-mode approximation. Second, if appropriate experimental data become available, a refit of the model over a wider range of conditions might be considered, as discusssed in Section 7.4. Finally, the extension to three- (or higher) mode approximations is possible, and perhaps necessary to model interaction phenomena for very-high-mode response of vortex-shedding structures. However, it is questionable whether the understanding gained from such an extension would be worth the considerable effort involved, at least until a model having firmer theoretical foundations is available. In the opinion of this author, establishing such foundations should be the central goal of further research.

NOTATION

The Table below lists the symbols used in this thesis alphabetically, as follows:

- Roman
- Greek
- Special (non-alphabetic).

The Table contains six columns, each of which requires some comment:

- *Column 1 (Symbol):* If the symbol (e.g. B_i) has different meanings in different parts of the thesis, the following distinction is made in column 1:
  - B_i (1) [referred to elsewhere as def. 1]
  - B_i (2) [referred to elsewhere as def. 2]

  Different definitions of the same symbol are never used within the same section,[1] so by reference to Column 4 ("Extent"), a particular usage should be unambiguous.

  Subscripted variables are sometimes listed with specific numeric subscipts (e.g. $a_0, \ldots, a_6$), and sometimes not (e.g. z_i), depending on the need to specify information in other columns of the Table. Column 2 (Description) should be consulted to specify the numeric values a subscript may assume (if any).

- *Column 2 (Description):* Verbal descriptions are usually given. When a convenint verbal description is not possible, the mathematical definition is given (if it is short enough) or the space is left blank.

- *Column 3 (Defined)* This column documents the location where a symbol is first defined or used. The following conventions are employed:

1. With one exception; see the footnote to Eq. (4.3.4).

- ( ) -- Equation number
- F. -- Figure number
- T. -- Table number
- fn. -- Footnote number (1)
- § -- Section number
- Ch. -- Chapter number

- *Column 4 (Extent):* This column documents the extent of usage of a symbol, by listing the section numbers in which the given definition is valid. Conventions (1) apply to note Equations and Sections. Additionally, the following abbreviations are used:
  - G: Global. The given definition is valid everywhere.
  - G–: Global with exceptions. The given definition is valid everywhere except where indicated by other definitions of the same symbol.
  - FORCED: "Forced Cylinder". The given definition is valid in Sections 2.3, 3.2, 5.3, 6.2, and 7.2.
  - SMC "Spring-Mounted Cylinder". The given definition is valid in Sections 2.4, 3.2, 5.4, 6.3, 6.4, and 7.3.
  - OMCA: "One-Mode Cable Approximation". The given definition is valid in Sections 3.4.4, 5.5, and 7.4.
  - 1-MODE: Same as FORCED + SMC + OMCA.
  - TMCA: "Two-Mode Cable Approximation." The given definition is valid in Section 3.4.5, 5.6, and 7.5.
  - TMCA-N: "Two-Mode Cable Approximation, the Nondegenerate case".

The given definition is valid in Sections 5.6.2 and 7.5.2.

- TMCA-D: "Two-Mode Cable Approximation, the Degenerate case". The given definition is valid in Sections 5.6.3 and 7.5.3.
- INDUCED: Same as SMC + OMCA + TMCA.

- *Column 5 (See Also)*: This column gives cross-references to other discussions of the symbol in question. The abbreviations itemized above are used.
- *Column 6 (Units)*: This column gives the dimensions of the symbol. The following abbreviations are used:
  - M -- Mass
  - L -- Length
  - T -- Time
  - F -- Force (MLT^{-2}).

Symbol	Description	Defined	Extent	See Also	Units
$\tilde{\alpha}$	Uniform Acceleration	§3.2	§3.2		LT^{-2}
a_0	Model constant (scales $\hat{Z}'$)	(3.2.1)	G	(6.5.4a)	--
a_1	Model constant	(3.2.6)	G	(6.5.4b)	--
a_2	Model constant	(3.2.6)	G	(6.5.4c)	--
a_3	Model constant	(3.2.7)	G	(6.5.4d)	--
a_4	Model constant	(3.2.7)	G	(6.5.4e)	--
a_5	Model constant	(3.2.7)	G	(6.5.4f)	--
a_6	Model constant	(3.2.6)	G	(3.2.12)	--
$\hat{a}_i$	Functions of Δ_{ri} appearing in $[P(t)]$; $i = 1, 2$	(5.6.53)	TMCA-D		--
A	Dimensionless amplitude of the fluid oscillator Z; abbreviation for A_1	(5.3.6a)	1-MODE	(5.4.15b) (5.5.2a)	--
A_i	Amplitude of $z_i^{(0)}$; $i = 1, 2$	(4.3.18)	G	(5.2.1)	--
b	Viscous damping coefficient per unit structural length	(2.4.2)	§2.4		FTL^{-2}
$\hat{b}_i$	Function of Δ_{ri} appearing in $[P(t)]$; $i=1, 2$	(5.3.53)	TMCA-D		--
B	Dimensionless structural amplitude; abbreviation for B_1	(2.3.3)	1-MODE	(5.2.1b) (5.3.6b)	--
B^*	Normalized form of B	(5.3.11b)	FORCED		--
$\hat{B}$	Peak value of B	§6.4	§6.4	(6.4.8) (6.4.14)	--
B_o	Experimentally observed amplitude threshold	§2.3	§2.3		--
B_i (1)	Amplitude of structural oscillator $y_i^{(0)}$, $i = 1, 2$	(4.3.15)	G-	(5.2.1)	--
B_i (2)	Value of B at the i^{th} experimental data point	§6.2	§6.2		--
B_m	Double amplitude of H_m, $m = 1, \ldots, 4$. Note: B_i (def. 1) and B_m are equivalent for $i = m = 1, 2$.	(4.3.13)	G-	(4.3.14) (4.3.15)	--

Symbol	Description	Defined	Extent	See Also	Units
c	Coupling coefficient in structural oscillator equation	(3.2.24a)	G	(3.2.21)	--
$\tilde{c}$	Coupling coefficient in structural oscillator equation	(3.2.24b)	G	(3.2.21)	--
c_1	Axis-stretching constant for σ (def. 2)	(5.3.10a)	FORCED	(5.3.11a) §6.2	--
c_2	Axis-stretching constant for B (in the forced case)	(5.3.10b)	FORCED	(5.3.11b) §6.2	--
c.c.	Complex conjugate of all preceding terms	(4.3.8)	§4.3		--
C (1)	Differential operator representing structural damping	(3.4.5)	Ch. 3	(3.4.11)	FTL^{-1}
C (2)	Model-predicted lock-in band-center	(6.3.7a)	§6.3	(6.3.8a) (6.3.15a)	--
C_1	Function defined locally for brevity	(4.3.10a)	§4.3		--
C_2	Function defined locally for brevity	(4.3.10b)	§4.3		--
C_i	Experimental value of lock-in band for i^{th} value of ζ	§6.3.3	§6.3.3	F. 6.3.2	--
d_{21}	Exact, intermodal detuning	(5.6.16c)	TMCA		--
d_f (1)	Exact, fluid-structure detuning. Note: Subscript f is not an index [see $(\ )_f$].	(5.4.13b) (2.4.4)	SMC		--
d_f (2)	Exact, mode averaged, fluid-structure detuning. Note: Subscript f is not an index [see $(\ )_f$].	(5.6.16b)	TMCA		--
d_r (1)	Exact, response- structure detuning. Note: Subscript r is not an index [see $(\ )_r$].	(2.4.5) (5.4.13a)	SMC		--
d_r (2)	Exact, mode averaged, response-structure detuning. Note: Subscript r is not an index [see $(\ )_r$].	(5.6.16a)	TMCA		--

Symbol	Description	Defined	Extent	See Also	Units
D	Characteristic cross-sectional dimension. For circular cross-sections, D is the diameter	(1.1)	G		L
D_0	$\frac{\partial}{\partial T_0}$	(4.2.6)	Ch. 4		--
D_1	$\frac{\partial}{\partial T_1}$	(4.2.6)	Ch. 4		--
e_1	$a_0 + a_3 + a_5$	(3.2.8)	G	(6.5.3)	--
e_2	$1 + a_3\eta$	(3.2.20)	G	fn. 1 of §3.2; (6.5.10)	--
E_1	Squared error	(6.2.6)	§6.2		--
E_2	Squared error	(6.2.13)	§6.2		--
E_3	Squared error	(6.3.18)	§6.3		--
E_4	Squared error	(6.4.16)	§6.4		--
f (1)	Vibrational response frequency of a system	(1.3)	INDUCED	§1.4	T^{-1}
f (2)	Forcing frequency	§2.3	FORCED		T^{-1}
$(\,)_f$	As a subscript, f is mnemonic for "fluid" in the fluid-structure detunings d_f, Δ_f, and Δ_{fi}. Note: subscript f is never an index.	(2.4.4)	G	(5.4.12) (5.6.15)	--
f^-, f^+	Lock-in band frequency-limits for the forced rigid cylinder	§2.3	§2.3		T^{-1}
f_i	Function of Δ_r (def.2), $i = 1, 2$	(5.6.26)	TMCA-N		--
f_n	n^{th} natural frequency of a structure ($n = 1, \ldots, \infty$)	(1.4)	G-	(2.4.1) §2.5	T^{-1}
f_s	Natural vortex-shedding frequency (Strouhal frequency). Note: Subscript s is not an index.	(1.1)	G	§1.4	T^{-1}
f_v	Frequency of vortex shedding. Note: Subscript v is not an index.	§1.1	§1.1		T^{-1}
$\mathbf{f}$	Function $\mathbf{f}(\mathbf{x}, \dot{\mathbf{x}})$	(4.1.6)	Ch. 4		--

Symbol	Description	Defined	Extent	See Also	Units
F	Function of σ (def.1),	(5.4.10a)	SMC		--
$\hat{F}$	Function of Δ_r (def.1),	(5.4.16a)	SMC		--
F_i	Function of σ (def.2), $i = 1, 2$	(5.6.7a)	TMCA-N		--
$\hat{F}_i$	Function of Δ_r (def.2), $i = 1, 2$	(5.6.19a)	TMCA-N		--
F_{int}	Fluid-structure interaction force	(3.2.3)	G	(3.2.7)	FL^{-1}
F	Function $\mathbf{F}(\mathbf{x}, \dot{\mathbf{x}}, \ddot{\mathbf{x}})$	(4.1.1)	Ch. 4		--
g_i	Function of Δ_r (def.2), $i = 1, 2$	(5.6.26)	TMCA-N		--
G	Function of σ (def.1)	(5.4.10b)	SMC		--
$\hat{G}$	Function of Δ_r (def.1)	(5.4.16b)	SMC		--
G_i	Function of σ (def.1), $i = 1, 2$	(5.6.7b)	TMCA-N		--
$\hat{G}_i$	Function of Δ_r (def.2), $i = 1, 2$	(5.6.19b)	TMCA-N		--
H_m	Complex amplitude for $x_m^{(0)}$; $m = 1, \ldots, N$	(4.2.11)	Ch. 4		--
i	$\sqrt{-1}$	(4.2.11)	§4.2 §4.3		--
$(\,)_i$ (1)	$i = 1, 2$, where (1,2) are used in a generic sense to indicate any two adjacent structural modes $i = k$, $k+1$ [def. 1 of $(\,)_k$]. Subscript i in this sense is used in conjunction with subscript j.	(3.4.24)	G–	(4.1.10)	--
$(\,)_i$ (2)	Index for experimental data	§6.2	Ch. 6		--
I_{ab}	Mode-shape integrals (in this local context, a and b are indices)	(3.4.22d)	(3.4.22)		--
$[I]$	Identity matrix	(5.4.28)	G		--

Symbol	Description	Defined	Extent	See Also	Units
$(\ )_j$	$j = 2, 1$, where (2,1) are used in a generic sense to indicate any two adjacent structural modes $j = k+1, k$ [def. 1 of $(\ )_k$]. Subscript j in this sense is used in conjunction with subscript i.	(3.4.24)	G	(4.1.10)	--
J	Momentum contained per unit depth of control volume	(3.2.2)	§3.2	(3.2.5)	MT^{-1}
J (1)	$\dot{\mathbf{X}} = \mathbf{J}(\mathbf{X})$ (def. 1 of **X**)	(5.3.14)	FORCED		--
J (2)	$\dot{\mathbf{X}} = \mathbf{J}(\mathbf{X})$ (def. 2 of **X**)	(5.4.22)	SMC	(5.4.24)	--
J (3)	$\dot{\mathbf{X}} = \mathbf{J}(\mathbf{X})$ (def. 3 of **X**)	§5.6.2.5	TMCA-N		--
$[J']_0$ (1)	Jacobian Matrix	(5.3.19)	FORCED	(5.3.21)	--
$[J']_0$ (2)	Jacobian Matrix	(5.4.25)	SMC	(5.4.27)	--
$[J']_0$ (3)	Jacobian Matrix	§5.6.2.5	TMCA-N	--	
k	Spring constant per unit structural length	(2.4.1)	§2.4	F. 2.4.1	FL^{-2}
$(\ )_k$ (1)	Subscript indicating a specific mode number; see $(\ )_n$ and $(\ )_i$	(3.4.15a)	Ch. 3		--
$(\ )_k$ (2)	Index for stability boundaries k = 1, 2, 3	(5.3.23)	FORCED	(5.3.24) §6.2	--
$(\ )_k$ (3)	Component index for **x** (def. 2)	§5.6.3.5	TMCA-D		--
$(\ )_k$ (4)	Index for P_k, a_k, k = 0, 1,..., 5	§6.1	§6.1 §6.5	--	
k_a	$\tilde{r}c - r\tilde{c}$ (a is not an index)	(5.4.11a)	G	(6.3.13)	--
k_b	$rc + \tilde{r}\tilde{c}$ (b is not an index)	(5.4.11b)	G	(6.3.13)	--
k_m (1)	Routhian stability constants; m = 0, 1, 2	(5.4.30)	SMC		--
k_m (2)	Routhian stability constants; m = 0, 1, 2	(5.6.49	TMCA-D		--
K_3	Function defined locally	(4.3.10c)	§4.3		--
L	Axial length of a vibrating structure	§2.5.2	§2.5 §3.4	(3.4.4)	--

Symbol	Description	Defined	Extent	See Also	Units
L_k	Stability boundary k, $k = 1, 2, 3$	(5.3.23)	FORCED	(5.4.24) §6.2	--
L_{ki}	$L_k(\sigma_i)$	(6.2.7)	§6.2	—	
$(\,)_m$ (1)	Refers to mode m of structure; $(m = 1, \ldots, \infty)$	(3.4.11)	Ch. 3		--
$(\,)_m$ (2)	Refers to component m of Eqs. (4.1.8), $(m = 1, \ldots, 4)$	(4.1.9)	Ch. 4		--
$(\,)_m$ (3)	Subscript for k_m; $m = 0, 1, 2$	(5.4.31)	§5.4 §5.6.3		--
M	Structural mass per unit length	(2.4.1)	G		ML^{-1}
M_{flux}	Momentum flux through control surfaces $(m = 1, \ldots, \infty)$	(3.4.11)	Ch. 3		--
$[M]$	Transformation matrix	(5.6.60)	TMCA-D		--
$(\,)_n$	Refers to mode n of a structure; $n = 1, \ldots, \infty$	§1.2	G		--
N (1)	Number of components in vector $\mathbf{x}$ (def. 1)	(4.2.2a)	Ch. 4	(4.3.1)	--
N (2)	Number of components in vector $\mathbf{x}$ (def. 2)	§5.6.3.5	TMCA-D		--
p	Coefficient of nonlinear term in generalized model equations	T. 4.1.1	G	(4.1.8)	--
P_0	Model parameter controlling the slope of stability boundaries for the forced case	(6.2.11)	G	(6.2.14) (6.2.15)	--
P_1	Model parameter controlling lock-in band-center C and band-width W for SMC	(6.3.14a)	G	(6.3.24a)	--
P_2	Another model parameter controlling C and W for SMC,	(6.3.14b)	G	(6.3.24b) (6.4.17a)	--
P_3	Model parameter controlling the dependence of C and W on reduced damping $\hat{\zeta}$	(6.3.14c)	G	(6.3.24c)	--

Symbol	Description	Defined	Extent	See Also	Units
P_4	Model parameter affecting peak structural amplitude for SMC as well as the stability boundaries for the forced case	(6.4.12)	G	(6.4.17b)	--
P_5	Model parameter left undetermined by regression analyses of Ch. 6, because of small-η approximation	(6.4.13)	G	(6.5.11)	--
P_k	Model parameters enumerated above; $k = 0, \ldots, 5$	§6.1	G		--
$[P(t)]$	Periodic matrix	(5.6.51)	TMCA-D		--
q	Coefficient of nonlinear coupling term in generalized model equations	T. 4.1.1	G	(4.1.8)	--
Q	$\frac{q}{3p}$	(5.6.8)	TMCA-N		--
Q_1, Q_2, Q_3	Functions of P_1, P_2, P_3	(6.3.19)	§6.3		--
Q_1^*, Q_2^*, Q_3^*	Optimal values of Q_1, Q_2, Q_3	(6.3.21)	§6.3		--
r	Coupling coefficient in fluid oscillator equation	(3.2.15c)	G	(3.2.14)	--
$(\,)_r$	As a subscript, r is mnemonic for "response" in the response-structure detunings d_r, Δ_r, and Δ_{ri}. Note: Subscript r is never an index.	(2.4.5)	G	(5.4.12) (5.6.15)	--
$\tilde{r}$	Coupling coefficient in fluid oscillator equation	(3.2.15d)	G	(3.2.14)	--
R (1)	Spin radius for Strouhal experiment	(2.5.2)	§2.5		L
R (2)	Function of Δ_r (def.1)	(5.4.26b)	§5.4		--
$[R]$	Transformation matrix	(5.6.59)	TMCA-D		--
Re	Reynolds number $\frac{UD}{\nu}$	F. 1.2	G	F. 2.2.2	--

Symbol	Description	Defined	Extent	See Also	Units
$()_s$	As a subscript, s is mnemonic for "Strouhal," as in the Strouhal frequency f_s. Note: Subscript s is never an index.	(1.1)	G	§2.2	--
S	Strouhal number	(1.1)	G	F. 2.2.2	--
t	Normalized time $\omega_s \tau$	(3.2.13b)	G		--
$()_t$	$\frac{\partial}{\partial t}$	(3.4.1)	Ch. 3		--
T (1)	Period of revolution	§2.5.2	§2.5		T
T (2)	Cable tension	(3.4.5)	Ch. 3		F
T (3)	Period of matrix [P(t)]	(5.6.56)	TMCA-D		--
T_0	One of two times scales used in the asympotitic method of Ch. 4 ($T_0 = t$)	(4.2.4)	Ch. 4		--
T_1	One of two times scales used in the asympotitic method of Ch. 4 ($T_1 = \varepsilon t$)	(4.2.4)	Ch. 4		--
u (1)	Normalized axial coordinate $\frac{x_1}{L}$	(3.4.4)	Ch. 3		--
u (2)	Function of Δ_r (def. 2)	(5.6.21a)	TMCA-N		--
$()_u$	$\frac{\partial}{\partial u}$ (def. 1 of u)	(3.4.6)	Ch. 3		--
u_0, u_1	Functions of Δ_r (def. 2)	(5.6.24)	TMCA-N		--
u_i	Perturbations in z_i, $i = 1, 2$	(5.6.42a)	TMCA-D		--
U (1)	Free stream flow velocity	(1.1)	G-		LT^{-1}
U (2)	Perturbation in Z	(5.6.45a)	TMCA-D		--
v	Function of Δ_r (def.2)	(5.6.21b)	TMCA-N		--
v_0, v_1	Functions of Δ_r (def. 2)	(5.6.24)	TMCA-N		--
v_2	Fluid velocity in x_2-direction	(3.2.1)	Ch. 3		LT^{-1}
v_i	Perturbation in y_i, $i = 1, 2$	(5.6.42b)	TMCA-D		--
V	Perturbation in Y	(5.6.45b)	TMCA-D		--
w	Function of Δ_r (def.2)	(5.6.21c)	TMCA-N		--
w_0, w_1	Functions of Δ_r (def. 2)	(5.6.24)	TMCA-N		--

Symbol	Description	Defined	Extent	See Also	Units
$\mathbf{w}^{(k)}$	k^{th} normal solution for $\mathbf{x}$ (def. 2), $k = 1, \ldots, N$ (def. 2); that is, the k^{th} column of $[W]$	§5.6.3.5	TMCA-D		--
W	Model-predicted lock-in band-width	(6.3.7b)	§6.3	(6.3.8) (6.3.15b)	--
W_i	Experimental value of lock-in band-width for i^{th} value of ζ	§6.3.3	§6.3.3	F. 6.3.2	--
$[W]$	Matrix whose columns are $\mathbf{w}^{(k)}$	(5.6.57)	TMCA-D		--
x	$\Delta_f - \Delta_r$ ($\equiv -\sigma$, def. 1)	(6.3.2)	Chs. 6-8		--
x_1	Cartesian coordinate along structural axis	F. 3.2	Ch. 3	(3.4.4)	L
$(\,)_{x_1}$	$\dfrac{\partial}{\partial x_1}$	(3.4.5)	Ch. 3		L^{-1}
x_2	Cartesian coordinate transverse to flow direction	F. 3.2	Ch. 3		L
x_3	Cartesian coordinate parallel to free stream	F. 3.2	Ch. 3		L
$x_l^{\pm}$	x-endpoints of the lock-in band	(6.3.5)	§6.3		--
$x_m^{(0)}$	Zeroth order solution for component m of vector x (def. 1)	(4.2.11)	Ch. 4		--
$\mathbf{x}$ (1)	Vector of component oscillators	(4.1.1)	Ch. 4	(4.3.1)	--
$\mathbf{x}$ (2)	Vector of perturbations	(5.6.52a)	TMCA-D		--
$\mathbf{x}_0$	Zeroth order asymptotic solution for $\mathbf{x}$ (def. 1)	(4.2.3)	Ch. 4		--
$\mathbf{x}_1$	First order asymptotic solution for $\mathbf{x}$ (def. 1)	(4.2.3)	Ch. 4		--
$\mathbf{x}^{(k)}$	k^{th} principle solution for $\mathbf{x}$ (def. 2) $k = 1, \ldots, N$ (def. 2); that is, the k^{th} column of $[X]$	(5.6.57)	TMCA-D		--
$\mathbf{X}$ (1)	Amplitude/phase vector	(5.3.15)	FORCED		--
$\mathbf{X}$ (2)	Amplitude/phase vector	(5.4.23)	SMC		--

Symbol	Description	Defined	Extent	See Also	Units
$\mathbf{X}$ (3)	Amplitude/phase vector	(5.6.35)	TMCA-N		--
$\hat{\mathbf{X}}$ (1)	Perturbation for $\mathbf{X}$ (def. 1)	(5.3.18)	FORCED		--
$\hat{\mathbf{X}}$ (2)	Perturbation for $\mathbf{X}$ (def. 2)	(5.4.25)	SMC	(5.4.27)	--
$\hat{\mathbf{X}}$ (3)	Perturbation for $\mathbf{X}$ (def. 3)	§5.6.2.5	TMCA-N		--
$\mathbf{X}_0$ (1)	Steady-state solution for $\mathbf{X}$ (def. 1)	(5.3.17)	FORCED		--
$\mathbf{X}_0$ (2)	Steady-state solution for $\mathbf{X}$ (def. 2)	§5.4.6	SMC		--
$\mathbf{X}_0$ (3)	Steady-state solution for $\mathbf{X}$ (def. 3)	§5.6.2.5	TMCA-N		--
$[X]$	Matrix whose columns are $\mathbf{x}^{(k)}$	(5.6.57)	TMCA-D		--
y_i	See y_n and $(\,)_i$ (def. 1)	Ch. 3	G	(4.1.10) *T. 4.1.1*	--
$y_i^{(0)}$	Approximate solution for $y_i(t)$; $i = 1, 2$	(4.3.15)	G	(5.2.1)	--
$y_i^{(s)}$	Exact, steady-state solution for $y_i(t)$; $i = 1, 2$	(5.6.42)	TMCA-D		--
y_k	See y_n and $(\,)_k$ (def. 1)	Ch. 3	G		--
y_n	Time function in eigenfunction expansion of $Y(u,t)$, $n = 1, \ldots, \infty$	(3.4.9b)	G		--
Y	Normalized $\hat{Y}$	(3.2.13a)	G		--
Y	Normalized $\hat{Y}$	(3.2.13a)	G		--
$\hat{Y}$	Displacement of structural axis	§3.2	G		L
$Y^{(0)}$ (1)	Prescribed sinusoidal forcing function	(5.3.4b)	FORCED		--
$Y^{(0)}$ (2)	Approximate solution for $Y(t)$	(5.4.3b)	SMC	(5.4.5b)	--
$Y^{(s)}$	Exact, steady-state solution for $Y(t)$	(5.6.45)	TMCA-D		--
z_i	See z_n and $(\,)_i$ (def. 1)	Ch. 3	G	(4.1.10) T. 4.1.1	--
$z_i^{(0)}$	Approximate solution for $z_i(t)$; $i = 1, 2$	(4.3.15)	G	(5.2.1)	--

Symbol	Description	Defined	Extent	See Also	Units
$z_i^{(e)}$	Exact, steady-state solution for $z_i(t)$; $i = 1, 2$	(5.6.42)	TMCA-D		--
z_f	See z_n and $(\ )_f$ (def. 1)	Ch. 3	G	(4.1.10) T. 4.1.1	--
z_k	See z_n and $(\ )_k$ (def. 1)	Ch. 3	G		--
z_n	Time function in eigenfunction expansion of $Z(u,t)$, $n = 1, \ldots, \infty$	(3.4.9a)	G		--
Z	Normalized $\hat{Z}$	(3.2.13a)	G		--
$\hat{Z}$	Fluid oscillator variable	(3.2.1)	G		L
$Z^{(0)}$	Approximate solution for $Z(t)$	(5.3.4b)	G	(5.4.3a) (5.4.5a)	--
$Z^{(e)}$	Exact, steady-state solution for $Z(t)$	(5.6.45)	TMCA-D		--
α	Negative damping coefficient in van der Pol type equation	(3.2.15a)	G	(3.2.14)	--
β	Coefficient of nonlinear term in van der Pol type equation	(3.2.15b)	G	(3.2.14) T. 4.1.1	--
γ	Normalized damping coefficient (includes both structural and fluid damping)	(3.2.22)	G		--
γ_n	n^{th} mode structural damping coefficient	(3.4.14)	G		--
Γ		(5.4.21)	§5.4		--
Γ_i	Function of Δ_{ri} appearing in $\hat{a}_i$ and $\hat{b}_i$, $i = 1, 2$	(5.6.54)	TMCA-D		--
δ_i	$1 - \Omega_i^2$	(4.3.4)	§4.3		--
δ_{mn}	Kronecker delta	(3.4.11)	§3.4		--
Δ_{21}	Approximate, intermodal detuning	(5.6.15c)	G		--
Δ_f (1)	Approximate, fluid-structure detuning. Note: Subscript f is not an index [see $(\ )_f$].	(5.4.12b)	SMC		--
Δ_f (2)	Approximate, mode-averaged, fluid-structure detuning. Note: Subscript f is not an index [see $(\ )_f$].	(5.6.15b)	TMCA		--

Symbol	Description	Defined	Extent	See Also	Units
Δ_{fi}	Equivalent to the one-mode detuning Δ_f (def. 1), but in a two-mode context. The subscript $i = 1, 2$ is appended to distinguish Δ_{fi} from Δ_f, def. 2. Note: Subscript f is not an index [see $(\ )_f$].	(5.6.38b)	TMCA-D		--
Δ_r (1)	Approximate, response-structure detuning. Note: Subscript r is not an index [see $(\ )_r$].	(5.4.12a)	SMC		--
Δ_r (2)	Approximate, mode-averaged, response-structure detuning. Note: Subscript r is not an index [see $(\ )_r$].	(5.6.15a)	TMCA		--
$\hat{\Delta}_r$	Value of Δ_r (def. 1) at which peak structural amplitude $\hat{B}$ occurs. Note: Subscript r is not an index [see $(\ )_r$].	§6.4	§6.4	(6.4.9)	--
Δ_{ri}	Equivalent to the one-mode detuning Δ_r (def. 1), but in a two-mode context. The subscript $i = 1, 2$ is appended to distinguish Δ_{ri} from Δ_r, def. 2. Note: Subscript r is not an index [see $(\ )_r$].	(5.6.38a)	TMCA-D		--
ε	A small quantity; $\varepsilon << 1$	(4.1.1)	G		--
ζ	Structural damping ratio (fraction of critical damping)	(2.4.2)	G	--	
$\hat{\zeta}$	Reduced damping $\frac{\zeta}{\eta}$	(6.3.16)	G		--

Symbol	Description	Defined	Extent	See Also	Units
ζ_i	i^{th} experimental value of ζ	§6.4.2	§6.4.2	F. 2.4.2 T. 6.4.1	--
ζ_n	n^{th}-mode structural damping ratio	(3.4.11)	G		--
η	Mass ratio $\frac{\rho D^2}{M}$	(2.4.3)	G		--
η_i	i^{th} experimental value of η	§6.4.2	§6.4.2	F. 2.4.2 T. 6.4.1	--
ϑ_i	Phase angle for $y_i^{(0)}$, $i = 1, 2$; excluding uniform drift attributable to frequency shift	(5.2.2a)	G		--
Θ_i	Phase angle for $y_i^{(0)}$, $i = 1, 2$; including uniform drift attributable to frequency shift	(4.3.13)	G	(4.3.14) (4.3.15)	--
Θ_m	Phase angle for H_m, $m = 1,\ldots, 4$;	(4.3.13)	G		--
κ_m	Functions of Δ_r (def.2); $m = 0,\ 1,\ 2$	(5.6.26)	TMCA-N		--
λ	Eigenvalue of $[J']_0$	(5.4.28)	§5.4.6		--
λ_k	k^{th} eigenvalue of $[M]$; $k = 1, \ldots, N$ (def. 2)	(5.6.62)	TMCA-D		--
Θ_i	Phase angle for $y_i^{(0)}$, $i = 1, 2$; including uniform drift attributable to frequency shift	(4.3.13)	G	(4.3.14) (4.3.15)	--
$[\Lambda]$ (1)	Diagonal matrix	(4.2.1)	Ch. 4		--
$[\Lambda]$ (2)	Diagonal matrix of eigenvalues	(5.6.62)	TMCA-D		--
μ	Abbreviation for μ_1	(5.4.5b)	SMC		--
μ_i	$\Theta_i - \Phi_i$; $i = 1,\ 2$	(4.3.20b)	G		--
ν	Kinematic viscoscity of a fluid	§2.2	G		L^2T^{-1}
ξ_n	n^{th} orthonormal eigenfunction of a structure	(3.4.8)	Ch. 3		--
ρ	Fluid density	(2.4.3)	G		ML^{-3}

Symbol	Description	Defined	Extent	See Also	Units
σ (1)	Response-fluid detuning for the case of induced vibrations: $\sigma \equiv \frac{f - f_s}{f_s} \equiv \Omega - 1$ (defs. 1 for f and Ω)	(5.2.6)	INDUCED		--
σ (2)	Detuning for the case of forced vibrations: $\sigma \equiv \frac{f - f_s}{f_s} \equiv \Omega - 1$ (defs. 2 for f and Ω)	(2.3.4)	FORCED	(5.2.1) (5.3.4b)	--
σ^-, σ^+	Values of σ (def. 2) corresponding to (f^-, f^+)	§2.3	§23		--
σ^*	Normalized form of σ (def. 2)	(5.3.11a)	FORCED		--
σ_i	Value of σ at i^{th} experimental data point	§6.2	§6.2		--
σ_T^* (1)	Value of σ^* at point T	(6.2.3)	§6.2		--
τ	Time	§3.2	G		T
$(\,)_\tau$	$\frac{\partial}{\partial \tau}$	(3.4.5)	Ch. 3		T^{-1}
φ	$\Phi_2 - \Phi_1 = \varphi_2 - \varphi_1$	(4.3.20a)	G	(5.2.1)	--
φ_{12}	$-\varphi_{21}$	(5.2.7)	G		--
φ_{21}	$\varphi_2 - \varphi_1$	(5.2.7)	G	(4.3.20a) (5.2.2b)	--
φ_i	Phase angle for $z_i^{(0)}$, $i = 1, 2$; excluding uniform drift attributable to frequency shift	(5.2.2b)	G	(5.2.7) (5.3.6a)	--
φ_{ji}	φ_{21} if $j = 2, i = 1$ φ_{12} if $j = 1, i = 2$	(5.2.5)	G	(5.2.7)	--
Φ_i	Phase angle for $z_i^{(0)}$, $i = 1, 2$; including uniform drift attributable to frequency shift	(4.3.15)	G		--
ω (1)	Angular response frequency for induced vibrations [$\omega = 2\pi f$ def. 1]	§1.4	G		T^{-1}
ω (2)	Angular forcing frequency for forced vibrations [$\omega = 2\pi f$ def. 2]	§1.4	G		T^{-1}

Symbol	Description	Defined	Extent	See Also	Units
ω_1 (1)	The first natural structural frequency	(3.2.18)	SMC		--
ω_1 (2)	Abbreviation for ω_k, where k (def. 2) is a particular value of the mode number n (see ω_n)	(3.4.19)	TMCA		--
ω_2	Abbreviation for ω_{k+1}, where k (def. 2) is a particular value of the mode number n (see ω_n)	(3.4.19)	TMCA		--
ω_n	Angular frequency corresponding to f_n ($\omega_n = 2\pi f_n$; $n = 1, \ldots, \infty$)	(3.2.18)	G	(3.4.10b)	T^{-1}
ω_s	Angular Strouhal frequency ($\omega_s = 2\pi f_s$)	(3.2.10)	G	§1.4 (3.2.11)	T^{-1}
Ω (1)	Normalized angular response frequency for induced vibrations; $\Omega \equiv \frac{\omega}{\omega_s}$	(5.2.1)	INDUCED	§1.4 (5.2.4)	--
Ω (2)	Normalized angular forcing frequency for forced vibrations; $\Omega \equiv \frac{\omega}{\omega_s}$	(5.3.4)	FORCED		--
Ω_1 (1)	Normalized form of the first natural structural frequency ω_1	(3.2.23)	SMC		--
Ω_1 (2)	Abbreviation for Ω_k, where k (def. 2) is a particular value of the mode number n (see Ω_n)	(4.1.8)	Ch. 4, TMCA	(4.1.10)	--
Ω_2	Abbreviation for Ω_{k+1}, where k (def. 2) is a particular value of the mode number n (see Ω_n)	(4.1.8)	Ch. 4, TMCA	(4.1.10)	--

Symbol	Description	Defined	Extent	See Also	Units
Ω_t	Refers to either Ω_1 (def. 2) or Ω_2	(3.4.25)	Ch. 4 TMAC		--
Ω_n	Normalized version of ω_n; $n = 1, \ldots, \infty$	(3.2.23)	Ch. 3	(3.4.10a) §1.4	--
Ω_s	Normalized Strouhal frequency; $\Omega_s \equiv \frac{\omega_s}{\omega_s} \equiv 1$. Note: Subscript s is not an index.	(5.4.4)	G		--
$(\dot{})$	$\frac{d}{dt}$	(3.2.13c)	G		--
$(\,)'$ (1)	$\frac{d}{d\tau}$	(3.2.1)	§3.2		T^{-1}
$(\,)'$ (2)	$\frac{d}{dT_1}$	(4.2.12)	Ch. 4		--
$\overline{(\,)}$	Complex conjugate	(4.2.11)	Ch. 4		--

REFERENCES

[1] Abernathy, F.H. and R. E. Kronauer, "The Formation of Vortex Streets," *J. Fluid Mech.*, vol. 13, part 1, pp. 1-20, May 1962.

[2] Bearman, P.W., "Investigation of the flow behind a two-dimensional model with a blunt trailing edge and fitted with splitter plates," *J. Fluid Mech.*, vol. 21, part 2, pp. 241-255, 1965.

[3] Benard,H.,"Formation de centres de giration à l'arriére d'un obstacle en mouvement," *Comptes Rendues (Académie des Sciences)* vol. 147,1908, pp. 839-842.

[4] Berger, E., "Analysis of Vortex-Induced Vibrations by an Improved Oscillator Model," 1980.

[5] Bishop, R.E.D., and A.Y. Hassan, "The Lift and Drag Forces on a Circular Cylinder in a Flowing FLuid," *Proc. Roy. Soc.* (London) Ser. A, vol. 277, pp. 32-75, 1964.

[6] Blevins, R.D., "Flow Induced Vibration of Bluff Structures," Ph.D. Thesis, California Institute of Technology, 1974.

[7] Blevins, R.D., **Flow Induced Vibrations,** Van Nostrand Reinhold Company, New York, 1977.

[8] Bogoliubov, N.N. and Y.A. Mitropolsky, **Asymptotic Methods in the Theory of Nonlinear Oscillations,** Hindustan Publishing Corporation, India, 1961.

[9] Cannon, Robert H., **Dynamics of Physical Systems,** McGraw Hill, 1967.

[10] Chen, Y.N., "Fluctuating Lift Forces of the Karman Vortex Streets on Single Circular Cylinder and in Tube Bundles," Parts 1 and 2, *J. Eng. for Industry*, vol. 94, pp. 603-622, May 1972.

[11] Currie, I.G., **Fundamentals of Fluid Mechanics,** McGraw Hill, N.Y., 1974.

[12] *Dale J., H. Menzel, and J. McCandless, "Dynamic Characteristics of* Underwater Cables; Flow Induced Transverse Vibrations," U.S. Naval Air Development Center, Aero-Electronic Technology Department, Report No. NADC-AE-6620, 1966.

[13] De Camp, L.S., **The Ancient Engineers,** Ballantine Books, N.Y., 1963.

[14] Fage, A., "The Air FLow Around a Circular Cylinder in the Region Where the Boundary Layer Separates from the Surface," Aeronautical Research Committee, Reports and Memoranda No. 1179 (Ae. 343), August 1928.

[15] Fage, A., and F.C. Johansen, "The Structure of Vortex Sheets," Aeronautical Research Committee, Reports and Memoranda No. 1143 (Ae. 311), vol. 31, 1927-28.

[16] Feng, C.C., "The Measurement of Vortex-Indiced Effects in Flow Past Stationary and Oscillating Circular and D-Section Cylinders," M.A. Sc. Thesis, University of British Columbia, 1968.

[17] Ferguson,N., "The Measurement of Wake and Surface Effects in the Subcritical Flow Past a Circulat Cylinder at Rest and in Vortex-Excited Oscillation," M.A.Sc. Thesis, University of British Columbia, September 1965.

[18] Ferguson, N., and G.V. Parkinson, "Surface and Wake Flow Phenomena of the Vortex-Excited Oscillation of a Circular Cylinder," *J. Eng. for Industry,*

vol. 89, pp. 831-838, November 1967.

[19] Fortik, D.F., "Forced Oscillations of a Cylinder in Uniform Flow," M.S. Thesis, Naval Postgraduate School, Monterey, CA, 1976.

[20] Gerrard, J.H., "The Calculation of the Fluctuating Lift on a Circular Cylinder and Its Application to the Determination of Aeolian Tone Intensity," NATO Advisory Group for Aeronautical Research and Development, Report No. 463, April 1963.

[21] Gerrard, J.H.., "The Mechanics of the Formation Region of Vortices Behind Bluff Bodies," *J. Fluid Mech.*, vol. 25, part 2, pp. 401-413, 1966.

[22] Griffin, O.M., and C.W. Votaw, "The Vortex Street in the Wake of a Vibrating Cylinder," *J. Fluid Mech.*, vol 51, part 1, pp. 31-48, 1972.

[23] Griffin, O.M., "Flow Near Self-Excited and Forced Vibrating Circular Cylinders," *J. Eng. for Industry*, vol. 94, pp. 539-547, May 1972.

[24] Griffin, O.M., R.A. Skop, and G.H. Koopman,"The Vortex-Excited Resonant Vibrations of Circular Cylinders," *J. Sound and Vibration*, vol. 31. part 2, pp. 235-249, 1973.

[25] Grffin, O.M., and S.E. Ramberg, "The Vortex-Street Wakes of Vibrating Cylinders," *J. FLuid Mech.*, vol 66, part 3, pp. 553-576, 1974.

[26] Griffin, O.M., and Koopman G.H., "The Vortex-Excited Lift and Resistance Forces on Resonantly Vibrating Cylinders," Advance Copy, 1976.

[27] Griffin, O.M., S.E. Ramberg, and R.A. Skop, "Flow-Induced Vibrations of Mooring Arrays," FY 1977 Final Report, Ocean Technology Division, Naval Research Laboratory, Wahington D.C., November 15, 1977.

[28] Griffin, O.M., "Vortex-Excited Unsteady Forces on Resonantly Vibrating Bluff Structures," Naval Research Laboratory Memorandum Report XXXX, Advance Copy, May 1978.

[29] Griffin, O.M., S.E. Ramberg, and R.A. Skop, "Flow-Induced Vibrations of Mooring Arrays," FY 1979 Final Report, Ocean Technology Division, Naval Research Laboratory, Wasington D.C., September 30, 1979.

[30] Griffin, O.M., "OTEC Cold Water Pipe Design for Problems Caused by Vortex-Excited Oscillations," Naval Research Laboratory Memorandum Report 4157, March 14, 1980.

[31] Halle, H., and W.P. Lawrence, "Crossflow-Induced Vibration of a Circular Cylinder in Water," *ASME Report 73-DET-68, 1973.*

[32] Harris. C.M. and C.E. Crede, **Shock and Vibration Handbook,** Second Ed., McGraw Hill, 1976.

[33] Hartlen, R.T., and I.G. Currie,"Lift Oscillation Model for Vortex-Induced Vibration," *J. Eng. Mech. Div., Am. Soc. Civil Engrs.*, vol. 96, pp. 577-591, 1970.

[34] Hilsenrath, J., *et. al.*, **Tables of Thermal Properties of Gases,** National Bureau of Standards Circular 564, 1955.

[35] Iwan, W.D. and Blevins, R.D., "A Model for Vortex Induced Oscillation of Structures," *J. Applied Mech.*, vol. 41, number 3, pp. 581-586, September 1974.

[36] Iwan, W.D., "The Vortex Induced Oscillation of Elastic Structural Elements," *J. Eng. for Industry*, vol. 97, pp. 1378-1382, November, 1975.

[37] Koopman, G.H., "The Vortex Wakes of Vibrating Cylinders at Low Reynolds Numbers," *J. Fluid Mech.*, vol. 28, part 3, pp. 501-512, 1967.

[38] Kretschmer, T.R., G.A. Edgerton, and N.D. Albertsen, "Seafloor Construction Experiment, Seacon II--An Instrumented Tri-Moor for Evaluating Undersea Cable Structure Technology," Naval Facilities Engineering Command, Technical Report R 848, December 1976.

[39] Leehey,P., and C.E. Hanson, "Aeolian Tones Associated with Resonant Vibration," *J. Sound and Vib.*, vol. 13, part 4, pp. 465-483, 1971.

[40] Marris, A.W., "A Review on Vortex Streets, Periodic Wakes, and Induced Vibration Phenomena," *J. Basic Eng.*, vol. 86, pp. 185-196, June 1964.

[41] Mazel, C.H., "Vortex-Excited Vibrations of Marine Cables," M.S. Thesis, M.I.T., June 1976.

[42] Mei, V.C., and I.G. Currie, "Flow Separation on a Vibrating Circular Cylinder," *The Physics of Fluids*, vol. 12, no. 11, pp. 2248-2254, November 1969.

[43] Miles, J.W., "Stability of Forced Oscillations of a Vibrating String," Journal of the Acoustical Society of America, vol. 38, pp. 855-861.

[44] Minorsky, Nicholas, **Nonlinear Oscillations,** Robert E. Krieger Publishing Co., Huntington, N.Y., 1974.

[45] Morrison, J.R., M.P. O'Brien, J.W. Johnson, and S.A. Schaaf, "The Force Exerted by Surface Waves on Piles," *Petroleum Transactions*, AIME, vol. 189, pp. 149-154, 1950.

[46] Nayfeh, A.H., **Perturbation Methods,** John Wiley and Sons, N.Y., 1973.

[47] Nayfeh, A.H., and D. T. Mook, **Nonlinear Oscillations,** John Wiley and Sons, N.Y., 1979.

[48] O'Malley, C.D., **Leonardo's Legacy: An International Symposium,** University of California Press, 1969.

[49] Ramberg, S.E., and O.M. Griffin, "Vortex Formation in the Wake of a Vibrating Flexible Cable," *J. Fluids Eng.*, vol. 96, pp. 317-322, December 1974.

[50] Ramberg, S.E., and O.M. Griffin, "Velocity Correlation and Vortex Spacing in the Wake of a Vibrating Cable," *J. Fluids Eng.*, vol. 98, pp. 10-18, March 1976.

[51] Raposo, P.A., "Transverse Oscillations of a Cylinder in Unioform Flow," M.S. Thesis, Naval Postgraduate School, Monterey, CA, 1976.

[52] Rayleigh, J.W.S., **Scientific Papers,** (Six Volumes Bound as Three), vols I-II, Dover Publications, N.Y.. 1964, §61 "The Aeolian Harp," pp. 413-414.

[53] Rayleigh, J.W.S., **The Theory of Sound** Vol. II, Second Ed., Dover Publications, N.Y., 1945.

[54] Rosenhead, L., "The Formation of Vortices from a Surface of Discontinuity," *Royal Society of London Proceedings*, Series A, vol. 134, pp. 170-192, 1931.

[55] Roshko, A., "A New Hodograph for Free-Streamline Theory," NACA TN 3168, 1954.

[56] Roshko, A., "On the Drag and Shedding Frequency of Two-Dimensional Bluff Bodies," TN 3169, 1954.

[57] Roshko, A., "Experiments on the Flow Past a Circular Cylinder at Very High Reynolds Number," *J. Fluid Mech.*, vol. 10, pp. 345-356, 1961.

[58] Sarpkaya,T., "An Analytical and Experimental Study of the In-Plane and Transverse Oscillations of a Circulat Cylinder in Uniform Flow," Report No. NPS-59SL75051-B, Naval Postgraduate School, Monterey, CA, May 30 1975.

[59] Sarpkaya, T., "Transverse Oscillations of Circular Cylinder in Uniform Flow, Part 1," Report No. NPS-69SL77071-R, Naval Postgraduate School, Monterey, CA, December 25, 1977.

[60] Sarpkaya, T., "Fluid Forces on Oscillating Cylinders," ASCE Fall Convention and Exhibit, Preprint 2921, October 1977.

[61] Schlichting, H., **Boundary Layer Theory,** Sixth Ed., McGraw Hill, 1968.

[62] Shiraishi, T., "The Vortex Induced Oscillation of Elastic Structural Elements," M.E. Thesis, California, Institute of Technology, 1977.

[63] Skop, R.A., and O.M. Griffin, "A Model for the Vortex-Excited Resonant Response of Bluff Cylinders," *J. Sound and Vib.*, vol. 27, p. 225-233, 1973.

[64] Skop, R.A., and O.M. Griffin, "On a theory for the Vortex-Excited Oscillations of Flexible Cylindrical Structures," *J. Sound and Vib.*, vol. 41, part 3, pp. 263-274, 1975.

[65] Strouhal, V., "Ueber eine Besondere Art der Tonerregung," *Ann. Physik* (Leipzig), 1878.

[66] Struble, R.A., **Nonlinear Differential Equations,** McGraw Hill, 1962.

[67] Toebes, G.H. "The Unsteady Flow and Wake Near an Oscillating Cylinder," *J. Basic Eng.*, vol. , pp. 493-505, September 1969.

[68] Van der Pol, B., "Forced Oscillations in a Circuit with Non-linear Resonance, *Phil. Mag.* S. 7, vol. 3, no. 13, pp. 65-80, 1927.

[69] Vandiver, J.K., "Performance Evaluation of Various Strumming Suppression Devices," Report no. 77-2, M.I.T. Ocean Engineering, March 1977.

[70] Vickery, B.J., "Fluctuating Lift and Drag on a Long Cylinder of Square Cross-Section in a Smooth and in a Turbulent Stream," *J. Fluid Mech.*, vol. 25, part 3, pp. 481-494, 1966.

[71] von Karman, Theodore,"Über den Mechanismus des Widerstandes denein bewegter Korper ub eubeb FlüssigkeitErfahrt", Nachr. Könige, 1912; available in translation from the National Translation Center, # 76-51072.

[72] Wood, Alexander, **Acoustics,** Dover Publications, N.Y., 1966.